Design and Development of a Single-Catheter Ambulatory Cystometry System with Motion Context Awareness for Motion Artifact Suppression

---

Savannah Haupt

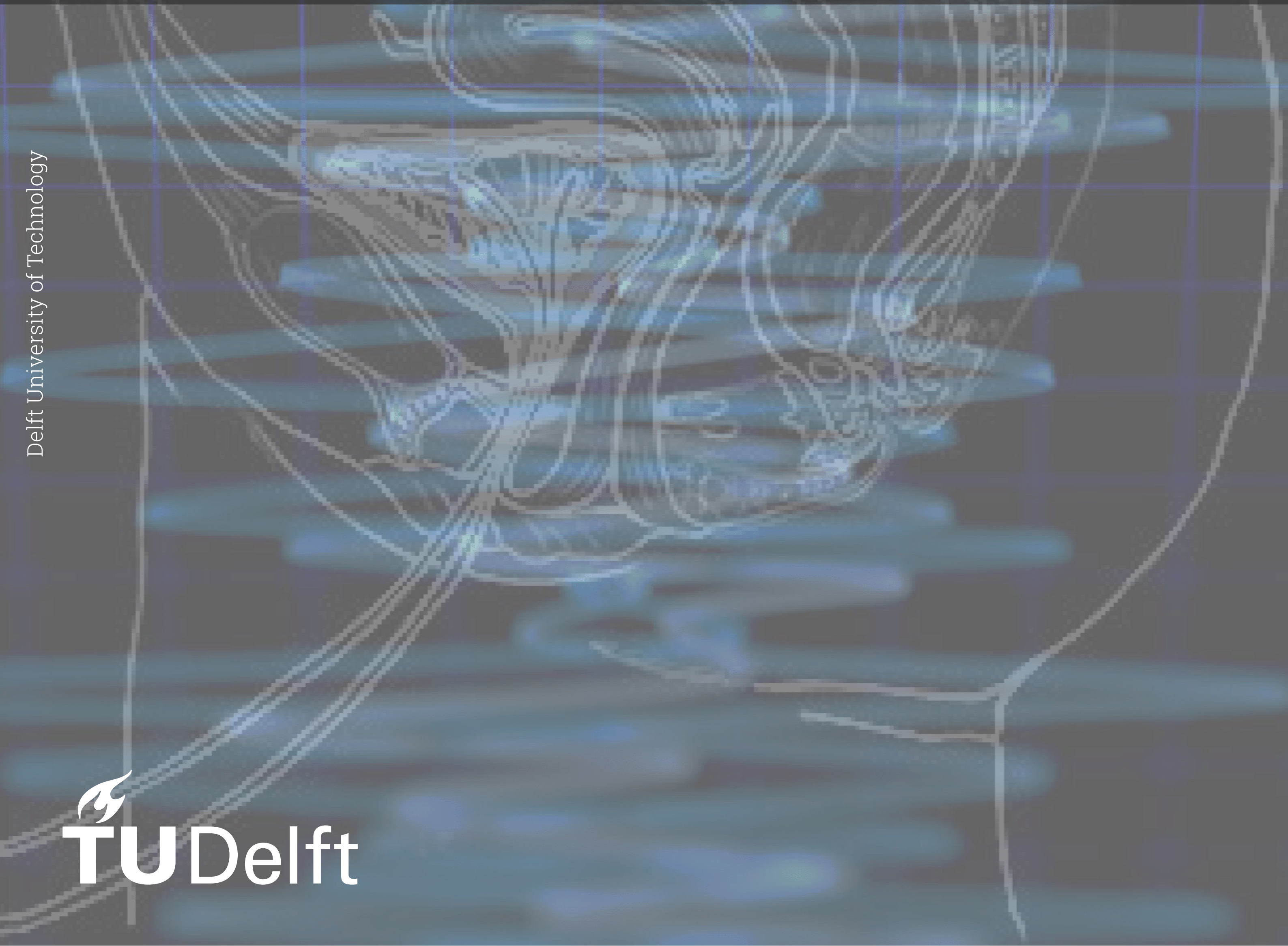

Delft University of Technology

TU Delft

Design and Development of a Single-Catheter Ambulatory Cystometry System with Motion Context Awareness for Motion Artifact Suppression

by

Savannah Haupt

to obtain the degree of Master of Science
at the Delft University of Technology,
to be defended publicly on Tuesday April 7, 2026 at 13:45.

Student number:	5317339
Project duration:	March, 2025 – March, 2026
Thesis committee:	Prof. dr. ir. T. Horeman, TU Delft, Chair Prof. dr. J. Dankelman, TU Delft, External Member

Preface

This thesis forms the final part of the Master of Science programme in Biomedical Engineering at Delft University of Technology. It presents the outcomes of a graduation project focused on improving motion context awareness in single-catheter ambulatory cystometry, with the aim of enabling reliable motion artifact suppression and improving cystometry interpretability.

Conventional cystometry is associated with several limitations, including high cost, invasiveness, limited accessibility, and strict procedural requirements that restrict patient movement. These constraints hinder its implementation in ambulatory settings and limit its scalability. Motivated by these challenges, this thesis investigates two approaches to incorporate motion context awareness into single-catheter ambulatory cystometry systems, thereby enabling downstream motion artifact suppression and improving signal quality for clinical interpretation and diagnosis.

The thesis is structured into two parts: Part A and Part B. Part A focuses on the development of a data processing and machine learning pipeline for motion artifact detection in ambulatory cystometry recordings through binary classification. Multiple classification approaches were explored, including feature-based models, neural networks, and hybrid strategies. This work was done in collaboration with RSI (India) and aimed to evaluate whether motion artifacts and detrusor activity can be reliably distinguished using single-channel bladder pressure recordings alone. However, the limited availability of annotated cystometry datasets prevented the development and validation of robust machine learning models, which consequently shifted the project focus toward system-level innovation in Part B.

Part B focuses on the design, development, and preliminary validation of a low-cost, single-catheter ambulatory cystometry system with integrated motion awareness through inertial measurement unit (IMU) sensing: the UroMonitor. The UroMonitor consolidates pressure sensing, motion sensing, data logging, Bluetooth Low Energy communication, and a custom mobile application for (1) real-time pressure and motion monitoring and (2) post-processing with motion artifact suppression for improved cystometry interpretability. System design was guided by strict constraints in cost, portability, and usability to support feasible clinical deployment. Together, Parts A and B investigate two alternative strategies for achieving motion context awareness in ambulatory bladder pressure monitoring.

This graduation project has been both challenging and rewarding, requiring interdisciplinary integration across biomedical engineering, embedded systems, data analysis, and software development. I would like to express my gratitude to my supervisor, Tim Horeman, for his guidance throughout this project. I am also thankful to my family for their encouragement and for proofreading many pages of this report. Finally, I would like to deeply thank Geraldo Gomes for his invaluable technical insight and guidance; his contribution has been instrumental to the completion of this work.

Savannah Haupt
Delft, April 2026

Abstract

Title of thesis: Design and Development of a Single-Catheter Ambulatory Cystometry System with Motion Context Awareness for Artifact Reduction
Author: Savannah Haupt
Date: 26 February 2026
Committee: Prof. Dr. Ir. T. Horeman
Prof. Dr. J. Dankelman

Lower urinary tract dysfunction (LUTD) refers to a range of disorders affecting the lower urinary tract and impacts millions of individuals worldwide, diminishing quality of life. Urodynamic studies (UDS), including cystometry, are used to diagnose LUTDs by measuring intravesical bladder pressure to assess bladder function. Conventional cystometry relies on a dual-catheter configuration, in which a second abdominal catheter serves as a reference signal to distinguish motion artifacts from true detrusor contractions. While effective, this approach increases invasiveness, is costly, and may limit bladder monitoring under natural conditions. Ambulatory cystometry enables real-world symptom replication during daily activities, but still relies on dual catheters.

This thesis investigates two strategies to enable motion context awareness in single-catheter ambulatory cystometry, aiming to reduce invasiveness, improve accessibility, and maintain diagnostic reliability.

Part A explores a machine learning–based approach to distinguish motion artifacts from detrusor contractions using a single pressure signal. A structured, posture-aware signal processing and classification pipeline was developed and evaluated using cystometry data from ten patients. Multiple modelling strategies were evaluated, including feature-based classifiers, neural network architectures, and hybrid strategies. Neural networks demonstrated superior overall performance, although increasing architectural complexity did not result in noticeable performance gains. While results are limited by cohort size, the findings indicate that motion artifacts and detrusor events exhibit distinguishable pressure characteristics and establish a scalable analytical framework for future dataset expansion.

Part B addresses motion context awareness through hardware integration. The UroMonitor, a low-cost, single-catheter ambulatory cystometry prototype, was independently designed and developed. The system integrates a pressure sensor, inertial measurement unit (IMU), microcontroller, wireless connectivity, and on-board storage within a portable, battery-powered platform. By simultaneously acquiring pressure and motion signals, the device enables correlation-based identification and suppression of motion artifacts without requiring a second catheter. Phantom testing demonstrated reliable motion detection, with acceleration magnitude signals achieving a mean recall of 95.4%. The prototype satisfied predefined physical, electrical, economic, physiological, and usability design constraints.

Together, these contributions demonstrate the technical feasibility of a low-cost, motion-aware, single-catheter ambulatory cystometry system through both machine learning and hardware-based strategies, providing a foundation for future clinical validation and scalable deployment, including in low-resource healthcare settings.

Contents

Nomenclature

Abbreviations

Abbreviation	Definition
AUDS	Ambulatory urodynamics
BD	Bladder diary
BLE	Bluetooth Low Energy
BO	Bladder oversensitivity
BOO	Bladder outlet obstruction
CMG	Cystometrogram
CNN	Convolutional neural network
CNS	Central nervous system
DAC	Detrusor acontractility
DL	Deep learning
DO	Detrusor overactivity
DRC	Design Rule Checking
DSD	Detrusor sphincter dyssynergia
DWT	Discrete wavelet transform
DU	Bladder underactivity
ECG	Electrocardiography
EEG	Electroencephalography
EMG	Electromyography
EMI	Electromagnetic Interference
FVC	Frequency-volume chart
HAR	Human activity recognition
ICS	International Continence Society
IMU	Inertial Measurement Unit
ISD	Intrinsic sphincter deficiency
LMICs	Low- and middle-income countries
LPP	Leak point pressure
LR	Logistic regression
LSTM	Long short-term memory
LUT	Lower urinary tract
LUTD	Lower urinary tract dysfunction
LUTS	Lower urinary tract symptoms
MA	Motion artifact
MCU	Microcontroller unit
ML	Machine learning
MLP	Multi-layer perceptron
MS	Multiple sclerosis
MUI	Mixed urinary incontinence
NDO	Neurogenic detrusor overactivity
PAG	Periaqueductal gray
PCA	Principal component analysis
PCB	Printed circuit board
PCBA	Printed circuit board assembly
PLI	Powerline interference
PMC	Pontine micturition centre
PNS	Peripheral nervous system

Abbreviation	Definition
PPG	Photoplethysmography
PR AUC	Precision–recall area under the curve
PVR	Post-void residual
RCSD	Reduced compliance storage dysfunction
RF	Random forest
RNN	Recurrent neural network
ROC AUC	Receiver operating characteristic - area under curve
SCI	Spinal cord injury
SNR	Signal-to-noise ratio
SUI	Stress urinary incontinence
SVM	Support vector machine
UDS	Urodynamic studies
UPP	Urethral pressure profilometry
USI	Urodynamic stress incontinence
UUI	Urgency urinary incontinence
VUDS	Video urodynamics
XGBoost	Extreme Gradient Boosting

Symbols

Symbol	Definition	Unit
P_{det}	Detrusor pressure	$\mathrm{cmH_2O}$
P_{abd}	Abdominal pressure	$\mathrm{cmH_2O}$
P_{ves}	Vesical pressure	$\mathrm{cmH_2O}$

1

Introduction

Lower urinary tract dysfunction (LUTD) encompasses a range of disorders affecting the lower urinary tract (LUT), affecting millions of individuals worldwide and significantly reducing quality of life [1]. Symptoms of LUTD, commonly referred to as lower urinary tract symptoms (LUTS), include urinary urgency, frequency, nocturia, incontinence, and incomplete bladder emptying, among others [2]. These symptoms may arise from detrusor overactivity, impaired contractility, outlet obstruction, or neurological dysfunction, requiring physiological assessment for accurate diagnosis.

Urodynamic studies (UDS) comprise a group of diagnostic tests designed to evaluate LUT function through the measurement of pressure and flow dynamics during bladder filling and voiding phases [3, 4, 5]. These investigations include uroflowmetry, post-void residual (PVR) measurement, cystometry, pressure-flow studies, electromyography (EMG), urethral pressure profiling (UPP), leak point pressure (LPP) measurement, and video urodynamics (VUDS) [5]. Among these, cystometry remains the gold standard for evaluating bladder storage function during filling [6, 7, 8]. It involves catheter-based measurement of intravesical pressure (P_{ves}) and intra-abdominal pressure (P_{abd}) via a transurethral bladder catheter and a rectal reference catheter [9, 7]. Detrusor pressure (P_{det}) is calculated as the difference between P_{ves} and P_{abd}, enabling differentiation between true detrusor contractions and pressure changes caused by abdominal straining, coughing, or posture changes [8]. The resulting pressure–time graph, termed a cystometrogram (CMG), provides key diagnostic information on bladder sensation, compliance, storage capacity, and involuntary contractions [8].

Despite its diagnostic value, conventional cystometry presents several limitations. The procedure is invasive, requiring dual catheterisation, which can cause discomfort, anxiety, embarrassment, and suppression of natural symptom expression [7, 5, 3, 10]. Catheterisation is also associated with risks including urinary tract infection, haematuria, and dysuria [11]. In addition, patients must remain relatively immobile during testing to minimise motion artifacts, which can obscure pressure signals and require manual annotation [12, 13].

Cystometry is also limited by its artificial clinical setting, controlled bladder filling rates, and short test duration, which may fail to replicate real-life symptom patterns [7, 5, 14]. Interpretation of cystometrograms is also highly dependent on clinician expertise and is subject to intra- and interobserver variability, particularly in artifact-contaminated recordings [4]. These factors, combined with high equipment and personnel costs, limit accessibility, particularly in low-resource settings [15, 16, 17, 18].

Ambulatory cystometry has emerged to address some of these limitations by enabling longer-term monitoring during natural daily activities. While this improves symptom replication, existing systems still rely on dual catheters and remain susceptible to motion artifacts, limiting their practicality and patient comfort [19, 7, 10].

Single-catheter approaches offer a promising alternative by improving comfort, reducing invasiveness, and enabling low-cost deployment. However, the absence of an abdominal reference signal removes the ability to directly distinguish between true detrusor contractions and motion-induced pressure changes. This creates a fundamental challenge in the reliable interpretation of bladder pressure signals in ambulatory environments.

Research Problem and Gaps

Based on these limitations, several key gaps remain in current urodynamic practice:

- Lack of minimally invasive, low-cost, and ambulatory cystometry systems capable of replicating physiological bladder behaviour in real-world environments.
- Absence of robust and objective methods for detecting and removing motion artifacts in single-channel bladder pressure recordings.
- Limited integration of motion context into cystometric analysis, restricting the ability to distinguish physiological events from artifacts.
- High reliance on clinician expertise, leading to interobserver variability and increased workload.
- Limited accessibility of urodynamic diagnostics in low-resource settings due to cost and infrastructure requirements.

These gaps define a fundamental technical challenge: how can bladder pressure be accurately and continuously measured, and how can motion artifacts and true detrusor contractions be reliably identified and interpreted in single-channel cystometry without an abdominal reference signal?

This problem can be further defined as follows:

- **Why:** Current cystometry methods are invasive, costly, and limited in their ability to replicate true bladder behaviour, while single-catheter approaches are not yet clinically established and lack reliable mechanisms to distinguish motion artifacts from true physiological events.
- **What:** Reliable measurement and interpretation of bladder pressure signals in the presence of motion artifacts, specifically the accurate identification of true detrusor contractions in single-channel cystometry.
- **Where:** Ambulatory, real-world environments where patients are mobile and engaged in daily activities.
- **When:** During bladder filling and storage phases over extended monitoring periods, where motion artifacts frequently overlap with physiological signals.
- **Who:** Patients requiring urodynamic assessment and clinicians who depend on accurate and interpretable diagnostic data.

Research Objectives and Questions

In response to these challenges, the primary objective of this thesis is to investigate two complementary motion-aware strategies for single-catheter ambulatory cystometry, referred to as Part A and Part B. Part A is conducted in collaboration with the Rural Surgery Innovation (RSI) group in India, who are developing *Uropine*, a single-catheter, semi-ambulatory urodynamic system aimed at improving access to bladder diagnostics in low-resource settings. The system is designed to record bladder pressure and patient-reported sensations, extract clinically relevant urodynamic parameters, and provide automated diagnostic insights while requiring minimal clinical infrastructure. Specifically, Part A focuses on machine learning–based motion artifact discrimination using signal-derived features from clinical datasets obtained with the Uropine system.

Part B focuses on integrated hardware-based motion sensing using inertial measurement to provide contextual motion information within a low-cost, ambulatory cystometry system. This includes the design and development of a prototype device that extends the goals of Uropine with additional capabilities for long-term, autonomous monitoring and motion artifact suppression. Together, these approaches aim to enable reliable interpretation of bladder pressure signals in ambulatory settings without the need for an abdominal reference channel.

The central research questions are:

1. Can motion artifacts be reliably distinguished from true detrusor contractions in single-channel cystometry using machine learning approaches?
2. Can low-cost inertial sensing provide a practical alternative to abdominal reference measurements?
3. Is it feasible to design a low-cost, ambulatory, motion-aware cystometry system for real-world deployment?

Thesis Contributions

This thesis makes the following contributions:

- Proposal and validation of a machine learning framework for motion artifact detection and removal in single-channel cystometry.
- Comparative evaluation of machine learning models for motion artifact discrimination in cystometrograms, highlighting performance trade-offs and applicability.
- Clinical validation of proposed machine learning models using patient data collected from RSI Uropine systems.
- Design and development of a low-cost, ambulatory, single-catheter cystometry device integrating inertial motion sensing for motion artifact detection.
- Demonstration of motion-aware cystometry through hardware and data-driven approaches.
- Contribution toward automated and scalable urodynamic diagnostics with reduced clinician workload and improved accessibility.

Chapter 2 provides background on LUT physiology, cystometry, motion artifacts, and existing approaches to artifact suppression. Chapter 3 presents Part A, focusing on machine learning–based motion artifact detection, including methodology and results. Chapter 4 presents Part B, describing the design, implementation, and validation of a low-cost ambulatory cystometry device. Chapter 5 discusses findings from both parts, evaluating technical and clinical feasibility and outlines future directions toward scalable, accessible, motion-aware ambulatory cystometry systems. Lastly, the conclusion is provided in Chapter 6.

2

Background and Fundamentals

2.1 The Lower Urinary Tract (LUT)

The *lower urinary tract (LUT)* consists of the *urinary bladder* and *urethra* in females, and additionally the *prostate* in males (see Figure 2.1). It serves two primary functions: the low-pressure storage of urine received from the upper urinary tract, and the controlled expulsion of urine when socially appropriate. These processes ensure *urinary continence* (bladder control) [20] and *voluntary micturition* (urination), relying on the coordinated activity of muscular, neural, and connective tissue components within the LUT. Several functional disorders can affect the LUT (see Section 2.3). Therefore, in-depth knowledge of the anatomy and physiology of the LUT is essential to understand the pathophysiological mechanisms underlying these disorders, as well as their diagnosis and treatment. This section explores the urinary bladder, urethra, and prostate, discussing their anatomy, functions, histology, and vascular and nerve supply, while also highlighting sex-specific differences [21, 22].

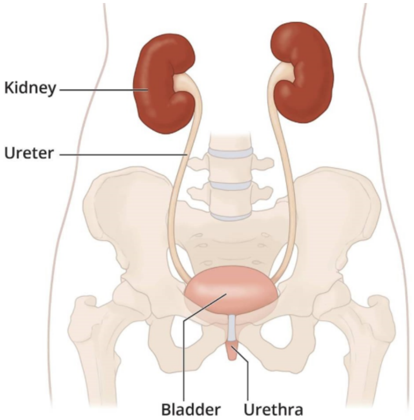

Figure 2.1: Schematic diagram of the urinary tract. The *upper urinary tract* consists of the kidneys and ureters, while the *lower urinary tract (LUT)* includes the urinary bladder and urethra in females, and additionally the prostate in males. Figure from [23].

2.1.1 Organs of the LUT

Urinary Bladder

The urinary bladder is a muscular, compliant organ that plays a central role in the two-phase cycle of the LUT: the low-pressure storage of urine and its high-pressure expulsion during voiding. During the storage phase, the bladder receives urine from the ureters, which transport it from the kidneys. Due to its high compliance, the bladder can accommodate increasing volumes of urine with minimal rises in intravesical pressure [22, 12].

When voiding becomes socially appropriate, the voiding phase is initiated. This is characterised by a forceful contraction of the detrusor muscle – the smooth muscle layer of the bladder wall – under the control of neural signals from the central nervous system (CNS). Simultaneous relaxation of the urethral sphincters accompanies this contraction, facilitating the complete emptying of the bladder [22, 12]. Together, these two tightly regulated functions – urine *storage* and *expulsion* – ensure urinary continence is maintained until voiding is both socially and physiologically appropriate.

The bladder is a hollow, muscular, and highly distensible organ located in the *pelvic cavity*, posterior to the *pubic symphysis* [22]. Its anatomical features (illustrated in Figure 2.2) enable it to accommodate urine at low pressures during filling and to coordinate high-pressure voiding during urination. In terms of shape and position, the bladder resembles a flattened tetrahedron when empty and lies entirely within the pelvic cavity. As it fills, it expands superiorly and anteriorly, becoming more spherical and rising above the pubic symphysis, eventually becoming palpable in the *suprapubic region*. In adults, average bladder capacity ranges from 300 to 500 mL, with slightly larger volumes typically observed in males [22, 5].

Anatomically, the bladder comprises several regions. The *apex* points anteriorly toward the superior edge of the pubic symphysis and is anchored to the *umbilicus* by the *median umbilical ligament* [22]. The *body* is the largest part of the bladder, spanning from the apex to the base [22]. The *base* (or fundus) lies posteroinferiorly, adjacent to the rectum and seminal vesicles in males, and to the anterior vaginal wall and uterus in females [22, 5]. The *neck* is the narrow, inferior segment leading into the urethra and is surrounded by the *internal urethral sphincter* [22, 24].

Internally, the bladder is lined with *transitional epithelium (urothelium)*, which forms folds known as *rugae* when the bladder is empty – these allow for expansion during filling [25]. A notable internal feature is the *trigone*, a smooth triangular area located on the bladder base. It is bounded by the two *ureteric orifices* at its upper corners and the *internal urethral orifice* at its apex [26, 22]. The trigone plays a key role in maintaining unidirectional flow and preventing vesicoureteral reflux [27].

The bladder is supported by several peritoneal and fascial structures that also accommodate its dynamic shape during filling. Its *superior surface* is covered by *peritoneum* and is in contact with the *sigmoid colon* and *small intestine*. In females, it also abuts the *anteverted uterus* [22, 5]. Pelvic floor support is provided by the *levator ani muscles*, while the *pubovesical ligaments* stabilise the bladder anteriorly [22]. The *rectovesical ligaments* and *median umbilical ligament* connect the bladder to the rectum and umbilicus, respectively [22]. Anteriorly, the *retropubic space (space of Retzius)* provides additional space for bladder expansion during filling [28].

The urinary bladder wall consists of four concentric layers, each with distinct structural and functional roles (Figure 2.3). Together, these layers support the bladder's two functions of low-pressure urine storage and high-pressure expulsion during voiding. The innermost layer is the *urothelium*, a specialised transitional epithelium that forms an impermeable barrier, preventing the diffusion of urine into underlying tissues [29, 22]. Beyond its barrier function, the urothelium serves as a *mechanosensor*: it stretches during bladder filling and releases signalling molecules such as ATP, acetylcholine, nitric oxide, and prostaglandins [30]. These molecules activate afferent nerve fibres embedded in the bladder wall, initiating reflex pathways that may ultimately trigger the micturition response if voiding is socially appropriate [22, 29, 31]. Beneath the urothelium lies the *lamina propria*, a vascularised connective tissue layer rich in nerves and interstitial cells. Functionally, it contributes to bladder compliance and sensory signalling, forming part of the bladder's afferent system that regulates the storage phase and micturition reflex [22, 32, 33].

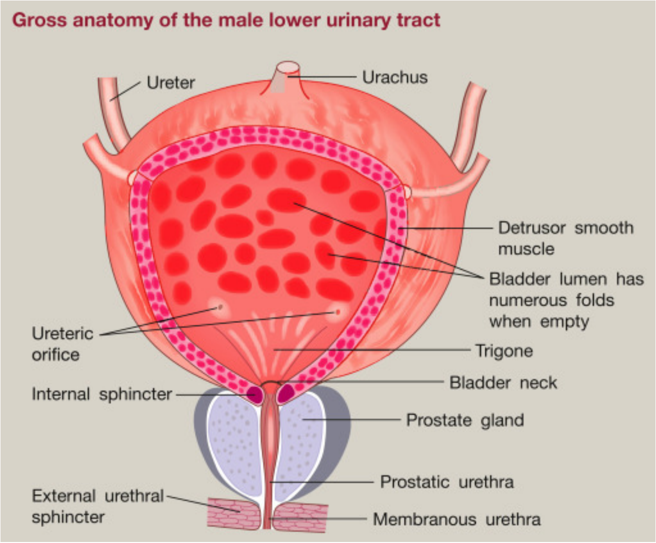

Figure 2.2: Gross anatomy of the male lower urinary tract, showing key anatomical structures of the urinary bladder, including the *body*, *trigone*, *bladder neck*, *detrusor smooth muscle*, and *internal urethral sphincter*, as well as its relationship to the *prostate gland* and *urethra*. The bladder lumen contains rugae when empty, allowing for expansion during filling. In females, the bladder has similar structures but lacks the prostate and features a shorter urethra. Figure from [34].

The *detrusor muscle* forms the thick muscular layer responsible for generating the pressure needed for voiding. While the muscle fibres are generally arranged in a random orientation, near the internal urethral orifice they become more organised into three layers: an inner longitudinal layer, a middle circular layer, and an outer longitudinal layer [22, 32, 35]. This arrangement gives rise to the *internal urethral sphincter*, a key structure in maintaining urinary continence [22]. The detrusor also exhibits viscoelastic properties, enabling it to stretch with minimal increases in intravesical pressure during filling [36]. Moreover, low-amplitude spontaneous contractions occur during the storage phase, even in the absence of neural input. These contractions are thought to preserve muscle tone and sarcomere length [37].

The outermost layer of the bladder varies depending on anatomical location. On the superior surface, the bladder is covered by the serosa, a thin connective tissue layer continuous with the peritoneal lining of the abdominal wall. Elsewhere, it is surrounded by the *adventitia*, which anchors the bladder to surrounding pelvic structures, providing structural support and stability [22, 33].

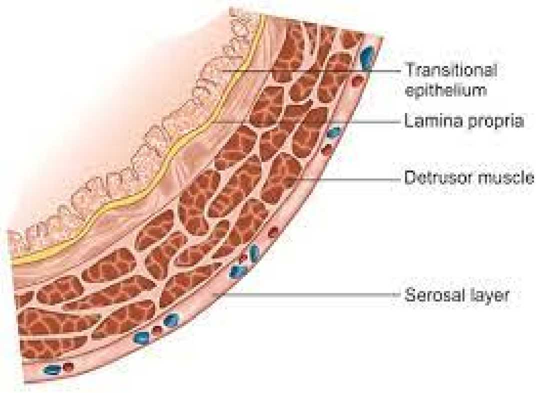

Figure 2.3: Histological structure of the urinary bladder wall, illustrating the four principal layers: *urothelium*, *lamina propria*, *detrusor muscle*, and *serosa*. The serosa covers only the superior surface; in other regions, it is replaced by the *adventitia*, which anchors the bladder to surrounding structures. These layers are present in both sexes. Figure from [38].

Urethra

The urethra provides a passage for urine expulsion in both sexes, and in males, it also functions as a passage for semen during ejaculation. It houses the *external urethral sphincter*, which maintains urinary continence and allows voluntary control of voiding [22, 39]. It is a fibromuscular tube extending from the bladder neck to the external environment. Its structure, including length and course, differs between males and females due to functional and genital differences between the sexes.

In females, the urethra is relatively short, measuring approximately 4 cm in length, and is embedded within the anterior vaginal wall. It extends from the bladder neck to the *external urethral orifice*, which opens into the *vestibule* between the clitoris and vaginal opening [40, 22, 41]. Mucus secretion is provided by *Skene's glands*, periurethral structures that are homologous to the male prostate and contribute to lubrication of the distal urethra [41].

In males, the urethra is considerably longer – approximately 20 cm – and is divided into posterior and anterior sections. The *posterior urethra* comprises the *prostatic urethra* and *membranous urethra* portions), while the *anterior urethra* includes the *bulbar urethra* and *penile urethra* (Figure 2.4) [22, 41, 40, 39]:

- *Prostatic urethra:* About 3-4 cm long, it extends from the bladder neck and is surrounded by the *internal urethral sphincter*. It traverses the *prostate gland* and joins the membranous urethra at the apex of the prostate [42, 39, 41].
- *Membranous urethra:* Approximately 2 cm long, this section passes through the *urogenital diaphragm* and is surrounded by the *external urethral sphincter*. It receives the openings of the vas deferens, prostate, seminal vesicles, and ampullary glands [42, 39, 41]
- *Bulbar urethra:* Located within the bulb of the corpus spongiosum, this segment redirects the urethra from a downward to an anterior trajectory [42, 39, 41].
- *Penile (spongy) urethra:* The longest segment, extending through the corpus spongiosum along the ventral aspect of the penis and terminating at the external urethral meatus on the glans penis [42, 39, 41].

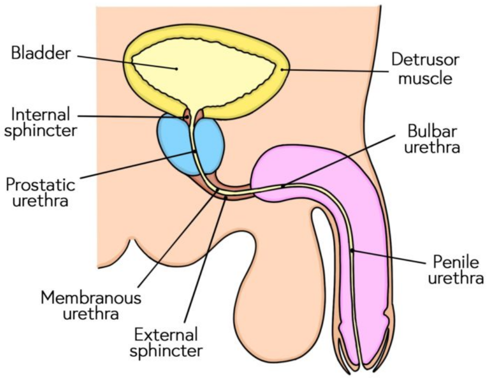

Figure 2.4: Anatomy of the male urethra, highlighting its four distinct segments: *prostatic*, *membranous*, *bulbar*, and *penile (spongy) urethra*. Figure from [42].

Figure 2.5 highlights the key differences between the male and female urethra, where the female urethra is significantly shorter.

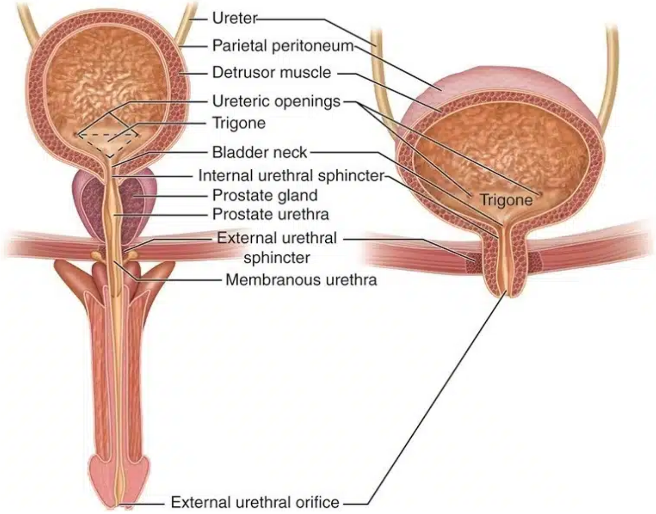

Figure 2.5: Comparison of male and female urethral anatomy. The female urethra is significantly shorter and embedded within the anterior vaginal wall, while the male urethra is longer and divided into multiple distinct segments. Figure from [43].

The urethra is composed of three principal layers: a luminal epithelial lining, a connective tissue-rich lamina propria, and surrounding muscle layers. While this general architecture is shared across sexes, the epithelial composition and associated accessory glands vary between males and females.

In females, the epithelial lining transitions along the urethral course. The proximal portion is lined by *transitional epithelium* (urothelium), which transitions to non-keratinising stratified squamous epithelium distally, and ultimately becomes keratinised epithelium at the external urethral orifice [44, 22]. Beneath the epithelium lies the *lamina propria*, a vascularised layer of connective tissue that provides flexibility and structural support [44]. This is enclosed by two smooth muscle layers — an inner longitudinal and an outer circular layer — which, near the bladder neck, form the internal urethral sphincter, an involuntary structure under autonomic control [44]. In the middle and distal urethra, a layer of striated muscle surrounds the urethra, forming the external urethral sphincter, which enables voluntary control over urination [22, 44].

In males, the epithelial lining varies more distinctly across its four anatomical regions. The prostatic urethra is lined by *transitional epithelium*, while the membranous urethra is lined by *pseudostratified columnar epithelium*. The bulbar and penile urethra are primarily lined by *non-keratinised stratified squamous epithelium* [45, 46, 47]. Like in females, the underlying *lamina propria* contains blood vessels, lymphatics, and nerve endings, but it also includes Cowper's glands and glands of Littre, which secrete mucous that protects the epithelium [47, 45]. The muscular layer consists of inner longitudinal and middle circular smooth muscle, along with an outer striated muscle component. At the bladder neck, the circular smooth muscle thickens to form the internal urethral sphincter. The outer striated muscle forms the external urethral sphincter [45, 47].

The involuntary *internal urethral sphincter* is formed by a continuation of the circular smooth muscle fibres of the detrusor muscle. It is located at the level of the bladder neck and remains tonically contracted under sympathetic control during the storage phase [48, 49, 50]. The voluntary *external urethral sphincter* is composed of striated muscle and encircles the distal urethra. It is controlled by the pudendal nerve, providing voluntary control of micturition [49, 48, 50]. Collectively, these two sphincters are referred to as the urethral sphincter complex.

These sphincters coordinate with the detrusor muscle to maintain continence during the storage phase and permit urine flow during voiding, when both sphincters relax as the detrusor muscle contracts [49, 48, 50]. In females, the sphincters are anatomically smaller and weaker, predisposing women to urinary incontinence (the inability to control one's bladder) [22].

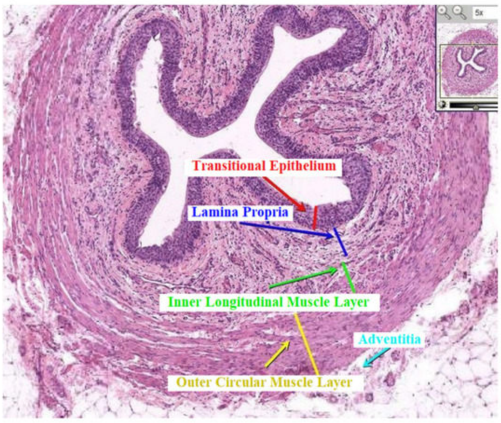

Figure 2.6: Histological section of the proximal urethra (common to both sexes), showing the *transitional epithelium (urothelium)*, *lamina propria*, *inner longitudinal smooth muscle layer*, *outer circular smooth muscle layer*, and *adventitia*. These layers form the basic histological structure in both males and females. Figure from [51].

Prostate (Male Only)

The *prostate gland* is an ovoid-shaped, fibromuscular, and glandular organ responsible for producing proteolytic enzymes in semen. It produces approximately 30% of seminal fluid volume, with the remaining volume primarily produced by the seminal vesicles [22, 52]. This walnut-sized gland is located in the pelvic cavity, just below the bladder neck and above the external urethral sphincter. Posteriorly, it is in close contact with the rectum [52].

2.1.2 Vascularisation, Lymphatic Drainage, and Innervation of the LUT

Arterial Supply

The LUT receives its arterial supply primarily from branches of the *anterior division of the internal iliac artery* (also known as the *hypogastric artery*), with notable sex-specific variations.

The *urinary bladder* is mainly supplied by the *superior vesical arteries*, which vascularise the bladder dome and body [22, 53, 54, 35]. The inferior and posterior regions of the bladder receive sex-specific arterial input. In females, these areas are supplied by the vaginal arteries [22, 53, 35], which are homologous to the inferior vesical arteries found in males [22, 53, 35]. Additional minor contributions arise from the *obturator* and *inferior gluteal arteries* [55, 22, 35].

The *urethra* demonstrates a segmental and sex-specific pattern of blood supply. In females, the *superior urethra* is supplied by branches of the *inferior vesical* and *vaginal arteries* [41, 44, 22], while the *inferior urethra* receives blood from branches of the *internal pudendal artery* [41, 44, 22]. In males, the *prostatic urethra* is supplied by the *inferior vesical artery*, a direct branch of the internal iliac artery) [41]. The *membranous urethra* is vascularised by the *bulbourethral (bulbar) artery*, which arises from the internal pudendal artery [41]. Blood to the *bulbar and penile urethra* is also delivered by branches of the *internal pudendal artery* [41].

Figure 2.7 illustrates the arterial supply of the female LUT, including the superior vesical, vaginal, inferior vesical, internal pudendal, and inferior gluteal arteries. In males, arterial supply to the LUT, including the bladder, urethra, and prostate, is shown in Figure 2.8. The *prostate* is primarily supplied by the *prostatic arteries*, with secondary contributions from the *middle rectal* and *internal pudendal arteries*. A close-up of the male urethral blood supply, particularly the course of the bulbourethral artery, is provided in Figure 2.9.

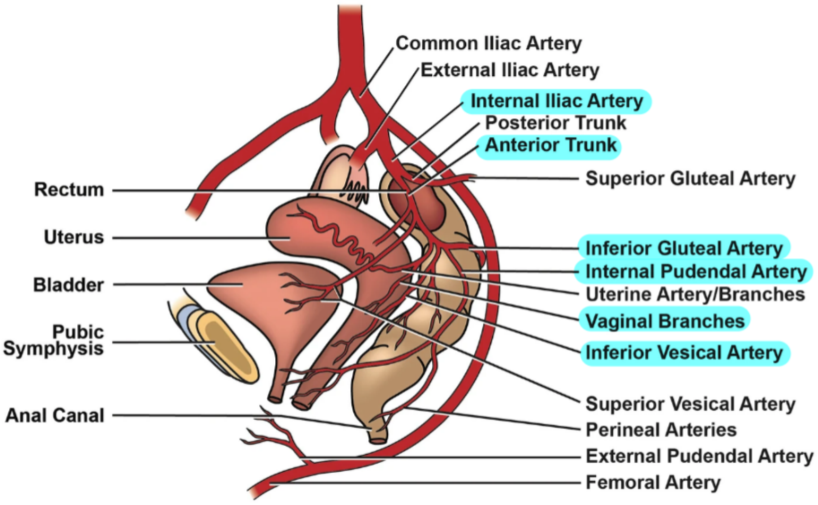

Figure 2.7: Arterial supply of the female lower urinary tract, illustrating branches of the anterior division of the *internal iliac artery*, including the *superior vesical*, *vaginal*, and *inferior vesical arteries*, as well as the *internal pudendal* and *inferior gluteal arteries*. The key arteries responsible for arterial supply of the female LUT are highlighted in blue. Figure adapted from [56].

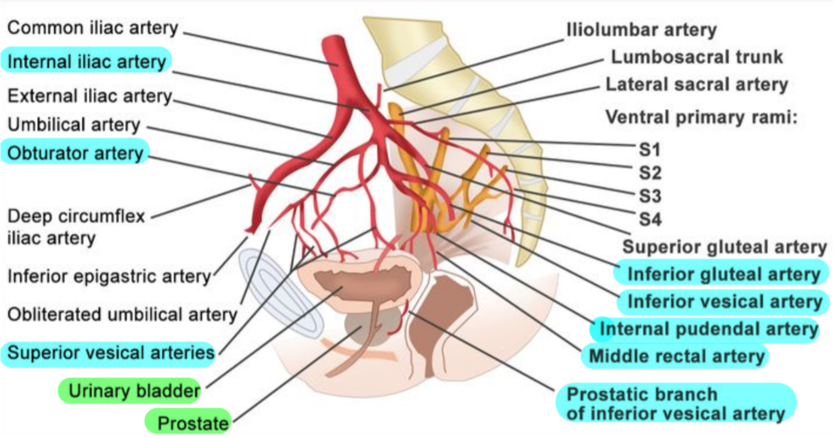

Figure 2.8: Arterial supply of the male lower urinary tract, showing branches of the anterior division of the *internal iliac artery*, including the *superior vesical*, *inferior vesical*, *obturator*, *inferior gluteal*, *internal pudendal*, and *prostatic arteries*. The key arteries responsible for arterial supply of the male LUT are highlighted in blue. Figure adapted from [57].

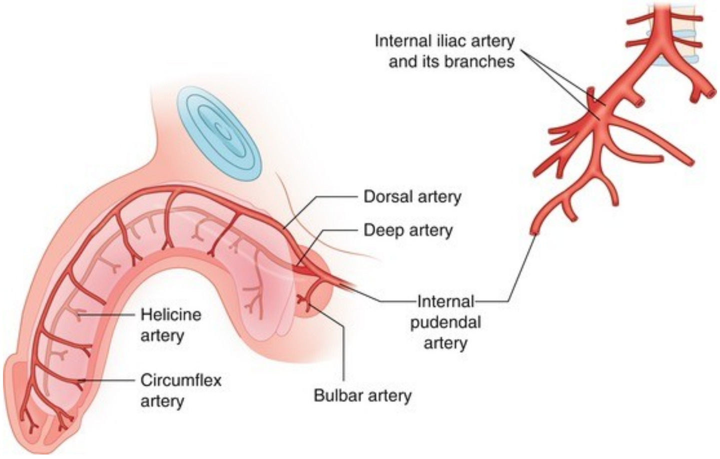

Figure 2.9: Close-up view of the arterial supply to the male urethra, highlighting the *bulbourethral (bulbar) artery*, a branch of the *internal pudendal artery*, which supplies the membranous urethra. Figure adapted from [58].

Venous Drainage

Venous drainage of the LUT closely mirrors the arterial supply, with notable sex-specific differences. In both sexes, the *urinary bladder* is primarily drained by the *vesical venous plexus*, a dense network of veins located at the base of the bladder. Blood from this plexus empties into the *internal iliac veins* via the *superior* and *inferior vesical veins* [35, 22]. In females, the *vesical venous plexus* connects with the *vaginal venous plexus*, providing an additional pathway for pelvic venous drainage [22, 53]. In males, this plexus is continuous with the *prostatic venous plexus*, forming an extensive network surrounding the bladder base, prostate, seminal vesicles, and ductus deferens [22, 53].

The urethra exhibits a segmental and sex-specific venous drainage pattern. In females, venous blood is returned via the *internal pudendal veins* and the *vesical venous plexus*, both of which ultimately drain into the *internal iliac veins* [44, 22]. In males, the proximal urethra – including the *prostatic and membranous urethra* segments -drains into the *prostatic venous plexus*, which subsequently empties into the *internal iliac veins* [39, 59]. More distally, the *bulbar* and *penile urethra* are drained by branches of the *internal pudendal veins*, which also ultimately drain to the *internal iliac veins* [59]. The *prostate* is drained by the *prostatic venous plexus*, which lies between the gland's true and false capsules. This plexus drains into the *internal iliac veins* [52, 22].

Figure 2.10 illustrates the venous drainage of the female LUT, highlighting the vesical and vaginal venous plexuses and their convergence into the internal iliac system. In the male pelvis, venous drainage of the LUT, including continuity between the vesical and prostatic venous plexuses, is shown in Figure 2.11.

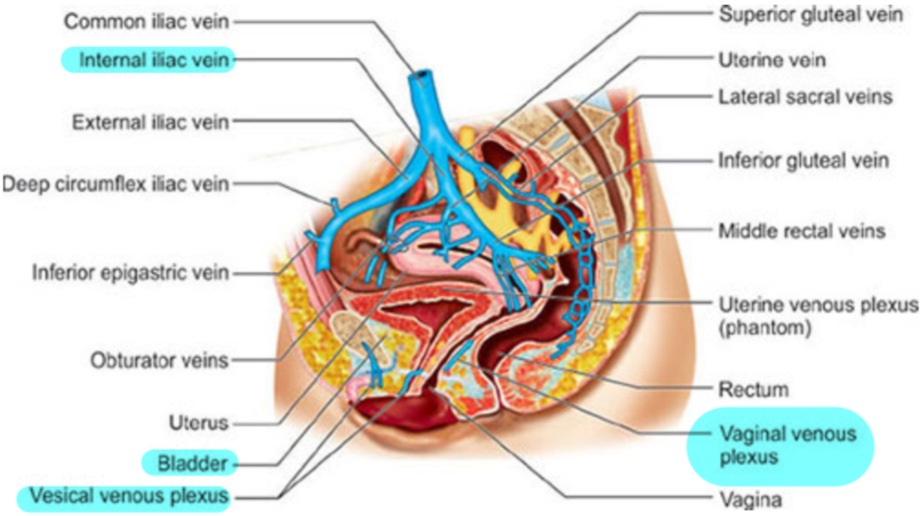

Figure 2.10: Venous drainage of the female lower urinary tract, illustrating the vesical and vaginal venous plexuses, which converge into the internal iliac veins (highlighted). Figure adapted from [60].

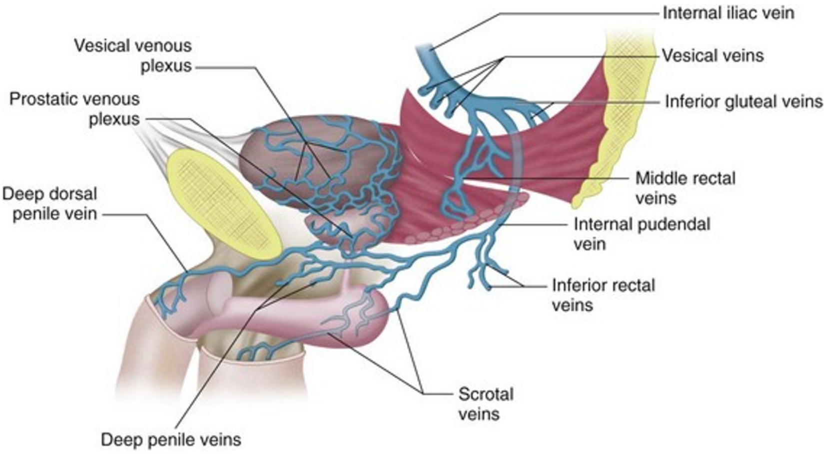

Figure 2.11: Lateral view of the venous drainage of the male lower urinary tract. The vesical venous plexus is continuous with the prostatic venous plexus, forming an interconnected network that surrounds the bladder, prostate, seminal vesicles, and ductus deferens. Drainage occurs primarily via the inferior vesical and internal pudendal veins into the internal iliac vein. Figure adapted from [61].

Lymphatic Drainage

The lymphatic drainage of the LUT varies by anatomical region and differs between sexes due to urethral segmentation and reproductive structures. For the *urinary bladder*, lymph from the *superolateral surfaces* drains primarily into the *external iliac lymph nodes* [22, 53, 35]. In contrast, lymph from the *bladder base and neck* drains into the *internal iliac, sacral* and *common iliac lymph nodes* [22, 53].

Lymphatic drainage of the *urethra* is segmental and sex-specific. In females, the *proximal urethra* drains into the *internal iliac lymph nodes* [41, 44, 22], while the *distal urethra* drains into the *inguinal* and *subinguinal lymph nodes* [41, 44, 22]. In males, the *prostatic and membranous urethra* drain into the *obturator* and *internal iliac lymph nodes* [41, 39], whereas the *bulbar and penile urethra* are drained by the *deep* and *superficial inguinal lymph nodes* [41, 39].

The prostate shares a drainage pattern similar to the bladder base and adjacent urethra, with lymph directed primarily to the *internal iliac* and *obturator lymph nodes* [22]. An overview of these drainage pathways is illustrated in Figure 2.12.

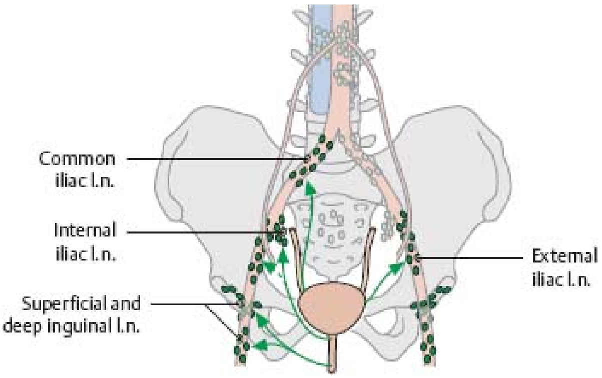

Figure 2.12: Lymphatic drainage of the LUT. The *superolateral bladder* drains to the *external iliac lymph nodes*, while the *bladder base, neck, and prostate* primarily drain to the *internal iliac*, *obturator*, *sacral*, and *common iliac lymph nodes*. Urethral drainage is segment-specific and sex-dependent: in males, the *prostatic and membranous urethra* drain to the *internal iliac* and *obturator nodes*, and the *bulbar and penile urethra* drain to the *inguinal lymph nodes*; in females, the *proximal urethra* drains to the *internal iliac nodes*, while the *distal urethra* drains to the *inguinal lymph nodes*. Figure from [62].

Innervation

The LUT is innervated by a coordinated network of *autonomic* (sympathetic and parasympathetic) and *somatic nerves*, which collectively regulate bladder filling, storage, and voiding functions.

Sympathetic fibres originate from thoracolumbar spinal segments (T10-L2) and travel via the *hypogastric nerves* into the *pelvic plexus* (also known as the inferior hypogastric plexus), a network of nerves in the pelvic cavity [22, 63, 64]. These fibres relax the detrusor muscle during bladder filling – allowing for low-pressure urine storage – and maintain tonic contraction of the involuntary internal urethral sphincter to support continence [22, 35, 65]. In males, sympathetic activity also promotes smooth muscle contraction in the prostate during ejaculation [22].

Parasympathetic fibres originate from sacral spinal segments (S2-S4) and enter the pelvic plexus via the *pelvic splanchnic nerves*. These fibres counteract sympathetic influence by contracting the detrusor muscle to generate voiding pressure and relaxing the internal urethral sphincter to enable urine flow [22, 35, 63, 65]. In males, parasympathetic input also facilitates prostatic secretion [22].

Somatic innervation is provided by motor fibres from the *pudendal nerves*, which also originate from S2-S4. These fibres innervate the external urethral sphincter, enabling voluntary control over micturition and ensuring continence until voiding is socially appropriate [49, 48, 50, 22].

Sensory (afferent) fibres, carried in both sympathetic and parasympathetic pathways, detect bladder fullness and noxious stimuli. These signals are relayed to the CNS and contribute to both reflexive and conscious control of micturition [22, 63].

In males, the *prostatic plexus*, an extension of the pelvic plexus, specifically innervates the urethra and prostate, coordinating continence and ejaculation [22, 66]. In females, the same parasympathetic and sympathetic pathways innervating the bladder and sphincters also supply the urethra directly, while somatic pudendal fibres ensure external urethral sphincter control [65, 22, 44].

Figure 2.13 illustrates the functional neurophysiology of LUT control during bladder filling and voiding. Figure 2.14 provides an anatomical overview of pelvic nerve plexuses, including the prostatic plexus in males. Table 2.1 summarises the primary innervation pathways, their spinal origins, and their target functions.

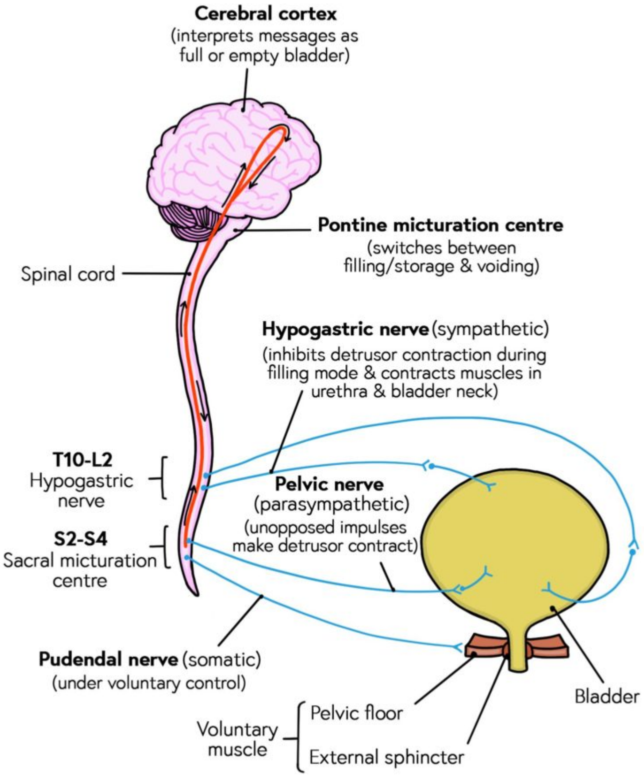

Figure 2.13: Functional innervation of the lower urinary tract (LUT). This schematic illustrates the roles of sympathetic (hypogastric), parasympathetic (pelvic), and somatic (pudendal) nerves in regulating bladder filling and voiding. During filling, the hypogastric nerve inhibits detrusor contraction and contracts the internal sphincter. During voiding, the pelvic nerve promotes detrusor contraction and internal sphincter relaxation. The pudendal nerve controls the external urethral sphincter voluntarily. Sensory feedback to the CNS coordinates these phases. Figure adapted from [67].

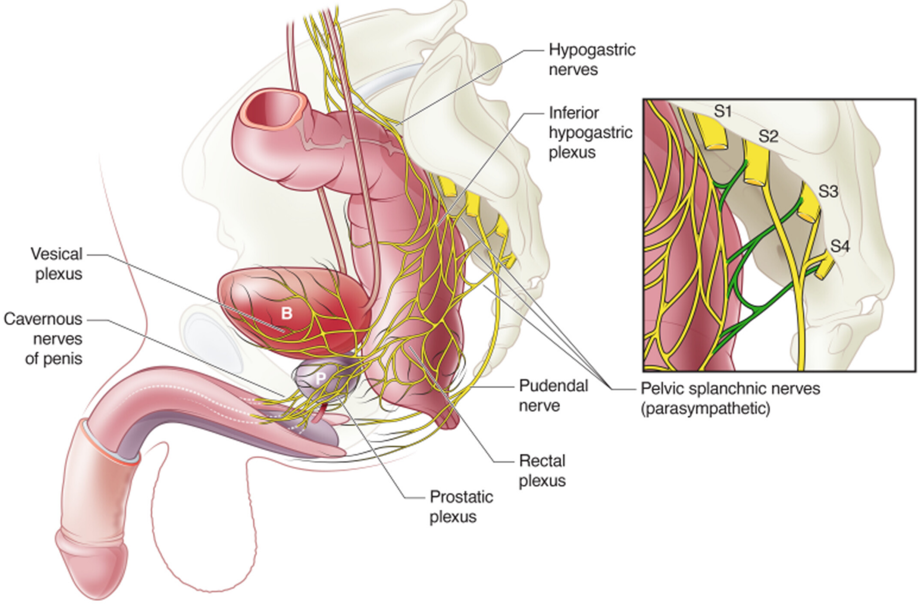

Figure 2.14: Anatomical overview of pelvic nerve plexuses and their target organs. The diagram shows the relationships of the hypogastric nerves, pelvic splanchnic nerves, pudendal nerve, and the pelvic (inferior hypogastric) plexus. The prostatic plexus, a male-specific autonomic network, is also highlighted. These pathways provide autonomic and somatic innervation to the bladder, urethra, and prostate. Figure from [68].

Table 2.1: Summary of the Innervation of the LUT. The table outlines: (1) the type of neural input involved, (2) the corresponding spinal cord segments of origin, (3) the primary nerves or plexuses responsible for conveying the input, and (4) the main target organs and associated functions.

Innervation Type	**Origin**	**Main Nerve / Plexus**	**Targets and Functions**
Sympathetic	T10–L2	Hypogastric nerves via pelvic plexus	– Relaxes detrusor muscle during bladder filling to allow urine storage. – Contracts internal urethral sphincter to maintain continence. – In males: contracts prostatic smooth muscle during ejaculation.
Parasympathetic	S2–S4	Pelvic splanchnic nerves via pelvic plexus	– Contracts detrusor muscle during voiding to expel urine. – Relaxes internal urethral sphincter during voiding. – Facilitates prostatic secretion in males.
Somatic	S2–S4	Pudendal nerve	– Provides voluntary control of the external urethral sphincter (striated muscle). – Enables conscious continence until voiding is appropriate.
Sensory (Afferent)	T10–L2 (sympathetic), S2–S4 (parasympathetic)	Hypogastric and pelvic nerves	– Convey information on bladder fullness and noxious stimuli to the CNS, triggering reflexive and voluntary micturition control.
Prostatic Plexus (Males)	T10–L2 (sympathetic), S2–S4 (parasympathetic)	Prostatic plexus (from pelvic plexus)	– Coordinates innervation of the urethra and prostate gland, supporting continence, ejaculation, and prostatic secretion.

2.2 The Micturition Process

Micturition, or urination, is a coordinated neurophysiological process regulated by a hierarchically organised neural network involving the brain, spinal cord, and peripheral nervous system (PNS). This system enables the bladder to function in two mutually exclusive modes: storage and voiding. These modes are governed by reflex circuits that maintain a reciprocal relationship between detrusor muscle activity and urethral outlet resistance, ensuring that urine is stored when necessary and expelled at socially appropriate times [50, 29].

While micturition is involuntary in infancy, voluntary control typically develops between the ages of three and five. Once established, this control allows the LUT to respond to behavioural, emotional, and environmental cues, coordinating autonomic, somatic, and sensory pathways to ensure proper bladder filling and emptying [50].

2.2.1 Phases of the Micturition Cycle

During the storage phase, sympathetic output via the hypogastric nerves maintains detrusor relaxation and contraction of the internal urethral sphincter. The relaxed state and viscoelastic properties of the detrusor muscle allow the bladder to accommodate increasing volumes of urine without significant increases in pressure. Simultaneously, tonic somatic input through the pudendal nerve sustains contraction of the external urethral sphincter, increasing urethral outlet resistance and maintaining continence [29, 5].

The transition to the voiding phase occurs when afferent signalling from mechanoreceptors in the bladder wall exceeds a functional threshold. These signals are relayed to the periaqueductal gray (PAG) in the midbrain, which integrates them with higher brain centre inputs. If voiding is deemed appropriate, the PAG is disinhibited and activates the pontine micturition centre (PMC). The PMC then orchestrates detrusor contraction alongside relaxation of the internal and external urethral sphincters, enabling urine flow [29, 5]. Figure 2.15 illustrates the coordinated changes in bladder shape, muscle tone, and nervous system activity that occur during the phases of the micturition cycle, including the roles of sympathetic and parasympathetic pathways.

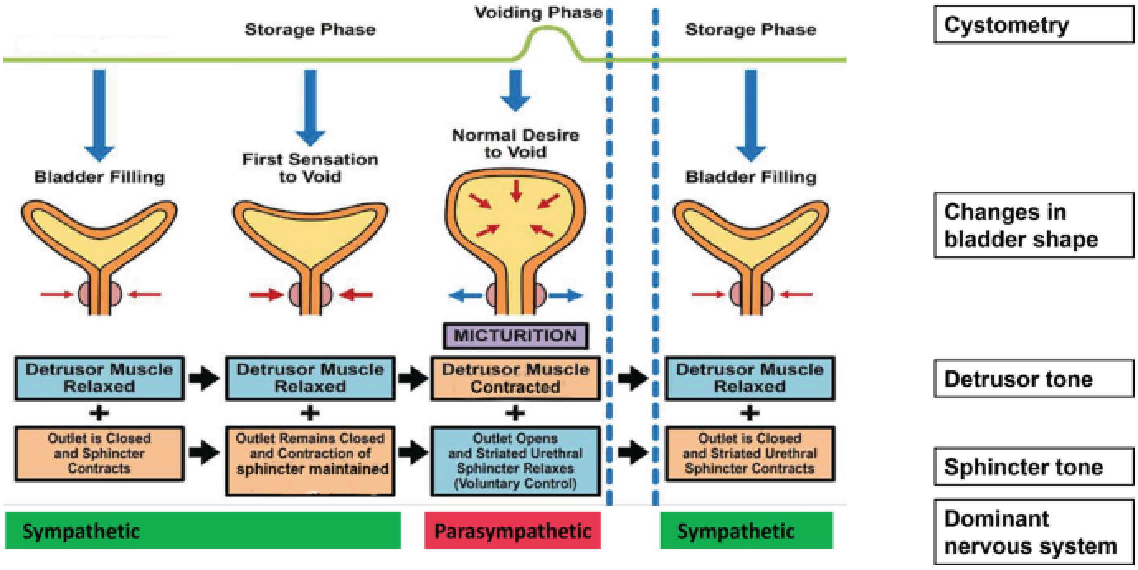

Figure 2.15: Phases of the micturition cycle, including neural control, detrusor and sphincter tone, and bladder shape changes. The diagram illustrates the transition from the storage phase (bladder filling and sensation to void) to the voiding phase (micturition), and then return to storage. During storage, sympathetic activation relaxes the detrusor muscle and contracts the outlet sphincters to maintain continence. During voiding, parasympathetic activation contracts the detrusor and relaxes the sphincters under voluntary control. Figure from [69].

2.2.2 Central Neural Coordination

Control of micturition is centrally coordinated by the PAG in the midbrain, the PMC in the brainstem, and higher brain centres including the prefrontal cortex, thalamus, insula, and hypothalamus. As the bladder fills, stretch-sensitive afferents send signals to the PAG, which relays them to higher centres that assess the appropriateness of voiding. If voiding is not appropriate, the prefrontal cortex suppresses PAG activity, maintaining the storage state. When voiding is consciously permitted, this inhibition is lifted, the PAG activates the PMC, and coordinated voiding is initiated [50].

The PMC acts as the final command centre, sending descending motor commands that stimulate parasympathetic efferents (to contract the detrusor) and inhibit sympathetic and somatic efferents (to relax both urethral sphincters). This coordinated response ensures efficient bladder emptying [50]. The overall organisation of this control pathway, including its connections to spinal centres and peripheral efferent targets, is summarised in Figure 2.16.

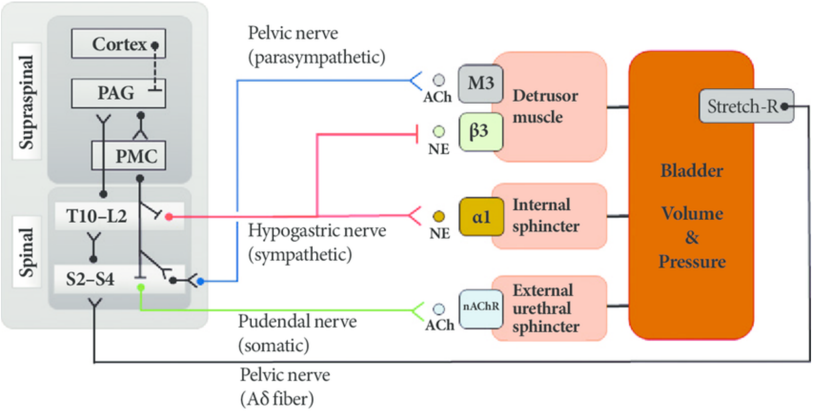

Figure 2.16: Block diagram showing the hierarchical organisation of micturition control: stretching activates afferent pathways that relay information to the PAG, which communicates with higher brain centres (prefrontal cortex, insula, hypothalamus). Upon conscious permission from higher brain centres, the PAG activates the PMC, which initiates detrusor contraction and sphincter relaxation through parasympathetic activation and somatic/ sympathetic inhibition, resulting in urine flow. PAG, periaqueductal gray; PMC, pontine micturition centre; ACh, acetylcholine; NE; norepinephrine; nAChR, nicotinic acetycholine receptor. Figure from [70].

2.2.3 Peripheral Efferent Pathways

Following PMC activation, motor signals travel via three efferent pathways: sympathetic, parasympathetic, and somatic. These pathways are tightly coordinated to ensure the bladder switches seamlessly between storage and voiding [71, 29].

During storage, sympathetic fibres (T10–L2) via the hypogastric nerve inhibit detrusor contraction and maintain tone in the internal urethral sphincter [22, 29]. Somatic motor neurons (S2–S4), via the pudendal nerve, sustain contraction of the external urethral sphincter for voluntary continence [22, 63, 29].During voiding, parasympathetic fibres (S2–S4) via the pelvic nerves release acetylcholine (ACh), which binds to M3 muscarinic receptors in the detrusor muscle, causing contraction. Parasympathetic output also relaxes the internal sphincter [22, 29, 35]. In parallel, PMC-mediated inhibition of the pudendal nerve relaxes the external urethral sphincter, enabling unobstructed urine flow [22, 63, 29]. Neurotransmitters involved in this switch include acetylcholine, norepinephrine, adenosine triphosphate (ATP), and neuropeptides [50].

2.2.4 Peripheral Afferent Signalling

Afferent sensory fibres play a central role in regulating bladder behaviour and initiating the micturition reflex. These fibres originate in the bladder wall, urethra, and pelvic floor, and travel through the pelvic, hypogastric, pudendal, and levator ani nerves to the spinal cord [22]. They detect changes in bladder wall tension during filling via mechanoreceptors and also respond to noxious stimuli such as irritation or inflammation [22, 29]. These signals are integrated in the PAG and higher brain centres. If voiding is inappropriate, cortical inhibition of the PAG maintains storage; if voiding is permitted, PAG disinhibition and PMC activation initiate the voiding phase [50].

2.3 Lower Urinary Tract Dysfunction (LUTD)

Lower urinary tract dysfunction (LUTD) encompasses a broad spectrum of pathophysiological disorders affecting LUT function. These dysfunctions may arise from neurological, anatomical, muscular, or sensory abnormalities, and impair either urinary storage, voiding, or both. LUTD represents the underlying pathophysiology responsible for the majority of lower urinary tract symptoms (LUTS) [72, 73]. It is prevalent in ageing populations and individuals with neurological or structural conditions, and is associated with a reduced quality of life [19, 31]. If left untreated, LUTD may result in complications such as recurrent urinary tract infections or acute kidney injury [7].

To aid diagnosis and guide treatment management, LUTDs are broadly classified according to the phase of the micturition cycle affected - storage, voiding, or both (International Continence Society (ICS)). LUTDs can be further subdivided based on the anatomical origin of the dysfunction. Disorders may arise from abnormal bladder activity or from issues related to the bladder outlet. Storage dysfunctions refer to diagnoses related to abnormal changes in bladder sensation, detrusor pressure or bladder capacity. Table 2.2 provides an overview of storage dysfunctions and their ICS definitions.

Table 2.2: ICS-defined bladder-related and outlet-related storage phase LUTDs [2]. Abbreviations: MS - multiple sclerosis; SCI - spinal cord injury.

LUTD Type	**ICS Definition**
Bladder-Related Storage Dysfunction	
Bladder Oversensitivity (BO)	Increased bladder sensation during filling, including earlier first desire to void, earlier strong desire to void, reduced cystometric bladder capacity, and no abnormal increases in detrusor pressure.
Detrusor Overactivity (DO)	Involuntary detrusor contractions during the bladder storage phase. Classified as idiopathic DO if there is no identifiable neurological cause and as neurogenic DO (NDO) if associated with a neurological condition (e.g., MS, SCI).
Reduced Compliance Storage Dysfunction (RCSD)	Occurrence of a non-phasic rise in detrusor pressure during filling with reduced capacity.
Reduced Compliance (RCSD) Incontinence	Involuntary leakage of urine due to elevated pressure from reduced compliance.
Bladder Outlet-Related Storage Dysfunction	
Urodynamic Stress Incontinence (USI)	Involuntary leakage of urine during filling, associated with increased intra-abdominal pressure in the absence of detrusor contractions.
Intrinsic Sphincter Deficiency (ISD)	A subtype of USI in which sphincter weakness contributes to reduced urethral closure pressures.

Voiding dysfunctions refer to diagnoses related to abnormally slow and/or incomplete bladder emptying. Table 2.3 provides an overview of common voiding dysfunctions and their ICS definitions.

Table 2.3: ICS-defined bladder-related and outlet-related voiding phase LUTDs [2].

LUTD Type	**Definition**
Bladder-Related Voiding Dysfunction	
Detrusor Underactivity (DU)	Weak or short detrusor contractions, usually resulting in prolonged or incomplete bladder emptying. If associated with a neurological condition, it is referred to as neurogenic detrusor underactivity (NDU).
Detrusor Acontractility (DAC)	Absence of detrusor contraction during attempted voiding, leading to an inability to void voluntarily. Can be subdivided into neurogenic and non-neurogenic DAC.
Bladder Outlet-Related Voiding Dysfunction	
Bladder Outlet Obstruction (BOO)	Obstruction during voiding, resulting in reduced urine flow rate with a simultaneously increased detrusor pressure.
Detrusor Sphincter Dyssynergia (DSD)	Dyscoordination between the detrusor and external urethral sphincter during voiding due to a neurological abnormality.
Dysfunctional Voiding	Inadequate or variable relaxation of the sphincters during voiding.

Some LUTDs affect both the storage and voiding phases of micturition. These mixed dysfunctions involve detrusor over- or underactivity coexisting with outlet resistance or abnormal coordination. Table 2.4 provides an overview of common mixed-phase LUTDs and their definitions.

Table 2.4: ICS-defined bladder-related and outlet-related mixed phase LUTDs [2, 74, 75, 76].

LUTD Type	Definition
Mixed Bladder and Outlet Dysfunction	
Bladder Outlet Obstruction (BOO) with Detrusor Underactivity (DU)	BOO leads to increased detrusor muscle effort to overcome outlet resistance, initially causing muscle hypertrophy. Prolonged hypertrophy results in chronic bladder wall ischemia-reperfusion injury, oxidative stress, and inflammation. Consequently, this results in fibrosis, urothelial dysfunction, and ultimately loss of detrusor contractility causing DU [74].
Bladder Outlet Obstruction (BOO) with Detrusor Overactivity (DO)	Obstruction may lead to detrusor overactivity in an attempt to overcome the resistance caused by the obstruction for efficient bladder emptying [75].
Detrusor Overactivity (DO) with Detrusor Underactivity (DU)	Bladder is overactive during the storage phase (DO) but empties ineffectively during the voiding phase (DU) [76, 77]
Neurological or Functional Mixed Dysfunction	
Neurogenic LUTD / Neurogenic Bladder	Lack of bladder control presenting as a combination of dysfunctions (e.g., DO, DSD, reduced compliance, acontractility), caused by neurological conditions such as multiple sclerosis (MS), spina bifida, or spinal cord injury (SCI) [78].
Overactive Pelvic Floor Muscles	Involuntary or non-relaxing contraction of pelvic floor muscles during bladder filling and/or voiding, which may result in urgency, incontinence, or incomplete bladder emptying.

2.3.1 Lower Urinary Tract Symptoms (LUTS)

Lower urinary tract symptoms (LUTS) encompass a range of clinical manifestations resulting from LUTD. They represent the primary way in which patients experience and report underlying dysfunction. However, LUTS are often non-specific and may arise from a range of different aetiologies [79, 80]. These symptoms typically affect the storage and voluntary control of urine, influencing the frequency, urgency, and overall quality of micturition [81, 2].

The International Continence Society (ICS), a UK charity focused on the development and research of incontinence [82], classifies LUTS into three distinct groups: storage, voiding, and post-voiding symptoms. Storage symptoms occur during the bladder storage phase and can be further subdivided into general storage symptoms, sensory symptoms, and incontinence symptoms. General symptoms include increased urinary frequency, increased daytime urinary frequency, nocturia, and polyuria. Sensory symptoms refer to abnormal sensations occurring during bladder filling and include altered bladder filling sensations (increased, reduced, absent, or non-specific) and urgency. Urinary incontinence describes the involuntary loss of urine experienced during the bladder storage phase, caused by abnormalities of bladder function (involuntary detrusor contractions or abnormal compliance), urethral function, or both [5]. Urinary incontinence includes urgency urinary incontinence (UUI) (involuntary leakage followed by urgency), stress urinary incontinence (SUI) (involuntary leakage with exertion, coughing, sneezing etc), detrusor overactivity incontinence (involuntary leakage with an involuntary bladder contraction), and mixed urinary incontinence (MUI) (involuntary leakage associated with urgency and exertion, coughing, sneezing, etc.) [2, 83, 81]. Table 2.5 gives an overview of the storage symptoms and their corresponding definitions.

Table 2.5: Storage Phase LUTS: ICS Classification and Definitions [2, 83, 81, 84, 85, 86, 87]

Symptom	Definition
General Storage Symptoms	
Increased urinary frequency	Urinating more frequently than normal.
Increased daytime urinary frequency	Voiding more often than usual during the day.
Nocturia	Waking up several times at night to urinate.
Polyuria	Larger urine excretion volume than normal. Can refer to diurnal or nocturnal polyuria.
Sensory Symptoms	
Altered bladder filling sensations	*Increased sensations* – sensation of bladder filling occurs earlier or more intensely than previously experienced. *Reduced sensations* – sensation of bladder filling is less intense or occurs later than previously experienced. *Absent sensations* – sensations of both bladder fullness and desire to void are absent. *Non-specific (atypical) sensation* – known as bladder dysesthesia and refers to the perception of vague abdominal bloating, vegetative symptoms (e.g., nausea, vomiting, faintness), or spasticity [88].
Urgency	Sudden, strong urge to urinate that is difficult to delay.
Incontinence Symptoms	
Urgency urinary incontinence (UUI)	Involuntary urine leakage associated with urgency.
Stress urinary incontinence (SUI)	Involuntary urine leakage on effort or physical exertion (e.g., coughing, sneezing, sporting activities).
Detrusor overactivity incontinence	Involuntary urine leakage due to involuntary detrusor contractions.
Mixed urinary incontinence (MUI)	Involuntary leakage associated with both urgency and effort or physical exertion.
Enuresis	Intermittent incontinence that occurs during sleep.
Continuous urinary incontinence	Continuous involuntary leakage.
Insensible urinary incontinence	Individual is aware of urine leakage but unaware of how or when it happened.
Postural urinary incontinence	Leakage associated with position or posture changes (e.g., supine or seated to standing).
Disability associated incontinence	Urinary incontinence resulting from a functional inability to reach a toilet in a timely manner due to a physical and/or mental impairment.
Overflow incontinence	Urinary incontinence in the presence of an over-full bladder.
Sexual arousal incontinence	Involuntary leakage during sexual arousal.
Climacturia	Urine leakage during orgasm (in males).

Voiding symptoms occur during the voiding phase. Voiding symptoms and definitions are provided in Table 2.6.

Table 2.6: Voiding Phase LUTS: ICS Classification and Definitions [81, 83, 2, 89, 90, 91, 92, 93, 94]

Symptom	Definition
Hesitancy	Delay in urine flow despite feeling the need to urinate.
Paruresis	Also known as ”bashful” or ”shy bladder” syndrome; refers to the inability to void in public or unfamiliar settings.
Episodic inability to void	Occasional inability to void despite relaxation or intensive effort (e.g., abdominal straining, Valsalva manoeuvre, or suprapubic pressure).
Straining to void	Needing to strain or push to initiate or complete urination.
Slow stream	Weak or reduced urine flow rate.
Intermittency	Urine flow that stops and starts during voiding.
Terminal dribbling	Flow tapers to drops or trickling at the end of voiding.
Spraying / Splitting of stream	Urine stream splits into multiple directions or sprays.
Position-dependent voiding	Need to assume a specific posture or position to initiate or improve bladder emptying.
Dysuria	Painful or burning sensation during urination.
Stranguria	Slow, painful urination marked by straining and spasms.
Hematuria	Presence of blood in the urine.
Pneumaturia	Passage of gas in the urine during or after voiding.
Fecaluria	Presence of feces in the urine.
Chyluria (albiduria)	Milky urine appearance caused by lymphatic leakage (chyle).
Urinary retention	Inability to completely empty the bladder, either acutely or chronically.

Lastly, post-voiding symptoms arise after voiding has ceased and include the feeling of incomplete bladder emptying, need to immediately re-void, post-voiding incontinence, and post-micturition urgency [81, 83, 2]. The post-voiding symptoms and definitions are provided in Table 2.7.

Table 2.7: Post-voiding LUTS: ICS Classification and Definitions [81, 83, 2, 95, 91]

Symptom	Definition
Feeling of incomplete bladder emptying	Sensation that the bladder has not fully emptied following urination.
Need to immediately re-void	Referred to as ”encore” or ”double” voiding, where voiding is necessary soon after urinating.
Post-voiding incontinence	Involuntary leakage of urine (incontinence) following the completion of voiding.
Post-micturition urgency	Persistent urgency after voiding.

2.3.2 Epidemiology

LUTS are prevalent in both sexes, with incidence increasing with age [81, 96]. It is estimated that over 50% of men above 50 years of age experience LUTS [81]. In 2008, 45.2% of the global population presented with at least one LUTS [1].

Several epidemiological studies have assessed the prevalence and characteristics of LUTS across diverse populations. A survey by the ICS involving 1271 male patients across twelve urology clinics revealed that voiding symptoms (90-94%) were more common than storage symptoms (66-71%); however, storage symptoms were reported to be more bothersome overall. Notably, post-micturition dribble was reported as the most prevalent symptom (96%) [97, 98].

The EPIC survey, involving 19 165 men and women from several countries (Canada, Germany, Italy, Sweden, Switzerland, and the UK), reported an overall LUTS prevalence of 62.5% in men and 66.6% in women. Distinct gender-related patterns were observed: storage symptoms were more prevalent among women (59.2% women vs 51.3% men), whereas voiding symptoms were more prevalent among men (25.7% men vs 19.5% women). Nocturia (one episode per night) was the most frequently reported storage symptom, affecting 54.5% of women and 48.6% of men. Moreover, terminal dribble was reported by 14.2% of men and 9.9% of women [99, 98].

The Boston Area Community Health (BACH) survey of 5506 subjects reported similar prevalence of LUTS among men and women (18.7% vs 18.6%) and confirmed the age-dependent increase in prevalence, where prevalence increased from 10.5% at 40 years to 26.5% at 70 years. Furthermore, prevalence appeared independent of race and ethnicity [96, 98].

The EpiLUTS study, conducted on over 30 000 participants aged above 40 years from the United States, United Kingdom, and Sweden, confirmed the aforementioned trends. It reported a similar prevalence among women (52.5%) and men (47.9%) and storage symptoms again emerged as more common in women than men, with nocturia (one episode per night) being reported by 75.8% of women and 69.4% of men and urgency being reported by 35.7% of women and 22.4% of men. Terminal dribble was prevalent, presenting in 45.5% of men and 38.3% of women. Post-micturition symptoms were also common, with incomplete emptying reported by 27.4% of women and 22.7% of men, and post-micturition leakage affecting 29.7% of men and 14.9% of women [100, 98].

Collectively, these studies demonstrate that LUTS are highly prevalent, with comparable prevalence between sexes. However, notable gender differences exist: storage symptoms are more common in women, while voiding symptoms are more common in men. Prevalence increases with age but appears independent of race and ethnicity.

2.3.3 Aetiologies

LUTD can result from a wide range of aetiologies that impair normal bladder storage, voiding, or both. These causes are commonly grouped into neurological, structural, hormonal and age-related, pelvic floor-related, infectious and inflammatory, metabolic and systemic, iatrogenic, lifestyle-related, and idiopathic categories (Figure 2.17). Each category may contribute to various dysfunction types – including DO, DU, RCSD, BOO, DSD, DAC, or USI – with individual dysfunctions often arising from multiple overlapping causes.

Neurological causes affect the central or peripheral neural pathways that regulate bladder and sphincter control. Conditions such as spinal cord injury (SCI), multiple sclerosis (MS), Parkinson's disease, diabetic neuropathy, and stroke can result in BO, DSD, NDO, DU, DAC, RCSD, BOO, and ISD. The resulting dysfunction depends on the location and nature of the neurological lesion [101, 102, 81, 2, 103, 104, 105, 106].

Structural causes refer to anatomical abnormalities that physically obstruct urinary flow or compromise sphincter integrity. These include:

- Benign prostate hyperplasia (BPH): enlarged prostate [107]
- Urethral strictures: narrowing of the urethra [108]

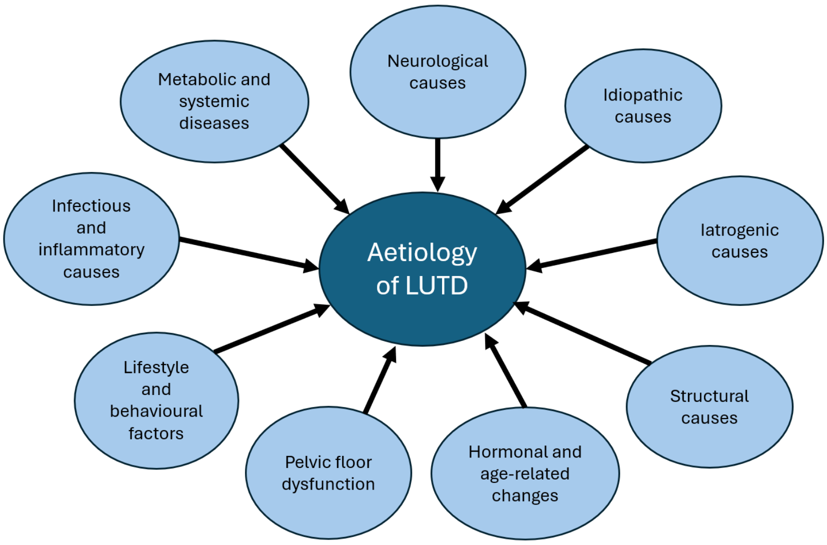

Figure 2.17: Aetiological factors contributing to LUTD. LUTD can arise from a wide range of causes, including neurological, metabolic, infectious, structural, hormonal, and behavioural factors. This diagram categorises the major known aetiologies into ten domains, each of which may contribute to storage, voiding, or post-micturition symptoms depending on the underlying dysfunction.

- Bladder neck stenosis: narrowing of the bladder neck [109]
- Pelvic organ prolapse: descent of pelvic organs causing urethral or bladder compression [110]
- Meatal stenosis: narrowing of the urethral opening [111]
- Bladder diverticula: pouches in the bladder wall [112]
- Urogenital malignancies: tumours in the prostate, bladder, rectal, or gynecological organs causing obstruction [113]

These abnormalities contribute to DU, BOO, secondary DO (via increased outlet resistance), or RCSD through detrusor wall hypertrophy in response to chronic obstruction [104, 101, 102, 81, 2].

Hormonal and age-related changes alter LUT function through changes in connective tissue composition, urothelial receptor sensitivity, inflammation, and detrusor fibrosis [114]. In women, menopause affects urethral mucosa and continence support, while ageing can lead to detrusor degeneration in both sexes, contributing to DO, USI, DU, and DAC [115, 116, 103, 117]. Ageing is also associated with ISD [105].

Pelvic floor dysfunction contributes to LUTD. Overactive pelvic floor muscles (e.g., due to tension or trauma) can prevent outlet relaxation, causing BOO [118, 119]. Conversely, underactive or weakened pelvic floor musculature - often resulting from childbirth or pelvic surgery - may lead to USI, dysfunctional voiding, and incomplete bladder emptying [119, 120, 2, 121, 122].

Infectious and inflammatory causes, including urinary tract infections (UTIs) and chronic cystitis, and infections affecting the nervous system, can provoke urgency, frequency, or altered compliance by damaging the endothelial lining and causing scarring. This may contribute to BO, DU, or DSD [104, 123, 115, 124, 125].

Metabolic and systemic diseases also contribute to LUTD. Diabetes mellitus, a major cause of autonomic neuropathy, is associated with DU and DAC [115, 101, 102, 116]. Hypertension has been linked to collagen deposition in the detrusor wall and is associated with DU [126]. Obesity increases intra-abdominal pressure and weakens pelvic floor muscles, which is associated with USI and outlet dysfunction [104, 101, 102, 115, 127, 103, 117, 120].

Iatrogenic causes include nerve damage or fibrosis resulting from surgery (e.g., prostatectomy, hysterectomy, stress incontinence surgery), pelvic radiation, or chemotherapy. These may lead to USI, DU, DAC, RCSD, or ISD, depending on the structures affected [120, 2, 116, 128, 105].

Lifestyle and behavioural factors, such as excessive caffeine or alcohol intake and smoking, can increase urinary frequency and urgency via bladder irritation or increased urine production. Chronic cough (e.g., from smoking) also increases the risk of USI by elevating abdominal pressure and straining pelvic support structures [115, 101, 102, 120]. Dysfunctional voiding can be a result of learned behaviours or toilet habits [129].

Idiopathic causes represent situations where no identifiable cause is found. Idiopathic DO and DAC are commonly diagnosed [2, 116, 128].

Evidently, LUTDs can arise from multiple and often overlapping aetiologies, making accurate diagnosis dependent on a thorough understanding of the underlying pathophysiology. This is achieved through comprehensive clinical history-taking, functional assessment, and targeted diagnostic investigations.

2.3.4 Impact on Quality of Life

LUTD can significantly affect an individual's quality of life (QoL), impacting not only physical health but also emotional wellbeing, daily activities, work productivity, and social relationships [1]. Although not typically life-threatening, LUTD can be chronic and often progressive, leading to serious complications such as recurrent UTIs, kidney damage, and sepsis [123, 130].

LUTS associated with LUTD are linked to several psychosocial burdens:

- *Sleep disturbances:* Nocturia disrupts sleep, contributing to chronic fatigue, impaired concentration, and anxiety [131].
- *Emotional distress and mental health effects:* Individuals with LUTS experience significantly higher rates of depression (11.5%) compared to those without symptoms (2.9%) [1, 132].
- *Reduced social and sexual engagement:* Fear of urgency or incontinence may cause patients to avoid social interactions and intimacy, resulting in isolation and relationship strain [1, 132].
- *Work productivity loss:* LUTS negatively affects job performance and productivity [1, 132].
- *Employment impact:* Individuals with LUTS are more likely to be unemployed (27.1% vs. 17.3%). Additionally, 2.1% report having changed jobs, retired early, or been dismissed due to their symptoms [1].

LUTS also impose a considerable economic burden. Direct costs include consultations, tests, medications, and surgical procedures, while indirect costs result from reduced work productivity [133].

Evidently, LUTS has a widespread impact across several areas of one's life, including societal and economic impact as well as psychological burden. This underscores the need for accurate diagnostic tools and testing.

2.4 Diagnostic Evaluation of LUTD

Accurate diagnosis of LUTD is crucial for guiding effective, targeted treatment and improving patient outcomes. Given the non-specific and overlapping nature of LUTS, a structured and multi-step diagnostic approach is required to distinguish between the various underlying dysfunctions. The diagnostic process begins with a detailed patient history and symptom assessment, followed by physical examination and non-invasive investigations. If these steps do not produce a clear diagnosis, urodynamic studies are performed to objectively assess LUT function and help identify the specific LUTD [73].

2.4.1 Initial Clinical Evaluation

History and Symptom Assessment

Evaluation begins with a comprehensive patient history, focusing on the nature of the LUTS, their duration, severity, impact on quality of life, and classification as storage, voiding, or post-micturition symptoms [73, 81, 5]. A detailed surgical and medical history should be obtained, as previous interventions or conditions may contribute to current dysfunction [73, 2]. Medication use should be reviewed, particularly agents known to affect bladder or sphincter function. Lifestyle factors, such as fluid intake, caffeine and alcohol consumption, and smoking habits should also be assessed [73]. In female patients, a complete obstetric and menstrual history is essential to identify factors that may influence pelvic floor integrity or urinary continence mechanisms [73].

Physical Examination

A targeted physical examination should follow, including assessment of the abdomen, genitalia, perineum, rectum, prostate, and lower back [73, 2, 81]. A neurological examination is also important to assess speech, gait, coordination, dexterity, and signs of motor or sensory weakness [73, 2]. The pelvic floor should be examined to identify dysfunction that may contribute to LUTS. Perineal or rectal examination can be used to assess pelvic floor musculature and classify it as normal, overactive, or underactive [2].

Laboratory Tests

Laboratory testing in the context of LUTD primarily involves urinalysis to screen for urinary tract infection (UTI), glycosuria, pyuria, proteinuria, or hematuria [134, 73]. Identifying and managing infection is crucial, as UTIs are a common cause of LUTS. Additional tests may include serum creatinine tests to evaluate renal function and measurement of prostate-specific antigen (PSA) levels in men to assess for prostate pathology such as BPH or prostate cancer [102, 135].

Symptom Monitoring

A frequency-volume chart (FVC) documents the time and volume of each void over a minimum of 24 hours [6]. It provides objective insight into voiding patterns and is useful for evaluating symptoms such as urinary frequency, urgency, incontinence, and nocturia [136].

A bladder diary (BD) is a more comprehensive tool that includes the FVC data while also tracking fluid intake (time and volume), incontinence episodes, their triggers (e.g., coughing, sneezing, movement, delayed access to a bathroom, unknown causes, or other), and severity. BD monitoring is typically performed over a three day period [137]. Together, the FVC and BD help assess daytime frequency, nocturia, maximum voided volume, and excessive fluid intake. They also provide insight into functional bladder capacity and the bladder volumes at which symptoms tend to occur [6].

2.4.2 Urodynamic Studies (UDS)

Urodynamic studies (UDS) are a group of diagnostic tests that objectively assess LUT function by measuring pressure and flow dynamics during bladder filling and voiding phases [3, 4, 5]. Key parameters include detrusor pressure, urinary flow rate, bladder capacity, sensation, compliance, urethral resistance, and post-void residual (PVR) volume [29, 5]. UDS is typically indicated when the cause of LUTS cannot be determined through clinical evaluation alone [3]. It provides objective data to help distinguish among common LUTDs such as DO, BOO, or DU.

Several UDS tests are available, including uroflowmetry, measurement of post-void residual (PVR) volume, cystometry, pressure-flow studies, electromyography (EMG), urethral pressure profile (UPP), leak point pressure (LPP) measurement, and video urodynamics (VUDS). The selection of tests depends on symptom complexity and the level of diagnostic information required [5]. Each test is described in the sections that follow.

Uroflowmetry

Uroflowmetry is a non-invasive test where the patient voids - ideally when experiencing a natural urge - into a flowmeter that records urine volume, flow rate, and voiding duration [138, 8]. This investigation provides insight into voiding dynamics and is particularly useful for evaluating flow patterns and flow rates [5]. It helps detect abnormalities in detrusor contractility and outlet resistance by analysing both the shape and magnitude of the flow curve. A normal flow curve is bell-shaped, with a Q_{max} typically greater than 15 - 20 mL/s [6, 5, 139]. Deviations from this pattern may suggest dysfunction:

- A flattened curve may indicate BOO or impaired detrusor contractility [5, 140, 139].
- An interrupted curve may be associated with obstruction, DU, or voiding by abdominal straining [5, 141, 139].

Figure 2.18 illustrates common pathological flow patterns.

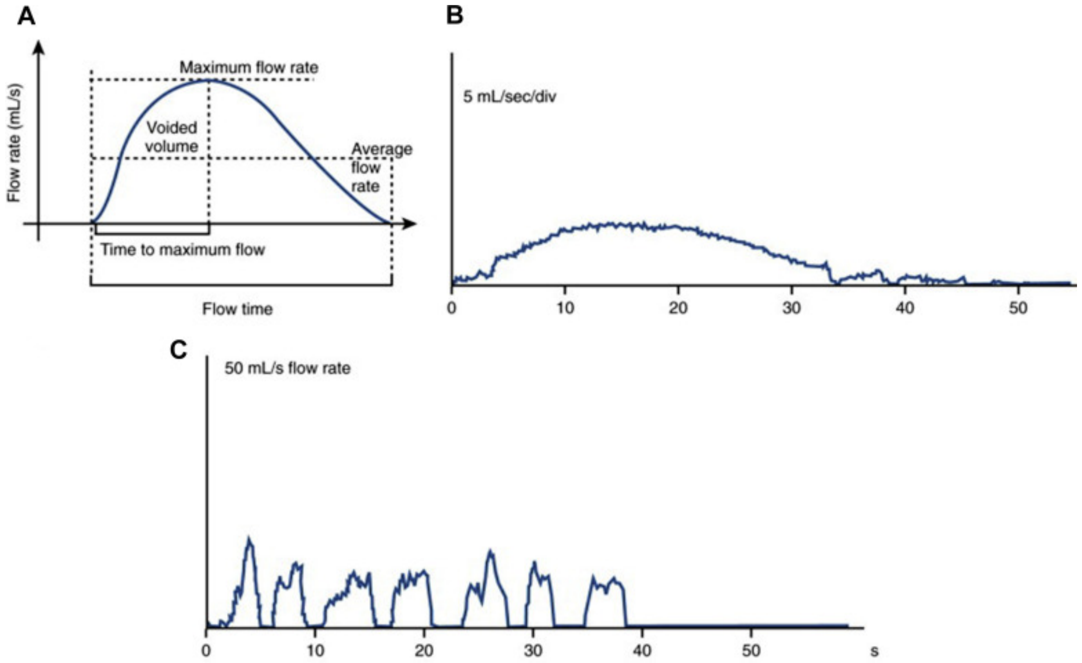

Figure 2.18: Examples of uroflow curves. (A) Normal bell-shaped pattern. (B) Flattened pattern, which may suggest BOO or impaired detrusor contractility. (C) Interrupted pattern, which can indicate obstruction, detrusor underactivity, or voiding by abdominal straining. Figure from [142].

Although useful as a screening test, uroflowmetry alone is insufficient to distinguish weak detrusor contractility and outlet obstruction, as it does not provide pressure measurements. Therefore, it is used to identify patients who need more detailed urodynamic studies to diagnose the underlying dysfunction [139]. Furthermore, uroflowmetry cannot assess bladder emptying efficiency [5].

Post-Void Residual (PVR) Volume

Post-void residual (PVR) refers to the volume of urine remaining in the bladder immediately after voluntary voiding. It is a simple yet essential measure of bladder emptying efficiency and is typically performed following uroflowmetry [5]. PVR can be measured non-invasively using bladder ultrasound or invasively via urethral catheterisation, with ultrasound preferred due to its minimal invasiveness [139]. Elevated PVR volumes may indicate DU, BOO, or a combination of both [5, 139]. However, PVR measurement cannot identify the underlying cause of incomplete bladder emptying. Like uroflowmetry, it is primarily used as a screening tool to determine whether further investigation is necessary [139].

Cystometry

Cystometry is a pressure-based urodynamic test used to measure detrusor pressure during bladder filling [6, 7, 8] and enable direct evaluation of detrusor activity, bladder compliance, and the mechanisms underlying storage and voiding dysfunction. It involves catheter-based measurement of both intravesical pressure (P_{ves}) and intra-abdominal pressure (P_{abd}) using a transurethral bladder catheter and a rectal (or vaginal) reference catheter [9, 7]. True detrusor pressure, reflecting bladder contractility, is calculated as:

$$P_{\text{det}} = P_{\text{ves}} - P_{\text{abd}}$$

and is expressed in centimetres of water (cmH_2O) [6, 7, 5, 19]. This calculation is critical for distinguishing genuine detrusor contractions from pressure increases caused by abdominal straining, coughing, or posture changes [8]. The resulting pressure-time graph, known as a cystometrogram (CMG), provides insight into filling pressures, bladder sensation, involuntary contractions, compliance, and storage capacity [8].

Filling cystometry is typically performed with the patient in a seated or upright position, ideally starting with an empty bladder [5]. The bladder is retrogradely filled with warm sterile saline via a separate filling line or dual-lumen vesical catheter – usually at supra-physiological rates, which may reduce bladder compliance and should be interpreted with caution. [6, 7, 19]. Filling is stopped when the patient reports a strong desire to void or experiences involuntary leakage. Voiding is initiated only after explicit instruction (”permission to void”) [6, 5] and is typically performed into a flowmeter [6]. The full cystometry setup is illustrated in Figure 2.19.

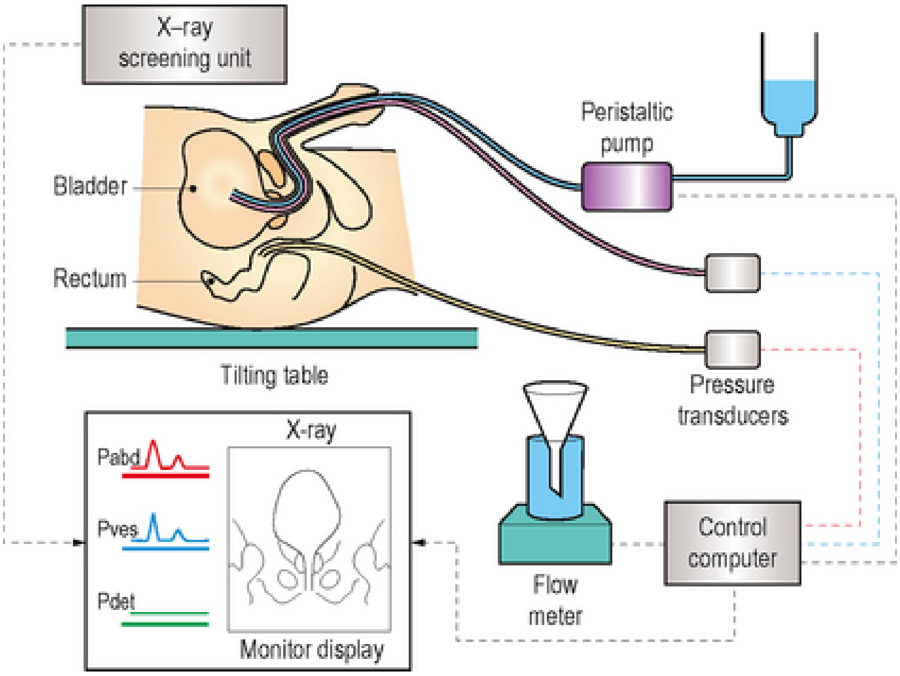

Figure 2.19: Schematic diagram of cystometry setup showing two catheters – one in the bladder, one in the rectum – and retrograde filling with saline. Recorded pressures include P_{ves} and P_{abd}, used to compute P_{det}. Figure from [143].

During filling, patients are asked to report specific sensations [6, 5]:

- First sensation of filling (FSF): Initial awareness of bladder filling.
- First desire to void (FDV): A desire to void that can be postponed.
- Strong desire to void (SDV): Persistent need to void without fear of leakage.

Other sensations such as urgency, pain, or pressure should be documented. These reports are annotated on the CMG trace for clinical interpretation. To provoke detrusor contractions or leakage, provocation manoeuvres such as coughing, Valsalva, heel bouncing, or posture changes may be performed (Figure [6, 5]. These can help identify DO or SUI, depending on the bladder and sphincter response to increased abdominal pressure [8, 15]. SUI presents as involuntary leakage of urine during increased abdominal pressure in the absence of detrusor contractions [6, 97].

In healthy individuals, detrusor pressure remains relatively stable during filling [6, 5]. Typical resting detrusor pressures during filling are:

- Supine: 0–18 cmH_2O [8]
- Sitting: 15–40 cmH_2O [8]
- Standing: 20–50 cmH_2O [8]

Voiding pressures typically range from 50–70 cmH_2O [144], generated by parasympathetic activity [37, 35].

The CMG provides diagnostic insights into various dysfunctions. Characteristic CMG patterns include the following:

- Normal: Low-pressure bladder filling [5] (Figure 2.20)
- DO: Sudden increases in P_{ves} not accompanied by increases in P_{abd} [5] (Figure 2.21)
- Reduced compliance (RCSD): Gradual rise in P_{det} during filling [5, 2] (Figure 2.22)

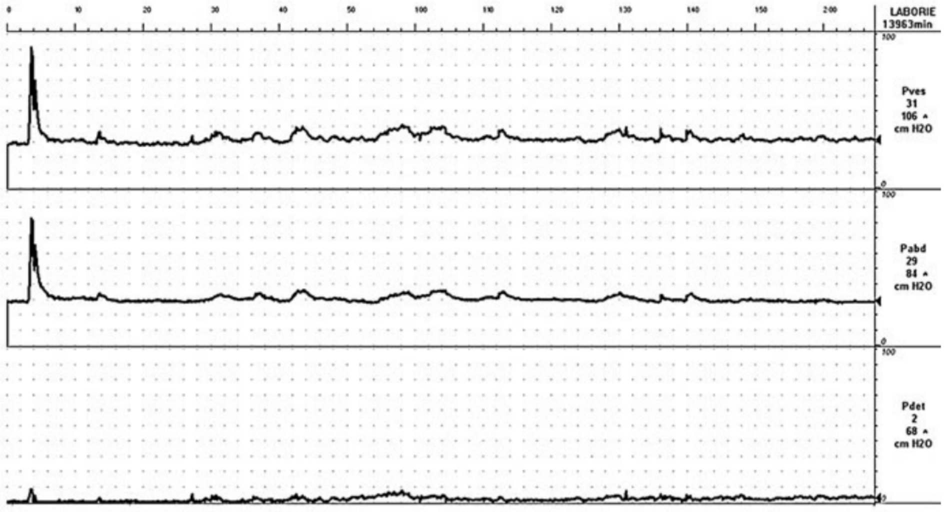

Figure 2.20: Normal cystometrogram showing low-pressure bladder filling. Top graph: P_{ves}, middle graph: P_{abd}, bottom graph: P_{det}. Figure from [5].

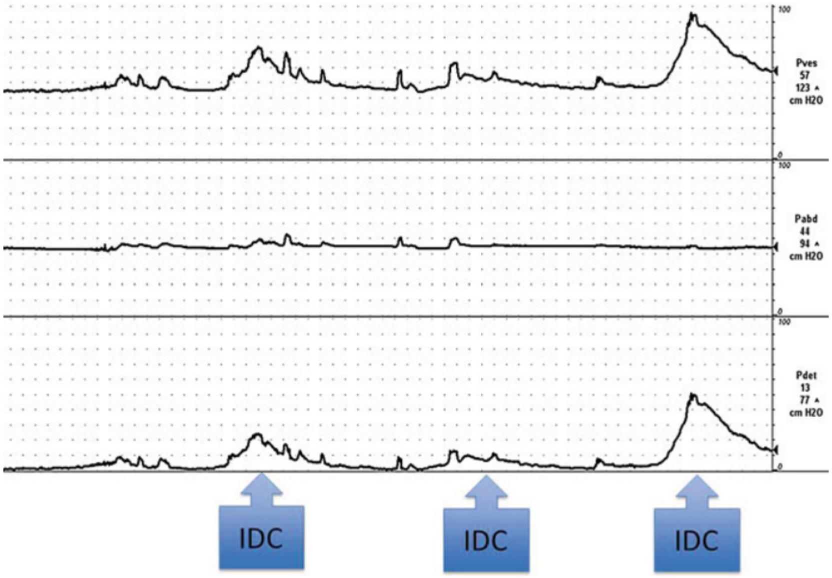

Figure 2.21: Cystometrogram indicating DO: P_{ves} rises in the absence of P_{abd} increase. IDO: Involuntary detrusor contraction. Top graph: P_{ves}, middle graph: P_{abd}, bottom graph: P_{det}. Figure from [5].

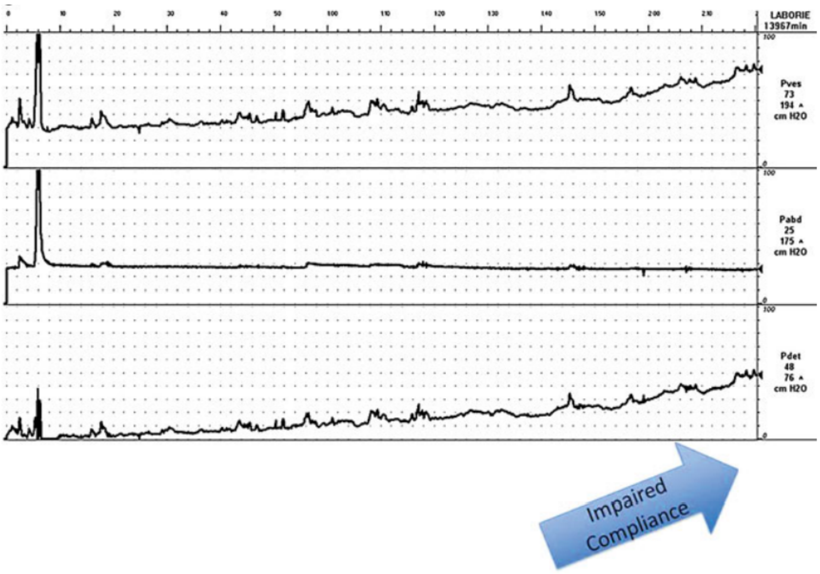

Figure 2.22: Cystometrogram showing reduced compliance (RCSD): P_{det} rises progressively during filling. Top graph: P_{ves}, middle graph: P_{abd}, bottom graph: P_{det}. Figure from [5].

While cystometry provides critical diagnostic information and is the gold standard for assessing bladder pressure during the filling and voiding phases, it also has several limitations. From a clinical perspective, cystometry is inherently invasive, requiring transurethral and rectal catheterisation [7, 15, 145, 5]. This can lead to discomfort, pain, anxiety, and embarrassment, with approximately 43% of patients reporting catheter-related discomfort [7, 5]. The procedure also carries risks such as urinary tract infection (1–10%), haematuria, and dysuria, with some studies reporting complication rates up to 45% [11, 6]. Additionally, the artificial testing environment - characterised by forced bladder filling, patient immobility, and short test durations (20–40 minutes) - may suppress or fail to reproduce patient symptoms, with up to 46% of cases not replicating true bladder functionality during testing [10]. This can lead to misleading or incomplete diagnostic outcomes [7, 146, 7].

From a technical standpoint, cystometry is highly susceptible to motion artifacts and measurement variability. Patients are required to remain stationary to minimise catheter displacement, limiting natural movement and reducing the likelihood of symptom replication [12, 7]. Motion artifacts can obscure pressure signals and require manual annotation, increasing clinician workload and introducing subjectivity [13, 8, 4]. Furthermore, pressure measurements are influenced by catheter type and transducer design. Fluid-filled transducers are widely used but sensitive to motion, air bubbles, and positioning errors; catheter-tip transducers offer improved responsiveness but are costly and position-dependent; and air-charged systems are easier to use but exhibit slower response and are less extensively validated in the literature [6, 147, 148]. These factors introduce variability in pressure readings and complicate interpretation.

At a system level, cystometry is limited by its reliance on specialised equipment and trained personnel, restricting accessibility, particularly in low-resource settings [15, 17, 18, 16]. The cost of urodynamic systems (€5100–€13700) further limits widespread adoption [149, 150]. In addition, interpretation of cystometry data remains dependent on clinical expertise and is subject to intra- and interobserver variability, especially in artifact-contaminated recordings [4].

Pressure-Flow Studies

Following cystometry, pressure-flow studies assess the dynamic relationship between detrusor pressure and urinary flow during voiding by combining simultaneous measurements from cystometry and uroflowmetry [5, 2]. This test is particularly valuable for distinguishing between obstructive and non-obstructive voiding dysfunction. By recording detrusor pressure and flow rate simultaneously, pressure-flow studies reveal characteristic pressure-flow patterns that support the diagnosis of various LUTDs, including BOO, DU, and DAC [5, 2, 151]. In healthy individuals, voiding is characterised by a coordinated increase in detrusor pressure and a bell-shaped flow curve, resulting in complete bladder emptying (Figure 2.23) [5, 151, 2]. In BOO, the detrusor muscle generates elevated pressure to overcome increased outlet resistance, yet flow rate remains low. DU presents as weak and/or short-lived detrusor contractions, resulting in low flow rate, prolonged voiding time, or incomplete emptying. In DAC, detrusor contracts may be entirely absent, preventing effective initiation or continuation of voiding [5, 151, 2].

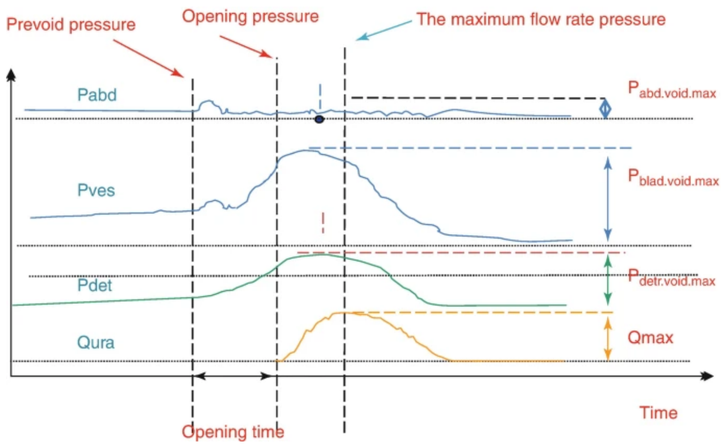

Figure 2.23: Pressure-flow curve of a healthy individual, demonstrating a coordinated rise in detrusor pressure (P_{det}) accompanied by a normal, bell-shaped flow curve. Figure from [152].

Electromyography (EMG)

Electromyography (EMG) complements pressure-based studies by assessing the electrical activity of the pelvic floor muscles and external urethral sphincter during bladder filling and voiding phases [7, 153]. It records the electrical potentials generated by muscle depolarisation and provides insight into the neurological control of the LUT, supporting the diagnosis of DSD and dysfunctional voiding. [5, 2, 154]. While EMG can be performed as a stand-alone test, it is most commonly combined with other UDS tests to provide a more comprehensive assessment [5].

Urethral Pressure Profilometry (UPP)

Urethral pressure profilometry (UPP) assesses urethral resistance to urinary flow, providing information regarding sphincteric competence, particularly in the evaluation of SUI. A specialised catheter with lateral pressure-sensing apertures is inserted into the bladder and slowly withdrawn through the urethra during continuous fluid infusion. As the catheter moves through the urethra, the pressure sensors measure the intraluminal pressure needed to overcome urethral closure forces. This pressure reflects the circumferential and radial stresses that maintain urethral closure [5, 155].

Leak Point Pressure (LPP) Measurement

Abdominal leak point pressure (ALPP) is a urodynamic measurement used to assess urethral sphincter competence during increases in intra-abdominal pressure. It is defined as the intravesical pressure at which involuntary urine leakage occurs — without a detrusor contraction — during manoeuvres that increase abdominal pressure (e.g., coughing or Valsalva) [5]. ALPP is particularly relevant in the evaluation of SUI, where lower ALPP values indicate weaker urethral sphincter function [5].

Video Urodynamics (VUDS)

Video urodynamics (VUDS) combines standard urodynamic testing with real-time fluoroscopic imaging to simultaneously assess LUT anatomy and function during the storage and voiding phases [5, 2, 153]. This enables direct visualisation of the bladder, bladder neck, urethra, and external urethral sphincter, allowing for more precise diagnosis than pressure measurements alone. VUDS is particularly useful in the evaluation of BOO, DSD, neurogenic bladder, and incontinence [5].

2.4.3 Diagnostic Tests and Characteristic Findings for LUTDs

Different types of LUTD present with distinct urodynamic profiles. Accurate diagnosis depends on selecting the appropriate tests and correctly interpreting the resulting data. Table 2.8 maps common LUTDs to their diagnostic tests and summarises the key findings typically associated with each condition. Reference values for normal urodynamic tests can be found in Appendix A.1.

Table 2.8: LUTDs grouped by storage and voiding category, with corresponding diagnostic tests and findings [2].

LUTD	Diagnostic Test(s)	Key Findings / Outcomes
Storage Phase LUTDs		
BO	Cystometry	Early first sensation and desire to void, low capacity, absence of DO [79].
DO	Cystometry	Rise in P_{ves} without increase in P_{abd}. NDO if associated with a neurological lesion [2].
RCSD	Cystometry	Gradual, non-phasic rise in P_{det} during bladder filling [2].
RCSD Incontinence	Cystometry, VUDS	Leakage at low bladder volumes due to poor compliance. VUDS confirms mechanism.
USI	Cystometry, ALPP, VUDS	Leakage during stress manoeuvres without detrusor contraction. Low ALPP indicates weak sphincter. VUDS detects leakage.
ISD	ALPP, UPP	ALPP < 60 cmH_2O, MUCP < 20 cmH_2O indicating sphincter deficiency.
Voiding Phase LUTDs		
DU	Pressure-flow study	Low P_{det}, short contraction duration, low flow rate, or incomplete emptying [2].
DAC	Pressure-flow study	Absence of detrusor contraction; no urine flow [151].

LUTD	Diagnostic Test(s)	Key Findings / Outcomes
BOO	Pressure-flow study, VUDS	High P_{det}, low Q_{max}. VUDS localises anatomical obstruction [2].
DSD	PVR, EMG, VUDS	Elevated P_{det} with sphincter contraction on EMG during voiding. An intermittent or reduced urinary stream may result in elevated PVR. VUDS confirms dyssynergia [2].
Dysfunctional voiding	Uroflowmetry, EMG	Intermittent flow with simultaneous EMG activity; no neurological lesion [15].

2.5 Treatment Strategies for LUTD

The management of LUTD is guided by clinical evaluation and urodynamic findings, with treatment tailored to the underlying dysfunction, symptom profile (storage, voiding, or mixed), and impact on quality of life [81].

Treatment typically follows a stepwise approach. Mild symptoms are initially managed conservatively through lifestyle and behavioural interventions, such as fluid and dietary modification, bladder training, and pelvic floor exercises. When symptoms persist, pharmacological therapies are introduced, including alpha-blockers and 5-alpha reductase inhibitors for BOO, and antimuscarinics or beta-3 agonists for DO, BO, or RCSD [81, 102, 115, 156, 157].

Pharmacological therapy is introduced when symptoms persist or affect daily functioning. For structural causes (e.g., BOO, diverticula, strictures), surgical or minimally invasive interventions may be necessary [158, 81]. For patients with refractory symptoms or structural abnormalities, surgical and minimally invasive interventions may be required [102]. These include procedures to relieve BOO (e.g., TURP, urethral dilation, prostatectomy, bladder neck incision), treat incontinence (e.g., sling procedures, artificial urinary sphincters), or address underlying neurological or anatomical causes (e.g., BOTOX, neurostimulation) [156, 115, 159, 160]. While effective, such interventions are typically reserved for cases where conservative and medical management are insufficient.

Given the wide range of treatment options and their dependence on the underlying pathophysiology, accurate diagnosis is critical. This highlights the importance of reliable urodynamic assessment in guiding appropriate and effective treatment strategies.

2.6 Motion Artifacts in Cystometry

As discussed in Section 2.4.2, a major limitation of cystometry is the presence of motion artifacts (MAs) in recorded signals. Artifacts are defined as signal distortions caused by sources unrelated to the physiological process being measured. These artifacts introduce noise [161, 162], degrade signal quality, and obscure clinically relevant features [163]. In biomedical applications, MAs are particularly problematic in continuous monitoring and diagnostic systems such as ECG, EEG, NIRS, and PPG, where they can lead to misclassification or misdiagnosis [164, 9, 165, 163, 5, 166]. Moreover, artifacts impact interobserver and intraobserver agreement in urodynamic studies [4].

In the context of cystometry, maintaining high data quality is critical to accurately identify pathological patterns such as DO, BO, RCSD, and USI [167] (see Section 2.4.3). Even small errors can result in false positives or false negatives, compromising diagnosis and treatment planning [162, 146, 168, 5]. MAs in cystometry arise from both technical and physiological sources:

- *Technical or equipment-related artifacts:* These include catheter displacement or expulsion, faulty or misaligned pressure transducers, air bubbles in fluid-filled systems, or disruptions in setup caused by patient movement [167, 169, 5].

- *Physiological artifacts:* These include voluntary or involuntary actions such as postural changes, coughing, sneezing, talking, abdominal straining, crying, or muscle contractions [162, 169, 13, 5]

These events can produce pressure spikes or baseline drift that mimic or obscure true detrusor contractions, leading to potential misinterpretation [5]. To reduce the likelihood of MA contamination, patients are generally instructed to remain as still as possible throughout the test [5, 170].

During the test, operators are expected to annotate non-physiological events (e.g., movement, coughing, talking, postural changes) on the pressure traces in real time. This annotation enables differentiation between physiological events and signal disturbances [13, 5]. Manual annotation is particularly important in paediatric urodynamic studies, where patient movement is more common [5]. However, this process is time-consuming, subjective, and susceptible to human error, which can impact diagnostic consistency [171, 172].

A key strategy for MA mitigation relies on the dual pressure recordings, where one catheter measures intravesical pressure, while the other records abdominal pressure. The true detrusor pressure can then be calculated by subtracting abdominal pressure from the intravesical pressure. This differential measurement compensates for artifacts that affect both the abdomen and bladder equally - such as coughing or abdominal straining - thereby isolating true bladder activity [8, 173, 5, 174]. Additionally, catheters and tubing are secured with adhesive tape to prevent mechanical displacement or tugging during patient movement, minimising artifact introduction during recording [5].

While several procedural practices are employed to minimise the introduction of motion artifacts during cystometry recordings, these approaches are often impractical, time-consuming, subjective, and invasive. Moreover, they are not foolproof solutions. Given the impact of MAs on data interpretation and consequently on diagnosis and treatment, recent research has explored signal processing and machine learning-based methods for automated artifact detection and removal. By detecting and removing artifacts, these emerging approaches ultimately improve consistency, reduce clinical workload, and boost diagnostic reliability.

2.7 Motion Artifact Removal Techniques

A literature study was conducted to review MA filtering techniques for biosignals, focusing on adaptive filtering and machine learning-based approaches. Although artifact suppression has been widely studied in signals such as electrocardiography (ECG), electroencephalography (EEG), photoplethysmography (PPG), there is comparatively minimal work focused on cystometry. Existing approaches for artifact reduction can be broadly classified into signal processing methods, machine learning methods, and hardware-based approaches.

2.7.1 Signal Processing Methods

Traditional Filtering

Traditional filtering approaches isolate signal components from unwanted noise or artifacts through fixed filtering techniques such as low-, high-, and band-pass filters [175, 176]. While effective for stationary noise sources like power line interference (PLI) or electromagnetic interference (EMI), such methods perform suboptimally with MA suppression due to their non-stationary, non-physiological nature and spectral overlap with physiological signals. Suppression of artifacts in such cases can result in signal degradation and increased false alarms [177, 165, 163, 178].

Adaptive filters (e.g., LMS, NLMS, RLS) update filter parameters in response to changing noise conditions and therefore offer improved handling of non-stationary artifacts [179, 180]. Despite improved flexibility, they remain limited when artifacts and physiological events overlap in frequency or morphology. In some cases, they can degrade the signal-to-noise ratio (SNR). Moreover, they increase computational complexity, making real-time implementation more challenging [179, 181, 180].

Decomposition Methods

Signal decomposition techniques such as the discrete wavelet transform (DWT) have been used to decompose signals into a series of basis waveforms, known as wavelets [182]. Karam et al. demonstrated that DWT with Daubechies wavelets could partially separate P_{ves} into P_{det} and P_{abd} components, with interval-dependent thresholding improving estimation accuracy [19]. A similar methodology was followed by Zareen et al. [183]. However, total separation remains challenging due to overlapping frequency bands.

2.7.2 Machine Learning Approaches

Machine learning (ML) techniques have gained traction in recent years as alternatives to traditional signal processing for MA suppression and biosignal denoising [165, 184]. Unlike traditional filtering methods, ML models use data-driven feature extraction and pattern recognition to distinguish artifacts from physiological signals, resulting in improved artifact suppression while preserving biosignal quality. Moreover, they are better suited for non-linear and non-stationary time series signals [185, 186, 9] and also are less reliant on expert opinion and post hoc tuning of parameters [9].

Classical Machine Learning

Classical ML models rely on manually selected (engineered) features that capture signal characteristics such as peak morphology, slope, variance, or spectral properties [187]. Models include algorithms such as Logistic Regression (LR), Support Vector Machine (SVM), Naive Bayes (NB), Random Forest (RF), and k-Nearest Neighbour (KNN) [188].

SVMs separate classes by determining an optimal decision boundary (hyperplane) in an N-dimensional space, where the hyperplane is calculated using support vectors [189]. They have been applied to ECGs for distinguishing artifact-induced peaks from true cardiac events, with sparse SVMs incorporating LASSO regularization for feature selection [190]. Other applications include human activity recognition (HAR), where SVMs were applied to distinguish between various daily activities [191].

While effective, these approaches are bounded by the quality of feature engineering, which is time-consuming and application-specific [192]

Deep Learning

Deep Learning (DL) is a subset of machine learning that utilises artificial neural networks with several layers to automatically learn complex patterns and characteristics of raw or minimally processed data, overcoming the dependency on engineered features [193]. Given this, there have been major breakthroughs in recent years in the fields of image recognition, speech recognition, natural language processing, and medical health [193], with several methods being implemented in biosignal denoising.

Multi-layer perceptrons (MLPs) are simple feedforward networks that have been applied to HAR from inertial signals [194]. *Convolutional neural networks (CNNs)* (Figure 2.24) have been used extensively in the denoising of biosignals [186]. CNNs extract local temporal patterns (e.g., peaks, valleys) from raw signals [186, 195], enabling robust MA detection and suppression in ECG [186, 196, 197, 198], PPG [199], EEGs [200], HAR [201, 202, 203], and EDA [204] without extensive preprocessing or feature engineering [205].

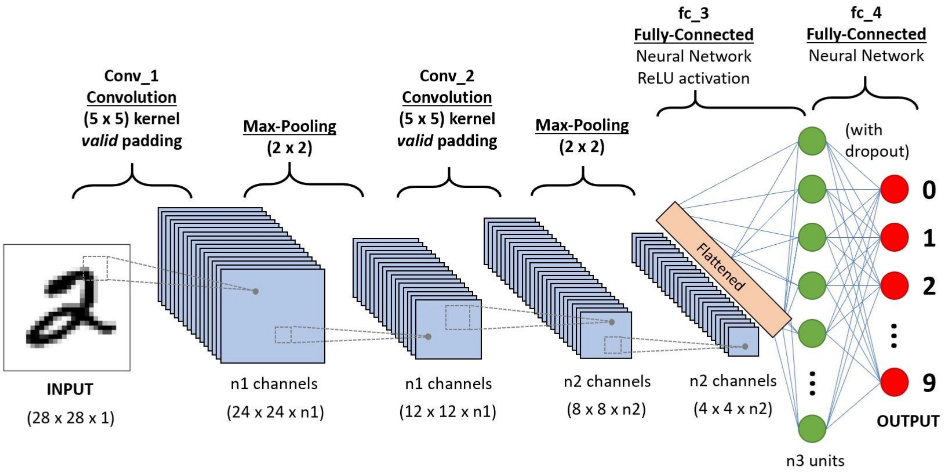

Figure 2.24: General CNN architecture, including convolution layers, kernels, pooling, and a fully connected layer. Figure from [206].

Recurrent Neural Networks (RNNs) are neural networks designed to handle sequential data by maintaining a hidden state that captures information from previous time steps, making them well suited to non-stationary signals. *Long short-term memory (LSTM)* networks (Figure 2.25) are a subtype of RNNs modified to capture long-term dependencies in sequential data [207]. LSTMs have been applied to ambulatory ECG denoising [208].

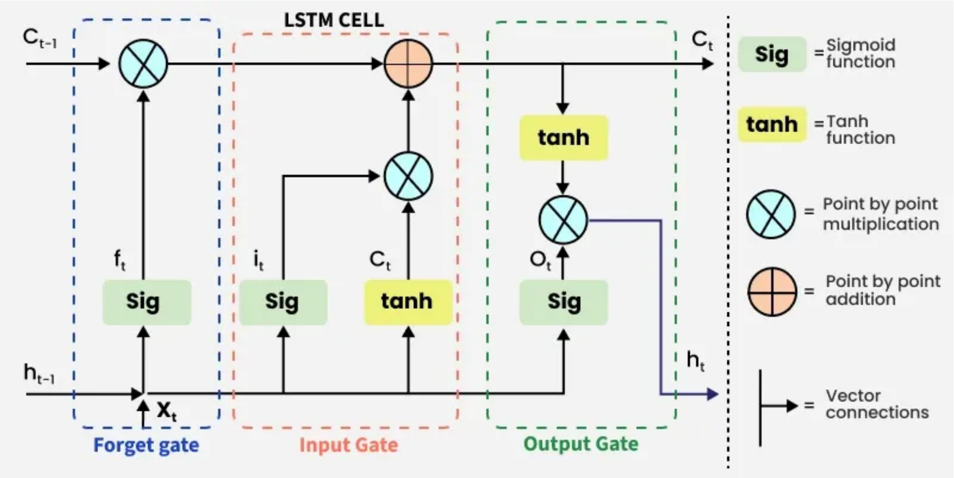

Figure 2.25: General LSTM architecture, containing the forget gate that removes unimportant information, the input gate that receives new useful information, and the output gate that determines which part of the current cell state should be sent as the hidden state. Figure from [207].

Autoencoders (AEs) learn compressed latent representations of input data and reconstruct denoised signals, with demonstrated success in ECG [209, 210, 211, 212, 213, 214] and HAR denoising [215, 216]. *Generative Adversarial Networks (GANs)* train generator-discriminator models to reconstruct clean signals and generate synthetic training data [217], and have been applied in EEG restoration [218] and HAR augmentation [219].

Hybrid Models

Hybrid architectures combine the strengths of multiple models. CNN-LSTM models are widely used, where CNNs capture local features and LSTMs provide temporal context. They have been successfully applied in HAR [220, 221, 222, 223] and automated epilepsy seizure detection [224]. Other hybrid model combinations include:

- Wavelet decomposition with SVMs for MA detection in EEG [225],
- KNN and one class SVM (OCSVM) for artifact reduction and emotion classification [226],
- Ensemble empirical mode decomposition (EEMD) and SVM for MA suppression in EEG [225],
- Nonlinear autoregressive with external output (NARX) plus Symlet window-based thresholding for MA removal in ECG signals [227],
- Cascaded CNN-RNN model for artifact suppression in EEG [228],
- OCSVM-GAN combination, where the OCSVM algorithm classified PPG segments as clean or noisy and the GAN network reconstructed the noisy segments [229],
- AE-GAN pipeline, where the AE produces a compact feature representation of the HAR data that is provided as input to the GAN discriminator [230],
- Ensemble learning with J48 decision tree, LR, and MLP classifiers using average of probabilities combination for HAR [231],
- Cascade ensemble learning comprised of Extremely Gradient Boosting Trees (XGBoost), RF, Extremely Randomized Trees (ExtraTrees), and Softmax regression for HAR with smartphones [193],
- PCA, LDA, and modified weighted SVM combination for HAR [232]

2.7.3 Hardware-Based Approaches

In addition to algorithmic and signal processing solutions, external motion sensors provide reference signals for MA detection. Inertial measurement units (IMUs), which integrate accelerometers, gyroscopes, and magnetometers, are widely used in wearable technology for human motion and posture recognition [233]. Wearable sensors offer several advantages, including compact form factor, long battery life, wearability, and low cost [183, 233].

In ambulatory urodynamics, accelerometer data have been combined with cystometry to detect and subtract MAs, improving event detection but at the expense of additional hardware. The integration of an IMU boosted bladder event classification accuracy. While promising, this study was only performed on Yucatan minipigs and has not been tested in human studies [183]. Similar multi-sensor approaches have been used for cough detection [234, 235] and in commercial systems such as the LEAF Patient Monitoring System, which utilises a 3-axis accelerometer for posture monitoring in hospitalised patients [236]. While sensors can improve artifact rejection through activity recognition, they can increase system complexity and power consumption, requiring careful integration [237].

Despite extensive research in ECG, EEG, and PPG, MA rejection in cystometry remains under-explored. Current artifact management relies heavily on manual clinician annotation, which is time-consuming, subjective and prone to error (see Section 2.6). There is limited work integrating motion sensing into ambulatory cystometry [183], and no standardized ML-based frameworks exist for automated artifact removal in CMGs. Given this, there is a clear need to develop and extend ML and hardware-augmented methodologies to ambulatory cystometry. Automated MA detection can reduce manual intervention, improve detrusor pressure estimation, and enable more reliable, real-time clinical assessment in ambulatory environments.

2.8 Ambulatory Urodynamics and Emerging Catheter-Free Diagnostics

The non-physiological nature of conventional cystometry in controlled clinical settings has driven the development of ambulatory urodynamic systems (AUDS). AUDS allows for continuous, real-world monitoring of bladder pressures during natural diuresis using portable systems [8, 7, 238, 6]. Like conventional cystometry, it employs dual catheters to record P_{ves} and P_{abd}. However, the patient remains ambulant during 2-4 hours of testing, improving symptom replication and diagnostic accuracy [238, 8].

By allowing patients to leave the examination room and perform their everyday activities, AUDS reduces embarrassment and better captures physiological bladder behaviour [7, 6]. Studies have demonstrated improved sensitivity for detecting DO and other dysfunctions not always captured in conventional testing [238, 8, 7]. Furthermore, AUDS enables outpatient evaluations and facilitates more regular assessments, reducing the need for time- and resource-consuming tests associated with conventional cystometry [15].

Despite these benefits, AUDS remains a second-line diagnostic tool, typically used when conventional cystometry fails to provide a definitive diagnosis [8, 7]. This is due to several technical and clinical limitations of AUDS, including invasiveness and discomfort associated with prolonged dual catheter use [19, 7, 10]; signal corruption due to MAs and catheter displacement [19, 7]; difficulty maintaining signal quality in uncontrolled ambulatory settings [239]; time-consuming data analysis requiring expert interpretation [239]; and high technical failure rates and variability in interpretation [10, 7].

To address the limitations of conventional and ambulatory catheter-based systems, telemetric ambulatory urodynamic monitoring (TAUDM) technologies have emerged as promising alternatives [7, 19]. These include wireless, catheter-free, and wearable or implantable devices that aim to enable long-term home monitoring and provide comprehensive insight into bladder functionality during natural filling [7, 19]. Such devices have several advantages, including reduced patient discomfort and invasiveness, lower risk of urinary tract infections, lower costs [240], and improved diagnosis of LUTDs such as incontinence [19]. These systems can be broadly categorised based on their sensing location and measurement modality, including intravesical, intradetrusor or extraluminal, and non-invasive optical approaches.

The most promising intravesical implant is currently the Glean Urodynamics System (formerly UroMonitor), developed by Bright Uro. This Bluetooth-enabled, catheter-free intravesical sensor remains in the bladder for up to seven days and transmits pressure data wirelessly to a receiver worn on the lower abdomen [7, 241, 242, 243]. The system includes a pressure sensor embedded in a flexible silicone tube, integrated software for clinicians and patients, and support for uroflowmetry, voiding diaries, and physiological data [7]. Another device, the UroMOCA, also records intravesical pressure and volume without catheters, using impedance-based volume estimation. The device is implanted via abdominal incision and has been tested in felines for 28 days [12].

Several additional intravesical prototypes exist, including:

- A battery-powered, off-line bladder pressure monitoring device small enough to be inserted via a cystoscope. Only a prototype was developed and no in vivo testing was reported [244].
- A C-shaped pressure-measuring device featuring an algorithm to select relevant pressure changes [245].
- A wirelessly powered implant operating on resonant inductive coupling with a communication range of 12 cm, tested in pigs [246].
- A silicone tube-based device that curls into a loop once inserted into the bladder via the urethra [247].
- A small, rechargeable, unanchored implantable pressure-volume sensor powered by inductive coupling, with approximately 40 hours of operation. Volume estimation is based on the direct current conducted by urine, which varies with both volume and concentration [248].
- A passive, minimally invasive implanted resonant pressure sensor that avoids battery-related limitations, though still in early stages of development [249].

- A miniature implantable wireless pressure sensor that transmits real-time data via a miniature radio frequency transmitter to an external receiver at a distance of up to 2 m. This study was preliminary [250].

More invasive approaches include intradetrusor and extraluminal devices implanted in the detrusor muscle or positioned adjacent to the bladder wall, with catheters inserted into the bladder lumen via the detrusor muscle [251, 10]. While these devices avoid direct urine contact and reduce corrosion risk, they require surgical placement and retrieval — procedures considered excessive and invasive for short-term diagnostics. Notably, erosion, migration, and biocompatibility issues have further limited their clinical translation [10, 252].

Non-invasive modalities such as near-infrared spectroscopy (NIRS) have been explored to measure detrusor oxygenation and haemodynamics [9, 5], where oxyhaemoglobin levels in the detrusor increase before voiding, followed by a decrease during voiding while deoxyhemoglobin levels increase. Dysfunction is therefore determined based on variations in typical haemodynamic and oxygen levels [9, 5]. However, NIRS does not provide absolute pressure values, is susceptible to MAs, and suffers from limited reproducibility [5, 145].

Despite significant advances in the realm of TAUDM, most devices remain at the preclinical or early clinical stage due to technical and physiological challenges [7, 10]. These include:

- *Hermeticity and biocompatibility*: Hermetic and biocompatible packaging is essential to prevent corrosion and immune response but increase device size and weight and may reduce sensor sensitivity.
- *Sensor drift and degradation*: Pressure baseline and sensitivity can drift due to moisture or biofouling.
- *Power supply limitations*: Batteries add weight and size to the system and have a limited lifetime, while wireless power transfer suffers from power loss due to attenuation by biological tissues and limited communication distance.
- *Telemetry and data sampling rate constraints*: Wireless communication must balance high-resolution data with power limitations.
- *Incompatibility with imaging (e.g., MRI)*: Most implants are incompatible with MRI, limiting their use in patients requiring multimodal diagnostics.
- *Lack of motion context*: Most systems are unable to monitor patient movement unlike conventional cystometry that records P_{abd} to subtract it from P_{ves} and isolate true detrusor pressure. This makes it difficult to differentiate between true bladder events and motion-induced pressure changes.
- *Surgical invasiveness*: Several devices require invasive surgical placement which is excessive in the context of short-term UDS

While the Glean Urodynamics System shows promise, it is not yet commercially available, and pricing remains unclear [242]. The device also requires subjective patient input for event annotation, which can reduce diagnostic accuracy and reproducibility [243]. Additionally, unanchored intravesical sensors may induce bladder irritation and urinary symptoms due to movement within the bladder [7]. These challenges continue to delay the clinical implementation of TAUDM systems. Addressing them requires integration of robust pressure sensing and motion-context acquisition within a compact and patient-friendly device.

2.9 Summary

This chapter has reviewed current urodynamic evaluation methods, with a focus on cystometry as the gold standard for assessing bladder function. Despite its clinical value, conventional cystometry is limited by its invasiveness, reliance on non-physiological testing conditions, susceptibility to motion artifacts, and dependence on clinician interpretation. These factors can reduce diagnostic reliability, limit accessibility, and hinder the accurate replication of real-world patient symptoms.

Existing approaches, including ambulatory urodynamic studies (AUDS) and emerging catheter-free technologies, attempt to address some of these limitations by enabling longer-term and more physiological monitoring. However, these systems remain either invasive, technically complex, underdeveloped, or insufficiently robust to motion artifacts, particularly in uncontrolled ambulatory environments. As a result, reliable interpretation of bladder pressure signals in the presence of motion remains a key unresolved challenge.

In particular, the absence of an abdominal reference signal in single-catheter configurations introduces a fundamental limitation and challenge: the inability to directly distinguish between motion artifacts and true detrusor contractions. This highlights the need for robust, objective, and automated methods for motion artifact detection and signal interpretation in single-channel cystometry. To address this challenge, the following chapters present Part A and Part B, which investigate two complementary motion-aware approaches for single-catheter cystometry.

3

Methods and Results - Part A: Machine Learning Pipeline for Motion Artifact Removal in Ambulatory Cystometry

3.1 Problem Definition and Design Objectives

Single-channel cystometry presents a challenging signal processing and machine learning problem due to the absence of a secondary reference channel for isolating motion artifacts. Unlike conventional dual-catheter cystometry, pressure variations caused by patient motion, posture changes, and physiological detrusor contractions are captured within a single measurement channel, complicating downstream clinical interpretation.

The objective of Part A was to develop a machine learning pipeline capable of binary classification of pressure segments extracted from time series cystometry data. Machine learning models are trained to differentiate between motion-contaminated pressure segments and detrusor activity segments, subsequently minimising the suppression of true bladder contractions.

The machine learning pipeline is composed of the following:

- Manual annotation, normalisation, and label taxonomy definition
- Posture, motion, and detrusor interval extraction
- Posture-aware signal artifact correction
- Posture-aware peak detection and peak interval extraction
- Dense per-sample ground truth label construction
- Data visualisation
- Peak-centred windowing
- Manual feature engineering
- Model selection, training, and evaluation

The full pipeline implementation, including patient data, is publicly available here.

3.2 Data Acquisition and Annotation Structure

This pipeline uses patient data captured by the Uropine system developed by RSI in India. The data consists of a single-channel intravesical pressure signal sampled at 1 Hz. Alongside the pressure trace, clinicians manually annotated clinically relevant events. Each annotation was defined by a label type (e.g., coughing, posture transitions, saline infusion, movement, detrusor activity, drinking) and corresponding start and end times aligned to the pressure signal. A total of 10 patients were included in the study. Table A.2 (Section A.2) summarises demographic information, relevant medical history, pre-clinical urinary symptoms, and key cystometric outcomes for the study cohort.

3.3 Data Preprocessing

3.3.1 Label Normalisation and Taxonomy

Raw clinician-provided annotations were normalised by converting label text to lowercase, underscore-separated formats to ensure consistency across patient data. Normalised labels were then validated against a predefined label taxonomy comprising motion artifact events (e.g. patient movement, drinking, coughing, posture change) and detrusor activity. Any label not matching one of the predefined labels raised an error, preventing data corruption and ensuring annotation integrity. Validated labels were subsequently categorised into two high-level classes: motion artifacts and detrusor activity.

3.3.2 Motion, Detrusor, and Posture Interval Extraction

Posture regions, representing a patient's continuous body position (supine, sitting, standing), were extracted from validated annotations describing posture changes. Discrete posture transition events were converted into continuous posture regions by assuming that each posture persists until the next annotated posture change. In the absence of an initial posture annotation at signal onset, a supine posture was assumed. Posture regions were required for downstream processing, as patient posture affects the recorded pressure baseline, thereby influencing both negative pressure artifact correction and peak detection.

Motion artifact intervals were extracted from the validated and classified annotations. Posture transitions were explicitly treated as motion artifacts to prevent transient pressure changes during movement from being misinterpreted as detrusor activity. Detrusor activity intervals were similarly extracted from the validated and classified annotations. These intervals are subsequently used downstream to map extracted pressure peaks to either motion artifacts or detrusor activity.

3.3.3 Negative Pressure Artifact Correction

Occasional negative pressure values were observed in the raw pressure recordings, caused by sensor artifacts and transient disconnections. Clipping or global thresholding of these values risked distorting pressure dynamics. Therefore, posture-aware correction was employed instead. Each posture region was processed independently, with a local baseline estimated using the median pressure value. Samples deviating below this baseline by a predefined margin were replaced using nearest valid neighbouring samples within the same posture region. This approach preserves pressure dynamics while removing sensor artifacts.

3.3.4 Posture-Aware Peak Detection and Interval Extraction

Peak detection was used to identify candidate pressure variations, including detrusor events not explicitly annotated. Pressure peaks were detected within individual posture regions using Scipy's $find_{peaks}$ algorithm, enabling locally adaptive thresholds that account for posture-induced baseline pressure changes. A high minimum prominence threshold was applied to reduce false detections caused by sensor noise or minor pressure fluctuations, capturing only clinically meaningful pressure changes.

A post-hoc validation step was subsequently applied. Specifically, for each manually annotated interval, covering both detrusor activity and motion artifacts, the algorithm verified the presence of, at minimum, one detected peak. If none was found, a single representative peak, defined as the maximum pressure within the interval, was added. This ensured that all annotated events contributed at least one peak-centred sample to downstream analyses.

Posture-aware peak intervals were then constructed to define event boundaries. For each detected peak, a local baseline was estimated as the median pressure within the corresponding posture region. Interval boundaries were then defined by searching backward and forward from the peak until the signal returned to within a predefined margin above this baseline. This yielded physiologically meaningful intervals that adapt to posture-specific baselines. Peaks not overlapping any manually annotated motion artifact interval were classified as detrusor events. These peak-derived detrusor intervals were concatenated with manual detrusor annotations during dense per-sample label construction, ensuring that unlabelled detrusor activities were retained.

3.3.5 Dense Per-Sample Ground Truth Label Construction

A dense per-sample ground truth vector was constructed for each patient recording by assigning a label to every pressure sample. Samples were initially labelled as baseline, then updated using manual detrusor activity intervals, followed by posture-aware peak-derived intervals used to label additional detrusor activity where no manual detrusor or motion artifact label was present. Motion artifact intervals were applied last. This produced a dense ground truth vector in which every sample was uniquely labelled as baseline, motion artifact, or detrusor activity, enabling validation and visual inspection.

3.3.6 Pipeline Validation via Data Visualisation

Patient recordings were visualised to validate the processing pipeline and provide qualitative insight into the data. Plots show the cleaned pressure signal overlaid with posture regions, motion artifact intervals, detrusor activity intervals, and detected peaks (Figure 3.1). These visualisations enabled verification of label correctness and temporal alignment as well as assessment of posture-aware baseline behaviour.

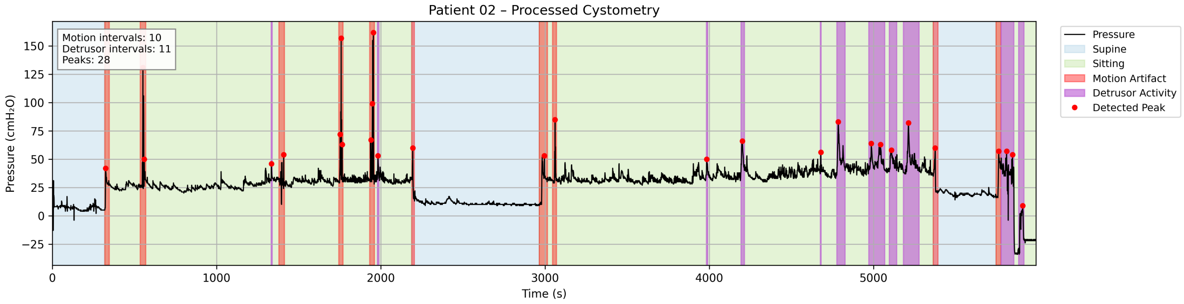

Figure 3.1: Example visualisation of a processed patient recording. The cleaned pressure signal is overlaid with posture regions, motion artifact intervals, detrusor activity intervals, and detected peaks.

3.3.7 Peak-Centred Window Extraction and Labelling

To enable supervised learning, fixed-length, peak-centred windows were extracted from the pressure signal. Each window represents a single training sample, temporally aligned to a detected pressure peak, and labelled as either motion artifact or detrusor activity based on the interval containing the peak. Window extraction was therefore restricted to motion and detrusor events, with baseline segments – accounting for the majority of the cystometry signal – excluded.

Manual event duration analysis yielded a mean annotated event duration of ≈40 s with a standard deviation ≈46.0 s. Based on this distribution, a symmetric 60 s window (±30 s around each peak) was selected to ensure that most annotated events were fully contained within a single window while maintaining consistent input dimensionality. In total, 312 windows were extracted, a subset of which was visually inspected to verify temporal alignment, signal morphology, and label assignment (Figure 3.2). This served as a qualitative sanity check on peak detection and window construction prior to model training.

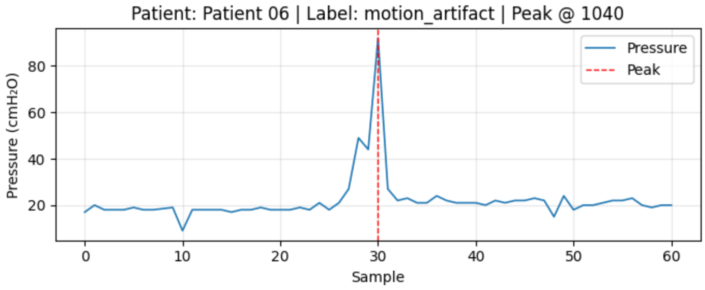

Figure 3.2: Example validation of extracted peak-centred windows. Each window is temporally aligned to a detected pressure peak and labelled as either motion artifact or detrusor activity.

3.4 Feature Extraction

Manual feature engineering was performed, where features were extracted from each peak-centred window to transform raw pressure signals into structured representations suitable for supervised machine learning. The centred peak within each window was used as a consistent reference point for morphological feature computation.

For each windowed pressure signal, a set of statistical features was computed to characterise overall pressure distribution and variability across motion artifacts and detrusor events. These included:

- Mean pressure
- Standard deviation
- Minimum and maximum pressure
- Pressure range
- Median pressure

Moreover, to capture slow pressure trends associated with posture transitions or prolonged detrusor contractions, a global slope feature was calculated as the difference between the final and initial window samples, normalised by window length.

In addition to global statistics, a set of peak morphology features was extracted relative to a window-specific baseline. Baseline pressure values were estimated separately on the rising and falling sides of the peak using a low-percentile statistic to reduce sensitivity to transient fluctuations. Baseline crossing points were then identified using a tolerance margin, enabling estimation of event duration and temporal symmetry. Morphological features extracted for each window included:

- Peak-to-baseline pressure difference
- Rise time and fall time
- Event duration and effective width
- Rise and fall slopes
- Event symmetry ratio
- Baseline shift across the window
- Peak prominence
- Ratios relating peak height and prominence to event width

Lastly, the area under the pressure curve relative to the estimated baseline was computed between baseline crossing points surrounding the peak. Combined, these features capture both global window pressure characteristics and local event morphology.

3.5 Binary Label Encoding

A binary target variable was defined, with motion artifact windows assigned the positive class (1) and detrusor activity windows assigned the negative class (0).

3.6 Model Selection

3.6.1 Feature-Based Models

Feature-based machine learning models were trained to classify windowed pressure segments using the manually extracted features. Four classifiers were selected to evaluate the separability of motion artifacts and detrusor activity under different modelling assumptions, including linear, margin-based, ensemble, and boosted tree approaches. The models included RF, XGBoost, SVM, and LR.

Random Forest (RF) Classification

The RF classifier was selected given its ability to model non-linear relationships while being robust to noise and feature scaling [253]. RF models consist of ensembles of decision trees trained on bootstrap samples of the training data, promoting decorrelation between individual trees and reducing overfitting [254].

Extreme Gradient Boosting (XGBoost) Classification

XGBoost was selected as a second tree-based model due to its ability to capture feature interactions through gradient-boosted decision trees. While RF trains trees independently in parallel, XGBoost constructs trees sequentially, with each new tree trained to correct errors made by the previous tree through a process called boosting [255].

Linear Support Vector Machine (SVM) Classification

SVMs were employed as margin-based classifiers that construct decision boundaries by maximising the separation margin between classes [256]. A linear SVM was selected to assess whether motion artifacts and detrusor activity are separable using a linear decision boundary in the proposed feature space.

Logistic Regression (LR) Classification

LR was also used as a complementary linear baseline model to assess class separability within the engineered feature space using class probabilities. Unlike SVMs, which optimise a margin-based decision boundary, LR estimates class probabilities by fitting a logistic function to a weighted combination of input features [257].

3.6.2 Neural Network Models

While feature-based models rely on manually engineered features of pressure windows, neural network models learn discriminative representations directly from raw pressure windows. This reduces dependence on manual feature engineering and allows training of models on non-linear temporal patterns. In Section 2.7.2, neural network architectures such as MLPs, CNNs, and LSTMs were shown to demonstrate strong performance in related motion artifact detection tasks. Therefore, these architecture models were selected in this work. All neural network models were trained on the derived fixed-length pressure windows represented as one-dimensional temporal sequences sampled at 1 Hz.

Multi-Layer Perceptron (MLP)

A MLP was selected for its simplicity and suitability as a baseline neural model for comparison against feature-based models and more advanced neural models.

Convolutional Neural Network (CNN) Architectures

CNNs were employed to exploit local temporal structure within pressure windows through convolutional filters. Four CNN architectures were evaluated:

- *Shallow 1D CNN:* A 1D CNN model with few convolutional layers [186]. This architecture served as a baseline to evaluate whether convolutional feature extraction alone demonstrates improved performance over feature-based and deeper neural models.
- *Lightweight U-Net (LUNet):* A lightweight U-Net–inspired encoder–decoder architecture incorporating skip connections and a dilated bottleneck. Skip connections prevent information loss during downsampling by connecting encoder and decoder layers, enabling lower-level features to be passed directly to the higher-level features, improving model performance. The dilated bottleneck expands the temporal receptive field without increasing model depth or parameter count [196].
- *Lightweight 1D CNN with Channel-Wise Attention:* A 1D CNN augmented with squeeze–excitation (SE) blocks for channel-wise attention. SE blocks adaptively adjust channel weights, amplifying informative channels while suppressing noisy or non-contributing channels [203].
- *Multi-branch 1D CNN with channel-wise attention:* A multi-branch 1D CNN comprising parallel convolutional branches with varying kernel sizes. Each branch is supplemented with SE blocks for scale-specific channel re-weighting and the resulting feature maps are concatenated to integrate information across multiple temporal resolutions [202].

Bidirectional LSTM (Bi-LSTM) with Attention

A Bi-LSTM network was implemented to model temporal dependencies within pressure windows. The model processes the input sequence in both forward and backward directions, capturing information from both preceding and succeeding samples. An attention mechanism was incorporated to allow the model to learn which regions of each window contributed most to the classification outcome [208].

3.6.3 Hybrid Models

In addition to stand-alone feature-based and neural network models, several hybrid architectures were selected and evaluated to combine the strengths of convolutional, recurrent, and feature-based models. Two categories of hybrid models were defined: CNN–LSTM architectures and feature–neural network fusion models.

CNN-LSTM Architectures

Both parallel and sequential CNN–LSTM architectures were implemented. In parallel CNN–LSTM models, convolutional and recurrent branches independently learn feature representations from input windows, and the learned representations are fused prior to classification [203, 258]. In sequential CNN–LSTM models, convolutional layers first extract local temporal features, which are then provided as input to an LSTM to capture longer-range temporal dependencies [224, 222, 223].

For architectural simplicity, the shallow 1D CNN architecture was selected for all CNN–LSTM models. The same Bi-LSTM architecture used in the standalone model was implemented to ensure comparability across architectures.

Feature-Neural Network Fusion Models

Hybrid feature–neural network models were also evaluated by combining neural network learned representations with manually engineered features. Two fusion strategies were defined:

- *Late Fusion:* The neural network model and the feature-based classifier were trained independently, and their predicted probabilities were combined at the decision level for final classification, where $p_{\text{fused}} = w_{\text{RF}} p_{\text{RF}} + w_{\text{CNN}} p_{\text{CNN}}$ and $w_{\text{RF}} = w_{\text{CNN}} = 0.5$.

- *Feature-Level Fusion:* The neural network model was used to learn a latent embedding representation from each input window, which was then concatenated with the manually engineered feature vector. A feature-based classifier was subsequently trained on the combined representation to produce the final prediction.

The neural network architecture selected for feature–neural fusion was chosen based on the best-performing stand-alone neural network model. This ensured that fusion implemented the most informative learned representations.

3.6.4 Feature Augmentation

The shallow 1D CNN was also trained on raw input windows combined with manually engineered features to determine if manually engineered features could boost performance in neural network model applications.

3.7 Model Training Strategy

3.7.1 Patient-Wise Data Splitting and Cross-Validation

To obtain an unbiased evaluation of model generalisation while maximising use of the limited dataset, a stratified group cross-validation strategy was used. All data splitting was performed on a patient-wise basis, ensuring that windows extracted from the same patient recording were never distributed across different folds. This prevents data leakage arising from intra-patient signal similarity and ensures that model evaluation reflects true inter-patient generalisation.

Stratified Group K-Fold cross-validation with $K = 5$ folds was used, with patient identifiers treated as grouping variables and window-level class labels for stratification. This preserved class balance across folds while maintaining patient-level separation. Given the small dataset size, five-fold cross-validation provides reliable performance estimates.

3.7.2 Core Training Parameters

Neural Network Optimisation

Neural network models were trained using the Adam optimiser with an initial learning rate of $1 * 10^{-3}$. Adam was selected for its adaptive learning rate ability that enables stable convergence behaviour in high-dimensional spaces [259].

An adaptive learning rate schedule was implemented using ReduceLROnPlateau, which halved the learning rate when validation loss failed to improve for five consecutive epochs. This enabled the models to fine-tune weights, subsequently stabilising training and increasing training speed [260]. A minimum learning rate of $1 * 10^{-6}$ was enforced to prevent early convergence.

Batch size defines the number of training samples processed together before the model's weights and biases are updated. Training was performed using mini-batches of size 32 or 64, tuned according to model validation results [261]. Models were trained for a maximum of 100 epochs, with early stopping applied based on validation loss to prevent overfitting.

Regularisation was applied to prevent overfitting in neural network models. Dropout was incorporated into the model architectures, randomly deactivating neurons during training, forcing the model to learn more robust, generalisable [262]. A dropout rate of 0.5 was used. In addition, early stopping was employed, implemented to stop model training once performance on a validation set stops improving

[263]. A patience of 10 epochs was used and the model parameters corresponding to the lowest validation loss were restored.

Loss Function

The loss function measures the error between the model's predictions and the ground truth label, where the model's internal weights and biases are updated to minimise the loss, guiding learning and performance evaluation [264]. For neural network models, binary cross-entropy loss was used, penalising confident misclassifications. It is the default loss function for binary classification problems [265]. Native loss functions were used for feature-based models.

Class Weighting

The dataset demonstrated class imbalance, with 126 detrusor activity windows and 186 motion artifact windows. To address class imbalance, fold-specific class weighting was implemented during training for all models. Class weights were computed using inverse class frequency within each training fold and applied during model training.

3.8 Hyperparameter Tuning

Hyperparameter grids were defined for all feature-based models and optimised using grid search (GridSearchCV) within each training fold, using three-fold internal cross-validation. Average precision was used as the optimisation metric to align with the clinically motivated evaluation strategy.

For each fold, the best-performing hyperparameter configuration identified via internal cross-validation was refit on the full training split and evaluated on the held-out validation data. The most frequently selected hyperparameter combination across folds was reported and chosen for final model instantiation.

For neural network models, hyperparameter tuning was performed manually, where architectural and training-related parameters were adjusted systematically, with model selection guided by validation performance. Hyperparameters included:

- Batch size (32 or 64)
- Pooling layers to reduce feature map size, including max pooling and average pooling.
- Activation layers enabling models to learn non-linear relationships, including ReLU, Sigmoid, SeLU, and Tanh.
- Batch normalisation layers to stabilise and accelerate training
- Number of convolutional and fully connected layers
- Convolutional kernel size for CNNs used to produce a new feature map, including kernel sizes of 3, 5, 7, 9, 11, 13, 15, 17, and 21.
- Number of filters per convolutional layer, determining the number of feature maps learned (i.e. the number of different learned patterns such as edges, textures, or shapes from the input), including 16, 32, 64, 128, and 256.
- Z-score normalisation

3.9 Experimental Setup

3.9.1 Randomness and Reproducibility

To ensure reproducibility, all experiments were conducted using fixed random seeds (42). Randomness was controlled across NumPy, Python, TensorFlow, and scikit-learn.

3.9.2 Computational Environment and Framework Versions

All models were trained and evaluated on a consumer-grade laptop (HP Envy x360 Convertible 15) equipped with an Intel Core i7 processor and 16 GB RAM. No dedicated GPU was used. Neural network models were implemented using TensorFlow/Keras, while feature-based classifiers were implemented using scikit-learn. NumPy and SciPy were used for numerical computation. The software versions used in this pipeline can be found in Appendix A.3.

3.10 Model Performance Evaluation

Model evaluation was designed to reflect the clinical consequences of classification errors. Within each fold, data were divided into training and validation subsets. The training subset was used to optimise model parameters, while the validation subset was used for threshold selection and performance evaluation. Performance metrics were computed at the window level and aggregated across folds, reported as mean ± standard deviation.

Given the class imbalance, classification accuracy was not used as a primary evaluation metric. Instead, evaluation focused on metrics robust to imbalance and aligned with clinical risk. False positives (FP) – where detrusor activity is incorrectly classified as motion artifact – were considered the most clinically harmful error, as they can lead to suppression of true bladder contractions and misinterpretation of physiological bladder function. In contrast, false negatives (FN) preserve detrusor activity but fail to suppress motion artifacts. Consequently, model evaluation prioritised minimisation of false positives, with average precision (area under the precision-recall curve, PR AUC) being selected as the primary optimisation metric during training. Higher PR AUC values reflect a stronger ability of the model to predict motion artifacts while limiting false alarms (misclassification of detrusor activity as motion artifact).

The following secondary metrics were also reported per fold:

- Precision, recall, and F_1 score for the motion artifact class
- Precision, recall, and F_1 score for the detrusor activity class

Precision for the motion artifact class was used as the primary clinically relevant evaluation metric for reporting of model performance.

In addition, threshold tuning was done. Specifically, during classification, models predict the probability (between 0 and 1) that the input belongs to the positive class (motion artifact). If the probability exceeds a defined threshold (default 0.5), the final prediction is the positive class. Otherwise, it is classified as the negative class (detrusor activity). To minimise the false positive rate (FPR), an FPR-constrained threshold selection strategy was used to control false positive errors.

The FPR is defined as:

$$\mathrm{FPR} = \frac{\mathrm{FP}}{\mathrm{FP} + \mathrm{TN}}, \tag{3.1}$$

where FP (false positive) denotes detrusor activity windows incorrectly classified as motion artifacts, and TN (true negative) denotes correctly classified detrusor activity windows.

Within each cross-validation fold, the decision thresholds were selected using validation data. Thresholds satisfying a predefined FPR constraint were identified, and among these, the threshold maximising motion artifact recall was selected. The chosen threshold was then applied for final metric computation within that fold.

To further capture model behaviour beyond aggregate performance metrics, an error profile analysis was done to evaluate the types of misclassification made by each model under the selected thresholds.

For each cross-validation fold, both false positive and false negative errors, as well as the FPR, were calculated using the fold-specific, FPR-constrained classification threshold.

Given the clinical priority of preserving true detrusor events, false positives were considered the more harmful error type. These error quantities were analysed to characterise model behaviour under clinically constrained thresholds and were not used directly for model ranking, as their effects are captured by the selected evaluation metrics.

Tables 3.1- 3.4 report mean ± standard deviation values for each evaluation metric across all models. Within each model category, the highest and lowest metric values are highlighted to assist in model comparison. For neural network models, the top two performing models per metric are highlighted to reflect the larger performance spread demonstrated within this group.

3.10.1 Feature-Based Models

Table 3.1 shows that the RF model achieved the highest values across most evaluation metrics among the feature-based models.

Table 3.1: Feature-based model performance comparison. Values are reported as mean ± standard deviation. Motion artifact is treated as the positive class. The highest metric value is highlighted in green and the lowest metric value is highlighted in red.

Model	Prec. (MA)	Rec. (MA)	F1 (MA)	Prec. (DA)	Rec. (DA)	F1 (DA)	PR AUC
Feature-Based Models							
Random Forest	0.899 ± 0.071	0.590 ± 0.179	0.697 ± 0.141	0.640 ± 0.176	0.935 ± 0.034	0.741 ± 0.135	0.865 ± 0.114
XGBoost	0.811 ± 0.209	0.524 ± 0.266	0.614 ± 0.273	0.615 ± 0.183	0.923 ± 0.014	0.720 ± 0.144	0.845 ± 0.148
SVM	0.802 ± 0.178	0.415 ± 0.259	0.521 ± 0.256	0.575 ± 0.149	0.929 ± 0.015	0.697 ± 0.129	0.796 ± 0.138
Logistic Regression	0.825 ± 0.126	0.421 ± 0.205	0.539 ± 0.202	0.561 ± 0.144	0.923 ± 0.014	0.685 ± 0.125	0.754 ± 0.167

3.10.2 Neural Network Models

Table 3.2 indicates that no single neural network model achieved the highest performance across all evaluation metrics. Performance varied across metrics, with the shallow 1D CNN and the multi-branch 1D CNN with channel-wise attention achieving the highest values for several metrics.

Table 3.2: Neural network model performance comparison. Values are reported as mean ± standard deviation. Motion artifact is treated as the positive class. For each metric, the two highest-performing models are highlighted in green (darker shading indicates higher performance), while the lowest-performing model is highlighted in red.

Model	**Prec. (MA)**	**Rec. (MA)**	**F1 (MA)**	**Prec. (DA)**	**Rec. (DA)**	**F1 (DA)**	**PR AUC**
MLP	0.747 ± 0.081	0.722 ± 0.099	0.728 ± 0.067	0.615 ± 0.192	0.632 ± 0.189	0.615 ± 0.181	0.784 ± 0.074
Shallow 1D CNN	0.902 ± 0.052	0.647 ± 0.087	0.751 ± 0.073	0.656 ± 0.128	0.923 ± 0.014	0.760 ± 0.092	0.858 ± 0.082
LUNet	0.914 ± 0.036	0.609 ± 0.245	0.698 ± 0.206	0.650 ± 0.208	0.934 ± 0.024	0.745 ± 0.155	0.859 ± 0.140
Lightweight 1D CNN with Channel-Wise Attention	0.885 ± 0.071	0.576 ± 0.178	0.684 ± 0.150	0.619 ± 0.178	0.923 ± 0.014	0.726 ± 0.135	0.856 ± 0.116
Multi-branch 1D CNN with channel-wise attention	0.916 ± 0.031	0.640 ± 0.156	0.740 ± 0.118	0.655 ± 0.201	0.929 ± 0.015	0.748 ± 0.162	0.885 ± 0.042
Bi-LSTM with Learned Temporal Attention	0.872 ± 0.108	0.608 ± 0.245	0.695 ± 0.217	0.644 ± 0.206	0.923 ± 0.014	0.740 ± 0.140	0.870 ± 0.114

3.10.3 Hybrid Models

As shown in Table 3.3, the sequential CNN–LSTM model achieved higher metric values than the parallel CNN–LSTM across all reported evaluation metrics. For feature–neural network fusion models, RF and the shallow 1D CNN were combined, with the feature-level fusion model achieving higher metric values than the late-fusion ensemble across all reported metrics.

Table 3.3: Model performance comparison across different architectures. Values are reported as mean ± standard deviation. Motion artifact is treated as the positive class. The highest metric value is highlighted in green and the lowest metric value is highlighted in red.

Model	Prec. (MA)	Rec. (MA)	F1 (MA)	Prec. (DA)	Rec. (DA)	F1 (DA)	PR AUC
Hybrid CNN-LSTM Models							
Sequential Hybrid CNN–LSTM Model	0.907 ± 0.048	0.648 ± 0.233	0.734 ± 0.168	0.705 ± 0.216	0.929 ± 0.016	0.779 ± 0.158	0.858 ± 0.109
Parallel Hybrid CNN–LSTM Model	0.853 ± 0.123	0.540 ± 0.207	0.646 ± 0.211	0.612 ± 0.141	0.923 ± 0.014	0.726 ± 0.107	0.845 ± 0.136
Hybrid Feature–Neural Network Fusion Models							
Late-Fusion RF–CNN Ensemble	0.881 ± 0.078	0.554 ± 0.216	0.659 ± 0.201	0.622 ± 0.168	0.929 ± 0.016	0.730 ± 0.130	0.860 ± 0.101
CNN–RF Feature-Level Hybrid	0.898 ± 0.061	0.563 ± 0.198	0.675 ± 0.174	0.629 ± 0.160	0.934 ± 0.015	0.739 ± 0.124	0.863 ± 0.099

3.10.4 Feature Augmentation Model Comparison

Table 3.4 compares the performance of the shallow 1D CNN trained on raw input windows versus raw windows combined with manually engineered features. Across all reported metrics, the shallow 1D CNN trained on raw windows achieved higher performance.

Table 3.4: Performance comparison of the shallow 1D CNN trained on raw input windows versus raw windows augmented with manually engineered features. Values are reported as mean ± standard deviation. Motion artifact is treated as the positive class.

Model	**Prec. (MA)**	**Rec. (MA)**	**F1 (MA)**	**Prec. (DA)**	**Rec. (DA)**	**F1 (DA)**	**PR AUC**
Shallow 1D CNN	0.902 ± 0.052	0.647 ± 0.087	0.751 ± 0.073	0.656 ± 0.128	0.923 ± 0.014	0.760 ± 0.092	0.858 ± 0.082
Shallow 1D CNN + Features	0.892 ± 0.052	0.563 ± 0.141	0.680 ± 0.110	0.621 ± 0.169	0.923 ± 0.014	0.726 ± 0.142	0.845 ± 0.052

3.10.5 Top-Performing Models

Based on the performance metrics reported in the preceding sections, a subset of models consistently achieved the highest values across multiple evaluation metrics within each model category. These models are:

- *Feature-based models:* RF
- *Neural network models:* Shallow 1D CNN and multi-branch 1D CNN with channel-wise attention
- *Hybrid models:* Sequential hybrid CNN–LSTM model and CNN–RF feature-level hybrid model

3.10.6 Error Profile Analysis

Table 3.5: Aggregated false negative (FN), false positive (FP), and false positive rate (FPR) statistics (mean ± standard deviation) across cross-validation folds for the top-performing models.

Model	**FN**	**FP**	**FPR (%)**
CNN–RF Feature-Level Hybrid	16.2 ± 9.9	1.6 ± 0.5	6.6 ± 1.5
Shallow 1D CNN	12.8 ± 5.6	2.0 ± 0.9	7.7 ± 1.4
Multi-branch Attention CNN	15.2 ± 12.5	1.8 ± 0.7	7.1 ± 1.5
Sequential CNN–LSTM	13.0 ± 12.4	1.8 ± 0.7	7.1 ± 1.6
Random Forest	15.6 ± 11.5	1.8 ± 1.2	6.5 ± 3.4

Aggregated confusion matrices for the top-performing models are provided in Appendix A.5 to illustrate the distribution of false positive and false negative errors per model.

3.11 Model Ranking

To enable clinically informed comparison of model performance, a weighted ranking framework was developed based on evaluation metrics and their clinical relevance. Each metric was assigned a weight reflecting its importance in minimising clinically harmful misclassifications, with all weights summing to unity.

The weighted metrics used for model ranking, ordered from highest to lowest clinical priority, were:

- MA Precision: 0.25 (higher precision reduces misclassification of detrusor activity as motion artifact)
- DA Recall: 0.20 (preservation of true detrusor activity)
- PR AUC: 0.20 (reflects overall discrimination of motion artifacts while limiting false positives)
- MA Recall: 0.15 (effective detection of motion artifacts)
- DA Precision: 0.10 (reduces misclassification of motion artifacts as detrusor activity)
- MA F_1 score: 0.05
- DA F_1 score: 0.05

F_1 scores were assigned lower weights, as they represent a balance between precision and recall already captured by higher-priority metrics.

To support interpretation and comparison, the aggregated evaluation metrics of the top-performing models were first visualised. Figure 3.3 presents the mean performance across cross-validation folds, with error bars indicating standard deviation. These visualisations provide a compact overview of performance trends and variability across models.

Models were then ranked for each metric, with ranks assigned from 1 (lowest performance) to 5 (highest performance). Ranking considered both mean performance and variability across folds; in cases of similar mean values, models with lower standard deviation were assigned higher ranks, reflecting more consistent performance.

A total score for each model was then calculated by multiplying the rank for each metric by its corresponding clinical weight and summing across all metrics. The resulting scores were normalised by dividing by the highest score, enabling relative comparison across models. The final normalised ranking scores are presented in Table 3.6, while detailed per-metric rankings and intermediate weighted scores are provided in Appendix A.6.

Table 3.6: Final model ranking based on weighted, normalised performance scores across clinically prioritised metrics.

Model	**Normalised Score**
Multi-branch 1D CNN with Attention	1.00
Shallow 1D CNN	0.76
Sequential CNN–LSTM	0.69
CNN–RF Feature-Level Hybrid	0.57
Random Forest	0.44

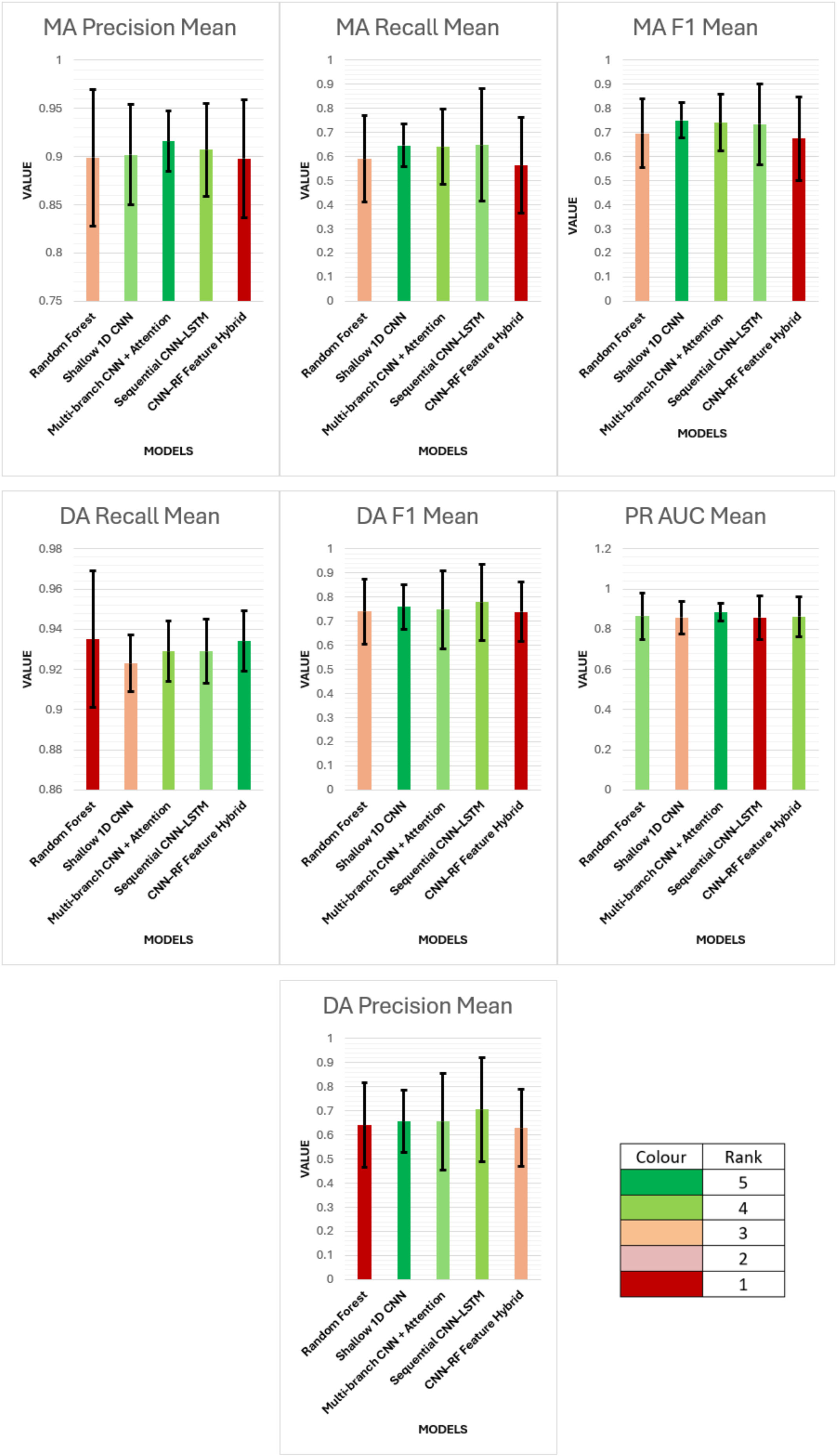

Colour	Rank
🟩	5
🟩	4
🟧	3
🟥	2
🟥	1

Figure 3.3: Comparison of aggregated evaluation metrics for the top-performing feature-based, neural network, and hybrid models. Values are reported as mean ± standard deviation across cross-validation folds.

3.12 Top-Performing Model Architectures and Hyperparameters

Final model architectures and hyperparameter configurations for the top-performing models identified are reported in this section. Full architecture definitions and hyperparameters for all evaluated models are provided in Appendix A.4.

3.12.1 Feature-Based Model

The RF model is trained on the manually engineered feature vectors extracted from peak-centred pressure windows. The final model consists of an ensemble of decision trees trained using bootstrap sampling, with each tree learning decision rules based on a random subset of input features at each split.

Table 3.7: Final hyperparameter configurations for the Random Forest model. Hyperparameters were selected using patient-level cross-validated grid search. Final models were retrained on the full labelled dataset using the selected configuration.

Model	Hyperparameter	Value
Random Forest	Number of trees ($n_{\text{estimators}}$)	200
	Maximum tree depth (max_depth)	10
	Minimum samples to split (min_samples_split)	2
	Minimum samples per leaf (min_samples_leaf)	1
	Features per split (max_features)	$\sqrt{p}$
	Evaluation metric	PR AUC
	Class weighting	balanced
	Split criterion	Gini
	Bootstrap sampling	enabled

All hyperparameters not listed in Table 3.7 were left at their scikit-learn default values.

3.12.2 Neural Network Models

The final shallow 1D CNN processes fixed-length pressure windows. The architecture consists of two convolutional blocks with ReLU activation and max pooling for hierarchical feature extraction, followed by a fully connected layer and a sigmoid-activated output layer for binary classification (Figure 3.4). Table 3.8 summarises the layer-wise configuration and output dimensions of the final model.

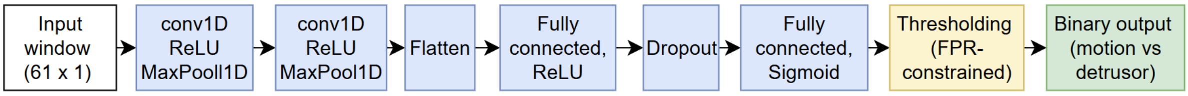

Figure 3.4: Schematic representation of the final shallow 1D CNN architecture used for pressure window classification.

Table 3.8: One-dimensional CNN architecture used for window-based pressure classification

Layer	Configuration	Output shape
Input	Pressure window	$(61, 1)$
Conv1D	64 filters, kernel size = 7, ReLU	$(61, 64)$
MaxPooling1D	Pool size = 2	$(30, 64)$
Conv1D	128 filters, kernel size = 5, ReLU	$(30, 128)$
MaxPooling1D	Pool size = 2	$(15, 128)$
Flatten	–	(1920)
Dense	64 units, ReLU	(64)
Dropout	$p = 0.5$	(64)
Dense (Output)	1 unit, Sigmoid	(1)

The multi-branch 1D CNN processes each pressure window through parallel convolutional branches with differing kernel sizes to capture temporal patterns at multiple resolutions. Channel-wise attention is incorporated using SE blocks applied independently to each branch prior to feature fusion (Figure 3.5). Within each SE block, global average pooling is first applied to summarise each channel into a single representative value. This summary is passed through a small two-layer network that temporarily reduces the number of channels to 4 before expanding back to the original channel dimension using a sigmoid activation. The resulting values act as channel-wise weights, which are applied to the feature maps to strengthen informative channels and reduce the influence of less relevant ones. Table 3.9 summarises the final layer configuration and output dimensions of the model.

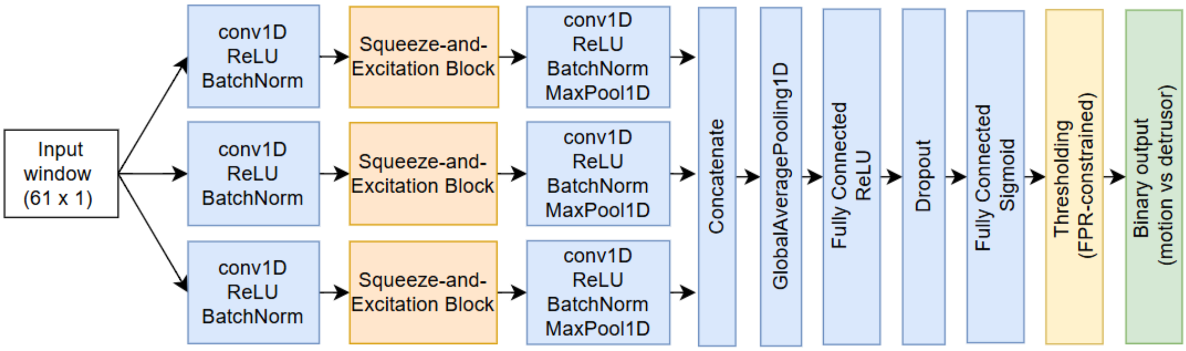

Figure 3.5: Schematic representation of the multi-branch 1D CNN with channel-wise attention, illustrating parallel convolutional branches, squeeze–excitation (SE) blocks, and feature fusion.

Table 3.9: Final architecture of the multi-branch 1D CNN with channel-wise attention.

Layer	Configuration	Output shape
Input	Pressure window	$(61, 1)$
Conv1D (Branch 1)	64 filters, kernel size = 3	$(61, 64)$
Conv1D (Branch 2)	64 filters, kernel size = 5	$(61, 64)$
Conv1D (Branch 3)	64 filters, kernel size = 7	$(61, 64)$
Batch Normalization	Applied per branch	$(61, 64)$
Global Average Pooling	Per branch	(64)
Dense	4 units, ReLU	(4)
Dense	64 units, Sigmoid	(64)
Reshape	Channel-wise weights	$(1, 64)$
Multiply	Attention-weighted features	$(61, 64)$
Conv1D	128 filters, kernel size = 3	$(61, 128)$
Batch Normalization	–	$(61, 128)$
MaxPooling1D	Pool size = 2	$(30, 128)$
Concatenate	Multi-branch fusion	$(30, 384)$
Global Average Pooling	Temporal aggregation	(384)
Dense	64 units, ReLU	(64)
Dropout	$p = 0.5$	(64)
Dense (Output)	1 unit, Sigmoid	(1)

3.12.3 Hybrid Models

The sequential hybrid CNN–LSTM model first applies the shallow 1D CNN architecture to extract local temporal features from pressure windows. These features are downsampled using max pooling and passed through three Bi-LSTM layers to model longer-range temporal dependencies. A temporal attention mechanism is applied to the Bi-LSTM output to assign higher weight to time steps that contribute more strongly to the final classification decision, producing a fixed-length context vector for downstream classification (Figure 3.6).

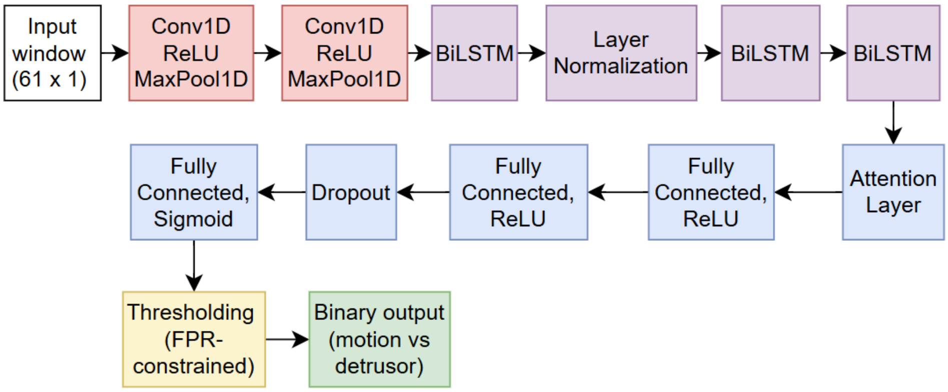

Figure 3.6: Schematic representation of the sequential hybrid CNN–LSTM architecture with temporal attention.

Table 3.10: Sequential Hybrid CNN-LSTM architecture for pressure window classification.

Layer	**Configuration**	**Output shape**
Input	Pressure window	$(61, 1)$
Conv1D	64 filters, kernel size = 3	$(61, 64)$
MaxPooling1D	Pool size = 2	$(30, 64)$
Conv1D	128 filters, kernel size = 3	$(30, 128)$
MaxPooling1D	Pool size = 2	$(15, 128)$
Bidirectional LSTM	32 units per direction, return sequences	$(15, 64)$
Layer Normalization	Applied across feature dimension	$(15, 64)$
Bidirectional LSTM	64 units per direction, return sequences	$(15, 128)$
Bidirectional LSTM	64 units per direction, return sequences	$(15, 128)$
Attention Layer	Trainable temporal attention	Context: (128) Attention weights: (15)
Dense	32 units, ReLU	(32)
Dense	64 units, ReLU	(64)
Dropout	$p = 0.5$	(64)
Dense (Output)	1 unit, Sigmoid	(1)

In the CNN-RF feature-level hybrid model, the CNN is used to learn a latent embedding from each pressure window. This embedding is concatenated with manually engineered features and provided as input to a Random Forest classifier, which produces the final class probability (Figure 3.7).

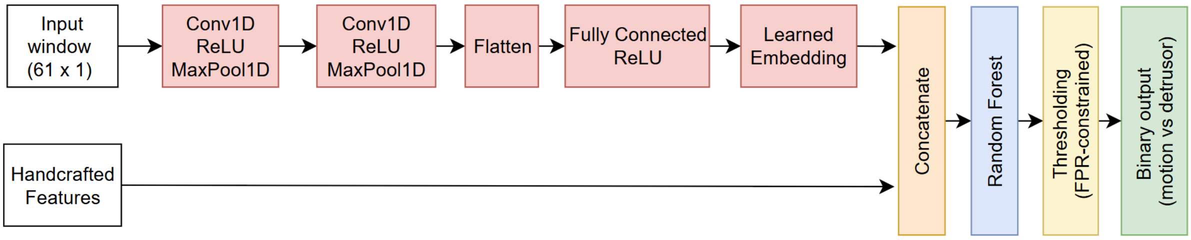

Figure 3.7: Schematic illustration of the feature-level CNN–RF hybrid model, where CNN-learned embeddings are concatenated with manually engineered features prior to Random Forest classification.

Table 3.11: CNN feature extractor used for learned embedding generation.

Layer	**Configuration**	**Output shape**
Input	Pressure window	$(T, 1)$
Conv1D	64 filters, kernel size = 7, ReLU, same padding	$(T, 64)$
MaxPooling1D	Pool size = 2	$(\lfloor T/2 \rfloor, 64)$
Conv1D	128 filters, kernel size = 5, ReLU, same padding	$(\lfloor T/2 \rfloor, 128)$
MaxPooling1D	Pool size = 2	$(\lfloor T/4 \rfloor, 128)$
Flatten	–	(N)
Dense (Embedding)	64 units, ReLU	(64)
Dense (Embedding)	1 unit, Sigmoid	(1)

Table 3.12: Random forest classifier trained on hybrid feature vectors.

Component	**Configuration**
Input features	Handcrafted features + CNN embeddings
Number of trees	200
Maximum depth	12
Minimum samples per leaf	3
Feature selection	$\sqrt{\text{features}}$ per split
Class weighting	Balanced (fold-specific)
Output	Binary class probability

4

Methods and Results - Part B: Design and Implementation of the UroMonitor System

4.1 Introduction

Part A of this thesis investigated machine learning approaches for MA detection in ambulatory cystometry using peak-centred pressure windows. While the results provided insight into model behaviour and architectural trade-offs, the findings were constrained by the limited size of the available patient dataset. Given that the acquisition of additional labelled clinical data was not possible, the results from Part A must be interpreted as indicative rather than definitive. These limitations motivated the exploration of an alternative approach for motion-context awareness in cystometry, specifically hardware improvements capable of enabling long-term, physiologically representative cystometry data acquisition. Given this, Part B addresses a complementary approach by focusing on the design and implementation of a novel ambulatory cystometry device with integrated inertial motion sensing.

The objective of Part B was therefore to design, implement, and validate a prototype ambulatory cystometry system, referred to as the **UroMonitor**, that addresses these needs through integrated hardware and software design. The system is intended to enable long-term, autonomous bladder pressure monitoring with embedded motion sensing and algorithmic MA suppression.

This chapter describes the system design requirements, component selection, circuit and PCB development, enclosure design, embedded firmware architecture, mobile application interface, and bench-top validation using a bladder phantom model. While evaluation in this work is limited to bench-top and phantom testing, the prototype establishes a technical foundation for future clinical investigation and translation.

4.2 Design Requirements

The development of the UroMonitor was guided by both clinical objectives and technical requirements. This section outlines the key objectives of the system and the constraints that informed design decisions.

4.2.1 Design Objectives

The primary objective of the UroMonitor was to develop a low-cost, ambulatory cystometry prototype capable of continuous vesical pressure monitoring under physiologically representative conditions, while compensating for motion artifacts through integrated sensor fusion. To meet this goal, the following functional requirements were identified:

- *Ambulatory:* The system must support ambulatory use.
- *Portability:* Compact and lightweight design to allow continuous ambulatory monitoring without interfering with daily life.
- *Cost-effectiveness:* Components and construction methods must minimize cost to facilitate use in low-resource settings.
- *Single-catheter operation:* Unlike conventional dual-catheter systems that measure vesical and abdominal pressure separately, this system must utilise a single catheter to limit invasiveness and improve comfort.
- *MA detection and removal:* Because abdominal pressure cannot be independently measured in a single-catheter configuration, the system must incorporate inertial sensing and algorithmic signal processing to estimate and suppress motion-related artifacts, thereby approximating detrusor pressure without direct P_{abd} measurement.
- *Real-time and offline data logging:* Pressure and motion signals must be synchronously recorded with sufficient temporal resolution for both real-time visualisation and offline analysis.
- *Autonomous and easy operation:* The system should operate without continuous clinician supervision. Automated data logging and analysis, motion tracking, and battery-powered functionality should be intuitive to use, reducing clinician dependency, minimizing interobserver variability, and facilitating broader deployment in resource-limited settings.
- *Modularity and scalability:* The hardware and software should be modular, allow future upgrades or extensions.

4.2.2 Design Constraints

In addition to functional objectives, practical constraints shaped the hardware and software architecture. Table 4.1 summarises the key design constraints, including size, weight, cost, power requirements, and physiological compatibility. These constraints ensure that the prototype is wearable, safe, and effective for extended ambulatory monitoring.

Table 4.1: Design constraints and specifications.

Criteria	Constraint
Physical Constraints	
Weight	Total device weight $\leq$ 300 g* to maintain wearability.
Size	All components housed within a compact enclosure ($\leq$ 120 $\times$ 90 $\times$ 60 mm)*.
Configuration	Single-catheter configuration to minimise invasiveness.
Economic Constraints	
Production cost	Total production cost $<$ €250 using commercially available components.
Component availability	Use of low-cost, widely available components compatible with open-source platforms (e.g., Arduino, ESP32).
Power Constraints	
Power source	Battery-powered operation only (no mains connection during use).
Operating time	Minimum continuous operating time $\geq$ 6 hours under active logging conditions.
Efficiency	Efficient power regulation to minimise energy consumption and thermal generation.
Physiological Constraints	
Pressure range	Operational sensing range of 0–150 cmH$_2$O.

Criteria	Constraint
Sensitivity	High resolution within the physiological range (15–70 cmH_2O) [144, 266].
Temporal resolution	Sampling frequency sufficient to capture transient detrusor events.
Electrical Constraints	
Power regulation	Regulated and protected power supply including overcurrent and short-circuit protection.
Isolation	Electrical isolation from external power sources during operation.
Signal acquisition	Stable analogue-to-digital conversion with sufficient resolution for clinical pressure measurement.
Usability Constraints	
Wearability	Form factor must not impede daily activities.
User interaction	Intuitive interface requiring minimal setup or calibration.
Safety and comfort	Use of patient-safe materials (e.g., medical-grade tubing) and mechanically secure enclosure design.
Autonomy	Operation without continuous clinician supervision.

Note: Weight and size estimates were informed by the Holter monitor ($\approx$ 99 g; 11 x 7 x 3 cm) [267], which served as a reference for practical wearable limits.

4.3 System Architecture

To meet the design objectives and constraints outlined in Section 4.2, the UroMonitor hardware architecture was organised into five primary hardware subsystems. Each system addresses dedicated aspects of ambulatory bladder pressure monitoring, including sensing and data acquisition, storage, power management, and user interaction.

The subsystems are outlined as follows:

- *Pressure and motion sensing subsystem:* Comprises the MPX5050DP pressure sensor and MPU6050 interial measurement unit (IMU). The MPX5050DP pressure sensor measures vesical pressure via a catheter, while the MPU6050 IMU captures both acceleration and angular velocity to enable identification and suppression of motion-induced artifacts through multi-sensor fusion.
- *Data acquisition, processing, and control subsystem:* An ESP32 microcontroller unit (MCU) coordinates synchronous sampling of the pressure and motion sensors, manages local storage on the microSD card, and formats data packets for wireless transmission via Bluetooth Low Energy (BLE).
- *Data logging and storage subsystem:* Pressure and motion data are stored locally on a microSD card for offline analysis, controlled via a latching push-button. In addition, the ESP32 MCU supports wireless data transmission via Bluetooth Low Energy (BLE) for real-time streaming to a mobile application, where visualisation and signal processing are performed.
- *Power management subsystem:* A 3.7 V, 2000 mAh lithium-polymer (LiPo) battery powers the system. A TP4056 charging module provides charging and battery protection, while an MT3608 boost converter regulates the voltage to meet 5 V power supply requirements of relevant components. A physical power switch allows manual control between charging and operation modes.
- *User interface subsystem:* An OLED display provides real-time feedback including system status, logging state, and operational instructions.

Figure 4.1 illustrates the overall system architecture.

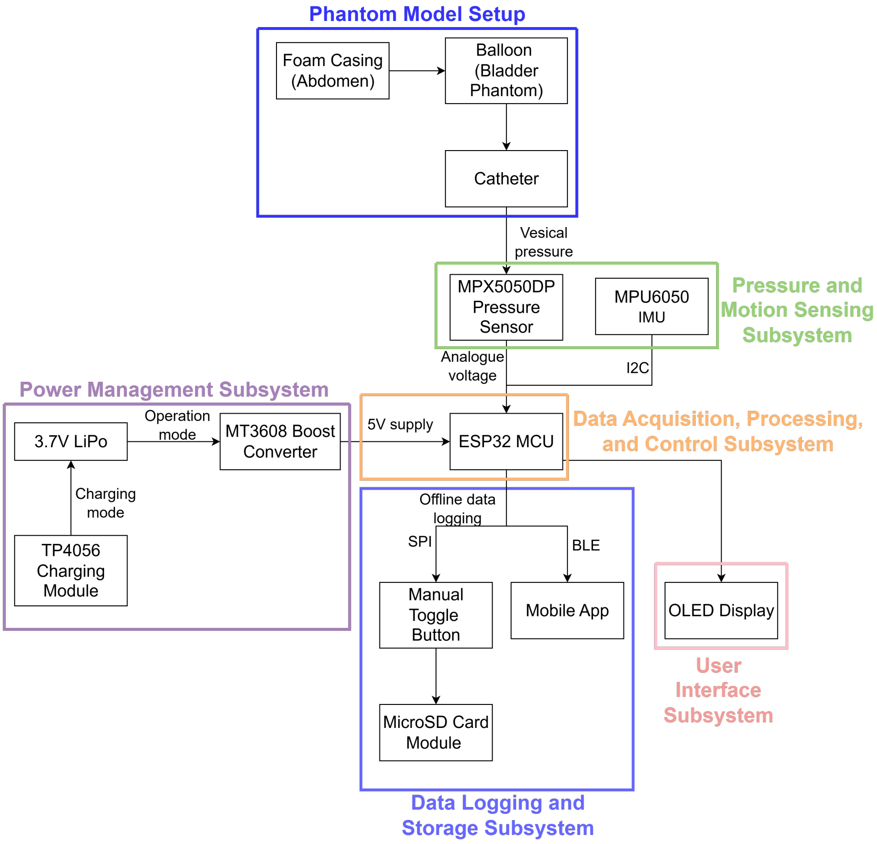

Figure 4.1: High-level system architecture of the UroMonitor. The system consists of five main subsystems: (1) pressure and motion sensing (MPX5050DP and MPU6050), (2) data acquisition and control (ESP32 MCU), (3) data logging and wireless communication (microSD and BLE), (4) power management (LiPo battery, TP4056 charger, MT3608 boost converter), and (5) user interface (OLED display). For validation, a bladder phantom is connected to the pressure sensor via a catheter interface. Abbreviations: MCU = Microcontroller Unit, IMU = Inertial Measurement Unit, ESP32 = DOIT ESP32 DevKit V1, MPX5050DP = Pressure sensor, MPU6050 = 6-axis motion sensor (accelerometer + gyroscope), LiPo = Lithium-Polymer battery, TP4056 = LiPo charger with protection, MT3608 = Boost (step-up) voltage converter, BLE = Bluetooth Low Energy. Designed using draw.io.

4.4 Component Selection and Justification

Following the system architecture defined in Section 4.3, individual components were selected for each subsystem based on performance requirements, electrical compatibility, cost constraints, and suitability for ambulatory use.

4.4.1 Pressure and Motion Sensing Subsystem

The MPX5050DP pressure sensor (NPX Semiconductors) was selected to capture intravesical pressures within the physiological range. It is a low-cost, monolithic differential pressure transducer selected for bladder pressure monitoring due to its measurement range, analogue output, and compatibility with microcontroller-based systems. It measures pressures between 0-50 kPa (0–510 cmH_2O), covering the physiological range of bladder pressures [8].

The sensor operates using a piezoresistive diaphragm, where the diaphragm undergoes mechanical strain under differential pressure, altering the resistance of integrated thin-film resistors bonded to its surface. These resistance changes are converted into an analogue voltage readable by the ESP32 [268]. A fluorosilicone gel layer isolates the die surface and wire bonds from the external environment while transmitting pressure to the diaphragm [268].

The sensor's high-pressure port is connected to a catheter leading to the bladder (or phantom bladder), while the low-pressure port is open to atmosphere to measure gauge pressure. This configuration allows real-time measurement of intravesical pressure relative to ambient conditions, suitable for ambulatory monitoring in a bench-top setting.

Given the 12-bit analogue-to-digital (ADC) channel of the ESP32 (4096 levels), the theoretical resolution of the sensor is approximately 0.124 cmH_2O per ADC count. In reality, resolution may be reduced due to analogue noise and ADC nonlinearity. However, resolution remains below the magnitude of clinically relevant pressure fluctuations. Additional key characteristics are summarised in Table 4.2.

Table 4.2: Key specifications of the MPX5050DP pressure sensor [269, 270, 268]

Parameter	**Value / Range**	**Notes**
Pressure range	0-50 kPa (0-510 cmH_2O)	Covers bladder physiological range
Supply voltage	5 V	Supplied by the MT3608 boost converter 5 V output
Sensitivity	90 mV/kPa or 8.83 mV/cmH_2O	Linear analogue output
Output voltage	0.2-4.7 V	Exceeds the ESP32 ADC input range (0-3.3 V) - requires a voltage divider to scale the signal safely
Interface	Analogue (ADC)	Outputs voltage proportional to pressure
Resolution	0.124 cmH_2O per ADC bit	Theoretical
Accuracy	± 2.5% full scale (FS) range (± 12.7 cmH_2O)	Over 0-85°C
Response time	1 ms	Suitable for real-time monitoring
Supply current	7 mA	Low-power operation
Size	Compact form factor	Assists in portability

Although the MPX5050DP pressure sensor provides suitable performance for this application, it is not a medical-grade transducer and lacks hermetic sealing or water resistance. Consequently, it is limited to proof-of-concept prototyping and bench-top validation rather than direct clinical use.

Motion sensing was implemented using the MPU6050 module, a six-degree-of-freedom (6-DoF) IMU that integrates a 3-axis accelerometer and 3-axis gyroscope on a single silicone die. It also incorporates an onboard Digital Motion Processor (DMP), which processes 6-axis MotionFusion algorithms that combine accelerometer and gyroscope data for improved motion estimation [271].

This component was selected for the following reasons:

- Digital I^2C digital interface reduces wiring complexity and supports multiple devices on the same bus.
- High sampling rate (up to 1 kHz) captures short-duration motion artifacts in real time.
- Compact form factor and low power consumption support portability and energy-efficient operation.
- Widely available, cost-effective, and supported by open-source libraries, facilitating rapid prototyping and system integration.

Key specifications are summarised in Table 4.3.

Table 4.3: Key specifications of the MPU6050 inertial measurement unit [271]

Parameter	Value / Range	Notes
Gyroscope range	±250, ±500, ±1000, ±2000°/s	Programmable
Accelerometer range	±2, ±4, ±8, ±16 g	Programmable
Sampling rate	Up to 1 kHz	1 ms intervals, sufficient for short duration motion artifacts
Supply voltage	2.3–3.4 V	Compatible with ESP32 logic levels
Supply current	3.9 mA	Low-power operation
Digital interface	I^2C	Reduces wiring complexity, allows multiple devices on the same bus
Size	15 x 20 x 1 mm	Small form factor, suitable for wearable applications

Motion data acquired from the MPU6050 is transmitted alongside pressure data for subsequent artifact identification within the mobile application or via offline analysis.

4.4.2 Data Acquisition, Processing and Control Subsystem

The DOIT ESP32 DevKit V1 (Espressif Systems) microcontroller serves as the central processing unit (CPU) of the UroMonitor. It coordinates acquisition of pressure and motion signals, manages data offline logging to a microSD card, and optionally streams wirelessly data to a mobile application via BLE.

Specifically, the ESP32 integrates analogue and digital signals using its 12-bit ADC channels for the MPX5050DP pressure sensor and digital I^2C communication for the MPU6050 IMU and OLED display. The SPI interface is used for high-speed communication with the microSD card module. The dual-core Xtensa LX6 processor processes data in real time, managing synchronous sensor sampling, timestamping, data packet formatting, and buffering within onboard memory prior to storage or wireless transmission. Logged data are written to the microSD card, and optionally transmitted via Bluetooth Low Energy (BLE) for real-time visualisation in the mobile application. Integrated Wi-Fi and BLE modules enable flexible communication without requiring additional hardware.

The ESP32 was chosen for the following reasons [272]:

- Dual-core 32-bit Xtensa LX6 processor running at 160-240 Mhz, providing sufficient computational power for real-time signal acquisition, logging, and communication.
- Integrated Wi-Fi, BLE, and Bluetooth 4.2 for optional wireless communication.
- Multiple 12-bit ADC channels compatible with analogue pressure readings, while digital interfaces (I^2C, SPI, UART) support all connected peripherals.
- Compact form factor and low power consumption, suitable for battery-operated ambulatory systems.
- Extensive open-source library support facilitates rapid prototyping and reproducibility.
- Low cost.

Table 4.4: Key specifications of the ESP32 DevKit V1 microcontroller [272].

Parameter	Value / Range	Notes
CPU	Dual-core 32-bit Xtensa LX6	160–240 MHz clock
Flash memory	4 MB	Stores firmware and temporary logging buffers
RAM	520 KB SRAM	Supports real-time processing and peripheral buffers
ADC	12-bit	Used for analogue pressure readings (0–3.3 V logic)
Digital interfaces	I^{2}C, SPI, UART	Communication with IMU, OLED, SD card, and peripherals
GPIO pins	30 usable	Supports multiple components
Wireless	Wi-Fi 802.11 b/g/n, Bluetooth 4.2, BLE	Optional data transmission
Supply voltage	3.3–3.6 V	Compatible with low-power battery operation
Typical current	80–260 mA (active)	Depends on peripherals and wireless use
Deep sleep mode	<10 µA	Extends battery life during idle periods
Package size	52 × 25.5 mm	Compact form factor

4.4.3 Data Logging and Storage Subsystem

Reliable data logging is needed to capture pressure and motion signals during ambulatory cystometry. To ensure robust operation in different use cases, the device supports two modes of operation:

1. *microSD-only logging:* sensor data is stored offline without relying on wireless communication.
2. *Hybrid logging:* data is simultaneously written to the microSD card and transmitted via BLE to the mobile application for real-time monitoring.

This flexibility allows uninterrupted data recording even when a mobile device is unavailable or BLE transmission is unreliable, while still offering real-time visualisation when needed or desired.

A dedicated SPI-based microSD card module was integrated to provide non-volatile storage of pressure and motion data [273]. The module communicates with the ESP32 over the SPI bus, enabling fast read-write operations. During operation, the ESP32 samples the MPX5050DP pressure sensor and the MPU6050 IMU, combines them into time-stamped data frames, and writes them to the microSD card in CSV format. If hybrid mode is selected, the same data is also streamed to the mobile application. The stored CSV files are compatible with common analysis platforms such as MATLAB, Python, or Excel, enabling simple post-processing and clinical interpretation.

Table 4.5: Key specifications of the SPI microSD card module [274].

Parameter	Value / Range	Notes
Interface	SPI	Compatible with ESP32 SPI bus
Logic level	3.3 V (with level shifter)	Ensures safe communication with ESP32
Storage type	microSD / microSDHC	FAT16/FAT32 file system support
Supported capacities	2–32 GB (microSDHC)	Suitable for hours of continuous logging
Supply voltage	4.5–5 V	Compatible with ESP32 DevKit supply
Dimensions	25 × 15 mm	Compact form factor

A manual latching push-button switch provides direct control over the logging process, independent of the mobile application. This allows the user to initiate or terminate recording even in disconnected or resource-constrained environments. Each press toggles a logging state in the ESP32 firmware, which either creates a new log file or safely closes the current one on the microSD card.

4.4.4 Power Management Subsystem

The ambulatory cystometry device is powered by a compact, rechargeable LiPo battery, with charging and voltage regulation circuitry to ensure safe, reliable operation. The power subsystem includes the TP4056 charging module, MT3608 boost converter, a single-cell LiPo battery, and a manual SPDT switch to control charging and operation modes.

A single-cell 3.7 V, 2000 mAh LiPo battery powers the system. It was selected for its rechargeability, high capacity, lightweight and compact form factor, and compatibility with wearable electronics [275].

Table 4.6: Key specifications of the single-cell 3.7 V 2000 mAh LiPo battery [276].

Parameter	Value / Range	Notes
Nominal voltage	3.7 V	Single-cell LiPo
Nominal capacity	2000 mAh	Supports extended operation
Charge voltage	4.2 V	Standard single-cell LiPo termination voltage
Standard charge current	0.5 C (1 A)	Applied using TP4056 charging module
Standard discharge current	0.5 C (1 A)	Sufficient for ESP32 and peripherals
Dimensions	50 × 34 × 10 mm	Compact form factor
Weight	32.30 g	Lightweight for ambulatory use
Chemistry	Li-ion polymer	Rechargeable, flexible packaging
Cycle life	300 cycles	Sufficient for UroMonitor usage profile
Protection	Built-in PCM	Prevents overcharge/ discharge and short circuit

To estimate device runtime, the total current draw of the device was estimated from the datasheets of the main components:

- ESP32 (active, Wi-Fi/BLE off): 150 mA
- MPX5050DP pressure sensor: 7 mA
- MPU6050 IMU: 3.9 mA
- microSD card (read/write active): 80 mA
- OLED display: 5 mA

The total estimated load current is therefore:

$$I_{load} = 150 + 7 + 3.9 + 80 + 5 \approx 246 \text{ mA} \tag{4.1}$$

The MT3608 boost converter has an efficiency of approximately $\eta = 90\%$ at the estimated load current. The effective current drawn from the battery is therefore:

$$I_{effective} = \frac{I_{load}}{\eta} = \frac{X}{0.9} = 273 \text{ mA} \tag{4.2}$$

The expected runtime is:

$$t_{hours} = \frac{C_{battery}}{I_{effective}} = \frac{2000}{273} \approx 7.3 \text{ hours} \tag{4.3}$$

Thus, the selected battery capacity meets the design target of $\geq$6 hours of operation.

The TP4056 charging module charges at a default current of 1 A (0.5 C). Assuming a charge efficiency of $\eta_{charge} \approx 90\%$, the charge time is:

$$t_{charge} = \frac{C_{battery}}{I_{charge}} \times \frac{1}{\eta_{charge}} = \frac{2000}{1000} \times \frac{1}{0.9} \approx 2.2 \text{ hours} \tag{4.4}$$

The TP4056 charging module is a lithium-ion battery charger module with integrated protection circuitry [277]. It regulates the charging process by applying a constant-current/ constant-voltage (CC/CV), ensuring the cell is safely charged up to its termination voltage of 4.2 V. The module includes built-in protection against overcharge, overdischarge, and short-circuit conditions, improving the reliability and safety of the power subsystem. The module also incorporates visual charge indicators: a red LED signals active charging, while a blue LED indicates full charge, providing intuitive user feedback.

The TP4056 charging module was selected due to its [277]:

- Compatibility with single-cell LiPo batteries.
- Adjustable charge current (via an external resistor) to match different battery capacities.
- Integrated protection circuitry using DW01A and 8205A MOSFETs.
- Trickle charge support for battery life extension.
- Compact size and low cost, ideal for wearable/ ambulatory systems.

Table 4.7: Key specifications of the TP4056 charging module [277].

Parameter	**Value / Range**	**Notes**
Input voltage	5.0 V DC	USB or external supply
Charge current	1 A (default)	Matches charge current of selected LiPo battery; programmable via external resistor
Trickle charge current	130 mA	For pre-conditioning deeply discharged cells
Battery compatibility	Single-cell Li-Ion / LiPo	1S configuration only
Charge termination voltage	4.1–4.2 V DC	Standard single-cell cut-off
Discharge protection voltage	2.5 V DC	Prevents deep discharge
Dimensions	29 × 17.1 × 3.5 mm	Compact form factor

The MT3608 is a step-up (boost) DC-DC converter that increases the nominal 3.7 V output of the LiPo battery to a regulated 5 V supply rail. This 5 V rail powers the ESP32 input (which internally regulates to 3.3 V logic levels) and the microSD card module, both of which require a 5 V supply [278]. Boost converters operate by first storing energy in an inductor and then transferring it to a capacitor, increasing the capacitor's voltage beyond the input voltage.

The MT3608 boost converter was selected for this system due to the following characteristics:

- Adjustable output voltage, easily configured to supply a stable 5 V for the ESP32.
- High efficiency (up to 97%), which minimises energy loss and extends battery life for portable applications.
- Compact and low cost module, compatible with system constraints.

Table 4.8: Key specifications of the MT3608 boost converter [278].

Parameter	Value / Range	Notes
Input voltage	2–24 V	Compatible with single-cell LiPo
Output voltage	Adjustable, up to 28 V	Set to 5 V for ESP32 operation
Efficiency	Up to 97%, around 90% for expected load	Depends on input voltage and load
Output current	2 A max	Sufficient for system components

A single-pole double-throw (SPDT) switch was incorporated to enable manual selection between charging mode and operation mode. This ensures both user safety and device reliability:

- *Charging mode:* The switch connects the battery directly to the TP4056 charging module while isolating the system load. This prevents simultaneous powering of the ESP32 and sensors during charging, ensuring safe battery recharging without electrical interference.
- *Operation mode:* The switch disconnects the TP4056 charging module and connects the battery output to the boost converter and downstream circuitry, thereby powering the ESP32, sensors, storage, and display.

This design ensures both safe charging and uninterrupted ambulatory operation.

4.4.5 User Interface Subsystem

The SSD1306 OLED display, operating over an I^{2}C interface, was selected to provide real-time feedback to the user. Its low power consumption, compact dimensions, and wide availability make it well-suited for integration in a portable, battery-powered, ambulatory device. The display communicates system messages such as:

- Instructions to initiate or stop manual logging via the latching push-button.
- Status of data acquisition (e.g., logging active or inactive).
- Connection status with the mobile application over BLE.

Table 4.9: Key specifications of the SSD1306 OLED display [279, 280, 281].

Parameter	Value / Range	Notes
Resolution	128 × 64 pixels	Suitable for text and simple graphics
Interface	I^{2}C	Compatible with ESP32 I^{2}C bus
Supply voltage	3.3 V or 5 V	Compatible with battery-powered ESP32 systems
Current consumption	1–7 mA	Varies with active pixels and refresh rate
Dimensions	27 × 25 mm	Small form factor suitable for portable devices
Operating temperature	-20°C to 60°C	Suitable for ambient use

The resolution of the OLED display is sufficient for textual UI only.

4.4.6 Catheter and Tubing

Silicone tubing, compatible with Luer lock connectors, was selected for pressure transmission between the bladder (or phantom model) and the MPX5050DP pressure sensor. For the current prototype, standard silicone tubing was used; however, for clinical deployment, certified medical-grade tubing would be required to meet sterility and safety standards. During selection of medical-grade tubing in future, the length and internal diameter of the tubing must be considered as these influence dynamic pressure transmission and may introduce damping effects.

4.5 System Integration and Circuit Design

With the ESP32 MCU serving as the central control unit of the UroMonitor, all sensing, data logging and storage, user interface, and power management subsystems were integrated around it to ensure reliable signal acquisition, safe power distribution, and compatibility of communication protocols. This section describes the routing, pin assignments, power distribution and protection mechanisms that enable safe and reliable operation in an ambulatory context. The complete circuit schematics were developed in EasyEDA and can be found in Appendix B.1.1.

The design prioritised:

- Logic-level compatibility between components,
- Stable analogue signal acquisition,
- Safe battery-powered operation,
- Modularity for future expansion.

4.5.1 Signal and Communication Interfaces

Analogue Pressure Signal Path

The MPX5050DP pressure sensor outputs an analogue voltage in the range 0.2–4.7 V corresponding to 0–50 kPa (0–510 cmH_2O). Since the ESP32 ADC input range is limited to 0–3.3 V, a resistive voltage divider was implemented to scale the signal. The divider output is given by:

$$V_{out} = V_{in} \frac{R_2}{R_1 + R_2} \tag{4.5}$$

Using $R_1 = 10\ k\Omega$ and $R_2 = 15\ k\Omega$:

$$V_{out} = V_{in} \times \frac{15}{10 + 15} = 0.6 V_{in} \tag{4.6}$$

This scales the sensor output to 0.12–2.82 V, which lies within the ESP32 ADC input limits. The scaled output is connected to GPIO34, an input-only ADC channel. The theoretical resolution of the 12-bit ADC (4096 levels) over the full 510 cmH_2O sensor range is 0.124cmH_2O per bit.

Digital Communication Interfaces

For communication and data exchange between components and devices, the Inter-Integrated Circuit (I^2C) and Serial Peripheral Interface (SPI) digital communication interfaces were used.

The MPU6050 IMU and SSD1306 OLED display share a common I^2C bus (GPIO21 - SDA, GPIO22 - SCL), where each device has a unique address, preventing bus conflicts. Both peripherals operate at 3.3 V logic levels and are powered from the ESP32's regulated 3.3 V output.

The microSD card module communicates via SPI, connected to the following GPIO pins:

- GPIO23 — MOSI
- GPIO19 — MISO
- GPIO18 — SCK
- GPIO5 — CS

The SPI interface provides sufficient throughput for synchronous logging of pressure and motion data to the microSD card. Data is written in time-stamped CSV format, enabling offline analysis. The microSD module is powered from the regulated 5 V rail.

GPIO Inputs

The latching push-button switch is connected to GPIO13, configured as a digital input [282]. The ESP32's internal pull-up resistor is enabled, pulling the pin to 3.3 V (logic HIGH) in the default state. When the button is pressed, the pin is connected to ground (GND), forcing the input LOW. This configuration ensures a defined logic state during idle and enables manual toggling of data logging independent of wireless connectivity.

Table 4.10 summarises the communication and power interfaces between the system components.

Table 4.10: Summary of electrical and communication interfaces between system components.

Component	Interface Type	Description
MPX5050DP Pressure Sensor	Analogue (ADC)	Voltage signal scaled and digitised by ESP32 12-bit ADC
MPU6050 IMU	I^2C	Digital motion data (accelerometer and gyroscope)
SSD1306 OLED Display	I^2C	Status and user feedback display
microSD Card Module	SPI	Time-stamped data logging in CSV format
Latching Push-Button	GPIO (Digital Input)	Manual logging control

4.5.2 Power Distribution and Voltage Regulation

The device is powered by a single-cell 3.7 V, 2000 mAh LiPo battery. During operation mode, battery output is directed through the MT3608 boost converter, which generates a regulated 5 V supply rail. This 5 V rail powers the ESP32 V_{IN} input, the MPX5050DP pressure sensor, and the microSD card module. The ESP32's onboard voltage regulator subsequently provides 3.3 V logic levels for the IMU and OLED display.

The TP4056 charging module charges the LiPo battery in charge mode. An SPDT switch isolates the load circuitry from the battery while charging, preventing simultaneous charge and discharge paths. This configuration reduces electrical stress on the battery and minimises potential interference with system electronics during charging. A common ground reference is maintained across analogue and digital domains to ensure stable ADC measurements and to minimise noise coupling between analogue and digital subsystems.

4.5.3 Protection and Safety Mechanisms

The integration of a battery-powered biomedical monitoring system necessitates careful protection circuitry to ensure safety, prolong component lifespan, and maintain stable operation. Accordingly, protective measures were incorporated at both the power supply and signal integrity levels.

The LiPo battery includes an integrated protection circuit module (PCM), preventing overcharge, overdischarge, overcurrent, and short circuit events [283]. This ensures the battery operates within its safe electrochemical limits, reducing the risk of degradation.

The SPDT switch allows manual selection between:

- Charging mode: Battery connected to TP4056 charger and load disconnected.
- Operation mode: Battery connected to MT3608 boost converter and TP4056 charger disconnected.

This prevents simultaneous charging and discharging, which can accelerate ageing, introduce voltage fluctuations, compromise battery health, and reduce device safety.

Positive temperature coefficient (PTC) resettable fuses are over-current protection passive components that increase in resistance when excessive current causes heating, thereby interrupting the conductive path. Once cooled, the device resets and restores normal operation. Two PTC resettable fuses were incorporated to protect the system against unsafe charging and abnormal load currents, improving user and device safety:

- *Charging protection fuse:* A 1.35 A hold current, 2.7 A trip current, and 40 A maximum current PTC fuse [284] was placed between the TP4056 charging module and LiPo battery. Given the battery's nominal charge current of 1 A (0.5 C), this fuse disconnects the circuit if an abnormally high charging current is delivered, thereby protecting the battery against unsafe charging conditions.
- *Load protection fuse:* A second fuse, with a hold current of 150 mA, trip current of 350 mA, and maximum current of 40 A [285], was added between the battery and MT3608 boost converter to safeguard against overcurrent during normal device operation. This ensures disconnection during excessive current draw while allowing normal operation.

Lastly, to ensure stable operation and reduce transient noise, both bulk (10 μF 16 V aluminium electrolytic [286]) and bypass capacitors (10 nF 50 V ceramic [287]) were placed near the supply pins of components.

4.5.4 Expansion Header for Future Development

To accommodate future modifications (e.g., integration of additional sensors), a header was included, providing access to GPIO27, GPIO33, GPIO35, and 3.3 V, 5 V, and GND pins. This facilitates future hardware extensibility.

4.5.5 ESP32 Pin Assignment Summary

The final GPIO assignments are summarised in Table 4.11. Pin selection was based on ESP32 MCU pinout assignment [288].

Table 4.11: ESP32 GPIO pin assignments and connected components.

ESP32 Pin	Function	Connected Component	Notes
GPIO34	Analogue Input (ADC)	MPX5050DP Pressure Sensor	Voltage divider used
GPIO21	I^2C SDA	MPU6050 IMU and OLED Display	Shared bus
GPIO22	I^2C SCL	MPU6050 IMU and OLED Display	Shared bus
GPIO5	SPI CS	microSD Card Module	
GPIO18	SPI CLK	microSD Card Module	
GPIO19	SPI MISO	microSD Card Module	
GPIO23	SPI MOSI	microSD Card Module	
GPIO13	Digital Input	Manual logging latching push-button	Internal pull-up
GPIO27, GPIO33, GPIO35	Expansion GPIO	Reserved header	Future development
VIN	Power Input	MT3608 Output (5 V)	Step-up regulated input
3V3	Regulated Output	MPU6050 IMU, OLED display, microSD card module	From ESP32 onboard regulator
GND	Ground	All modules	Common ground reference

4.6 Breadboard Prototype Implementation and Validation

A breadboard prototype was developed to (1) validate system functionality, signal integrity, and communication interfaces, and (2) debug hardware connections and firmware prior to PCB fabrication.

4.6.1 Breadboard Setup

During prototyping, the ESP32 was powered through its USB interface, which supplied 5 V to the development board. The board's onboard voltage regulator provided a stable 3.3 V logic rail for low-voltage peripherals. Specifically, the 5 V rail (derived from the ESP32 board input) powered the MPX5050DP pressure sensor and microSD card module and the 3.3 V rail powered the MPU6050 IMU and the SSD1306 OLED display. All ground rails were tied to a common reference for stable analogue-to-digital conversion. The MPX5050DP analogue output was directed through the voltage divider (10 kΩ / 15 kΩ) before connection to GPIO34. The I^2C bus (GPIO21/22) was shared between the IMU and OLED, while the SPI bus (GPIO5, 18, 19, 23) connected the microSD card module to the ESP32. Figure 4.2 shows the assembled breadboard prototype.

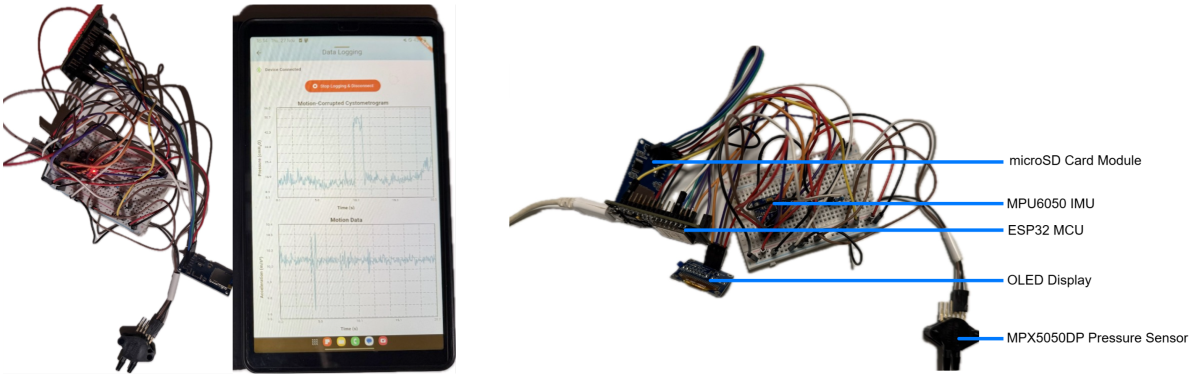

(a) Breadboard prototype demonstrating live BLE data transmission to the UroMonitor mobile application.

(b) Overview of breadboard wiring, including ESP32 MCU, MPX5050DP pressure sensor, MPU6050 IMU, OLED display, and microSD card module.

Figure 4.2: Breadboard prototype and system setup.

4.6.2 Electrical Verification

Electrical verification was performed prior to functional testing to ensure safe operation. A digital multimeter was used to confirm 5 V rail stability under active operation and 3.3 V regulator output stability. The MPX5050DP output scaling was verified by measuring both the raw sensor output voltage and the post-divider voltage at GPIO34 to confirm that the scaling ratio matched the expected ratio of 0.6.

Continuity testing was performed using a multimeter to verify:

- Ground continuity across all modules
- Continuity of jumper wires
- Correct SPI line routing (MOSI, MISO, SCK, CS)
- Correct I^2C connections (SDA/SCL)
- No short circuits

4.6.3 Functional Validation

To isolate potential hardware or firmware issues, each subsystem was validated independently using dedicated firmware scripts executed via the Arduino IDE serial monitor.

For pressure sensor validation, a stand-alone script continuously sampled GPIO34 and printed raw

ADC values to the serial monitor to verify correct response to manually applied pressure. The ADC readings increased proportionally with applied pressure and returned to baseline without instability. Similarly, an I^2C test script was used for MPU6050 IMU validation, streaming accelerometer and gyroscope data to the serial monitor. The readings varied appropriately with device motion, confirming successful bus communication. An additional I^2C script verified OLED functionality by displaying predefined messages on the screen.

For microSD logging validation, a dedicated script was developed to (1) create test CSV files and (2) write timestamped dummy sensor values. File creation and integrity were then manually inspected, where continuous logging demonstrated successful file generation without write failures.

Finally, a BLE test script verified that formatted pressure and motion packets were correctly transmitted and received by the UroMonitor mobile application. The tests confirmed reliable real-time data streaming without noticeable delay or data loss. Within the app, live plots updated continuously, demonstrating synchronised data acquisition and transmission as well as an adequate sampling rate. Figure 4.2a illustrates real-time BLE data streaming during prototype testing.

4.6.4 Integrated System Validation

After individual subsystem validation, a full integration test was performed to test simultaneous pressure sensing, motion detection, microSD logging, BLE streaming, and OLED status updates. Continuous logging sessions were conducted to further verify stable I^2C communication, no SPI bus issues, no firmware crashes, and consistent file creation on the SD card. These tests confirmed that the combined hardware and firmware architecture functioned as intended during operation.

4.7 Firmware Architecture

Firmware was developed in C++ for the ESP32-based UroMonitor system using the Arduino IDE framework. Core libraries used included the ESP32 BLE library, Wire (for I^2C communication) Adafruit MPU650 and SSD1306 display libraries, and SPI and SD libraries. The complete firmware implementation is available at: UroMonitor Device GitHub Repository.

The firmware performs five primary functions:

- *Synchronous sensor acquisition* from MPX5050DP pressure sensor and MPU6050 IMU at a fixed sampling rate.
- *Timestamping and data packaging* into structured CSV format.
- *Dual-output handling:* continuous microSD logging and optional BLE streaming.
- *User interaction management* via push-button control.
- *Real-time system feedback* via OLED display.

Importantly, no signal filtering or artifact removal is performed on-device. The firmware streams raw sensor values for downstream processing within the mobile application or offline.

4.7.1 Sampling and Timing Logic

A sampling rate of 20 Hz is used for pressure and motion data acquisition. This frequency was selected to (1) efficiently capture bladder pressure dynamics and motion artifacts occurring at low frequencies, (2) reduce SD write frequency and BLE bandwidth, and (3) lower computational overhead and power consumption.

4.7.2 Pressure Signal Acquisition and Calibration

The MPX5050DP pressure sensor output is connected to GPIO34 and read via the ESP32's 12-bit ADC (0–4095 counts).

Calibration Procedure

Manual calibration was performed using:

- A 100 mL syringe,
- An analogue pressure gauge (0–1 bar; 0–1019.72 cmH_2O),
- Incremental plunger displacement.

The syringe was first connected to the analogue pressure gauge. The plunger was displaced in 2 mL increments and the corresponding reference pressure recorded. The syringe was then connected to the MPX5050DP pressure sensor, and the procedure repeated while recording the ESP32 ADC values.

Linear regression was performed to map ADC counts to pressure, yielding:

$$\text{Pressure (cmH}_2\text{O)} = 0.1346 \times \text{ADC}, \quad R^2 = 0.995 \tag{4.7}$$

This high coefficient of determination confirmed linearity within the tested range. The regression equation was implemented directly into the firmware to convert raw ADC values into calibrated pressure readings.

4.7.3 Motion Signal Acquisition

The MPU6050 IMU is sampled via I^2C (GPIO21/22) communication. Acceleration values in the X, Y, and Z axes are acquired at each sampling interval. Acceleration magnitude (acceleration vector length) is computed from the axial acceleration values and transmitted alongside pressure data for subsequent motion artifact detection within the mobile application. No onboard filtering or Digital Motion Processor (DMP) functionality is used.

4.7.4 Data Packaging and Transmission

At each sampling interval, sensor readings are assembled into a CSV-formatted row containing `timestamp`, `adcValue`, `pressure (cmH2O)`, `a_x`, `a_y`, `a_z`, `accMag`, `gyro_x`, `gyro_y`, `gyro_z`.

Data are written line-by-line to the microSD card and transmitted via BLE notifications when connected. Logging to microSD continues regardless of BLE connection state, ensuring uninterrupted offline recording. Line-by-line SD writes were chosen to minimise RAM usage and reduce the risk of data loss in the case of unexpected power interruption.

4.7.5 User Interaction and OLED Feedback

The OLED display provides:

- Boot state indication
- SD card initialisation status
- BLE connection state
- Active file name
- Logging state indicator
- User instructions for BLE connection and manual logging

The latching push-button toggles manual logging to the microSD card. Simple software debouncing ensures stable state transitions and prevents false triggering due to mechanical switch bounce.

4.7.6 System Stability and Error Handling

Ensuring reliable operation during prolonged ambulatory monitoring is critical. The firmware incorporates several mechanisms to enhance stability across sensor sampling, BLE communication, and data storage.

SD Card Handling

- *SD initialisation:* Initialisation is checked during boot. If unsuccessful, an error message is shown on the OLED and the system continues in BLE-only mode.
- *Write protection:* Each write operation is opened, written, and closed immediately. This prevents data corruption if power is lost mid-session.
- *File name collision prevention:* Previous file names are checked and the new file name receives the next consecutive file number to ensure each session is logged separately to prevent overwriting previous sessions.

BLE Handling

- *Connection Callbacks:* BLE connection and disconnection events are handled using callback functions from the ESP32 BLE library. This prevents the firmware from entering blocking waiting states while monitoring the connection status. This enables uninterrupted sensor acquisition and SD-card logging, ensuring continuous data collection even when no mobile device is connected.
- *Non-blocking Notifications:* BLE data transmission is implemented using non-blocking notifications. The firmware periodically sends data without waiting for acknowledgment from the mobile device. This prevents delays or queue build-up from interfering with the acquisition loop, ensuring stability and real-time logging even if the receiving device experiences temporary latency.

Power-Loss Resilience

Power-loss resilience is implemented by closing files after each write, where sudden power interruption results in at most one incomplete sample rather than total file corruption.

4.8 UroMonitor Mobile Application Design and Workflow

The UroMonitor mobile application was developed as the user-facing interface for the UroMonitor system. Its function is to acquire real-time pressure and motion data transmitted wirelessly from the ESP32-based hardware, perform signal processing to remove motion artifacts from the bladder pressure signal, and present clinicians with interpretable visualisations and automated preliminary diagnostic information. The application was developed using the Flutter framework and the Dart programming language, allowing cross-platform deployment and efficient UI rendering. The full UroMonitor mobile application code can be found here.

Bluetooth Low Energy (BLE) communication was implemented using the `flutter_reactive_ble` package, enabling continuous low-latency streaming of sensor data. Time-series visualization was implemented using the `fl_chart` library.

The application follows a structured workflow:

1. Home Screen
2. Monitoring Screen
3. Results Screen
4. Diagnosis Screen

Each stage is described in the subsequent sections, and screenshots of each screen can be found in Appendix B.2.

4.8.1 Home Screen

The Home Screen serves as the application entry point upon launch and is responsible for session initialisation and patient metadata capture. Upon pushing the ”Start Monitoring” button, the user is prompted to enter the following patient details via the provided input fields:

- Patient name
- Age
- Sex
- Optional clinical notes or medical history

This information is stored in memory and passed to subsequent screens, ensuring data availability throughout the session. No local database is used; instead, session data remains active only during runtime until export. The input fields have to be populated before proceeding. This ensures that monitoring begins only after explicit user input and system readiness, reducing unintended recordings and improving clinical traceability. Upon confirmation, the application initialises a BLE instance and transitions to the Monitoring Screen.

4.8.2 Monitoring Screen

The Monitoring Screen is responsible for UroMonitor device discovery, BLE communication management, real-time data acquisition, structured signal storage, and live visualisation.

Upon entering the Monitoring Screen, the application prompts the user to connect to the UroMonitor system via the ”Scan & Connect” button, where a BLE scan is then initialised using the `flutter_reactive_ble` library. Discovered devices are filtered based on identifiable characteristics (device name and service UUID) corresponding to the custom ESP32 firmware. Once the target device is selected, a connection is established and a subscription is created to the device’s characteristic stream. The connection lifecycle is actively managed, with explicit handling for:

- Successful connection,
- Disconnection events,
- Stream cancellation,
- Manual logging termination.

This ensures robust behaviour during ambulatory monitoring, where intermittent connectivity may occur.

The ESP32 transmits pressure and motion data as formatted ASCII strings using the structure `P:xx.xx; A:yy.yy;`, where `P` represents intravesical pressure (cmH_2O), and `A` represents motion acceleration magnitude derived from the MPU6050 IMU accelerometer data (m/s^2). Incoming byte streams are decoded to UTF-8 strings and parsed by splitting on semicolon delimiters. Each packet is validated before extraction of numeric values.

Parsed values are stored internally using dynamic lists, where each entry follows the format `'time': DateTime, 'value': double`. Time stamps are generated on the mobile device at the moment of packet receipt using the system clock. This ensures consistent temporal indexing for downstream signal processing and visualisation. Separate lists are maintained for raw pressure data and raw motion (acceleration magnitude data).

Live pressure and motion data are displayed using a single-axis time-series line chart implemented with the `fl_chart` library. This allows visual assessment of signal quality, patient movement,and bladder dynamics. The full dataset remains stored in memory throughout the monitoring session, ensuring complete signal availability for subsequent processing in the Results Screen.

Upon termination of monitoring, a rule-based post-processing algorithm is applied to the recorded pressure and acceleration datasets to suppress motion-induced artifacts in the cystometrogram. The algorithm operates on synchronised pressure and motion samples acquired at a fixed sampling frequency.

First, baseline values for both signals are estimated from the initial 30 seconds of recording, corresponding to a stationary reference period. The pressure baseline is computed as the modal pressure value within this interval to provide a robust estimate of resting vesical pressure. Similarly, the motion baseline is determined from the initial segment of the acceleration magnitude signal to approximate the gravitational reference. Pressure peaks are then identified as samples exceeding a predefined threshold above the pressure baseline (15 cmH_2O). Motion peaks are identified as samples for which the absolute deviation of acceleration magnitude from the motion baseline exceeds a predefined motion threshold (0.3 m/s^2).

Temporal coincidence between pressure and motion peaks is determined using an index-based window corresponding to a fixed time interval ($\pm$2 seconds). A pressure peak is classified as motion-induced if it occurs within this coincidence window of any detected motion peak. Only pressure samples meeting both criteria (i.e. exceeding the pressure threshold and occurring within the defined temporal window to a motion peak) are subject to suppression. For each identified coincident pressure sample, a local baseline estimate is computed from surrounding non-coincident pressure values within a defined context window. The replacement value is taken as the median of these neighbouring samples to ensure robustness against outliers. If insufficient surrounding clean samples are available, the global pressure baseline is used as a fallback.

This algorithm produces a motion artifact–suppressed pressure signal in which only coincident motion-related pressure peaks are suppressed, preserving physiologically relevant detrusor contractions that occur independently of motion events. The cleaned pressure dataset, together with the original pressure and motion signals, is subsequently transferred to the Results Screen for visualisation, overlap verification, and further interpretation.

4.8.3 Results Screen

The user pushes the ”Results” button to navigate to the Results Screen. The Results Screen receives the raw pressure, motion, and cleaned pressure time-series generated during post-processing in the Monitoring Screen.

The motion artifact-suppressed pressure signal is displayed as a single-axis time-series cystometrogram. This plot reflects the output of the suppression algorithm executed during the monitoring stage and represents the primary signal used for subsequent downstream preliminary diagnosis.

To support interpretability, a second, dual-axis chart displays the original pressure and motion signals concurrently. Pressure is mapped to the primary y-axis and motion magnitude to the secondary y-axis, allowing temporal comparison between physiological pressure changes and patient movement. Motion peaks and pressure peaks are re-identified using threshold-based detection, and regions of temporal coincidence are visually highlighted. This highlighting visually depicts the coincidence condition used during motion artifact suppression. It enables clinicians to verify that removed pressure peaks correspond to motion events and that isolated pressure rises are preserved as potential detrusor activity.

Figure 4.3 shows the two plots: the cleaned pressure signal and the overlapping plot of the pressure and motion signals. In the overlapping plot, eight regions are highlighted, indicating pressure and motion temporal coincidence. The pressure peaks within these eight regions are replaced with baseline values as seen in the cleaned pressure signal, demonstrating the motion artifact suppression algorithm implemented within the app. After review of the two plots, the cleaned pressure dataset is forwarded to the Diagnosis Screen for preliminary clinical interpretation.

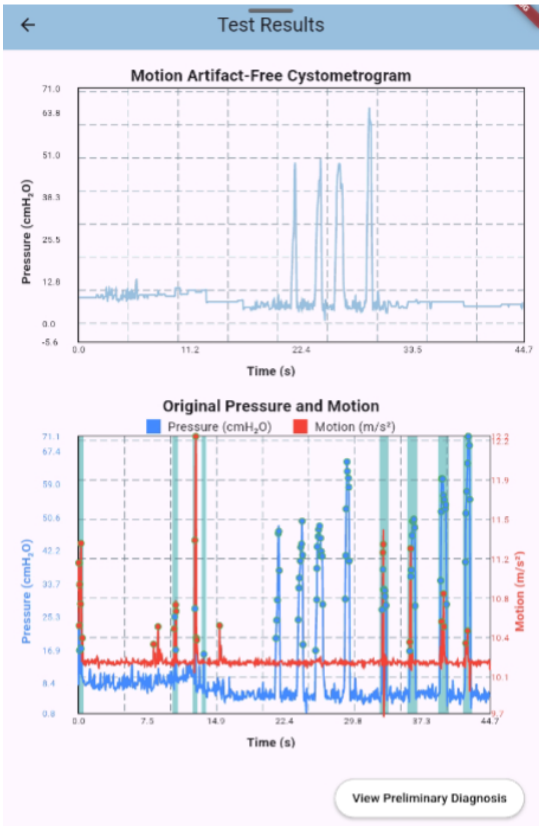

Figure 4.3: Results Screen showing the cleaned pressure graph (top) and the overlapping plot of the pressure and motion signals (bottom). The pale blue shaded regions in the overlapping plot represent regions where pressure peaks and motion events coincide.

4.8.4 Diagnosis Screen

The Diagnosis Screen (Figure B.6) provides a preliminary diagnosis, derived from the cleaned pressure signal and peak detection results. It receives the cleaned pressure signal, original pressure and motion datasets, patient metadata, and chart images generated in the Results Screen.

A rule-based diagnostic algorithm is applied to the cleaned pressure signal to determine summary metrics and detect clinically relevant pressure peaks. First, descriptive statistics are computed, including maximum, minimum, and average pressure values. Peak detection is then performed using a threshold-based approach applied to the cleaned signal. A pressure sample is classified as a peak when its magnitude exceeds a predefined threshold. A minimum temporal separation between consecutive peaks is enforced to ensure that only peaks separated by more than the predefined time interval are counted as independent events.

Based on the detected peak count and global pressure characteristics, a simple rule-based decision tree generates a preliminary diagnosis. For example, repeated pressure peaks beyond a specified count indicate potential DO, whereas persistently low average pressure may suggest DUA. Extremely high peak pressures trigger a warning recommending clinical follow-up. If none of these conditions are diagnosed, pressure is considered within a nominal range, indicating healthy bladder function.

The generated diagnostic interpretation is displayed alongside general treatment and monitoring recommendations. An on-screen warning emphasises that the output is preliminary and does not replace professional medical evaluation.

To support clinical documentation and further offline analysis, the Diagnosis Screen includes an integrated export function. When the ”Save Report” button is pressed, two report formats are generated:

- A CSV file containing time-stamped original pressure, motion magnitude, and cleaned pressure signals for quantitative, offline analysis.
- A PDF report including patient details, captured visualisations of the cleaned cystometrogram and pressure–motion comparison plot, the generated preliminary diagnosis, and recommendations.

4.9 Printed Circuit Board (PCB) Design

Following validation of the breadboard prototype, a custom printed circuit board (PCB) was developed in EasyEDA [289] to integrate all electronic subsystems into a compact and robust platform suitable for ambulatory use. The design adhered to JLCPCB manufacturing guidelines [290], with key objectives including compactness, low-noise analogue measurement, stable battery-powered operation, mechanical robustness, modularity, and cost-efficient fabrication using a standard 2-layer FR-4 stack-up. These objectives informed all subsequent component placement, schematic, and layout decisions.

4.9.1 Layout and Integration

Component placement was driven by electrical performance, mechanical accessibility, and enclosure integration. Power components (TP4056 charging module and MT3608 boost converter) were grouped to form a dedicated power region, minimising high-current trace lengths. The ESP32 was mounted on headers, allowing passive components and the TP4056 charging module to be placed beneath it, reducing board footprint.

Sensor components (MPX5050DP pressure sensor and MPU6050 IMU) were grouped to simplify routing and reduce electromagnetic interference. User-facing connections (OLED display, push-button, switch, and USB interfaces) were aligned along a common PCB board edge to match enclosure cutouts and improve accessibility. Off-board components (OLED display, MPX5050DP pressure sensor, microSD card module, and LiPo battery) were connected via headers, enabling modularity, simplified debugging, and future upgrades without PCB redesign. Mechanical mounting points, including non-plated through-holes for enclosure fixation and IMU stabilisation, ensured structural rigidity and accurate motion sensing. The final layout is provided in Appendix B.3, with a 3D render shown in Figure 4.4.

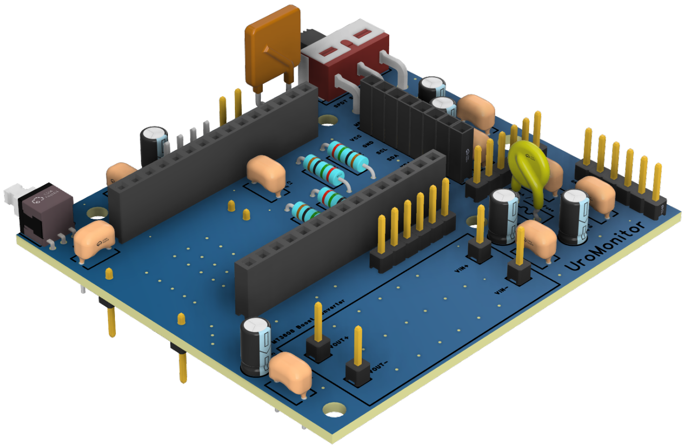

Figure 4.4: 3D render of the assembled PCB within EasyEDA, showing component stacking and spatial arrangement.

3D assembly validation was performed using imported STL component models to verify spatial compatibility, component clearance, and enclosure integration (Figure 4.5).

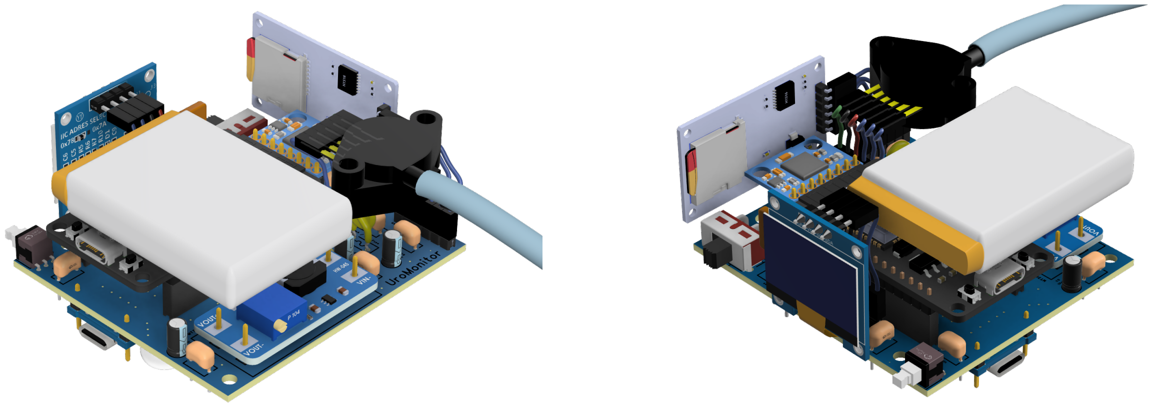

(a) Perspective view of assembled PCB, specifically showing the MPX5050DP pressure sensor, catheter, MT3608 boost converter, and LiPo battery.

(b) Perspective view of assembled PCB, specifically showing the OLED display, SPDT switch, latching push-button, microSD card module, and USB ports.

Figure 4.5: 3D assembly validation using imported STL component models [291, 289].

4.9.2 Electrical Design and Signal Integrity

PCB layout prioritised signal integrity and stable power delivery. High-frequency and analogue traces were kept short and separated from high-current paths to minimise noise coupling. Continuous ground planes were implemented on both layers to provide a low-impedance return path and stable reference for analogue measurements.

Decoupling capacitors (10 µF electrolytic and 10 nF ceramic) were placed close to component power pins to suppress noise and stabilise supply voltages. Heat-generating components were positioned near ventilation regions to support passive thermal management.

Trace widths were selected based on current requirements and verified using an online calculator [292]. Wider traces reduce resistive and thermal losses according to $R = \rho L/A$, improving power stability. The final trace widths were:

- 0.254 mm — low-current signal lines
- 0.35 mm — 3.3 V rail
- 0.6 mm — 5 V rail
- 1.2 mm — LiPo battery to TP4056 charging module, limiting thermal rise to approximately 1°C under expected load conditions

High-current paths between the LiPo battery, TP4056 module, and MT3608 converter were routed using widened traces to reduce resistive voltage drop and thermal rise.

4.9.3 Fabrication, Manufacturing, and Validation

Silkscreen layers were used to label component positions, pin assignments, and polarity, improving assembly accuracy and maintainability. Initial routing was generated using EasyEDA's autorouter and refined manually to optimise trace paths, minimise ground return loops, and ensure clearance compliance. Trace angles were restricted to 45°, with a minimum spacing of 0.2 mm.

The design was iteratively validated using EasyEDA's DRC and JLCPCB's Design for Manufacturing (JLCDFM) tools [289, 293], ensuring compliance with fabrication constraints, including trace spacing, via dimensions, solder mask clearance, and silkscreen legibility. No design violations or unconnected nets were identified prior to fabrication.

Following layout finalisation, the PCB design (62 × 70 mm) was exported as Gerber files from EasyEDA and fabricated by JLCPCB [294] using a standard 2-layer FR-4 stack-up (1.6 mm thickness, 1 oz copper) with HASL surface finish.

The fabricated PCB met standard manufacturing specifications, including 2-layer FR-4 construction, tented vias, and minimum via dimensions of 0.3 mm. No fabrication defects were observed, with correct silkscreen alignment, solder mask integrity, and via placement (Figure 4.6).

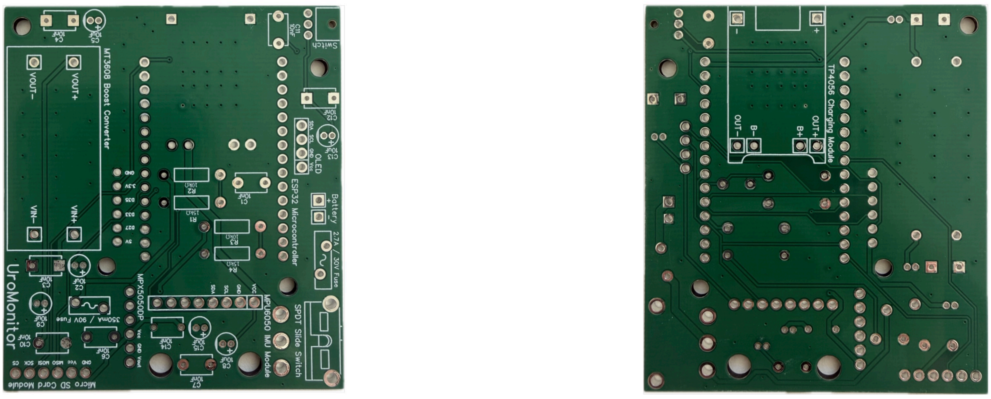

(a) Top View

(b) Bottom View

Figure 4.6: Fabricated UroMonitor PCB: top (left) and bottom (right) views of the manufactured board prior to component population.

Two PCB revisions were produced. Initial testing of Version 1 revealed functional issues, including unreliable SPI communication with the microSD module due to routing errors, and system boot instability caused by connecting the push-button to GPIO15 (a bootstrap pin on the ESP32).

These issues were resolved in Version 2 by correcting SPI trace routing and relocating the push-button to GPIO13. The revised design demonstrated stable boot behaviour and reliable SD card communication, with all components functioning as intended.

4.9.4 Post-Assembly Electrical Verification

Following PCB assembly, electrical and functional validation was performed prior to enclosure integration and phantom testing. The verification protocol included continuity inspection, voltage rail validation, battery charging assessment, subsystem testing, and integrated system evaluation.

All power and ground nets were verified using a digital multimeter in continuity mode to confirm correct routing and absence of short circuits. Particular attention was given to the LiPo battery terminals, 5 V boost converter output, 3.3 V logic rail, and ground plane continuity across layers. Inspection revealed no unintended shorts or open circuits across power and ground nets, confirming correct routing and solder integrity.

With the LiPo battery connected, voltage levels were measured using a calibrated digital multimeter to verify correct operation of the power management system. The TP4056 charging module was evaluated under controlled conditions, with charging current and termination voltage monitored. The fully charged battery reached 4.12 V after approximately two hours of charging. The boost converter output remained stable at 5.00 V, while the ESP32 logic rail was regulated to 3.3 V. Measured values were consistent with expected specifications and remained stable under load. Charging current through the TP4056 module was approximately 1 A, with termination occurring at 4.12 V, indicating proper charge regulation. During active system operation, the battery exhibited stable discharge behaviour with no observable voltage drop under simultaneous sensing, logging, and wireless communication.

Each subsystem was individually validated using the Arduino test scripts, following the same protocol defined in Section 4.6.3. Following individual subsystem verification, the complete system was operated under simulated monitoring conditions to assess concurrent subsystem performance and system stability. During this testing, a supply dip was observed under full operational load. Investigation identified the cause as incorrect specification of the resettable PTC fuse (hold current: 150 mA; trip current: 350 mA; maximum current: 40 A [285]). Measured steady-state system current exceeded the hold current rating during peak operational activity, resulting in tripping.

To proceed with validation testing, the PTC fuse was bypassed. The second fuse remained in place, providing overcurrent protection during evaluation. Following bypass, the system demonstrated stable operation under simultaneous pressure acquisition, motion sensing, BLE streaming, OLED output, and SD logging. No observable supply dips, communication dropouts, unexpected resets, or excessive thermal behaviour were detected during subsequent test sessions.

Overall, electrical validation of Version 2 confirmed correct subsystem integration and system-level stability, enabling progression to enclosure integration and phantom evaluation.

4.10 3D-Printed Enclosure

A custom 3D-printed enclosure was developed to house the printed circuit board assembly (PCBA), providing mechanical protection, user accessibility, and ambulatory portability, transforming the electronic prototype into a wearable device. The design was constrained by ergonomic, mechanical, electrical, and fabrication requirements associated with wearable operation.

Key requirements included:

- Maximum external dimensions of 120 x 90 x 60 mm (see Section 4.2.2), ensuring comfort, torso-mounted wearability, and discretion.
- Wearability by incorporating Velcro strap slits to enable secure attachment to the body.
- Mechanical durability suitable for daily use.
- Compatibility with the available FDM printer (Creality K1).
- Passive thermal management via ventilation near heat-generating components (TP4056 charging module, MT3608 boost converter, and ESP32 microcontroller).
- Accessible cutouts for:
  - TP4056 charger USB-C charging port,
  - TP4056 charger LED (for charging status).
  - ESP32 USB programming port,
  - MPX5050DP pressure ports,
  - MicroSD card slot,
  - Latching push-button and power switch,
  - OLED display,
- Mounting holes for PCB and off-board component fixation using M2-M4 screws as appropriate.
- Rigid mechanical coupling of the MPU6050 IMU to the enclosure to ensure accurate motion sensing and prevent relative vibration between the IMU and housing.

These constraints informed both internal layout and external geometry.

4.10.1 Design and Layout

The enclosure geometry was derived from the PCB footprint (62 × 70 mm) and component height constraints. A wall thickness of 2.8 mm was selected to balance strength, printability, and compactness, resulting in final dimensions of 70 × 80.2 × 46 mm, within the specified dimensional constraint ($\leq$ 120 × 90 × 60 mm) (Section 4.2.2).

The enclosure consists of two interlocking parts: a bottom base for PCB mounting and a removable top housing containing the battery compartment and off-board components. User-facing components (OLED display, microSD slot, push-button, and power switch) were positioned on the superior surface to enable intuitive interaction, while the MPX5050DP pressure sensor was mounted on the inferior surface to allow downward catheter routing, reducing bending stress and improving concealment. Figure 4.7 shows the enclosure design.

The LiPo battery was integrated into the upper housing using sliding rails (Appendix B.4.2, Figure B.12). Remaining components were mounted directly or via headers on the PCB, (see Figure 4.4) with their placement defining enclosure cutout placement. The two enclosure parts were secured using self-tapping flat-head screws, selected for flush mounting, load distribution, support minimisation, and elimination of printed threads.

3D validation confirmed correct alignment of external interfaces, adequate wiring clearance, absence of mechanical interference, and appropriate catheter routing.

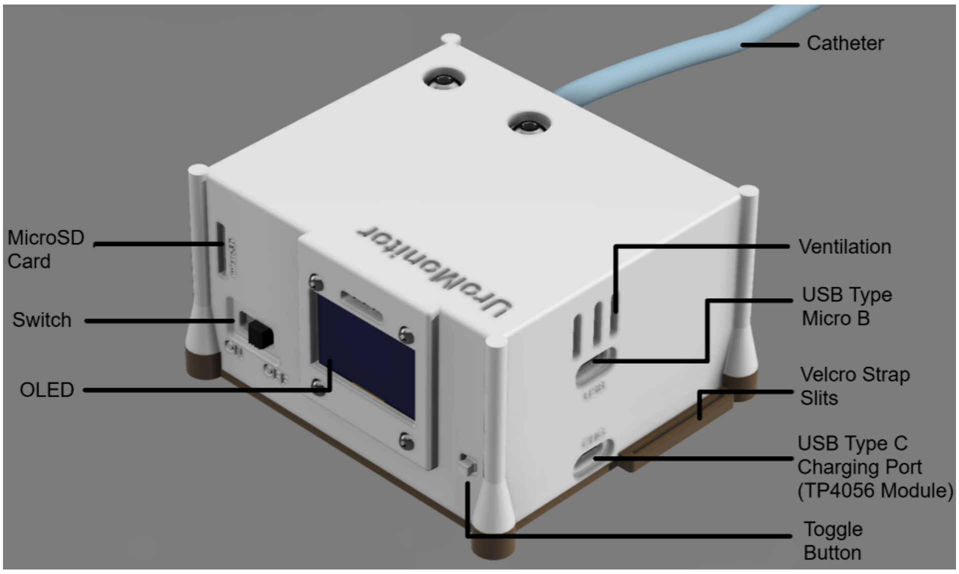

Figure 4.7: Labelled enclosure rendering identifying key external interfaces including OLED display, charging port, microSD slot, ventilation, and strap slots.

Refer to Appendix B.4.1 for fully dimensioned CAD drawings of the enclosure, including front, back, top, bottom, left, and right orthographic views. Rendered assembly views of the enclosure with the integrated PCB and modules can be found in Appendix B.4.2.

4.10.2 Fabrication

The enclosure geometry was optimised to minimise support material through the use of chamfers, fillets, and tapered surfaces. Print orientation was selected to ensure dimensional accuracy, clean cutouts, and reduced warping. Tree supports were applied where necessary.

The enclosure was printed using polylactic acid (PLA), chosen for its ease of use, low cost, dimensional accuracy, smooth surface finish, and stiffness [295]. Printing was done by a Creality K1 FMD printer with a build volume of 220 x 220 x 250 mm and high printing speed (600 mm/s), enabling rapid prototyping [296]. Both components were printed with a 0.4 mm nozzle using a 40% infill and 0.08 mm layer height. The bottom component took 3 h 10 min to print and weighted 49.11 g, while the top component took 1 h 06 min and weighted 24.90 g. No reprints were required, indicating accurate tolerance estimation during the design phase.

4.10.3 Assembly and Performance

Printed components exhibited consistent layer deposition with no observable warping or dimensional distortion. All cutouts aligned with hardware components (Figures 4.8–4.9), ensuring accessibility of the OLED display, controls, ports, and catheter interface.

The PCB was secured to the bottom base using M4 screws, while the LiPo battery and MPX5050DP pressure sensor were housed in the upper enclosure, as shown in Figures 4.8-4.9. Assembly of all components was achieved, although internal wiring density required careful routing to avoid strain and ensure proper enclosure closure.

A minor mechanical issue with push-button cutout alignment was observed due to slight vertical displacement from the PCB during use. This was resolved by mechanically securing the push-button to the PCB using adhesive reinforcement and manually increasing the cutout clearance to ensure reliable external access.

Following assembly, the enclosure demonstrated sufficient structural rigidity for handheld and torso-mounted use, stable PCB fixation, effective passive ventilation, and full accessibility of user interfaces (microSD card, switch, and push-button). The enclosure successfully protected all electronic subsystems while maintaining functionality for charging, logging, wireless operation, and data access.

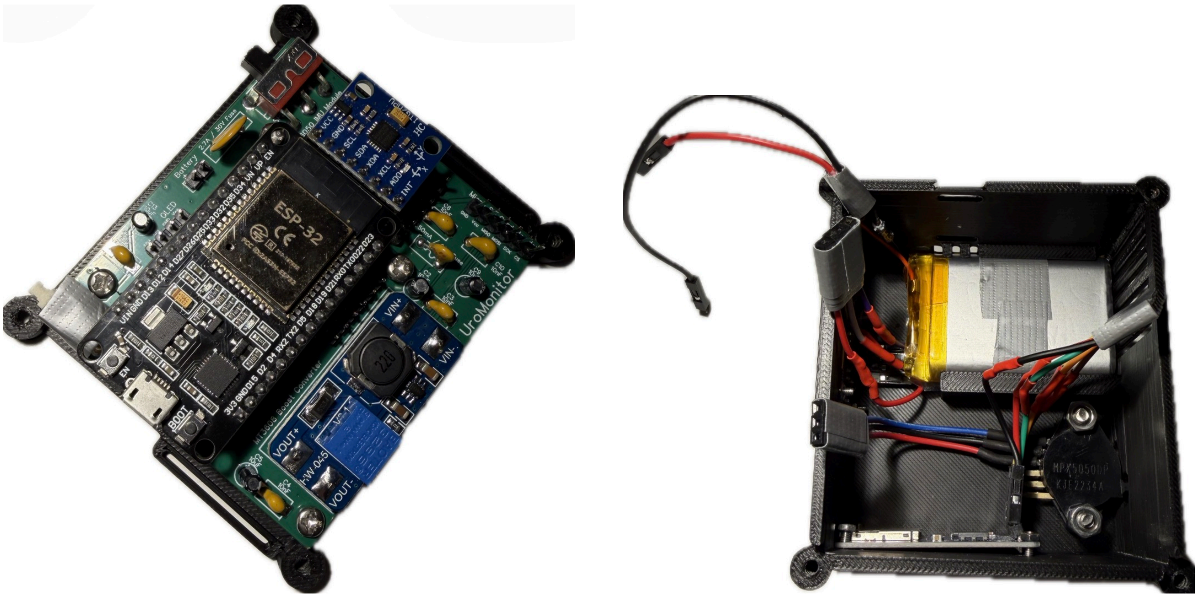

(a) PCB mounted onto the bottom base of the enclosure prior to final assembly.

(b) LiPo battery and MPX5050DP pressure sensor positioned within the upper enclosure component.

Figure 4.8: 3D-printed UroMonitor enclosure and internal assembly configuration.

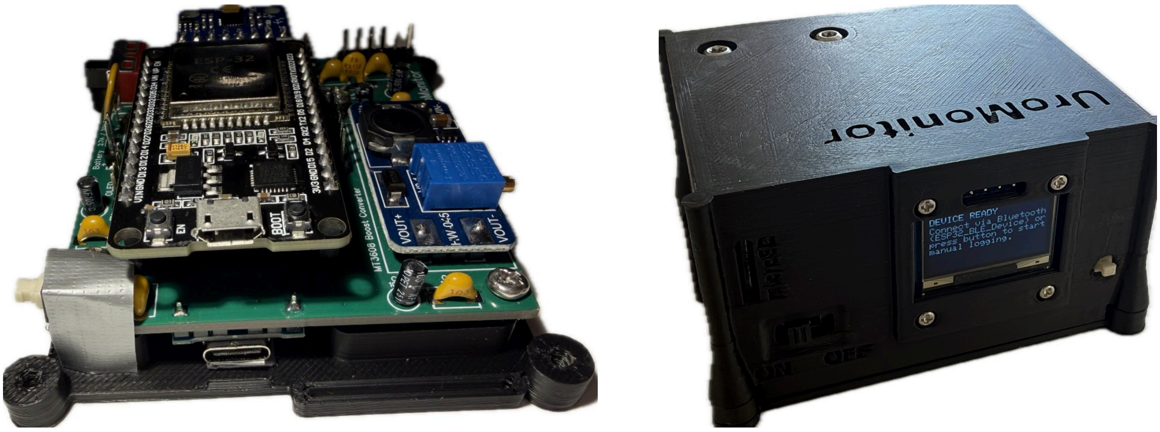

(a) Side view of the PCB mounted onto the bottom base of the enclosure.

(b) Fully assembled enclosure showing OLED display, power switch, push-button, and microSD access.

(c) Assembled enclosure with catheter connection and lateral ventilation slots visible.

Figure 4.9: 3D-printed UroMonitor enclosure and internal assembly configuration.

4.11 Phantom Design for System Testing and Characterisation

Controlled bench testing was performed to validate that the UroMonitor could simultaneously record bladder pressure and motion signals under known and repeatable conditions. Specifically, a phantom model was developed to simulate:

- A compliant bladder.
- Transmission of pressure via catheter to the MPX5050DP pressure sensor.
- External abdominal compression during cough and Valsalva manoeuvres.
- Motion artifacts caused by posture changes.
- Whole-body tilting to replicate supine-to-sitting transitions.

The phantom was not intended to replicate human anatomy, but rather to provide a means to perform repeatable mechanical tests that generate controlled pressure perturbations and motion artifacts representative of ambulatory cystometry situations.

4.11.1 Mechanical Structure and Materials

To satisfy these requirements, the phantom incorporated a compliant internal bladder surrounded by compressible material representing internal organs. A rigid spine element and hinged base allowed repeatable positional transitions.

Compliant Bladder

A balloon was used to represent the bladder. The balloon was connected to the MPX5050DP pressure sensor via a short catheter line to minimise damping and delay effects.

Cavity Fill

A compressible foam block (torso) was used to simulate internal organs. The foam allowed redistribution under compression, producing pressure shifts during motion events.

External Pressure Mechanisms

A small inflatable diaphragm bag was connected to a manual pump. Rapid inflation (0.5–1 s) simulated cough pulses. Sustained inflation (2–10 s) simulated Valsalva manoeuvres and sustained abdominal loading. The inflatable diaphragm bag was positioned such that it compresses the internal bladder, transmitting pressure variations.

A pressure band was also implemented and positioned around the bladder to apply controlled external compression to the bladder during postural changes and rotation, mimicking external compression forces that would be applied to the bladder by abdominal muscles in normal conditions.

Spine and Tilt Platform

A rigid wooden spine structure was coupled to a base via a hinge joint, allowing controlled tilt between supine and seated configurations. This enabled repeatable posture transitions.

Figure 4.10 shows a schematic representation of the phantom model architecture.

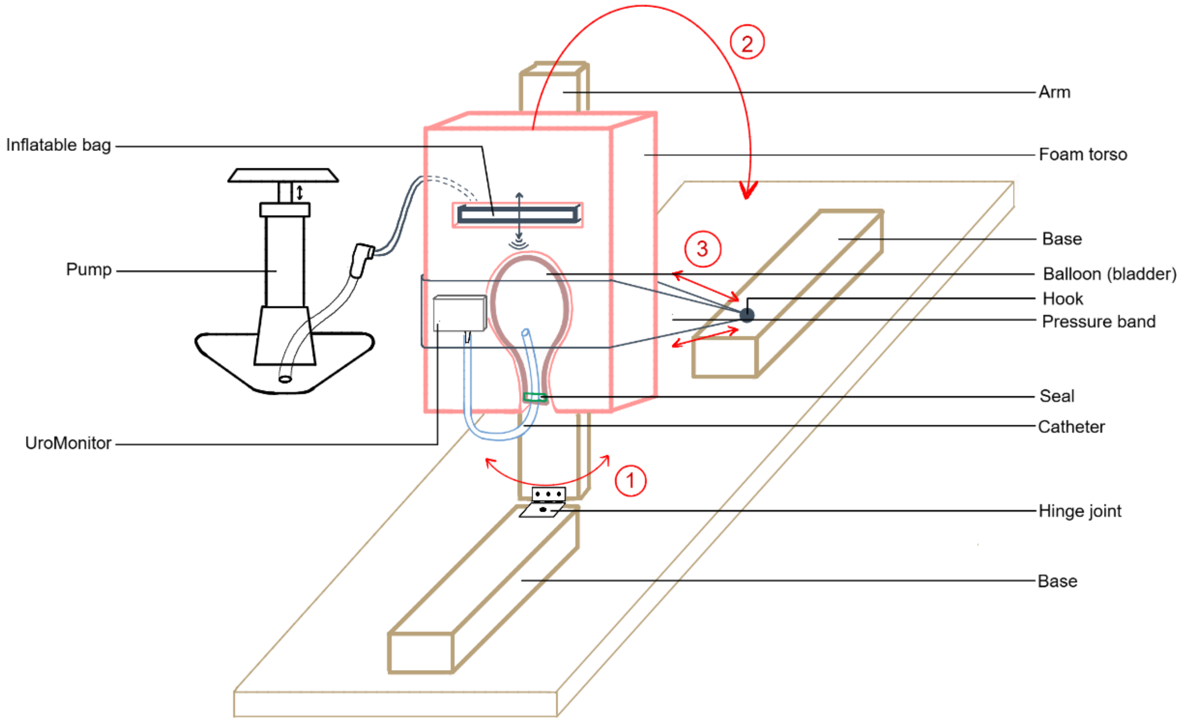

Figure 4.10: Schematic of the custom bladder phantom model developed for ambulatory cystometry device testing. The setup comprises a foam torso housing an inflatable compliant bladder (balloon) connected to a catheter and UroMonitor, and a external pressure mechanism that utilises a second inflatable diaphragm bag to transmit pressure to the inflatable bladder. A manual pump regulates is used to inflate the bag. The torso is mounted on a hinged base to reproduce posture changes, and enables torso rotation. A pressure band applies controlled external compression to the bladder region during postural changes and rotation. This configuration allows reproducible simulation of filling, movement, and external abdominal pressure conditions during ambulatory urodynamic evaluation.

4.12 Device Performance Results - Experimental Validation

System performance was evaluated using the phantom model and experimental protocols outlined below. Due to delays in the first PCB revision, experiments were conducted using the validated breadboard prototype, positioned within the enclosure housing to approximate final deployment conditions (Figure 4.11). A total of six controlled phantom tests were performed, with data analysed using a custom Google Colab pipeline.

Figure 4.11: Experimental phantom validation setup with breadboard prototype positioned within the enclosure housing and connected to the pressure model while streaming data via BLE.

Phantom testing aimed to verify simultaneous pressure and motion acquisition, assess whether induced motion events produced measurable inertial responses, and determine whether these events generated coincident pressure perturbations relevant for artifact suppression.

4.12.1 Experimental Protocol

All tests were recorded at 20 Hz, capturing pressure (cmH_2O), tri-axial acceleration, and acceleration magnitude. Data were logged to microSD and streamed via BLE. Motion events were manually annotated using a stopwatch, with timestamps added to the recorded data.

Six test conditions were evaluated: seated rotation, supine rotation, cough pulses, Valsalva manoeuvres, postural transitions, and random perturbations. Each test was repeated 20 times, with a 30 s stationary baseline recorded prior to each trial. The individual test protocols were defined as follows:

1. *Seated Rotation:* The phantom was positioned in the seated position (upright). The phantom was then rotated $\pm 45^\circ$ from the centre with 5 s holds in each position (left rotation, centre, and right rotation). The expected outcome was clear acceleration peaks (yaw) and possible coincident pressure peaks.
2. *Supine Rotation:* The phantom was positioned in the supine position. The phantom was then rolled left and right from supine with 5 s holds in each position (left, centre, and right). The expected outcome was clear acceleration peaks and possible coincident pressure peaks.

3. *Cough Pulses:* Rapid 0.5–1 s diaphragm inflation bursts were delivered using the manual pump, simulating a cough. The expected outcome was sharp pressure spikes with coincident acceleration changes.
4. *Valsalva Manoeuvre:* For simulating Valsalva manoeuvres, slow inflation of the inflatable diaphragm bag (2-4 s) was done using the pump, intended to simulate sustained intra-abdominal pressure. After inflation, the pressure was held for 10 s and then released. The expected outcome was sustained pressure elevation and low-frequency motion.
5. *Postural Changes:* The phantom was positioned in the supine position. Supine-to-sitting transitions (and vice versa) were done via hinge tilt. Each postion was held for 5 s before the next transition. The expected outcome was large acceleration changes and pressure baseline shifts.
6. *Random Perturbations:* To replicate random perturbations, the enclosure was tapped repeatedly with moderate force. A total of 21 taps were done. The expected outcome was sharp inertial peaks without pressure change (isolated motion events).

4.12.2 Motion Detection Analysis

Motion detection performance was evaluated by comparing detected inertial peaks with manually annotated motion events. To account for annotation delay and motion duration, each annotated timestamp was expanded into a ± 3 s window representing the ground-truth motion interval.

Peaks were extracted from inertial signals using an adaptive `find_peaks` approach, where detection thresholds were scaled according to signal variability. This approach enabled robust peak extraction across signals with differing amplitudes and noise characteristics. A motion event was considered successfully detected if at least one peak occurred within its corresponding window. Performance was quantified using recall, defined as the proportion of annotated events correctly identified.

Results

Motion events were captured by the IMU, with clear peak responses observed in accelerometer, gyroscope, and derived acceleration magnitude signals. Figure 4.12 shows the acceleration magnitude (AccMag) signal for Test 6, where 21 induced perturbations correspond to distinct detected peaks. Minor temporal offsets between manual annotations and peaks were attributed to manual timing and finite motion duration.

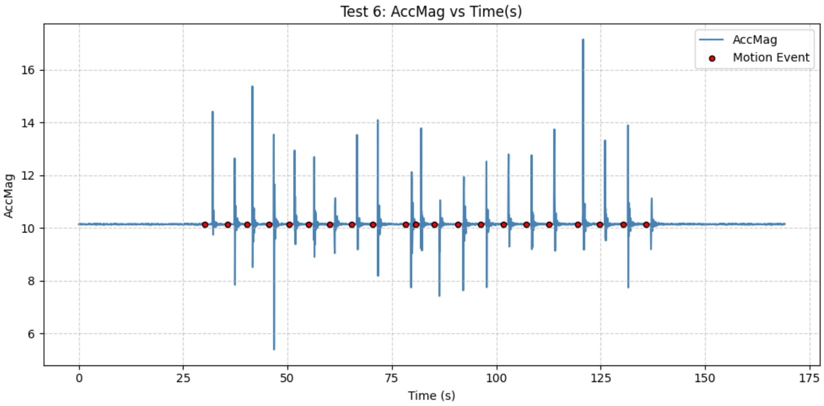

Figure 4.12: Acceleration magnitude (AccMag) signal for Phantom Test 6. Twenty-one distinct peaks correspond to manually induced perturbations.

Recall performance was aggregated across all tests for each signal to assess signal reliability (Table 4.12). Acceleration magnitude (AccMag) achieved the highest overall performance, with a mean recall of 0.954, low variability (standard deviation 0.033), and a minimum recall of 0.905. AccelZ showed comparable performance but with greater variability, while gyroscope signals exhibited greater variability and lower worst-case performance, particularly GyroZ.

Table 4.12: Ranking of inertial motion signals based on recall consistency across phantom tests. Signals are ordered from best to worst overall performance.

Rank	Signal	Mean Recall	Median Recall	Std. Recall	Min. Recall	No. Tests
1	AccMag	0.954	0.953	0.033	0.905	6
2	AccelZ	0.947	0.955	0.043	0.889	6
3	GyroX	0.915	0.921	0.075	0.803	6
4	GyroY	0.870	0.958	0.164	0.600	6
5	AccelY	0.863	0.927	0.173	0.526	6
6	AccelX	0.844	0.910	0.180	0.533	6
7	GyroZ	0.806	0.965	0.391	0.012	6

Given its superior performance and consistency, acceleration magnitude was selected as the primary motion reference signal. Per-test results (Table 4.13) show recall values between 90.5% and 100%, with a mean exceeding 95%. Even in the lowest-performing test (Test 6), 19 of 21 events were successfully detected.

Table 4.13: Per-test motion event detection performance for the acceleration magnitude (AccMag) signal across phantom experiments.

Test	Signal	Motion Events	Detected Motion Events	Recall (%)
1	AccMag	81	77	95.1
2	AccMag	76	76	100.0
3	AccMag	22	21	95.5
4	AccMag	45	42	93.3
5	AccMag	45	44	97.8
6	AccMag	21	19	90.5

These results demonstrate that the UroMonitor system reliably detects motion events using inertial sensing, with acceleration magnitude (AccMag) providing the most stable and repeatable signal for downstream motion artifact identification and suppression.

4.12.3 Pressure Signal Analysis

Pressure signal analysis followed the same framework used for motion signal analysis. Controlled pressure events were induced during phantom testing and manually annotated, with a ±3 s tolerance window applied to account for manual delays and event duration. Pressure peaks were extracted using the `find_peaks` function, and detection performance was quantified using recall, defined as the proportion of annotated events containing at least one detected peak. Across all six phantom experiments, expected transient pressure responses were not observed in the recorded signal. As shown in Figure 4.13, pressure remained within a narrow range of approximately 40–42 cmH$_2$O, with no distinct peaks corresponding to induced mechanical events.

To determine whether this behaviour was due to sensor malfunctions or phantom model limitations, prior calibration results were revisited (Section 4.7.2). Syringe-based calibration demonstrated a strong linear relationship between applied pressure and ADC output:

$$P_{\text{cmH}_2\text{O}} = 0.1461 \times \text{ADC} - 28.127 \tag{4.8}$$

with $R^2 = 0.9911$, confirming accurate and stable sensor performance across the operating range.

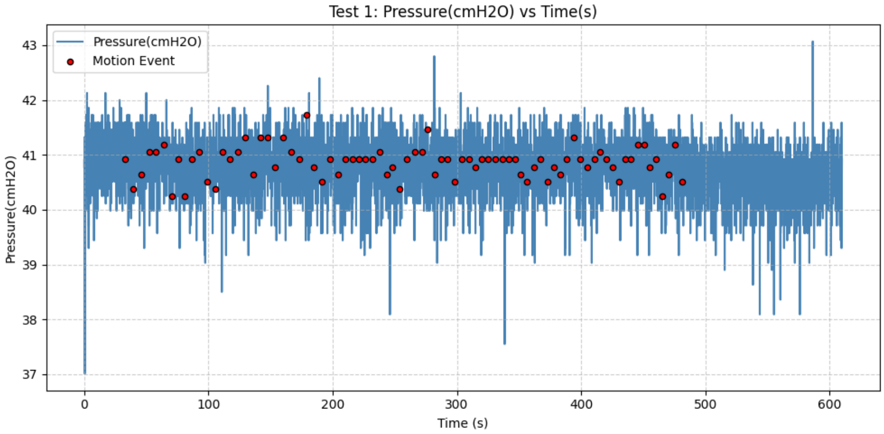

Figure 4.13: Representative pressure trace from Phantom Test 1. Despite induced mechanical events, no corresponding transient pressure elevations were observed.

Further validation was performed using an adjustable voltage source to simulate sensor output. The MPX5050DP transfer function [268] is defined as:

$$V_{out} = V_S(0.018P + 0.04) \tag{4.9}$$

where P is pressure in kPa and V_S is the supply voltage (5 V). Rearranging this gives:

$$P = \frac{\frac{V_{out}}{V_S} - 0.04}{0.018} \tag{4.10}$$

Substituted voltage inputs produced theoretical pressure values that showed alignment with ADC-derived measurements. The combined calibration results are shown in Figure 4.14.

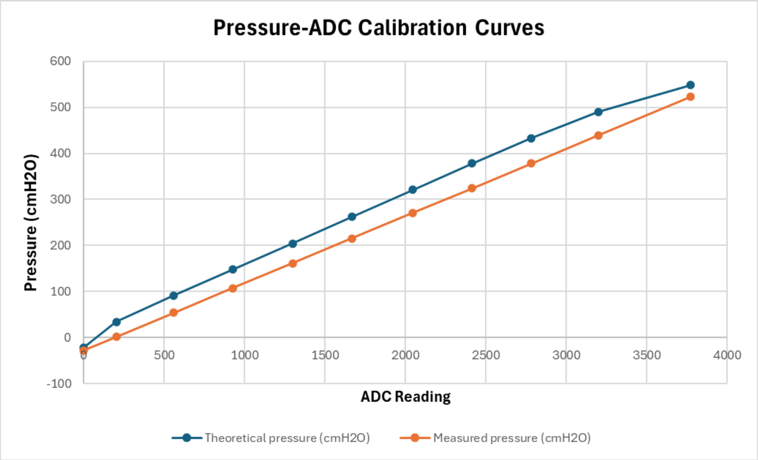

Figure 4.14: Calibration results for the MPX5050DP pressure sensor, demonstrating linear alignment between applied pressure, theoretical transfer function values, and ADC measurements.

These findings indicate that the absence of observable pressure transients during phantom testing is not attributable to sensor or acquisition limitations, but is more likely due to insufficient pressure transmission within the phantom model. This highlights a limitation of the experimental setup, where induced mechanical perturbations did not generate measurable intravesical pressure changes comparable to physiological conditions.

4.12.4 Wearable Balloon-Based Pressure and Motion Artifact Suppression Validation

Due to the absence of dynamic pressure transmission during phantom testing, an additional wearable validation experiment was conducted to assess pressure responsiveness and motion artifact suppression under controlled human movement conditions. Specifically, the UroMonitor device was secured to the torso and connected via catheter tubing to a compliant balloon bladder. Manual balloon compression was used to simulate transient intravesical pressure elevations. This configuration enabled controlled isolation of pressure-only events, motion-only events, and combined motion–pressure events. Note that for this test, the Version 2 PCB was used and not the breadboard prototype.

Experimental Protocol

The protocol encompassed six different movement categories, capturing posture transitions, coughing, rotation, and Valsalva manoeuvres. The protocol was structured in repeated blocks to isolate different movement categories while maintaining temporal spacing between events.

Initial Baseline:

1. Device powered on and initialised.
2. 30 seconds stationary baseline recording.

Block 1 – Cough-Based Events: Each repetition consisted of:

1. Balloon compression only (participant stationary).
2. 10 second interval.
3. Cough only (no balloon compression).
4. 10 second interval.
5. Combined cough and balloon compression.
6. 10 second interval.

This full sequence was repeated twice, followed by a 30 second stationary recovery period.

Block 2 – Postural Transitions (Supine):

1. Balloon compression only (participant stationary).
2. 10 second interval.
3. Sitting-to-supine transition (no balloon compression).
4. 10 second interval.
5. Supine-to-sitting transition with balloon compression.
6. 10 second interval.

This full sequence was repeated twice, followed by a 30 second stationary recovery period.

Block 3 – Postural Transitions (Standing):
The sequence from Block 2 was repeated, replacing sitting-to-supine transitions with sitting-to-standing transitions, followed by a 30 second stationary recovery period.

Block 4 – Seated Rotations:

1. Seated rotation to the left (no balloon compression).
2. 10 second interval.
3. Seated rotation to centre (with balloon compression).
4. 10 second interval.
5. Seated rotation to the right (with balloon compression).
6. 10 second interval.

The above sequence was then repeated twice with all rotation events (including rotation to the left) performed with balloon compression, followed by a 30 second stationary recovery period.

Block 5 – Supine Rotations: The sequence from Block 4 was repeated, replacing seated rotations with supine rotations, followed by a 30 second stationary recovery period.

Block 6 – Valsalva Manoeuvres: Each repetition consisted of:

1. Balloon compression only (participant stationary).
2. 10 second interval.
3. Valsalva manoeuvre (deep breathing) only.
4. 10 second interval.
5. Combined Valsalva manoeuvre and balloon compression.
6. 10 second interval.

This full sequence was repeated twice, concluding the protocol.

The 30 second stationary recovery periods separated movement categories. In addition, the 10 second intervals served as temporal reference markers. A stopwatch was used to lap event onset times to generate cumulative timestamps for overlay during analysis.

This protocol enabled explicit separation of:

- Pure pressure events,
- Pure motion events,
- Combined motion–pressure events.

UroMonitor App Signal Visualisation

Figure 4.15a shows the raw pressure and acceleration magnitude signals recorded in the UroMonitor application during testing. Distinct transient pressure peaks corresponding to balloon compression are visible, alongside motion spikes generated by coughing, posture transitions, rotations, and Valsalva manoeuvres. Figure 4.15b shows the motion-suppressed cystometrogram produced by the defined motion artifact suppression algorithm. The bottom plot displays overlapping raw pressure and motion signals to visualise coincident event detection.

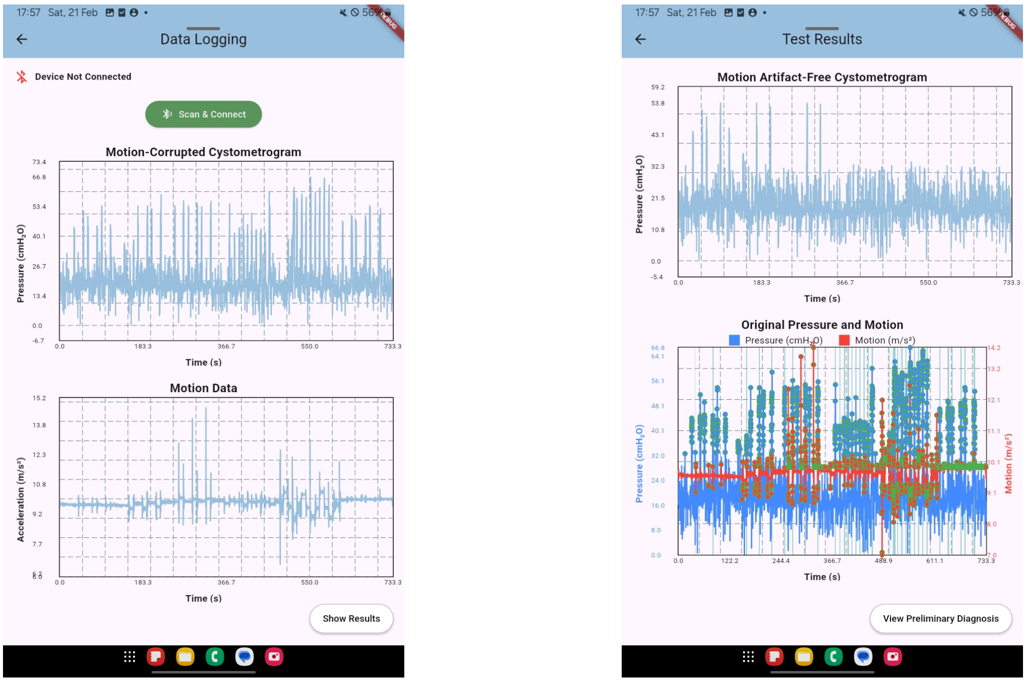

(a) Raw pressure (top) and motion (bottom) signals recorded in the UroMonitor mobile application during wearable balloon validation. Transient pressure and motion peaks are observed.

(b) UroMonitor mobile app-generated motion artifact-free cystometrogram (top) and combined raw pressure–motion view (bottom) illustrating coincident event detection and motion artifact suppression.

Figure 4.15: UroMonitor mobile application screens during wearable balloon validation.

Offline Signal Analysis and Event Classification

To independently validate application-level processing, the exported CSV file was analysed in a separate Google Colab environment. Figure 4.16 shows raw pressure (black dashed), cleaned pressure (red), and scaled motion (cyan) signals with event window overlays. Purple shading denotes pressure-only events, green denotes motion-only events, and red indicates combined motion–pressure events. The figure was segmented into 6 regions, corresponding to the six different movement categories defined in the protocol.

Figure 4.17 displays raw and cleaned pressure traces without overlay to highlight suppressed peaks. Visible black dashed peaks with no cleaned pressure overlay reflect pressure peaks that were removed by the motion suppression algorithm. Figure 4.18 shows the motion signal with event window overlays. Finally, Figure 4.19 shows the final cleaned pressure signal, representing the motion artifact-suppressed cystometrogram intended for clinical interpretation.

In total, across all six movement blocks, event-level classification performance was quantified to evaluate the effectiveness of the motion artifact suppression algorithm:

- Pressure-only events: 8 of 12 peaks were preserved.
- Motion-only events: 14 of 14 peaks were correctly detected.
- Combined motion–pressure events: 30 of 32 coincident peaks were suppressed (93.75%).

The two unsuppressed combined events corresponded to motion amplitudes below the predefined detection threshold. Four pressure-only peaks were suppressed during manual balloon compression.

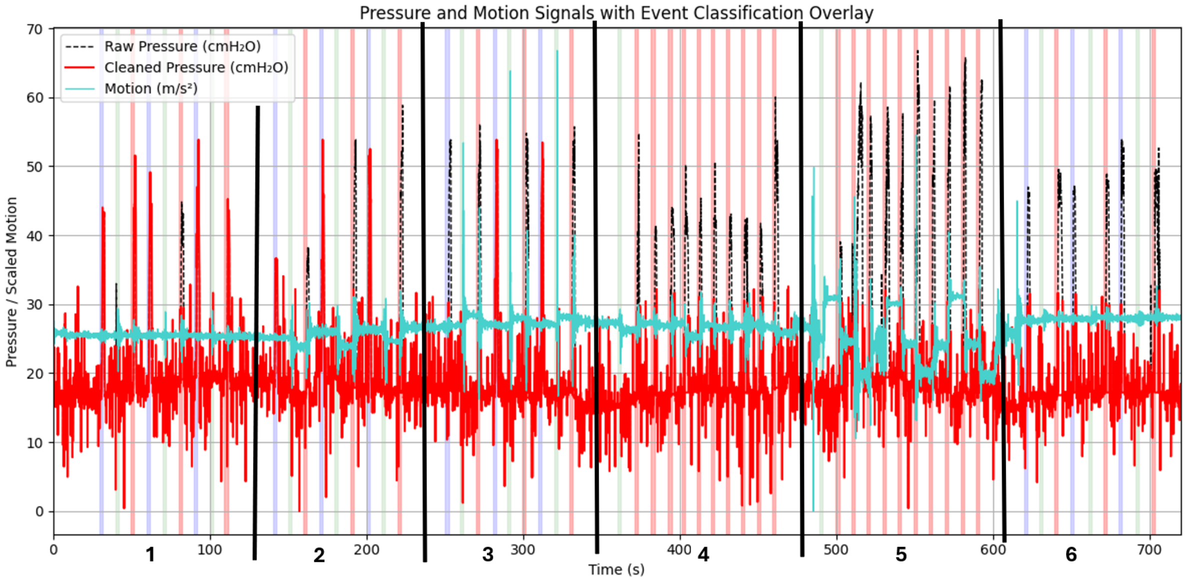

Figure 4.16: Raw pressure (black dashed), cleaned pressure (red), and scaled motion (cyan) signals with annotated event window overlays. Purple = pressure-only, green = motion-only, red = combined events.

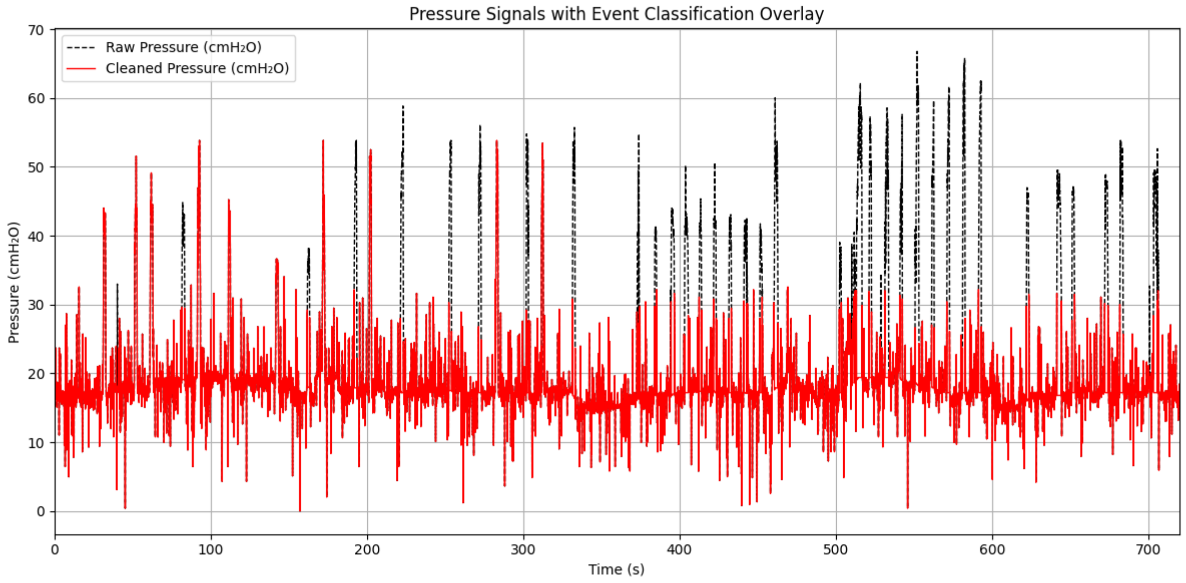

Figure 4.17: Raw (black dashed) and cleaned (red) pressure signals without overlay. Suppressed motion-correlated peaks are visible as dashed peaks without cleaned (red) pressure signal overlay.

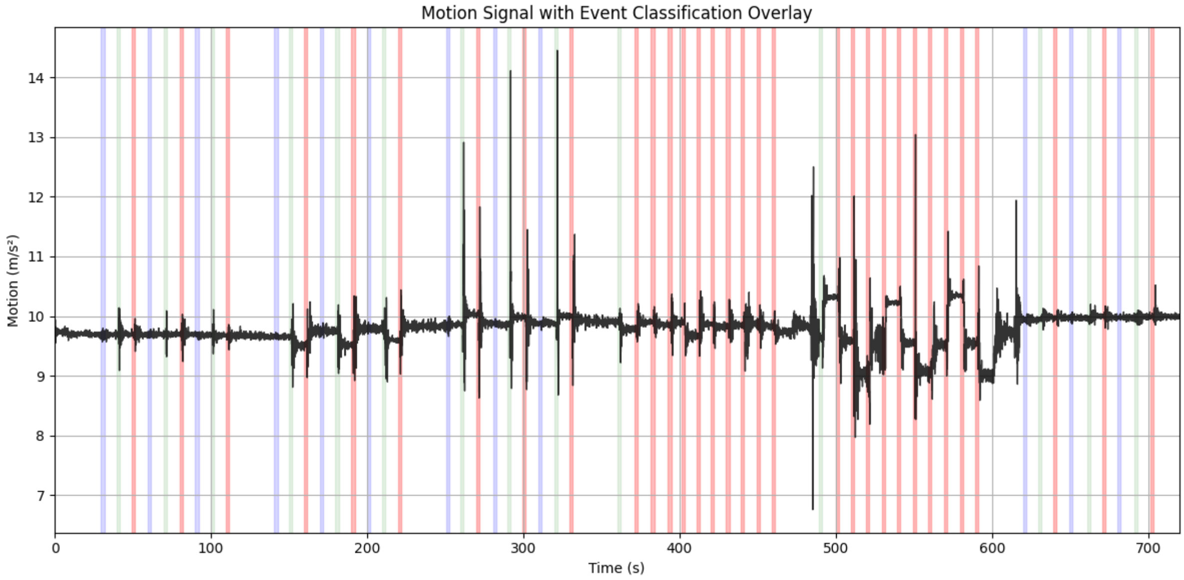

Figure 4.18: Acceleration magnitude signal with event window overlays. Motion-only and combined events show peak alignment within annotated intervals.

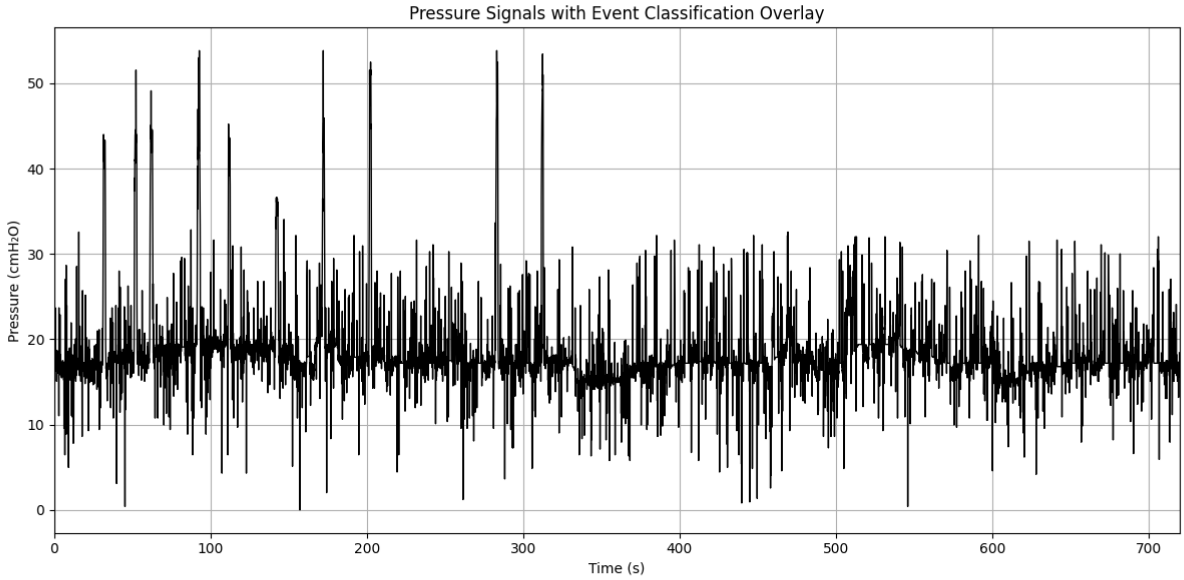

Figure 4.19: Final motion-suppressed pressure signal representing the motion artifact-reduced cystometrogram.

4.13 Intended Ambulatory Setup and Operational Procedure

The following procedure outlines the intended ambulatory deployment and operation of the UroMonitor system.

1. Pre-Use Preparation

Prior to deployment, the system should be prepared and verified:

- Inspect the enclosure, catheter, and ports for any visible damage.
- Fully charge the LiPo battery via the TP4056 charging module (blue LED indicates full charge).

- Ensure the mobile device (if used) is sufficiently charged.
- Record patient details within the application or via alternative documentation.
- Calibrate the MPX5050DP pressure sensor against a known reference.

2. Device Setup

Once the system is prepared, the device should be positioned and connected to the patient:

- Secure the UroMonitor to the lower abdomen using Velcro straps, ensuring that user-facing components (OLED display, microSD slot, switch, push-button) are oriented upward for visibility and access.
- Insert the catheter according to standard sterile clinical procedure and connect it to the pressure sensor port.
- Ensure the catheter is routed downward with minimal slack, avoiding kinks, tugging, or tension.

3. Monitoring

Following setup, monitoring should be initiated in a controlled manner to establish a stable baseline:

- Power on the device and confirm operation via the OLED display.
- Establish a BLE connection with the mobile application (if used) and verify real-time signal visibility.
- Instruct the patient to remain stationary for approximately 30 s to establish baseline pressure and motion conditions.
- Begin data logging via the push-button (SD card) or mobile application (BLE and SD logging).

4.13.1 4. Ambulatory Use

Once monitoring has commenced, the patient may proceed with normal daily activities while the device continuously records pressure and motion data.

4.13.2 5. Session Completion

At the end of the monitoring period, the session should be properly terminated and data secured for analysis:

- Stop data recording via the device or application.
- Confirm successful data storage on the SD card and/or application export.
- Remove the device and catheter following standard clinical practice.
- Analyse recorded data using the mobile application or offline processing.

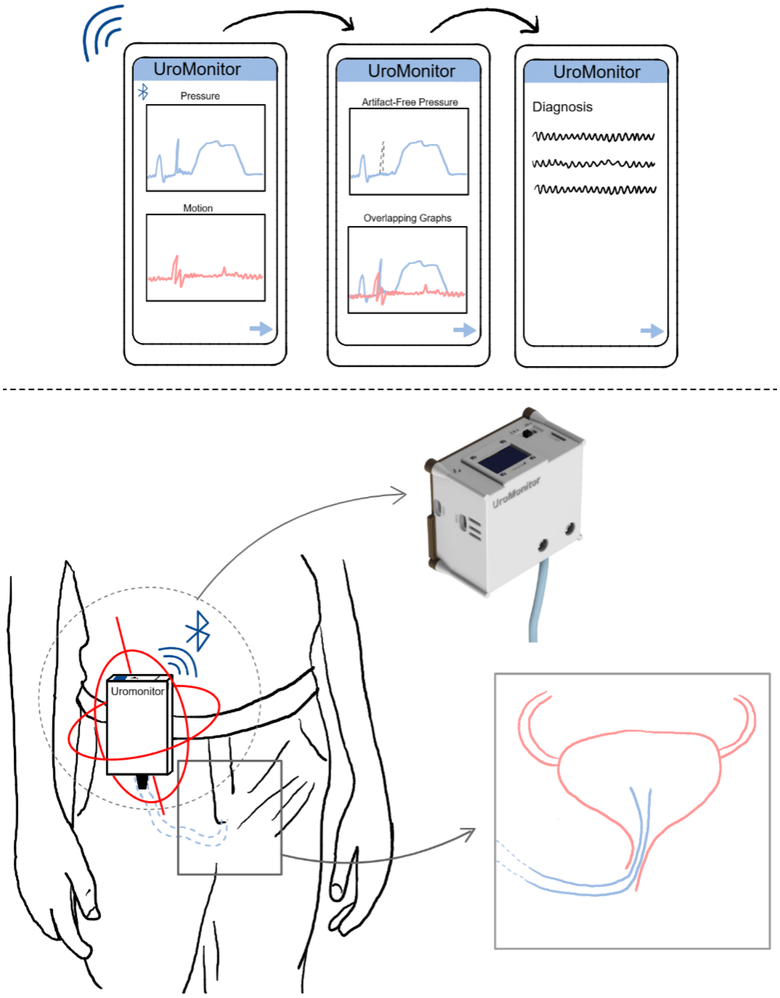

Figure 4.20: Conceptual overview of intended ambulatory deployment. The UroMonitor is secured to the torso with the catheter routed inferiorly toward the bladder. BLE transmission enables real-time visualisation in the UroMonitor mobile application, including monitoring, artifact-suppressed (cleaned pressure) results, and preliminary diagnostic screens.

4.14 End-to-End System Performance and Design Constraint Verification

Following testing and validation of pressure sensing, motion detection, motion artifact suppression, PCB implementation, and enclosure integration, the UroMonitor prototype was evaluated as a fully integrated ambulatory monitoring system. This section reports complete end-to-end operational performance, including simultaneous data acquisition, SD card logging, BLE transmission, real-time visualisation, motion artifact suppression within the mobile application, and data export functionality. In addition, system-level engineering metrics are presented, including runtime, charging performance, hardware cost, device mass, and verification against predefined defined constraints.

4.14.1 Operational Reliability

Across all phantom and wearable validation experiments, the microSD card successfully mounted in all trials and all test files were written without corruption. Error handling mechanisms operated as intended (e.g., missing SD card detection). BLE connectivity remained stable with no unintended disconnections or communication dropouts, real-time plotting exhibited no visible latency, and CSV and PDF exports were generated with complete datasets. No thermal instability of the device was observed. Low-amplitude baseline fluctuations were observed in the pressure signal (see Figure 4.19).

4.14.2 Device Runtime

Battery runtime was evaluated from a fully charged state under two operating configurations:

- **Offline mode (SD logging only):** 13.01 hours
- **Simultaneous BLE streaming and SD logging:** 11.65 hours

Simultaneous BLE transmission reduced runtime by approximately 1.36 hours relative to offline operation. In both configurations, the device exceeded the predefined minimum design requirement of 6 hours of continuous operation.

4.14.3 Charging Performance

Following full discharge, the 3.7 V, 2000 mAh LiPo battery required approximately 2 hours to recharge using the integrated TP4056 charging module. Charging behaviour was stable, and no abnormal heating was observed during the process.

4.14.4 Weight Analysis

The measured mass of the complete UroMonitor device, excluding the Velcro strap and catheter, was 169 g. This is below the predefined maximum allowable weight of 300 g defined to ensure comfort during ambulatory use.

4.14.5 Cost Analysis

The total hardware cost of the prototype was €71.27, excluding delivery and import fees. Appendix B.5.1 presents the component-level cost breakdown of the UroMonitor prototype.

4.14.6 Compliance with Design Constraints

The final prototype was evaluated against the predefined constraints outlined in Section 4.2.2. Table 4.1 summarises the outcomes and shows that the prototype UroMonitor device met all predefined design constraints within the scope of this study. In particular:

- The device weight (169 g) and enclosure dimensions (70 × 80.2 × 46 mm) were within specified limits.
- Total hardware cost (€71.27) remained well below the €250 production constraint.
- Continuous operating time exceeded the minimum 6-hour requirement under both operating modes.
- The pressure sensing range (0–50 kPa) exceeded the required physiological range of 0–150 cmH_2O.
- Sampling at 20 Hz was sufficient to capture transient detrusor contractions and motion artifacts.

Table 4.14: Verification of UroMonitor prototype performance against design constraints defined in Section 4.2.2.

Criteria	Constraint	Result
Physical Constraints		
Weight	Total device weight $\leq$ 300 g* to maintain wearability.	169 g, excluding catheter and Velcro straps.
Size	All components housed within a compact enclosure ($\leq 120 \times 90 \times 60$ mm)*.	Enclosure size: $70 \times 80.2 \times 46$ mm.
Configuration	Single-catheter configuration to minimise invasiveness.	Single-catheter operation achieved.
Economic Constraints		
Production cost	Total production cost $<$ €250 using commercially available components.	€71.27, excluding shipping fees.
Component availability	Use of low-cost, widely available components compatible with open-source platforms (e.g., Arduino, ESP32).	All components sourced from accessible online electronics retailers (TEMU, bol.com, Otronic).
Power Constraints		
Power source	Battery-powered operation only (no mains connection during use).	Operates on a 3.7 V, 2000 mAh LiPo battery.
Operating time	Minimum continuous operating time $\geq$ 6 hours under active logging conditions.	13.01 h (SD logging only) and 11.65 h (BLE + SD logging).
Efficiency	Efficient power regulation to minimise energy consumption and thermal generation.	Stable 5 V and 3.3 V regulation achieved using the MT3608 boost converter and onboard ESP32 regulation; no observable thermal rise.
Physiological Constraints		
Pressure range	Operational sensing range of 0–150 cmH_2O.	Achieved using a calibrated MPX5050DP sensor (0–50 kPa), exceeding the required physiological range.
Sensitivity	High resolution within the physiological range (15–70 cmH_2O) [144, 266].	0.124 cmH_2O per ADC bit.
Temporal resolution	Sampling frequency sufficient to capture transient detrusor events.	20 Hz sampling captures transient detrusor contractions and motion artifacts.
Electrical Constraints		
Power regulation	Regulated and protected power supply including overcurrent and short-circuit protection.	Battery protection circuitry included; additional fuses implemented (one to be updated); dual modes prevent simultaneous operation and charging.
Isolation	Electrical isolation from external power sources during operation.	Dual operational modes prevent simultaneous device operation and charging.
Signal acquisition	Stable analogue-to-digital conversion with sufficient resolution for clinical pressure measurement.	Real-time visualisation shows negligible delay, reliably capturing pressure and motion events.
Usability Constraints		
Wearability	Form factor must not impede daily activities.	Compact form factor supports daily use.
User interaction	Intuitive interface requiring minimal setup or calibration.	OLED provides user guidance and the mobile application is intuitive; occasional pressure calibration may be required.
Safety and comfort	Use of patient-safe materials (e.g., medical-grade tubing) and mechanically secure enclosure design.	Mechanically secure device with electrical protection; prototype uses silicone tubing, replaceable with medical-grade tubing.
Autonomy	Operation without continuous clinician supervision.	Device is intuitive to set up and operate; once running, the user can continue normal daily activities without intervention.

5

Discussion

This thesis investigated two complementary approaches to enable motion context awareness in single-catheter ambulatory cystometry. Conventional cystometry employs a dual-catheter configuration, where a second catheter provides an abdominal reference signal to distinguish motion artifacts from true detrusor contractions. While effective, this approach is invasive and may influence physiological bladder behaviour, thereby limiting bladder monitoring under natural conditions. Moreover, conventional cystometry is expensive. These limitations restrict accessibility and may fail to reproduce patients' everyday symptoms, potentially hindering accurate diagnosis.

To address this, ambulatory cystometry has been explored to allow continuous, real-world monitoring of bladder pressure during daily activities using portable systems. This improves symptom replication and diagnostic accuracy. However, existing ambulatory systems continue to rely on dual catheters and therefore do not reduce the invasiveness associated with conventional cystometry, addressing only the symptom replication challenge. A single-catheter configuration minimises invasiveness but removes the abdominal reference channel required for motion artifact detection. Consequently, this thesis focused on two alternative motion context awareness strategies for single-catheter ambulatory cystometry, aimed at improving diagnostic reliability while reducing invasiveness and increasing accessibility:

- Part A investigated a data-driven approach, using machine learning models to classify motion artifacts from pressure signal morphology.
- Part B focused on a hardware-based approach, integrating inertial motion sensing into a low-cost ambulatory cystometry device (UroMonitor) to enable real-time identification of motion-correlated pressure events.

This chapter discusses the results from both parts, evaluates their respective strengths and limitations, and examines how they may contribute to the development of robust, low-cost, single-catheter ambulatory cystometry systems.

Part A - Machine Learning Pipeline for Motion Artifact Removal in Ambulatory Cystometry

Section 3.10 presented model performance across multiple evaluation metrics. Within each model category (feature-based, neural network, hybrid CNN–LSTM, and feature–neural network fusion), the highest and lowest scores were highlighted. For neural networks, the top two scores were reported due to comparable performance across models. Model ranking (Section 3.11 considered both mean and standard deviation, with lower variability prioritised to reflect consistent generalisation across patient-wise cross-validation folds. The top-performing models were the RF (feature-based), the shallow 1D

CNN and multi-branch CNN (neural networks), and the sequential CNN–LSTM and CNN–RF feature-level hybrid (hybrid models). These models were selected based on both mean performance and variability across patient-wise folds.

Feature-Based Models

Table 3.1 summarises feature-based model performance. The RF classifier demonstrated the strongest overall performance across most evaluation metrics. The only exception was detrusor activity recall, where the SVM achieved a marginally higher score due to lower variability (RF: 0.935±0.034, SVM: 0.929±0.015). Given the use of patient-wise cross-validation, reduced standard deviation was prioritised as it reflects more reliable generalisation to unseen patients.

The RF achieved high motion artifact precision (0.899±0.071) but lower recall (0.590±0.179), indicating conservative classification behaviour - avoiding false-positive motion classification at the expense of missing some true motion artifacts. Clinically, this is desirable, as suppressing true detrusor activity is more harmful than retaining motion-contaminated pressure segments. In contrast, detrusor activity recall exceeded 0.9 across all feature-based models, suggesting that detrusor events exhibit more consistent and distinguishable morphology, whereas motion artifacts are more heterogeneous, arising from behaviours such as coughing, posture changes, and general movement.

XGBoost achieved comparable mean performance to the RF but exhibited greater variability across folds. This likely arises from its boosting strategy, which emphasises difficult samples and may overfit ambiguous peak-centred windows. In contrast, the RF's bagging approach reduces variance through averaging over decorrelated trees, resulting in more stable performance in the presence of noise and inter-patient variability.

Linear models, including logistic regression and linear SVM, consistently underperformed. This indicates that the extracted feature space is not linearly separable and requires non-linear decision boundaries. PR AUC trends further support these findings, with the RF maintaining higher precision across thresholds while partially recovering motion artifact events.

Overall, these results suggest that non-linear ensemble methods are best suited to feature-based classification of peak-centred cystometry windows, with the RF providing the most balanced performance in terms of accuracy, consistency, and interpretability.

Neural Network Models

Table 3.2 summarises neural network performance across a wide range of architectural variations, including depth, kernel size, pooling strategies, dropout, batch normalisation, attention mechanisms, and recurrent configurations. Across most metrics, the shallow 1D CNN and multi-branch CNN achieved the strongest performance, with neither consistently outperforming the other. The multi-branch CNN achieved the highest motion artifact precision (0.916±0.031), closely followed by LUNet (0.914±0.036), while LUNet marginally outperformed in detrusor activity recall (0.934±0.024 versus 0.929±0.015).

Motion artifact recall was highest for the MLP (0.722±0.099), followed by the shallow 1D CNN (0.647 ± 0.087). However, this increase in recall came at the cost of reduced MA precision and overall performance, indicating over-classification of motion artifacts and limiting its practical application in cystometry. For the remaining metrics, including F1-scores and detrusor precision, the shallow 1D CNN consistently performed best, while the multi-branch CNN achieved the highest precision–recall AUC (0.885±0.042).

The MLP was the weakest overall model, highlighting the limitations of fully connected architectures for time-series data. Without convolutional operations, the MLP lacks an inductive bias for local temporal structure, making it less effective at learning meaningful representations of pressure dynamics from peak-centred windows.

Both top-performing CNN models exhibited similar behaviour: approximately 65% of windows were classified as motion artifacts with around 90% precision, while detrusor activity recall remained high (approximately 92–93%) with around 66% precision. This similarity indicates that increased architectural complexity does not yield meaningful performance gains. Superior performance by two CNN models suggests that local temporal patterns around pressure peaks are the dominant discriminative features for motion artifact detection. Convolutional architectures are well suited to capturing such localised patterns, whereas recurrent models (e.g., Bi-LSTM) are designed to model longer temporal dependencies that are less relevant in fixed-length, peak-centred windows. This explains why convolutional models consistently outperformed LSTM-based architectures.

Similarly, attention and squeeze–excitation mechanisms did not improve performance, indicating that relevant information is already effectively captured by convolutional feature maps. Additional mechanisms therefore introduce unnecessary complexity without performance benefits. Nevertheless, all neural network models except the MLP achieved comparable or superior performance to the RF classifier, demonstrating that learned representations from raw pressure windows can match or exceed manually engineered features.

Overall, shallow convolutional architectures appear sufficient for this binary classification task, with additional complexity providing limited additional performance benefit.

Hybrid Models

Tables 3.3 and 3.4 summarise CNN–LSTM hybrids and feature–neural network fusion models. Two CNN–LSTM hybrid architectures were evaluated: a sequential architecture, in which convolutional features are passed to a Bi-LSTM, and a parallel architecture, in which convolutional and recurrent branches operate independently before fusion (Section 3.6.3). In both cases, the stand-alone shallow 1D CNN and the Bi-LSTM with learned temporal attention were used as the base components.

The sequential CNN–LSTM consistently outperformed the parallel architecture, while the parallel model underperformed relative to the stand-alone shallow 1D CNN (Table 3.2), suggesting that independently learned recurrent features (via the Bi-LSTM branch) introduce noise rather than complementary information.

The sequential hybrid showed only marginal improvement in motion artifact precision (0.907 ± 0.048 vs 0.902 ± 0.052) compared to the shallow 1D CNN, with reduced performance across other metrics and higher variability. It also outperformed the stand-alone Bi-LSTM, indicating that recurrent models benefit from operating on convolutionally extracted features rather than raw signals. These findings reinforce that long-range temporal modelling offers limited benefit for peak-centred windows, where discriminative information is dominated by local dynamics.

For feature–neural network fusion, the top-performing feature-based and neural network models were combined using both feature-level and late-fusion strategies. Specifically, the RF classifier was fused with the shallow 1D CNN, which was selected over the multi-branch CNN due to its simpler architecture and largely comparable performance. The feature-level CNN–RF model outperformed the late-fusion ensemble, indicating that joint representations are more effective than post-hoc decision fusion. However, the feature-level model underperformed both stand-alone RF and shallow 1D CNN models. Only marginal improvements were observed for detrusor recall and PR AUC, which did not offset overall performance degradation. This indicates that the addition of CNN-learned features does not enhance, and even degrades, the performance of the RF classifier when combined with manually engineered features. This likely reflects a representational mismatch: engineered features capture physiological characteristics such as amplitude and duration, whereas CNN features encode local temporal patterns. Combining these representations introduces redundancy and reduces classifier effectiveness.

Overall, increased architectural or representational complexity does not improve performance. Sequential integration of convolutional and recurrent components produces limited gains over convolutional models alone, while feature-level fusion fails to outperform stand-alone approaches.

Feature Augmentation

Feature augmentation did not improve performance. The shallow 1D CNN trained on raw windows outperformed the augmented model (trained on raw windows and engineered features) across all metrics except detrusor recall (identical performance) (Table 3.4). This confirms that the CNN internally learns the same discriminative information as engineered features. Augmentation introduces unnecessary complexity without performance gain.

Error Profile Analysis

Error analysis (Section 3.10.6, Table 3.5) evaluated false positives (FP), false negatives (FN), and false positive rate (FPR) for the top-performing models, where false positives (suppression of true detrusor activity) were considered more clinically harmful than false negatives (residual motion artifacts).

All models achieved FPR values below 10%, with no statistically meaningful separation between them. The CNN–RF hybrid achieved the lowest FPR (6.6±1.5%), while the shallow CNN exhibited the highest (7.7±1.4%), although these differences fall within one standard deviation.

The shallow 1D CNN achieved the lowest FN count and variability (12.8±5.6), indicating consistent motion artifact detection across patients. In contrast, the CNN–RF hybrid showed higher FN counts and variability (16.2±9.9). Feature-based and hybrid models demonstrated more conservative behaviour, reflected by low FP rates but higher FN counts, prioritising preservation of detrusor activity at the cost of reduced MA removal.

Overall, the shallow 1D CNN achieved the most balanced error profile, combining low FN, acceptable FP, and low variability. This balanced error profile aligns most closely with the clinical objective of suppressing motion artifacts while preserving true detrusor activity.

Model Ranking and Final Selection

Table 3.6 presents the final model ranking based on weighted, normalised performance scores computed across clinically prioritised evaluation metrics. The resulting score is intended for relative comparison between models, rather than to imply absolute superiority of one model over another. The multi-branch CNN with channel-wise attention ranked highest due to strong motion artifact precision and PR AUC. However, its advantage over the shallow CNN was modest and within fold variability (Figure 3.3). The shallow 1D CNN ranked second (score: 0.76) and demonstrated a more balanced and stable error profile, suggesting that the difference between the top two ranked models reflects a trade-off between slightly improved discrimination (multi-branch CNN) and greater stability and balance (shallow 1D CNN), rather than a clear performance gap. The sequential CNN–LSTM ranked third, followed by the CNN–RF hybrid and RF.

Overall, while the multi-branch 1D CNN with attention achieves the highest aggregated score, the shallow 1D CNN emerges as a strong alternative with comparable aggregated metric performance and a more balanced and stable error profile with a simpler architecture. These results reinforce the conclusion that architectural simplicity can achieve performance comparable to more complex models.

Although Part A provides insight into model behaviour and design trade-offs for motion artifact detection in ambulatory cystometry, the limited dataset size constrains generalisability, and the findings should be interpreted as indicative rather than definitive.

No single model consistently outperformed others across all metrics. Instead, performance was governed by trade-offs between motion artifact precision, motion artifact recall, and preservation of detrusor activity. Models optimised for high precision tended to exhibit reduced recall, reflecting conservative classification strategies that prioritise avoiding incorrect suppression of detrusor activity. This trade-off is clinically meaningful, as false positives are more clinically harmful than missed artifacts.

Neural network models outperformed feature-based approaches and reduce reliance on manual feature engineering, which is otherwise time-consuming and dependent on domain expertise. However, increasing architectural complexity did not consistently improve performance. While the multi-branch CNN achieved the highest overall score, its advantage over the shallow CNN was modest and inconsistent, with greater variability across patient folds.

The shallow 1D CNN achieved the most balanced performance, combining low false negatives, acceptable false positives, and low variability across patient folds. Its simplicity, consistency, and balanced error characteristics make it the most robust and clinically suitable model within the constraints of the current dataset.

Part B - Design and Implementation of the UroMonitor System

Given the limited dataset available for definitive results in Part A, Part B explored motion context awareness through direct hardware integration. The UroMonitor was designed as a low-cost, single-catheter ambulatory cystometry prototype incorporating an inertial measurement unit (IMU) for real-time motion detection. By acquiring pressure and motion signals simultaneously, the system enables correlation-based identification of motion-induced pressure peaks, allowing motion artifacts to be detected and suppressed without requiring a second catheter. Reducing reliance on a second catheter has the potential to improve patient comfort, reduce procedural invasiveness, and enable more natural bladder behaviour during ambulatory monitoring.

The system integrates a pressure sensor (MPX5050DP), MPU6050 IMU, ESP32 microcontroller, microSD storage, BLE connectivity, and battery-powered operation within a compact, portable form factor. A custom mobile application was developed to support real-time visualisation, automated motion artifact suppression, preliminary diagnostic interpretation, and data export in CSV and PDF formats. The system also supports offline operation via direct SD card logging, improving robustness during ambulatory use.

Overall, the UroMonitor prototype met all predefined physical, electrical, economic, physiological, and usability constraints, demonstrating the feasibility of a compact, low-cost, single-catheter, ambulatory cystometry system with embedded motion awareness.

System Design and Hardware Performance

The Version 2 PCB resolved stability issues present in the initial Version 1 design, including startup instability and unreliable SD card communication caused by incorrect pin selection and routing issues. These issues were addressed through corrected routing and reassignment of the latching push-button to a non-bootstrap GPIO pin. After these updates, the system demonstrated stable operation under full load, including simultaneous pressure acquisition, motion sensing, BLE transmission, OLED output, and SD logging. No unexpected resets, communication failures, or thermal issues were observed. This stability is essential for ambulatory deployment, where uninterrupted long-duration monitoring is required.

The 3D-printed enclosure successfully housed all components within a compact form factor suitable for torso-mounted ambulatory use. Adequate structural integrity and protection were achieved without requiring major design iterations, although minor modifications were needed to improve button alignment. Specifically, the cut-out for the latching push-button needed to be enlarged to improve alignment and user accessibility. Internal wiring density increased assembly complexity, indicating that future iterations would benefit from improved cable management or slightly increased enclosure volume.

Pressure Sensing Performance

Pressure calibration results (Figure 4.14) confirmed correct functionality of the MPX5050DP pressure sensor. A linear relationship between applied pressure and ADC output was observed, with close agreement between experimental measurements and the manufacturer transfer function [268]. Minor deviations were attributed to measurement uncertainty in the analogue reference sensor, manual syringe-based pressure application, and inherent sensor error margins.

No transient pressure peaks were observed during phantom testing (Section 4.12.3). However, the absence of these transient peaks reflects limitations of the phantom model rather than sensor capability (as functionality was proven via calibration). This conclusion is supported by wearable balloon validation, where clear transient pressure peaks were successfully captured. These findings confirm that the pressure sensing subsystem was functioning as intended, and that phantom design, rather than hardware limitations, prevented dynamic pressure transmission during testing.

Motion Detection Performance

Motion detection performance was evaluated using multiple inertial signals, where the inertial signals were ranked according to recall performance across the six phantom tests (see Table 4.12). Recall represents the proportion of annotated motion events that were successfully captured by the UroMonitor device. Acceleration magnitude (AccMag) demonstrated the highest and most consistent performance, achieving a mean recall of 95.4%, a standard deviation of 3.3%, and a minimum recall of 90.5% across all tests. The similarity between mean and median values indicates stable performance without significant outliers. The low standard deviation underscores the consistency of AccMag detection across varying movement types. Even in the lowest-performing case (Test 6, random perturbations), more than 90% of motion events were successfully detected (Table 4.13).

AccMag outperformed individual accelerometer axes. By computing the vector magnitude of the three orthogonal acceleration components, AccMag reduces sensitivity to device orientation relative to gravity and body posture, improving motion detection. In contrast, individual axes exhibited greater variability due to orientation dependence. Gyroscope signals showed lower recall and higher variability, indicating limited suitability for motion detection. This supports the use of AccMag as a reliable replacement for abdominal reference signals in single-catheter systems, where reliable motion detection is critical for maintaining diagnostic confidence, as accurate suppression of motion artifacts reduces the risk of misinterpreting non-physiological pressure changes as detrusor activity.

Overall, the MPU6050 IMU demonstrated reliable and repeatable detection of motion events across a range of movement types, supporting its use as the primary motion reference for artifact suppression.

Wearable Balloon-Based Pressure and Motion Artifact Suppression Validation

Wearable balloon validation provided a more physiologically representative test environment compared to the phantom model, allowing simultaneous evaluation of pressure and motion signals under controlled human movement conditions. Figures 4.15a and 4.15b show the raw and processed signals from the UroMonitor mobile application. Further offline analysis (Figure 4.16) was performed for detailed evaluation of pressure-only, motion-only, and combined motion–pressure events. Manual event annotations were overlaid to assess algorithm behaviour. Purple shading represents pressure-only events (balloon compression without movement), green represents motion-only events, and red represents simultaneous motion–pressure events. For purple regions, a preserved pressure peak was expected; for green regions, a motion peak without pressure elevation; and for red regions, a coincident motion and raw pressure peak with suppression of the cleaned pressure signal. Note that slight temporal offsets between shaded annotation windows and signal peaks were observed. These are attributable to manual timekeeping and reaction delay during event marking.

The recording was divided into six segments corresponding to the six different movement categories defined in the protocol. Across most segments, the system correctly distinguished between pressure-only, motion-only, and combined motion–pressure events, demonstrating correct motion artifact suppression and detrusor activity preservation behaviour. Segments involving posture transitions and rotational movements (Segments 2, 4, and 5) showed consistently correct classification across all event types, indicating robust performance under typical ambulatory conditions. Deviations from expected behaviour were observed in Segments 1, 3, and 6.

Segment 1 – Coughing: While pressure-only and motion-only events were correctly detected, only one of three combined motion–pressure events was suppressed. Inspection of the motion signal (Figure 4.18) shows relatively small amplitude fluctuations during certain cough events. As the suppression algorithm requires a motion deviation exceeding the baseline value by 0.3 m/s^2 to flag a motion event, sub-threshold fluctuations did not trigger suppression.

Segment 3 – Sitting to Standing Transitions: One pressure-only event was incorrectly suppressed. Although no intentional movement occurred, minor torso motion during manual balloon compression exceeded the motion threshold, highlighting the sensitivity of the system to subtle movement.

Segment 6 – Valsalva Manoeuvres: Pressure-only events were suppressed due to coincident motion detected during exertion, again reflecting sensitivity to small movement generated during pressure generation.

Collectively, across all test segments, all motion-only events were detected, and the system successfully suppressed 93.75% (30 of 32) of motion-correlated pressure events, demonstrating strong baseline performance for motion artifact mitigation. The two unsuppressed combined events corresponded to motion amplitudes below the 0.3 m/s^2 threshold. Pressure-only events were preserved in 8 of 12 cases, with the suppressed pressure peaks reflecting suppression due to subtle coincident motion peaks exceeding the motion threshold.

The final cleaned pressure plots (Figures 4.15b and 4.19) show that distinct pressure-only peaks remain visible after suppression, while the majority of motion-correlated artifacts are removed. Although baseline noise persists, detrusor-like pressure elevations are unobscured by the baseline noise, supporting the feasibility of real-time motion artifact mitigation within the mobile application.

These results highlight a key trade-off of threshold-based detection. Lower thresholds increase sensitivity but risk suppressing true pressure events, while higher thresholds preserve detrusor activity but may miss subtle motion artifacts. Observed misclassifications were primarily associated with low-amplitude motion or minor body movement during manual balloon compression. This suggests that in clinical scenarios, careful tuning of motion thresholds will be required to minimise suppression of true detrusor contractions.

Despite these limitations, the cleaned pressure signals retained clear detrusor-like peaks while removing the majority of motion-induced artifacts, demonstrating the effectiveness of the suppression algorithm. This is essential for accurate interpretation of baldder function. The results confirm that the system provides robust baseline performance with tunable behaviour via threshold adjustment.

End-to-End System Performance

End-to-end evaluation of the UroMonitor demonstrated stable integration of hardware and software subsystems. The complete pipeline (including sensing, SD logging, BLE transmission, real-time visualisation, artifact suppression, and data export) operated without failure across all experiments.

Real-time acquisition, transmission, and plotting at 20 Hz were sustained without latency, indicating that the ESP32 platform is sufficient for continuous ambulatory monitoring. Minor baseline noise was observed but remained below clinically relevant pressure variations and did not affect signal interpretability (see Figure 4.19). This noise may be caused by minor sensor drift or wires tightly packed together to fit within the enclosure.

Battery performance exceeded design requirements, achieving 13.01 hours of SD-only operation and 11.65 hours with simultaneous BLE streaming. The reduction in runtime during BLE operation reflects increased power consumption but remains within acceptable limits for ambulatory monitoring, meeting the predefined 6 hour minimum operating constraint. Full battery recharge was achieved in $\approx$2 hours using the integrated TP4056 charging module. No abnormal heating was observed during charge or discharge cycles, indicating safe battery performance under normal operation.

Design Constraints

The prototype met all predefined design constraints (Table 4.14), including cost (€71.27), weight (169 g), operating time (11.65–13.01 hours), and enclosure dimensions (70 × 80.2 × 46 mm). These results support the feasibility of developing a compact, low-cost ambulatory cystometry system using widely available components.

Electrical safety was ensured through regulated 5 V and 3.3 V supply rails, integrated battery protection circuitry, fuse implementation, and a dual-mode switch configuration preventing simultaneous charging and operation. During testing, one fuse was found to be incorrectly specified, resulting in unintended tripping due to an insufficient hold and trip current rating under system load. This issue was identified and is resolved through appropriate fuse selection, as discussed in Section 5. These characteristics are critical for enabling ambulatory deployment in low-resource settings. Overall, the system achieves a balance between cost, portability, and functional performance.

System-Level Feasibility and Clinical Implications

The UroMonitor prototype demonstrates the feasibility of integrating pressure sensing, inertial motion detection, and real-time signal processing within a portable, battery-powered system for single-catheter ambulatory cystometry. While clinical validation is required, the system highlights several potential implications for both clinical practice and healthcare accessibility.

The compact and wearable design enables continuous monitoring during normal daily activities, in contrast to conventional cystometry where patients remain largely stationary. This has the potential to capture more physiologically representative bladder behaviour, improving detection of symptoms that may not manifest during short in-clinic assessments.

The low hardware cost and use of widely available components support deployment beyond specialised clinical environments. Combined with a 3D-printable enclosure and portable form factor, the system may enable decentralised production and use in outpatient or resource-limited settings, where conventional urodynamic systems are often inaccessible.

The single-catheter configuration reduces invasiveness compared to dual-catheter systems, potentially improving patient comfort and compliance. Automated motion artifact suppression and structured data export may also reduce reliance on manual trace interpretation, supporting more efficient and consistent analysis, particularly in settings with limited specialist expertise. In addition, the relatively simple hardware architecture and user interface makes training of healthcare personnel in both device assembly and operational use more likely, supporting scalability in healthcare environments.

Overall, the prototype establishes a proof-of-concept for a low-cost, motion-aware, ambulatory single-catheter cystometry system capable of real-time, continuous bladder pressure monitoring with integrated motion artifact suppression. While further optimisation and clinical validation are required, the results support the potential for translation toward more accessible, less invasive, and more representative bladder monitoring in real-world settings.

Integration of Machine Learning and Hardware-Based Motion Context Awareness Approaches in Ambulatory Cystometry

The two approaches to motion context awareness explored in this thesis address the same challenge of distinguishing motion artifacts from true detrusor activity in cystometry. However, Part A adopts a data-driven approach, where machine learning models infer motion artifacts from pressure signal morphology, while Part B introduces direct measurement of motion through inertial sensing, enabling explicit identification of motion-correlated pressure events.

The machine learning approach in Part A offers the advantage of requiring no additional sensing hardware, making it simple from a system design perspective. It is capable of capturing complex, non-linear relationships within pressure signals and can identify subtle artifacts that may not correspond to large or easily measurable motion. However, its performance is dependent on the availability and diversity of labelled training data. In contrast, the hardware-based approach in Part B provides motion context through direct physical measurement, removing the need to infer motion indirectly from pressure morphology. This enables reliable detection of motion-correlated events independent of training data, making it inherently more robust to inter-patient variability and previously unseen motion patterns.

However, the threshold-based suppression strategy used in Part B introduces a sensitivity–specificity trade-off. While the system demonstrates strong performance in suppressing motion-correlated artifacts, its behaviour depends on threshold selection, which may lead to missed low-amplitude motion artifacts or unintended suppression of true pressure events during subtle movement. In contrast, machine learning models may better capture ambiguous or low-amplitude events, although at the cost of increased data dependency. Importantly, both approaches replace the need for an abdominal reference catheter with a non-invasive sensing modality, representing a shift toward less invasive cystometry system design.

These findings suggest that the two approaches are not competing but complementary. A hybrid system integrating IMU-based motion sensing with machine learning classification could combine the strengths of both methods: using inertial sensing to provide reliable, real-time motion context, while leveraging machine learning to refine classification of ambiguous events and reduce reliance on fixed thresholds.

Challenges and Limitations

Several limitations were encountered in both Part A and Part B, reflecting constraints in dataset availability, experimental design, and system validation.

Part A: Data and Model Limitations

The primary limitation in Part A was the restricted size and diversity of the patient dataset, which limits statistical power and generalisability. As a result, model performance should be interpreted as indicative rather than definitive. Inter-patient variability in bladder behaviour, movement patterns, and annotation practices may not be fully represented, constraining the ability of models to generalise to unseen clinical scenarios.

Additionally, recordings varied in duration, structure, and protocol. This resulted in unequal numbers of extracted peak-centred windows per patient, introducing potential class imbalance and contributing to variability across cross-validation folds. Variations in calibration procedures, recording conditions, and manual annotation further introduce noise into the dataset. As supervised learning models rely directly on these annotations, any subjectivity or inconsistency in labelling propagates into both model training and evaluation.

A further limitation arises from the use of fixed-length, peak-centred windows. Both motion artifacts and detrusor events exhibit substantial variability in temporal duration and morphology. Fixed windowing may therefore capture inconsistent proportions of signal context, truncating longer events or obscuring shorter ones with baseline data. This constrains the ability of models to fully learn event dynamics and may limit classification performance.

Collectively, these limitations indicate that the reported results are constrained by dataset size and experimental variability, and that validation on larger, standardised datasets is required for robust clinical translation.

Part B: System and Validation Limitations

While the UroMonitor prototype demonstrated functional feasibility, several technical, experimental, and logistical limitations were met during development and validation.

Pressure Measurement: Calibration was performed using an analogue reference sensor and manual syringe-based pressure application. Although strong linearity was observed, measurement uncertainty associated with manual pressure generation and analogue instrumentation may introduce minor deviations. More precise calibration using a digital reference transducer or U-tube manometer would improve measurement accuracy.

Experimental Models: Both the phantom and wearable balloon models provide simplified representations of bladder behaviour. The phantom model was unable to reproduce dynamic pressure responses, highlighting the difficulty of replicating detrusor contractions and bladder compliance mechanically. The wearable balloon model enabled controlled testing but was limited to a single participant and relied on manual pressure generation, which introduces variability and does not replicate true physiological contraction patterns or involuntary motion.

Motion Detection and Suppression: The motion artifact suppression algorithm relies on a fixed acceleration threshold (0.3 m/s^2 deviation from baseline) and temporal coincidence logic. While effective in controlled experiments, this approach introduces an inherent sensitivity–specificity trade-off. Low-amplitude motion may not exceed the detection threshold, while subtle body movement during genuine pressure events may lead to unintended suppression. This trade-off needs to be further validated in real-world scenarios where motion characteristics are highly variable.

Absence of Clinical Validation: No patient-based validation was performed. Consequently, system performance has not been evaluated under true physiological conditions, including natural detrusor activity, complex patient movement, and long-duration ambulatory monitoring. Clinical validation is required to assess diagnostic reliability and real-world usability.

Resource and Development Constraints: Development was influenced by limited access to medical-grade instrumentation and fabrication resources, as well as component delivery delays. These factors constrained the number of hardware iterations and the precision of validation procedures. Access to specialised equipment would enable more rigorous testing and accelerated system optimisation.

Overall, both approaches were evaluated in controlled settings and have not yet been validated under fully representative ambulatory conditions. Real-world deployment introduces additional challenges, including unpredictable patient movement, sensor drift, long-term wearability, and variability in physiological response.

Future Work

The results of this thesis highlight several directions for future research, focused on three main areas: (i) large-scale data collection and clinical validation, (ii) refinement of data-driven and hardware-based approaches, and (iii) integration of these approaches to improve robustness and diagnostic reliability.

Part A: Model and Signal Processing Improvements

For Part A, future work should focus on the collection of larger, standardised patient datasets. Expanded data acquisition across diverse patient populations, combined with consistent calibration procedures and annotation protocols, would improve model generalisability and enable more reliable evaluation of motion artifact detection ability. In addition, future work could focus on extending the current window-based classification framework toward full-signal cystometry analysis. This includes reconstructing cleaned pressure traces suitable for clinical interpretation and integrating motion artifact detection into an end-to-end processing pipeline.

Alternative modelling approaches may also be explored, particularly if performance plateaus with current architectures. These include temporal CNNs, transformer-based models, and hybrid architectures capable of capturing both local and longer-range temporal dependencies. Additionally, adaptive or event-driven windowing strategies could be investigated to better capture the variability in duration and morphology of both motion artifacts and detrusor activity.

Part B: System and Algorithm Improvements

Future development of the UroMonitor system should focus on improving algorithm robustness, system usability, and clinical validation.

Hardware and Sensing: Calibration accuracy could be improved through the use of medical-grade reference instruments. Future iterations may also explore fluid-compatible pressure sensing solutions or diaphragm-based interfaces to better replicate physiological conditions. Improvements in enclosure design (specifically the redesign of the latching push-button cutout and correction of IMU mounting hole dimensions) and cable management would enhance durability and ease of assembly. In addition, mechanical durability testing should be performed to assess device robustness. Alternative materials such as PETG or ABS could also be explored to assess material impact on robustness, cost, and weight. Luer-lock connectors for secure catheter attachment to the MPX5050DP pressure sensor should be explored for improved device robustness during ambulatory monitoring. Lastly, the incorrectly specified fuse needs to be replaced with a fuse of the following specifications:

- Minimum hold current: ≥ 1.1 A
- Minimum trip current: ≥ 1.5 A

This ensures reliable operation during peak load while still providing protection under fault conditions.

Full calculations can be found in Appendix B.6.

Motion Detection and Signal Processing: The current threshold-based artifact suppression approach could be further developed through adaptive thresholding based on baseline motion variability or multi-sensor fusion to improve robustness under varying motion conditions. In particular, combining accelerometer and gyroscope data may improve detection of complex movement patterns. This would reduce the reliance on a fixed 0.3 m/s^2 threshold and potentially improve sensitivity–specificity balance.

System Functionality and Usability: Further development of firmware and the mobile application could include battery level monitoring, extended-duration stability testing, and support for additional platforms (i.e., iOS-compatible version). Automated power management (as opposed to current manual switching between charging and operation modes) would enhance usability for real-world deployment.

Experimental Validation: Future testing should include long-duration ambulatory studies and controlled experiments varying motion amplitude and frequency to optimise suppression parameters and thresholding. More physiologically representative phantom models would improve validation of pressure dynamics. Two phantom model redesigns are proposed:

- *Fluid-Coupled Hydrostatic Bladder Phantom:* Involves placing a compliant, fluid-filled bladder within a larger fluid-filled chamber that represents surrounding abdominal contents. In this setup, the outer chamber fluid transmits hydrostatic pressure onto the inner bladder through gravity-dependent redistribution. When positioned upright, the surrounding fluid would pool inferiorly, increasing hydrostatic pressure exerted on the bladder, increasing intravesical pressure. In a supine position, fluid would distribute more horizontally, decreasing compressive force on the bladder. This setup would therefore generate posture-dependent pressure variation driven by gravitational effects, more closely mimicking in vivo intra-abdominal pressure changes.
- *Mechanical Compression Model:* Involves placing the bladder on a rigid base with a central catheter outlet. A mesh structure surrounding the bladder surface could be connected to a controllable rod. Downward or angled force application would allow controlled compression of the bladder, simulating coughing, abdominal strain, or rotational loading.

Integration of Data-Driven and Hardware-Based Approaches

A key future direction lies in exploring the integration of machine learning and hardware-based motion sensing to determine whether the two approaches could complement each other and boost motion artifact suppression performance. Such an approach could reduce reliance on fixed thresholds, improve generalisability across patients and conditions, and enhance diagnostic reliability.

Translation Toward Clinical Deployment

Ultimately, future work should focus on translating the proposed system into a clinically viable solution. This includes clinical studies, regulatory considerations, safety validation, and evaluation of patient comfort and clinician usability. Integration with existing urodynamic tests (e.g., uroflowmetry) could further enhance clinical value. These developments would support the transition from a feasibility prototype toward a scalable, accessible, and clinically validated single-catheter ambulatory cystometry system.

6

Conclusion

This thesis investigated two approaches to enable motion context awareness in single-catheter ambulatory cystometry.

Part A developed a posture-aware signal processing and machine learning pipeline to distinguish detrusor contractions from motion artifacts using a single pressure signal. The pipeline included preprocessing, peak detection, window generation, feature extraction, and patient-level data splitting to avoid data leakage. Neural networks outperformed traditional feature-based models, indicating that learned representations better capture subtle signal differences. However, increased model complexity yielded only marginal improvements: the multi-branch 1D CNN with channel-wise attention was substantially more complex but only modestly outperformed the shallow 1D CNN. Due to the small cohort (ten patients), results are indicative but demonstrate that motion artifacts and detrusor contractions are distinguishable. The pipeline provides a foundation for future studies on larger datasets.

Part B introduced the UroMonitor, a low-cost ambulatory cystometry prototype integrating pressure sensing with an inertial measurement unit for real-time motion detection. The system enables correlation-based artifact identification and suppression, supported by a custom mobile application for monitoring, data export, and offline logging. Phantom testing confirmed reliable motion detection.

Together, these approaches demonstrate two complementary pathways toward motion-aware single-catheter cystometry: a scalable machine learning framework and a functional hardware solution. While further validation is required, this work establishes the feasibility of replacing dual-catheter systems with low-cost, motion-aware single-channel solutions, improving patient comfort, accessibility, and portability, and enabling wider deployment of ambulatory urodynamic diagnostics.

References

[1] Tae Hyoung Kim et al. “The impact of lower urinary tract symptoms on quality of life, work productivity, depressive symptoms, and sexuality in Korean men aged 40 years and older: A population-based survey”. In: *International Neurourology Journal* 19.2 (2015), pp. 120–129. DOI: `10.5213/inj.2015.19.2.120`. URL: `https://doi.org/10.5213/inj.2015.19.2.120`.

[2] Carlos D’Ancona et al. “The International Continence Society (ICS) report on the terminology for adult male lower urinary tract and pelvic floor symptoms and dysfunction”. In: *Neurourology and Urodynamics* 38.2 (2019), pp. 433–477. DOI: `10.1002/nau.23897`. URL: `https://doi.org/10.1002/nau.23897`.

[3] Seokhwan Bang et al. “Feasibility of a Deep Learning-Based Diagnostic Platform to Evaluate Lower Urinary Tract Disorders in Men Using Simple Uroflowmetry”. In: *Investigative and Clinical Urology* 63.3 (2022), pp. 301–308. DOI: `10.4111/icu.20210434`. URL: `https://pmc.ncbi.nlm.nih.gov/articles/PMC9091823/`.

[4] Arzu Canmemis and Seyhmus K. Ozel. “The impact of artifact levels on intra- and interobserver agreement in pediatric urodynamic traces”. In: *Journal of Pediatric Urology* 21.2 (2025), pp. 362–369. ISSN: 1477-5131. DOI: `https://doi.org/10.1016/j.jpurol.2024.12.010`. URL: `https://www.sciencedirect.com/science/article/pii/S1477513124006272`.

[5] Eric Rovner and Michelle Koski. *Rapid and Practical Interpretation of Urodynamics*. Springer, Jan. 2015. ISBN: 978-1-4939-1763-1. DOI: `10.1007/978-1-4939-1764-8`.

[6] Rebecca Hall and Karen Ward. “Basic understanding of urodynamics”. In: *Obstetrics, Gynaecology Reproductive Medicine* 32.6 (2022), pp. 110–119. ISSN: 1751-7214. DOI: `https://doi.org/10.1016/j.ogrm.2022.04.003`. URL: `https://www.sciencedirect.com/science/article/pii/S1751721422000586`.

[7] Benoît Vogt. “Catheter-Free Urodynamics Testing: Current Insights and Clinical Potential”. In: *Research and Reports in Urology* 16 (2024), pp. 1–17. DOI: `10.2147/RRU.S387757`. URL: `https://doi.org/10.2147/RRU.S387757`.

[8] M. Yao and A. Simoes. *Urodynamic Testing and Interpretation*. Accessed: 2025-05-23. Treasure Island, FL: StatPearls Publishing, Aug. 2023. URL: `https://www.ncbi.nlm.nih.gov/books/NBK562310/`.

[9] Alexander Koven and Sender Herschorn. “NIRS: Past, Present, and Future in Functional Urology”. In: *Current Bladder Dysfunction Reports* 17 (Aug. 2022). DOI: `10.1007/s11884-022-00665-4`.

[10] B. Abelson et al. “Ambulatory urodynamic monitoring: state of the art and future directions”. In: *Nature Reviews Urology* 16.5 (2019), pp. 291–301. DOI: `10.1038/s41585-019-0175-5`. URL: `https://doi.org/10.1038/s41585-019-0175-5`.

[11] D. Porru et al. “Evaluation of morbidity of multi-channel pressure-flow studies”. In: *Neurourology and Urodynamics* 18.6 (1999), pp. 647–652. DOI: `10.1002/(sici)1520-6777(1999)18:6<647::aid-nau15>3.0.co;2-n`. URL: `https://doi.org/10.1002/(sici)1520-6777(1999)18:6%3C647::aid-nau15%3E3.0.co;2-n`.

[12] Steve J.A Majerus et al. “A Catheter-Free Bladder Pressure-Volume Sensor”. In: *2022 IEEE Sensors*. 2022, pp. 1–4. DOI: `10.1109/SENSORS52175.2022.9967317`.

[13] Women’s Health and Education Center (WHEC). *Pitfalls in Urodynamic Studies Interpretation*. Accessed June 27, 2025. n.d. URL: `http://www.womenshealthsection.com/content/print.php3?title=urog019&cat=4&lng=english`.

[14] International Continence Society. *Detrusor Overactivity (DO) - Filling Cystometry*. `https://www.ics.org/glossary/investigation/detrusoroveractivitydofillingcystometry`. Accessed: 2025-07-07. 2025.

[15] Jonas Kurniawan et al. “Noninvasive multichannel urodynamic system: Obtaining cutaneous electrical signals from the human urinary bladder”. In: *Lifestyle Medicine* 5 (Nov. 2023). DOI: `10.1002/lim2.93`.

[16] Jean jacques Wyndaele and David B. Vodušek. “Chapter 9 - Approach to the male patient with lower urinary tract dysfunction”. In: *Neurology of Sexual and Bladder Disorders*. Ed. by David B. Vodušek and François Boller. Vol. 130. Handbook of Clinical Neurology. Elsevier, 2015, pp. 143–164. DOI: `https://doi.org/10.1016/B978-0-444-63247-0.00009-2`. URL: `https://www.sciencedirect.com/science/article/pii/B9780444632470000092`.

[17] I. Metzler et al. “Challenges facing the urologist in low- and middle-income countries”. In: *World Journal of Urology* 38.11 (2020), pp. 2987–2994. DOI: `10.1007/s00345-020-03101-6`. URL: `https://doi.org/10.1007/s00345-020-03101-6`.

[18] S. A. Nedjim and C. S. Biyani. “Addressing Disparities in Urological Training Across Low- and Middle-Income Countries. Comment on Baqain et al. Post-Graduate Urology Training in Low- and Middle-Income Countries”. In: *Société Internationale d’Urologie Journal* 5.6 (2024), pp. 339–348. DOI: `10.3390/siuj5060066`. URL: `https://doi.org/10.3390/siuj5060066`.

[19] M. Abdelhady et al. “Detrusor Pressure Estimation from Single Channel Bladder Pressure Recordings”. In: *2022 IEEE Signal Processing in Medicine and Biology Symposium (SPMB)*. 2022, pp. 1–5. DOI: `10.1109/SPMB55497.2022.10014843`.

[20] Cambridge. *Continence*. *Cambridge Dictionary*. Cambridge University Press. Retrieved April 16, 2025, from https://dictionary.cambridge.org/dictionary/english/continence. n.d.

[21] William C. de Groat. “Anatomy and physiology of the lower urinary tract”. In: *Urologic Clinics of North America* 20.3 (1993), pp. 383–401. URL: `https://pubmed.ncbi.nlm.nih.gov/8351765/`.

[22] Anand K. Patel and Christopher R. Chapple. “Anatomy of the lower urinary tract”. In: *Surgery (Oxford)* 26.4 (2008). Renal and urology I, pp. 127–132. ISSN: 0263-9319. DOI: `https://doi.org/10.1016/j.mpsur.2008.03.011`. URL: `https://www.sciencedirect.com/science/article/pii/S0263931908000471`.

[23] National Institute of Diabetes and Digestive and Kidney Diseases. *The urinary tract & how it works*. `https://www.niddk.nih.gov/health-information/urologic-diseases/urinary-tract-how-it-works`. Accessed: 2025-05-23. 2020.

[24] Altaf Mangera, Anand K. Patel, and Christopher R. Chapple. “Anatomy of the lower urinary tract”. In: *Surgery (Oxford)* 28.7 (2010). Renal and Urology I, pp. 307–313. ISSN: 0263-9319. DOI: `https://doi.org/10.1016/j.mpsur.2010.03.002`. URL: `https://www.sciencedirect.com/science/article/pii/S0263931910000700`.

[25] National Cancer Institute. *Urinary bladder*. `https://training.seer.cancer.gov/anatomy/urinary/components/bladder.html`. Accessed: 2025-05-23. n.d.

[26] Luis M. Chiva and Javier Magrina. “Chapter 2 - Abdominal and Pelvic Anatomy”. In: *Principles of Gynecologic Oncology Surgery*. Ed. by Pedro T. Ramirez, Michael Frumovitz, and Nadeem R. Abu-Rustum. Elsevier, 2018, pp. 3–49. ISBN: 978-0-323-42878-1. DOI: `https://doi.org/10.1016/B978-0-323-42878-1.00002-X`. URL: `https://www.sciencedirect.com/science/article/pii/B978032342878100002X`.

[27] SEER Training Program. *Urinary System: Bladder*. `https://training.seer.cancer.gov/anatomy/urinary/components/bladder.html`. Accessed 2024-04-14. National Cancer Institute’s SEER Training Modules.

[28] Ayush Goel and Mohd Ashyiraff Ilani Bin Ismail. *Retropubic space*. `https://radiopaedia.org/articles/retropubic-space`. Accessed: 2025-05-23. 2014.

[29] William C. de Groat and Naoki Yoshimura. “Chapter 5 - Anatomy and physiology of the lower urinary tract”. In: *Neurology of Sexual and Bladder Disorders*. Ed. by David B. Vodušek and François Boller. Vol. 130. Handbook of Clinical Neurology. Elsevier, 2015, pp. 61–108. DOI: `https://doi.org/10.1016/B978-0-444-63247-0.00005-5`. URL: `https://www.sciencedirect.com/science/article/pii/B9780444632470000055`.

[30] Lori A. Birder et al. “How does the urothelium affect bladder function in health and disease?” In: *Neurourology and Urodynamics* 31.3 (2012), pp. 293–299. DOI: `10.1002/nau.22195`.

[31] Xu Li et al. “Mechanotransduction in the urothelium: ATP signalling and mechanoreceptors”. In: *Heliyon* 9.9 (2023), e19427. ISSN: 2405-8440. DOI: `https://doi.org/10.1016/j.heliyon.2023.e19427`. URL: `https://www.sciencedirect.com/science/article/pii/S2405844023066355`.

[32] C.H. Fry et al. “The function of suburothelial myofibroblasts in the bladder”. In: *Neurourology and Urodynamics* 26.S6 (2007), pp. 914–919. DOI: `https://doi.org/10.1002/nau.20483`. eprint: `https://onlinelibrary.wiley.com/doi/pdf/10.1002/nau.20483`. URL: `https://onlinelibrary.wiley.com/doi/abs/10.1002/nau.20483`.

[33] S. R. Bolla, N. Odeluga, R. Amraei, et al. *Histology, Bladder*. Accessed: 2025-05-23. Treasure Island, FL: StatPearls Publishing, Feb. 2023. URL: `https://www.ncbi.nlm.nih.gov/books/NBK540963/`.

[34] Chandran Tanabalan and Andrew Ballaro. “The physiology and pharmacology of the lower urinary tract”. In: *Surgery (Oxford)* 37.7 (2019), pp. 365–371. ISSN: 0263-9319. DOI: `https://doi.org/10.1016/j.mpsur.2019.04.001`. URL: `https://www.sciencedirect.com/science/article/pii/S0263931919300882`.

[35] Peter Sam, Ahmad Nassereddin, and Corey A. LaGrange. “Anatomy, Abdomen and Pelvis: Bladder Detrusor Muscle”. In: *StatPearls*. StatPearls Publishing, 2025. Chap. NBK482181. URL: `https://www.ncbi.nlm.nih.gov/books/NBK482181/`.

[36] J.K. Weaver et al. “Why are pediatric urologists unable to predict renal deterioration using urodynamics? A focused narrative review of the shortcomings of the literature”. In: *Journal of Pediatric Urology* 18.4 (2022), pp. 493–498. ISSN: 1477-5131. DOI: `https://doi.org/10.1016/j.jpurol.2022.05.015`. URL: `https://www.sciencedirect.com/science/article/pii/S1477513122002157`.

[37] John T. Stoffel. “Neuroanatomy and Neurophysiology”. In: *Female Genitourinary and Pelvic Floor Reconstruction*. Ed. by Francisco E. Martins et al. Cham: Springer International Publishing, 2022, pp. 1–22. ISBN: 978-3-030-71112-2. DOI: `10.1007/978-3-030-71112-2_3-1`. URL: `https://doi.org/10.1007/978-3-030-71112-2_3-1`.

[38] Susmita Bhattacharya and L. Ranjit Singh. “Anatomy of Urinary Bladder, Urethra and Pelvic Ureter”. In: *Urogynecology & Pelvic Reconstructive Surgery*. 1st ed. Jaypee Brothers, 2016, pp. 7–xx. ISBN: 9789385891984. DOI: `10.5005/jp/books/12783_3`. URL: `https://doi.org/10.5005/jp/books/12783_3`.

[39] Kenhub. *The male urethra*. `https://www.kenhub.com/en/library/anatomy/the-male-urethra`. Accessed: 2025-05-23. 2023.

[40] Medscape Contributors. *Male Urethra Anatomy*. `https://emedicine.medscape.com/article/1972482-overview`. Accessed 2024-04-14.

[41] Oliver Jones. *The urethra*. `https://teachmeanatomy.info/pelvis/viscera/urethra/`. Accessed: 2025-05-23. 2025.

[42] FutureLearn. *Male urethra*. `https://www.futurelearn.com/info/courses/understanding-continence-promotion/0/steps/46066`. Accessed: 2025-05-23. n.d.

[43] RN Speak. *Anatomy and physiology: The urinary system*. `https://rnspeak.com/anatomy-and-physiology-the-urinary-system/`. Accessed: 2025-05-23. 2023.

[44] Medscape. *Female urethra anatomy*. `https://emedicine.medscape.com/article/1972504-overview`. Accessed: 2025-05-23. Mar. 2025.

[45] Antonio Galzerano, Antonio Lopez-Beltran, and Maria Rosaria Raspollini. “Urinary Tract, Normal Histology”. In: *Encyclopedia of Pathology*. Ed. by J.H.J.M. van Krieken. Cham: Springer International Publishing, 2020, pp. 1–5. ISBN: 978-3-319-28845-1. DOI: `10.1007/978-3-319-28845-1_4979-1`. URL: `https://doi.org/10.1007/978-3-319-28845-1_4979-1`.

[46] N. Stoddard and S. W. Leslie. *Histology, Male Urethra*. Accessed: 2025-05-23. Treasure Island, FL: StatPearls Publishing, May 2023. URL: `https://www.ncbi.nlm.nih.gov/books/NBK542238/`.

[47] Osmosis from Elsevier. *Ureter, bladder and urethra histology*. `https://www.osmosis.org/learn/Ureter,_bladder_and_urethra_histology`. Accessed: 2025-05-23. n.d.

[48] Gordana Sendić. *Urethral sphincters: Anatomy and function*. `https://www.kenhub.com/en/library/anatomy/urethral-sphincters`. Accessed 2024-04-14. 2023.

[49] Peter Sam and Corey A. LaGrange. “Anatomy, Abdomen and Pelvis, Sphincter Urethrae”. In: *StatPearls*. StatPearls Publishing, 2023. URL: `https://www.ncbi.nlm.nih.gov/books/NBK482438/`.

[50] Clare J. Fowler, Derek Griffiths, and William C. de Groat. “The neural control of micturition”. In: *Nature Reviews Neuroscience* 9.6 (2008), pp. 453–466. DOI: `10.1038/nrn2401`. URL: `https://doi.org/10.1038/nrn2401`.

[51] Michele Serpilli et al. “A Preliminary Validation of a New Surgical Procedure for the Treatment of Primary Bladder Neck Obstruction Using a Computational Modeling Approach”. In: *Bioengineering* 8 (June 2021), p. 87. DOI: `10.3390/bioengineering8070087`.

[52] Mike Bath. *The prostate gland*. `https://teachmeanatomy.info/pelvis/the-male-reproductive-system/prostate-gland/`. Accessed: 2025-05-23. 2025.

[53] Oliver Jones. *The Urinary Bladder*. `https://teachmeanatomy.info/pelvis/viscera/bladder/`. Accessed 2024-04-14. 2025.

[54] Kenhub Authors. *Superior vesical artery*. `https://www.kenhub.com/en/library/anatomy/superior-vesical-artery`. Accessed 2024-04-14. 2022.

[55] Emmanuel S. Shermadou, Syed Rahman, and Stephen W. Leslie. “Anatomy, Abdomen and Pelvis: Bladder”. In: *StatPearls [Internet]*. Treasure Island (FL): StatPearls Publishing, 2023. URL: `https://www.ncbi.nlm.nih.gov/books/NBK531465/`.

[56] Christopher Gonzales-Alabastro, Bailey Goyette, and Stephanie J. Kielb. “Urethrovaginal Fistula Repair”. In: *Female Genitourinary and Pelvic Floor Reconstruction*. Ed. by Francisco E. Martins et al. Cham: Springer International Publishing, 2023, pp. 693–705. ISBN: 978-3-031-19598-3. DOI: `10.1007/978-3-031-19598-3_41`. URL: `https://doi.org/10.1007/978-3-031-19598-3_41`.

[57] Bodytomy. *Anatomy and function of common iliac artery with labeled diagrams*. `https://bodytomy.com/anatomy-function-of-common-iliac-artery-with-labeled-diagrams`. Accessed: 2025-05-29. n.d.

[58] Mona Sharma and Anand Kumar. “Neurovascular Supply and Lymphatic Drainage of Male Reproductive Organs”. In: *Basics of Human Andrology: A Textbook*. Ed. by Anand Kumar and Mona Sharma. Singapore: Springer Singapore, 2017, pp. 55–66. ISBN: 978-981-10-3695-8. DOI: `10.1007/978-981-10-3695-8_5`. URL: `https://doi.org/10.1007/978-981-10-3695-8_5`.

[59] Ian Bickle and Craig Hacking. *Male urethra*. `https://radiopaedia.org/articles/male-urethra`. Accessed: 2025-05-23. 2024.

[60] Kaushal, Rajesh K. “Pelvis”. English. In: *Self Assessment and Review of Anatomy*. Jaypee Brothers Medical Publishers (P) Ltd., 2018. DOI: `10.5005/jp/books/13116_11`. URL: `https://doi.org/10.5005/jp/books/13116_11`.

[61] ClinicalGate. *Venous anatomy of the abdomen and pelvis*. `https://clinicalgate.com/venous-anatomy-of-the-abdomen-and-pelvis/`. Accessed: 2025-05-23. 2015.

[62] DoctorLib. *Lymph nodes of the abdomen & pelvis*. `https://doctorlib.org/medical/anatomy/18.html`. Accessed: 2025-05-23. n.d.

[63] Naoki Yoshimura and Michael B. Chancellor. “Neurophysiology of lower urinary tract function and dysfunction”. In: *Reviews in Urology* 5.Suppl 8 (2003), S3–S10. URL: `https://pubmed.ncbi.nlm.nih.gov/16985987/`.

[64] IMAIOS. *Inferior hypogastric plexus*. `https://www.imaios.com/en/e-anatomy/anatomical-structures/inferior-hypogastric-plexus-1557867324`. Accessed: 2025-05-29. n.d.

[65] Jana Vaskovic. *Urinary bladder and urethra*. `https://www.kenhub.com/en/library/anatomy/urinary-bladder-and-urethra`. Accessed: 2025-05-23. 2023.

[66] Christina Loukopoulou. *The prostate gland*. `https://www.kenhub.com/en/library/anatomy/the-prostate-gland`. Accessed: 2025-05-23. 2023.

[67] FutureLearn. *Understanding continence promotion*. `https://www.futurelearn.com/info/courses/understanding-continence-promotion/0/steps/46074`. Accessed 2024-04-14.

[68] David C. Dangerfield and Christopher J. Coombs. "'Case of the Month' from the University of Melbourne, Melbourne, Australia: treatment of iatrogenic erectile dysfunction with somatic-to-autonomic sural nerve grafting". In: *BJU International* 132.3 (2023), pp. 262–265. DOI: `https://doi.org/10.1111/bju.16034`. eprint: `https://bjui-journals.onlinelibrary.wiley.com/doi/pdf/10.1111/bju.16034`. URL: `https://bjui-journals.onlinelibrary.wiley.com/doi/abs/10.1111/bju.16034`.

[69] Kwanjin Park. "Urological Aspects of Spinal Dysraphism". In: *Spinal Dysraphic Malformations: Science and Surgery - Volume 47*. Ed. by Dachling Pang and Kyu-Chang Wang. Cham: Springer International Publishing, 2023, pp. 273–289. ISBN: 978-3-031-34981-2. DOI: `10.1007/978-3-031-34981-2_10`. URL: `https://doi.org/10.1007/978-3-031-34981-2_10`.

[70] Jee-Woong Lee et al. "Emerging Neural Stimulation Technologies for Bladder Dysfunctions". In: *International neurourology journal* 19 (Mar. 2015), pp. 3–11. DOI: `10.5213/inj.2015.19.1.3`.

[71] Anna Hernandez. *Afferent vs. Efferent Neurons*. `https://www.osmosis.org/answers/afferent-vs-efferent-neurons`. Accessed 2024-04-14. 2025.

[72] III McDonough Robert C. and Stephen T. Ryan. 2016. DOI: `10.1016/j.suc.2016.02.003`. URL: `https://doi.org/10.1016/j.suc.2016.02.003`.

[73] Robert C. McDonough and Stephen T. Ryan. "Diagnosis and Management of Lower Urinary Tract Dysfunction". In: *Surgical Clinics of North America* 96.3 (2016). Practical Urology for the General Surgeon, pp. 441–452. ISSN: 0039-6109. DOI: `https://doi.org/10.1016/j.suc.2016.02.003`. URL: `https://www.sciencedirect.com/science/article/pii/S0039610916000050`.

[74] Hsiao-Yuan Lee, Chien-Sheng Wang, and Yu-Sheng Juan. "Detrusor underactivity in men with bladder outlet obstruction". In: *Biomedicines* 10.11 (2022), p. 2954. DOI: `10.3390/biomedicines10112954`. URL: `https://doi.org/10.3390/biomedicines10112954`.

[75] Vincenzo Mirone et al. "The Detrusor Muscle: An Innocent Victim of Bladder Outlet Obstruction". In: *European Urology* 51.1 (2007), pp. 57–66. ISSN: 0302-2838. DOI: `https://doi.org/10.1016/j.eururo.2006.07.050`. URL: `https://www.sciencedirect.com/science/article/pii/S0302283806008906`.

[76] Jessica J. Rueb and Howard B. Goldman. "Detrusor Overactivity with Detrusor Underactivity". In: *Non-Neurogenic Bladder Dysfunctions*. Ed. by Matteo Balzarro and Vincenzo Li Marzi. Cham: Springer International Publishing, 2021, pp. 139–148. ISBN: 978-3-030-57393-5. DOI: `10.1007/978-3-030-57393-5_12`. URL: `https://doi.org/10.1007/978-3-030-57393-5_12`.

[77] International Urogynecological Association. "Detrusor Overactivity with Impaired Contractility or the Co-existing Overactive-Underactive Bladder Syndrome (COUB): A Management Conundrum". In: *IUGA Spotlight* 17.5 (2024). Accessed: 2025-06-03. URL: `https://www.iuga.org/spotlight-v17-5/detrusor-overactivity-with-impaired-contractility-or-the-co-existing-overactive-underactive-bladder-syndrome-coub-a-management-conundrum`.

[78] Urology Care Foundation. *Neurogenic bladder*. `https://www.urologyhealth.org/urology-a-z/n/neurogenic-bladder`. Accessed: 2025-06-03. 2021.

[79] International Continence Society. *Assessment of lower urinary tract symptoms*. `https://www.ics.org/public/factsheets/assessmentoflowerurinarytractsymptoms`. Accessed: 2025-06-03. n.d.

[80] McVary, Kevin and Saini, Rajiv. *Lower urinary tract symptoms in males*. `https://www.uptodate.com/contents/lower-urinary-tract-symptoms-in-males`. Accessed: 2025-06-03. 2025.

[81] TeachMeSurgery Authors. *Lower urinary tract symptoms (LUTS)*. `https://teachmesurgery.com/urology/presentations/lower-urinary-tract-symptoms/`. Accessed 2024-04-14. 2022.

[82] International Continence Society. *International Continence Society (ICS)*. `https://www.ics.org`. Accessed: 2025-06-03. n.d.

[83] “Male Lower Urinary Tract Symptoms in Primary Care Setting”. In: *Bush Beats* 3 (2023). URL: `https://wbhf.walterbushnell.com/publications/bush-beats/item/73-male-lower-urinary-tract-symptoms-in-primary-care-setting`.

[84] C. Chapple et al. “The Impact of Nocturia in Patients with LUTS/BPH: Need for New Recommendations”. In: *European Urology* 5 (2006), pp. 12–18. DOI: `doi:10.1016/j.eursup.2005.10.002`. URL: `https://www.eu-openscience.europeanurology.com/article/S1569-9056(05)00114-4/pdf`.

[85] Cleveland Clinic. *Urinary Urgency: Causes, Diagnosis & Treatment*. 2024. URL: `https://my.clevelandclinic.org/health/symptoms/urinary-urgency`.

[86] National Health Service. *Urinary Incontinence*. 2023. URL: `https://www.nhs.uk/conditions/urinary-incontinence/`.

[87] R. Heeringa et al. “Normal bladder sensations in healthy volunteers: a focus group investigation”. In: *Neurourology and Urodynamics* 30.7 (2011), pp. 1350–1355. DOI: `10.1002/nau.21052`. URL: `https://doi.org/10.1002/nau.21052`.

[88] C. D. D’Ancona et al. “An International Continence Society (ICS) Report on the Terminology for Adult Male Lower Urinary Tract and Pelvic Floor Symptoms and Dysfunction”. In: *Neurourology and Urodynamics* 38.2 (2019), pp. 433–477. DOI: `10.1002/nau.23897`. URL: `https://doi.org/10.1002/nau.23897`.

[89] Geetha Maddukuri. *Urinary Hesitating, Straining, and Dribbling*. 2024. URL: `https://www.msdmanuals.com/home/kidney-and-urinary-tract-disorders/symptoms-of-kidney-and-urinary-tract-disorders/urinary-hesitating-straining-and-dribbling`.

[90] Jae Heon Kim et al. “Terminal dribbling in male patients with lower urinary tract symptoms: relationship with International Prostate Symptom Score and with intravesical prostatic protrusion”. In: *BMC Urology* 15 (2015), p. 89. DOI: `10.1186/s12894-015-0082-x`. URL: `https://doi.org/10.1186/s12894-015-0082-x`.

[91] Reem Aldamanhori. “Lower urinary tract symptoms and feeling of incomplete emptying in Saudi Arabian men and its correlation with postvoid residual urine”. In: *Urology Annals* 11.2 (2019), pp. 132–134. DOI: `10.4103/UA.UA_133_18`. URL: `https://www.ncbi.nlm.nih.gov/pmc/articles/PMC6476222/`.

[92] Urology Austin. *Lower Urinary Tract Symptoms*. URL: `https://urologyaustin.com/general-urology/lower-urinary-tract-symptoms/`.

[93] Jr. White J. Maxwell and III O’Brien David P. “Incontinence and Stream Abnormalities”. In: *Clinical Methods: The History, Physical, and Laboratory Examinations*. Ed. by H. Kenneth Walker, W. Dallas Hall, and J. Willis Hurst. 3rd. Boston: Butterworths, 1990. Chap. 185. URL: `https://www.ncbi.nlm.nih.gov/books/NBK295/`.

[94] International Continence Society. *Spraying/Splitting of Urinary Stream - ICS Glossary*. Accessed: 2023-03-16. URL: `https://www.ics.org/glossary/symptom/sprayingsplittingofurinarystream`.

[95] Dae Yul Yang and Won Ki Lee. “A current perspective on post-micturition dribble in males”. In: *Investigative and Clinical Urology* 60.3 (2019), pp. 142–147. DOI: `10.4111/icu.2019.60.3.142`. URL: `https://doi.org/10.4111/icu.2019.60.3.142`.

[96] Varant Kupelian et al. “Prevalence of lower urinary tract symptoms and effect on quality of life in a racially and ethnically diverse random sample: The Boston Area Community Health (BACH) Survey”. In: *Archives of Internal Medicine* 166.21 (2006), pp. 2381–2387. DOI: `10.1001/archinte.166.21.2381`. URL: `https://doi.org/10.1001/archinte.166.21.2381`.

[97] Paul Abrams et al. “International Continence Society ”Benign Prostatic Hyperplasia” Study: Background, aims, and methodology”. In: *Neurourology and Urodynamics* 16.2 (1997), pp. 79–91. DOI: `10.1002/(SICI)1520-6777(1997)16:2<79::AID-NAU1>3.0.CO;2-Z`.

[98] European Association of Urology. “New Concepts in Epidemiology of Lower Urinary Tract Symptoms in Men”. In: *European Urology Supplements* 9.6 (2010). Accessed 2024-04-14, pp. 477–481. DOI: `10.1016/j.eursup.2010.04.004`. URL: `https://www.eu-openscience.europeanurology.com/article/S1569-9056(10)00056-4/pdf`.

[99] Diane E. Irwin et al. “Population-based survey of urinary incontinence, overactive bladder, and other lower urinary tract symptoms in five countries: Results of the EPIC study”. In: *European Urology* 50.6 (2006), pp. 1306–1315. DOI: `10.1016/j.eururo.2006.09.019`. URL: `https://doi.org/10.1016/j.eururo.2006.09.019`.

[100] Karin S. Coyne et al. “The prevalence of lower urinary tract symptoms (LUTS) in the USA, the UK and Sweden: Results from the Epidemiology of LUTS (EpiLUTS) study”. In: *BJU International* 104.3 (2009), pp. 352–360. DOI: `10.1111/j.1464-410X.2009.08427.x`. URL: `https://doi.org/10.1111/j.1464-410X.2009.08427.x`.

[101] Alysa Hullett. *Lower urinary tract symptoms (LUTS) and what causes them*. `https://www.healthline.com/health/lower-urinary-tract-symptoms`. Medically reviewed by Megan Soliman, MD. 2023. (Visited on 04/16/2025).

[102] Cleveland Clinic. *Lower Urinary Tract Symptoms (LUTS)*. Accessed: 2025-04-16. 2022. URL: `https://my.clevelandclinic.org/health/symptoms/24248-lower-urinary-tract-symptoms`.

[103] S. Srakocic. *What is Underactive Bladder?* `https://www.healthline.com/health/what-is-underactive-bladder`. Accessed 2024-04-16. 2023.

[104] Mayo Clinic Staff. *Overactive bladder*. `https://www.mayoclinic.org/diseases-conditions/overactive-bladder/symptoms-causes/syc-20355715`. Accessed 2024-04-16. 2025.

[105] Yale Medicine. *Intrinsic sphincter deficiency*. `https://www.yalemedicine.org/clinical-keywords/intrinsic-sphincter-deficiency`. Accessed: 2025-06-06. n.d.

[106] Claire C. Yang. “Bladder Management in Multiple Sclerosis”. In: *Physical Medicine and Rehabilitation Clinics of North America* 24.4 (2013). Multiple Sclerosis Rehabilitation, pp. 673–686. ISSN: 1047-9651. DOI: `https://doi.org/10.1016/j.pmr.2013.06.004`. URL: `https://www.sciencedirect.com/science/article/pii/S1047965113000314`.

[107] Mayo Clinic Staff. *Benign prostatic hyperplasia (BPH): Symptoms and causes*. `https://www.mayoclinic.org/diseases-conditions/benign-prostatic-hyperplasia/symptoms-causes/syc-20370087`. Accessed: 2025-06-06. Sept. 2024.

[108] B. M. Abdeen, S. W. Leslie, and A. M. Badreldin. *Urethral Strictures*. Accessed: 2025-05-29. Treasure Island, FL: StatPearls Publishing, Oct. 2024. URL: `https://www.ncbi.nlm.nih.gov/books/NBK564297/`.

[109] H. L. Nicholson et al. “Management of bladder neck stenosis and urethral stricture and stenosis following treatment for prostate cancer”. In: *Translational Andrology and Urology* 6.Suppl 2 (2017), S92–S102. DOI: `10.21037/tau.2017.04.33`. URL: `https://doi.org/10.21037/tau.2017.04.33`.

[110] M. K. Moslemi, M. Abedinzadeh, and A. Nazari. “Obstructive uropathy due to prolapsed lower ureters and bladder in patients with severe procidentia: A report of two cases”. In: *International Journal of Surgery Case Reports* 4.3 (2013), pp. 348–350. DOI: `10.1016/j.ijscr.2012.11.026`. URL: `https://doi.org/10.1016/j.ijscr.2012.11.026`.

[111] Cincinnati Children’s Hospital. *Meatal stenosis*. `https://www.cincinnatichildrens.org/health/m/meatal-stenosis`. Accessed: 2025-06-06. n.d.

[112] Urology Care Foundation. *Bladder diverticulum*. `https://www.urologyhealth.org/urology-a-z/b/bladder-diverticulum`. Accessed: 2025-06-06. 2024.

[113] Chukwuma O. Kalu and Ala Abudayyeh. “Obstructive Uropathy in Critically Ill Cancer Patients”. In: *Oncologic Critical Care*. Ed. by Joseph L. Nates and Kristen J. Price. Cham: Springer International Publishing, 2020, pp. 969–975. ISBN: 978-3-319-74588-6. DOI: `10.1007/978-3-319-74588-6_78`. URL: `https://doi.org/10.1007/978-3-319-74588-6_78`.

[114] Rosie Chess-Williams and David J. Sellers. “Pathophysiological mechanisms involved in overactive bladder/detrusor overactivity”. In: *Current Bladder Dysfunction Reports* 18 (2023), pp. 79–88. DOI: `10.1007/s11884-023-00690-x`. URL: `https://doi.org/10.1007/s11884-023-00690-x`.

[115] Narayana Health. *Lower Urinary Tract - Causes, Symptoms and Treatment Options*. `https://www.narayanahealth.org/blog/what-is-lower-urinary-tract-symptoms`. Accessed 2024-04-16. 2024.

[116] Georgios Gakis et al. “Functional Detrusor Myoplasty for Bladder Acontractility: Long-Term Results”. In: *The Journal of urology* 185 (Feb. 2011), pp. 593–599. DOI: `10.1016/j.juro.2010.09.112`.

[117] Yi-Huei Chang et al. “Review of underactive bladder”. In: *Journal of the Formosan Medical Association* 117.3 (2018), pp. 178–184. ISSN: 0929-6646. DOI: `https://doi.org/10.1016/j.jfma.2017.09.006`. URL: `https://www.sciencedirect.com/science/article/pii/S0929664617303674`.

[118] T. Lazaros, T. Ioannis, S. Vasileios, et al. “The effect of pelvic floor muscle training in women with functional bladder outlet obstruction”. In: *Archives of Gynecology and Obstetrics* 307 (2023), pp. 1489–1494. DOI: `10.1007/s00404-023-06930-z`. URL: `https://doi.org/10.1007/s00404-023-06930-z`.

[119] Christopher J. Chermansky and Pamela A. Moalli. “Role of pelvic floor in lower urinary tract function”. In: *Autonomic Neuroscience* 200 (2016). Autonomic nervous control of the urinary tract, pp. 43–48. ISSN: 1566-0702. DOI: `https://doi.org/10.1016/j.autneu.2015.06.003`. URL: `https://www.sciencedirect.com/science/article/pii/S1566070215300059`.

[120] Mayo Clinic Staff. *Stress incontinence*. `https://www.mayoclinic.org/diseases-conditions/stress-incontinence/symptoms-causes/syc-20355727`. Accessed 2024-04-16. 2024.

[121] Better Health Channel. *Pelvic floor*. `https://www.betterhealth.vic.gov.au/health/conditionsandtreatments/pelvic-floor`. Accessed: 2025-06-03. Oct. 2021.

[122] Sanjay Sinha. “Dysfunctional voiding: A review of the terminology, presentation, evaluation and management in children and adults”. In: *Indian Journal of Urology: IJU, Journal of the Urological Society of India* 27.4 (2011), pp. 437–447. DOI: `10.4103/0970-1591.91429`. URL: `https://doi.org/10.4103/0970-1591.91429`.

[123] Mayo Clinic Staff. *Urinary tract infection (UTI)*. `https://www.mayoclinic.org/diseases-conditions/urinary-tract-infection/symptoms-causes/syc-20353447`. Accessed 2024-04-16. 2022.

[124] Mayo Clinic Staff. *Urethral stricture*. `https://www.mayoclinic.org/diseases-conditions/urethral-stricture/symptoms-causes/syc-20362330`. Accessed 2024-04-16.

[125] Y. Lim, S. W. Leslie, and S. O’Rourke. *Interstitial Cystitis/Bladder Pain Syndrome*. Accessed: 2025-05-29. Treasure Island, FL: StatPearls Publishing, Oct. 2024. URL: `https://www.ncbi.nlm.nih.gov/books/NBK570588/`.

[126] Victor Rogério Garcia Batista et al. “High-Intensity Interval Training Minimizes the Deleterious Effects of Arterial Hypertension on the Urinary Bladder of Spontaneously Hypertensive Rats”. In: *Oxidative Medicine and Cellular Longevity* 2023.1 (2023), p. 9979397. DOI: `https://doi.org/10.1155/2023/9979397`. eprint: `https://onlinelibrary.wiley.com/doi/pdf/10.1155/2023/9979397`. URL: `https://onlinelibrary.wiley.com/doi/abs/10.1155/2023/9979397`.

[127] Urology Care Foundation. *Diabetes and its impact on your urinary and sexual health*. `https://www.urologyhealth.org/healthy-living/urologyhealth-extra/magazine-archives/spring-2017/diabetes-and-its-impact-on-your-urinary-and-sexual-health`. Accessed 2024-04-16. 2017.

[128] Badlani, Gopal. “Call it by any name: Bladder that does not work”. In: *Urology Times Journal* 50.09 (Aug. 2022). Accessed 2024-04-16.

[129] Children’s Hospital of Orange County. *Dysfunctional bladder*. `https://choc.org/conditions/urology/dysfunctional-bladder/`. Accessed: 2025-06-15. n.d.

[130] Mayo Clinic Staff. *Urinary tract infection (UTI): Symptoms and causes*. `https://www.mayoclinic.org/diseases-conditions/urinary-tract-infection/symptoms-causes/syc-20353447`. Accessed: 2025-06-05. Sept. 2022.

[131] Mikolaj Przydacz et al. "Association between lower urinary tract symptoms and sleep quality of patients with depression". In: *Medicina* 57.4 (2021), p. 394. DOI: `10.3390/medicina57040394`. URL: `https://doi.org/10.3390/medicina57040394`.

[132] Sarah Sutcliffe et al. "The spectrum of bladder health: The relationship between lower urinary tract symptoms and interference with activities". In: *Journal of Women's Health* 28.6 (2019), pp. 827–841. DOI: `10.1089/jwh.2018.7364`. URL: `https://doi.org/10.1089/jwh.2018.7364`.

[133] Ali Abedi et al. "Health care economic burden of treatment and rehabilitation for neurogenic lower urinary tract dysfunction: A systematic review". In: *Journal of Urology* 208.4 (2022), pp. 773–783. DOI: `10.1097/JU.0000000000002862`. URL: `https://doi.org/10.1097/JU.0000000000002862`.

[134] Mayo Clinic Staff. *Urinalysis*. `https://www.mayoclinic.org/tests-procedures/urinalysis/about/pac-20384907`. Accessed: 2025-06-06. Oct. 2023.

[135] American Kidney Fund. *Serum creatinine test for kidney disease*. `https://www.kidneyfund.org/all-about-kidneys/tests/serum-creatinine-test`. Accessed: 2025-06-15. 2024.

[136] Prasanna Sooriakumaran, Christian Brown, and Mark Emberton. "Frequency volume charts should be used in men with lower urinary tract symptoms". In: *International Journal of Surgery* 3.2 (2005), pp. 147–150. ISSN: 1743-9191. DOI: `https://doi.org/10.1016/j.ijsu.2005.03.015`. URL: `https://www.sciencedirect.com/science/article/pii/S1743919105000166`.

[137] The Urology Foundation. *Bladder diary*. `https://www.theurologyfoundation.org/app/uploads/2024/01/Bladder-diary.pdf`. Accessed: 2025-06-06. 2024.

[138] Instituto da Próstata. *Uroflowmetry*. `https://www.institutodaprostata.com/en/analyses-and-tests/uroflowmetry`. Accessed: 2025-06-13. n.d.

[139] Christopher E. Kelly. "Evaluation of voiding dysfunction and measurement of bladder volume". In: *Reviews in Urology* 6.Suppl 1 (2004), S32–S37.

[140] Lara S. MacLachlan and Eric S. Rovner. "Good Urodynamic Practice: Keys to Performing A Quality UDS Study". In: *Urologic Clinics of North America* 41.3 (2014). Urodynamics, pp. 363–373. ISSN: 0094-0143. DOI: `https://doi.org/10.1016/j.ucl.2014.04.005`. URL: `https://www.sciencedirect.com/science/article/pii/S0094014314000378`.

[141] Lola Bladt et al. "First-year Experience Of Managing Urology Patients With Home Uroflowmetry: a Descriptive Retrospective Analysis (Preprint)". In: *JMIR Formative Research* 7 (July 2023). DOI: `10.2196/51019`.

[142] Joseph E. Yared and E. Ann Gormley. "The Role of Urodynamics in Elderly Patients". In: *Clinics in Geriatric Medicine* 31.4 (2015). Geriatric Urology, pp. 567–579. ISSN: 0749-0690. DOI: `https://doi.org/10.1016/j.cger.2015.06.003`. URL: `https://www.sciencedirect.com/science/article/pii/S0749069015000531`.

[143] Abdominal Key. *Pressure/flow cystometry*. `https://abdominalkey.com/pressureflow-cystometry/`. Accessed: 2025-06-13. 2016.

[144] S. Tekgul et al. "Diagnosis and Management of Urinary Incontinence in Childhood". In: *International Consultation on Incontinence*. 4th. Accessed: 2025-05-23. International Continence Society, n.d. Pp. 702–749. URL: `https://www.ics.org/publications/ici_4/files-book/comite-9.pdf`.

[145] Fawzy Farag and John Heesakkers. "Non-Invasive Techniques in the Diagnosis of Bladder Storage Disorders". In: *Neurourology and urodynamics* 30 (Nov. 2011), pp. 1422–8. DOI: `10.1002/nau.21155`.

[146] Rachaneni, S and McCooty, S and Middleton, LJ. *Bladder ultrasonography for diagnosing detrusor overactivity: test accuracy study and economic evaluation.* Accessed 30 June 2025. NIHR Journals Library, 2016.

[147] Giancarlo Vignoli. "How to Perform Conventional Urodynamic Investigation: The "Good Urodynamic Practice"". In: *Urodynamics for Urogynecologists: A Pocket Guide for Clinical Practice*. Cham: Springer International Publishing, 2018, pp. 41–60. ISBN: 978-3-319-74005-8. DOI: `10.1007/978-3-319-74005-8_4`. URL: `https://doi.org/10.1007/978-3-319-74005-8_4`.

[148] P. M. Lotze. "A comparison of external transducers and microtransducers in urodynamic studies of female patients". In: *Current Urology Reports* 6 (2005), pp. 326–334. DOI: `10.1007/s11934-005-0048-8`.

[149] Santron Meditronic. *Cystometry Urodynamic Machine*. `https://www.indiamart.com/proddetail/cystometry-urodynamic-machine-2855461849012.html`. Accessed: 2025-07-07. 2025.

[150] Potent Medical. *High-Precision Cystometry Test Apparatus Urodynamics NHS for Hospital*. `https://potentmedical.en.made-in-china.com/product/ZJzUYRpKqEVl/China-High-Precision-Cystometry-Test-Apparatus-Urodynamics-NHS-for-Hospital.html`. Accessed: 2025-07-07. 2025.

[151] Juan Pablo Valdevenito and Annerleim Walton-Diaz. "Diagnosis of voiding dysfunction by pressure-flow study in women". In: *World Journal of Clinical Urology* 5.1 (2016), pp. 29–36. DOI: `10.5410/wjcu.v5.i1.29`. URL: `https://www.wjgnet.com/2219-2816/full/v5/i1/29.htm`.

[152] Jian Guo Wen. "Cystometry, Pressure Flow Study and Urethral Pressure Measurement". In: *Clinical Urodynamics in Childhood and Adolescence*. Ed. by Giovanni Mosiello et al. Cham: Springer International Publishing, 2018, pp. 73–93. ISBN: 978-3-319-42193-3. DOI: `10.1007/978-3-319-42193-3_8`. URL: `https://doi.org/10.1007/978-3-319-42193-3_8`.

[153] National Institute of Diabetes and Digestive and Kidney Diseases. *Urodynamic testing*. `https://www.niddk.nih.gov/health-information/diagnostic-tests/urodynamic-testing`. Accessed: 2025-06-15. 2021.

[154] Abdominal Key. *Bladder emptying: Coordination of bladder and sphincters*. `https://abdominalkey.com/bladder-emptying-coordination-of-bladder-and-sphincters/`. Accessed: 2025-06-13. 2017.

[155] Abdominal Key. *Urodynamic studies: Types and indications*. `https://abdominalkey.com/urodynamic-studies-types-and-indications/`. Accessed: 2025-06-15. 2017.

[156] Matthew R. Macey and Michael C. Raynor. "Medical and surgical treatment modalities for lower urinary tract symptoms in the male patient secondary to benign prostatic hyperplasia: A review". In: *Seminars in Interventional Radiology* 33.3 (2016), pp. 217–223. DOI: `10.1055/s-0036-1586142`. URL: `https://doi.org/10.1055/s-0036-1586142`.

[157] "Lower urinary tract symptoms". In: *Australian Journal for General Practitioners* 40.10 (Oct. 2011), pp. 758–767. URL: `https://www.racgp.org.au/afp/2011/october/lower-urinary-tract-symptoms`.

[158] Bouhadana, David and Sadri, Iman. *An approach to the management of lower urinary tract symptoms secondary to benign prostatic hyperplasia*. `https://mjm.mcgill.ca/article/view/330/675`. Accessed: 2025-06-24. 2021.

[159] Cleveland Clinic. *Artificial Urinary Sphincter*. `https://my.clevelandclinic.org/health/treatments/artificial-urinary-sphincter`. Last reviewed on July 3, 2024, Accessed June 24, 2025. 2024.

[160] Your Pelvic Floor. *Botulinum Toxin A (BOTA) for Overactive Bladder and Neurogenic Detrusor Overactivity*. `https://www.yourpelvicfloor.org/conditions/botulinum-toxin-a-bota-for-overactive-bladder-and-neurogenic-detrusor-overactivity/`. Accessed June 24, 2025. n.d.

[161] *Overview of artifact detection*. Accessed June 27, 2025. MNE-Python. 2025. URL: `https://mne.tools/stable/auto_tutorials/preprocessing/10_preprocessing_overview.html`.

[162] Reeba Oliver and Ranee Thakar. "Urodynamic artefacts". In: *Urodynamics Illustrated*. Ed. by Ranee Thakar, Philip Toosz-Hobson, and LuciaEditors Dolan. Cambridge University Press, 2011, pp. 81–90.

[163] Udit Satija, Barathram Ramkumar, and M. Sabarimalai Manikandan. “A new automated signal quality-aware ECG beat classification method for unsupervised ECG diagnosis environments”. In: *IEEE Sensors Journal* 19 (Oct. 2018). DOI: `10.1109/JSEN.2018.2877055`.

[164] Dongyeol Seok et al. “Motion Artifact Removal Techniques for Wearable EEG and PPG Sensor Systems”. In: *Frontiers in Electronics* Volume 2 - 2021 (2021). ISSN: 2673-5857. DOI: `10.3389/felec.2021.685513`. URL: `https://www.frontiersin.org/journals/electronics/articles/10.3389/felec.2021.685513`.

[165] A. Prabakaran and E. Rufus. “Review on the wearable health-care monitoring system with robust motion artifacts reduction techniques”. In: *Sensor Review* 42.1 (2022), pp. 19–38. DOI: `10.1108/SR-05-2021-0150`. URL: `https://doi-org.tudelft.idm.oclc.org/10.1108/SR-05-2021-0150`.

[166] Ingelin Clausen, Lars Geir W. Tvedt, and Thomas Glott. “Measurement of Urinary Bladder Pressure: A Comparison of Methods”. In: *Sensors* 18.7 (2018). ISSN: 1424-8220. DOI: `10.3390/s18072128`. URL: `https://www.mdpi.com/1424-8220/18/7/2128`.

[167] Dr. Peter Steinberg. *Urodynamics Artifacts: Identification and Correction*. Retrieved June 27, 2025. 2018. URL: `https://info.bhnco.com/blog/urodynamics-artifacts-identification-and-correction`.

[168] Rien J.M. Nijman. “CHAPTER 9 - URODYNAMIC STUDIES OF THE LOWER URINARY TRACT”. In: *Pediatric Urology (Second Edition)*. Ed. by John P. Gearhart, Richard C. Rink, and Pierre D.E. Mouriquand. Second Edition. Philadelphia: W.B. Saunders, 2010, pp. 127–140. ISBN: 978-1-4160-3204-5. DOI: `https://doi.org/10.1016/B978-1-4160-3204-5.00009-8`. URL: `https://www.sciencedirect.com/science/article/pii/B9781416032045000098`.

[169] A. Gammie, S. Hogan, and P. Abrams. “Urodynamic features and artefacts”. In: *Neurourology and Urodynamics* 31.7 (2012), pp. 1104–1117. DOI: `10.1002/nau.22209`. URL: `https://onlinelibrary.wiley.com/doi/10.1002/nau.22209`.

[170] Z. Abdool. *Urodynamics - Basic concepts*. O&G Forum, 22, 32–34. Accessed: 2025-07-04. 2012. URL: `https://repository.up.ac.za/server/api/core/bitstreams/707b546f-d8b1-421b-816b-be520a5ab841/content`.

[171] A. Sylolypavan et al. “The impact of inconsistent human annotations on AI driven clinical decision making”. In: *NPJ Digital Medicine* 6.1 (2023), p. 26. DOI: `10.1038/s41746-023-00773-3`.

[172] Toufique Ahmed et al. “Can LLMs Replace Manual Annotation of Software Engineering Artifacts?” In: *2025 IEEE/ACM 22nd International Conference on Mining Software Repositories (MSR)*. Apr. 2025, pp. 526–538. DOI: `10.1109/MSR66628.2025.00086`.

[173] S. Salvatore et al. “Reducing artefacts in ambulatory urodynamics”. In: *British Journal of Urology International* 81 (1998), pp. 211–214. DOI: `10.1046/j.1464-410X.1998.00537.x`. URL: `https://onlinelibrary.wiley.com/doi/10.1046/j.1464-410X.1998.00537.x`.

[174] Hashim Hashim. *W17: Basic Urodynamics - An Interactive Workshop*. `https://www.ics.org/Workshops/HandoutFiles/000687.pdf`. Workshop held on 12 September 2017, International Continence Society (ICS). 2017.

[175] R.G. Soumya, N. Naveen, and M.J. Lal. “Application of Adaptive Filter Using Adaptive Line Enhancer Techniques”. In: *2013 Third International Conference on Advances in Computing and Communications*. 2013, pp. 165–168. DOI: `10.1109/ICACC.2013.39`.

[176] Komal Borisagar, Dr Thanki, and Bhavin Sedani. “Fourier Transform, Short-Time Fourier Transform, and Wavelet Transform”. In: Springer Nature Switzerland, Jan. 2019, pp. 63–74. ISBN: 978-3-319-96820-9. DOI: `10.1007/978-3-319-96821-6_4`.

[177] S. Banerjee and G.K. Singh. “A new moving horizon estimation based real-time motion artifact removal from wavelet subbands of ECG signal using particle filter”. In: *Journal of Signal Processing Systems* 95 (2023), pp. 1021–1035. DOI: `10.1007/s11265-023-01887-3`. URL: `https://doi-org.tudelft.idm.oclc.org/10.1007/s11265-023-01887-3`.

[178] Utako Yamamoto et al. “Improving the accuracy of the method for removing motion artifacts from fNIRS data using ICA and an accelerometer”. In: *2014 World Automation Congress (WAC)*. 2014, pp. 131–136. DOI: `10.1109/WAC.2014.6935730`.

[179] Tanja Lampl et al. “Noise cancellation with LMS, NLMS, and RLS filtering algorithms to improve the fault detection of an industrial measurement system”. In: *ResearchGate Preprint* (2023). Preprint, Accessed: 2025-02-17. DOI: `10.21203/rs.3.rs-2639549/v1`.

[180] Zhihan Huang. “A Review of the Challenges of Adaptive Filtering Technology in High-fidelity Audio Signal Processing”. In: *Theoretical and Natural Science* 55 (Nov. 2024), pp. 61–66. DOI: `10.54254/2753-8818/55/20240192`.

[181] Krishna Kumar et al. “Robust and sparsity-aware adaptive filters: A Review”. In: *Signal Processing* 189 (2021), p. 108276. ISSN: 0165-1684. DOI: `https://doi.org/10.1016/j.sigpro.2021.108276`. URL: `https://www.sciencedirect.com/science/article/pii/S0165168421003133`.

[182] University of St Andrews. *Discrete Wavelet Transform (DWT) Tutorial*. `https://www.st-andrews.ac.uk/~wjh/dataview/tutorials/dwt.html`. Accessed August 27, 2025. 2025.

[183] Farhath Zareen et al. “Optimization of activity-driven event detection for long-term ambulatory urodynamics”. In: *Proceedings of the Institution of Mechanical Engineers. Part H, Journal of engineering in medicine* 238 (Aug. 2024), p. 9544119241264304. DOI: `10.1177/09544119241264304`.

[184] Kafiul Islam, Amir Rastegarnia, and Saeid Sanei. “Signal artifacts and techniques for artifacts and noise removal”. In: *Signal Processing Techniques for Computational Health Informatics*. Springer, Oct. 2020. ISBN: 978-3-030-54932-9. DOI: `https://doi.org/10.1007/978-3-030-54932-9_2`.

[185] Brenda Wang et al. “Comparative assessment of machine learning strategies for electrocardiogram denoising”. In: *AI 2023: Advances in Artificial Intelligence*. Ed. by Tongliang Liu et al. Singapore: Springer Nature Singapore, 2024, pp. 495–506. ISBN: 978-981-99-8388-9.

[186] Eoin Brophy et al. “Improved electrode motion artefact denoising in ECG using convolutional neural networks and a custom loss function”. In: *IEEE Access* 10 (2022), pp. 54891–54898. DOI: `10.1109/ACCESS.2022.3176971`.

[187] Amazon Web Services. *What’s the Difference Between Machine Learning and Deep Learning?* `https://aws.amazon.com/compare/the-difference-between-machine-learning-and-deep-learning/`. Accessed August 27, 2025. 2025.

[188] Bardh Rushiti. *Classical Machine Learning — Supervised Learning Edition*. `https://medium.com/swlh/classical-machine-learning-7efc6674fca1`. Accessed August 27, 2025. Oct. 2020.

[189] GeeksforGeeks. *Support Vector Machine Algorithm*. `https://www.geeksforgeeks.org/machine-learning/support-vector-machine-algorithm`. Accessed August 25, 2025. 2025.

[190] Qingxue Zhang, Dian Zhou, and Xuan Zeng. “A novel machine learning-enabled framework for instantaneous heart rate monitoring from motion-artifact-corrupted electrocardiogram signals”. In: *Physiological Measurement* 37.11 (Sept. 2016), p. 1945. DOI: `10.1088/0967-3334/37/11/1945`. URL: `https://dx.doi.org/10.1088/0967-3334/37/11/1945`.

[191] Davide Anguita et al. “A Public Domain Dataset for Human Activity Recognition Using Smartphones”. In: *Proceedings of the European Symposium on Artificial Neural Networks, Computational Intelligence and Machine Learning (ESANN)*. Accessed August 25, 2025. Bruges, Belgium: i6doc.com publ., 2013, pp. 437–442. ISBN: 978-2-87419-081-0. URL: `https://www.esann.org/sites/default/files/proceedings/legacy/es2013-84.pdf`.

[192] Mohamed Abdel-Basset et al. “ST-DeepHAR: Deep Learning Model for Human Activity Recognition in IoHT Applications”. In: *IEEE INTERNET OF THINGS JOURNAL* 8 (2021). Accessed August 26, 2025. URL: `https://ieeexplore-ieee-org.tudelft.idm.oclc.org/stamp/stamp.jsp?tp=&arnumber=9238036&tag=1`.

[193] Shoujiang Xu et al. “A Cascade Ensemble Learning Model for Human Activity Recognition with Smartphones”. In: *Sensors* 19.10 (2019). ISSN: 1424-8220. DOI: `10.3390/s19102307`. URL: `https://www.mdpi.com/1424-8220/19/10/2307`.

[194] Fahad Mehfooz. *Human Activity Recognition With Neural Networks*. `https://www.kaggle.com/code/fahadmehfoooz/human-activity-recognition-with-neural-networks`. Accessed August 25, 2025. 2021.

[195] IBM. *What are Convolutional Neural Networks?* `https://www.ibm.com/think/topics/convolutional-neural-networks`. Accessed August 25, 2025.

[196] Lei Hu et al. "A lightweight U-Net model for denoising and noise localization of ECG signals". In: *Biomedical Signal Processing and Control* 88 (Feb. 2024), p. 105504. DOI: `10.1016/j.bspc.2023.105504`.

[197] Vignesh Ravichandran et al. "Deep network for capacitive ECG denoising". In: *IEEE International Symposium on Medical Measurements and Applications* (Mar. 2019). DOI: `10.48550/arXiv.1903.12536`.

[198] Natasa Reljin et al. "Using the redundant convolutional encoder-decoder to denoise QRS complexes in ECG signals recorded with an armband wearable device". In: *Sensors* 20 (Aug. 2020), p. 4611. DOI: `10.3390/s20164611`.

[199] Xiangmao Chang et al. "DeepHeart: a deep learning approach for accurate heart rate estimation from PPG signals". In: *ACM Transactions on Sensor Networks* 17 (Jan. 2021), pp. 1–18. DOI: `10.1145/3441626`.

[200] Sakib Mahmud and Md Shafayet Hossain. "MLMRS-Net: Electroencephalography (EEG) motion artifacts removal using a multi-layer multi-resolution spatially pooled 1D signal reconstruction network". In: *Neural Computing and Applications* 22 (Dec. 2022), p. 6. DOI: `10.1007/s00521-022-08111-6`.

[201] Mohammed G. Ragab, Said Jadid Abdulkadir, and Norshakirah Aziz. "Random Search One Dimensional CNN for Human Activity Recognition". In: *2020 International Conference on Computational Intelligence (ICCI)*. 2020, pp. 86–91. DOI: `10.1109/ICCI51257.2020.9247810`.

[202] Zanobya N. Khan and Jamil Ahmad. "Attention induced multi-head convolutional neural network for human activity recognition". In: *Applied Soft Computing* 110 (2021), p. 107671. ISSN: 1568-4946. DOI: `https://doi.org/10.1016/j.asoc.2021.107671`. URL: `https://www.sciencedirect.com/science/article/pii/S1568494621005925`.

[203] Ayokunle Ige and Mohd Halim Mohd Noor. "A lightweight deep learning with feature weighting for activity recognition". In: *Computational Intelligence* 39 (Dec. 2022). DOI: `10.1111/coin.12565`.

[204] Youngsun Kong et al. "Automatic motion artifact detection in electrodermal activity signals using 1D U-net architecture". In: *Computers in Biology and Medicine* 182 (2024), p. 109139. ISSN: 0010-4825. DOI: `https://doi.org/10.1016/j.compbiomed.2024.109139`. URL: `https://www.sciencedirect.com/science/article/pii/S0010482524012241`.

[205] J. Suto et al. "Comparison of offline and real-time human activity recognition results using machine learning techniques". In: *Neural Computing and Applications* 32 (2020). Accessed August 26, 2025, pp. 15673–15686. DOI: `10.1007/s00521-018-3437-x`. URL: `https://doi-org.tudelft.idm.oclc.org/10.1007/s00521-018-3437-x`.

[206] Analytics Vidhya. *What is the Convolutional Neural Network Architecture?* `https://www.analyticsvidhya.com/blog/2020/10/what-is-the-convolutional-neural-network-architecture`. Accessed August 25, 2025. May 2025.

[207] GeeksforGeeks. *What is LSTM - Long Short Term Memory?* `https://www.geeksforgeeks.org/deep-learning/deep-learning-introduction-to-long-short-term-memory`. Accessed August 25, 2025. 2025.

[208] Vinit Kumar and Priya Ranjan Muduli. "Attentive bi-LSTM-based method for noise suppression in ambulatory ECG measurements". In: *IEEE Transactions on Instrumentation and Measurement* 72 (2023), pp. 1–9. DOI: `10.1109/TIM.2023.3330182`.

[209] Yu-Syuan Jhang et al. "Integration design of portable ECG signal acquisition with deep-learning based electrode motion artifact removal on an embedded system". In: *IEEE Access* 10 (Jan. 2022), pp. 1–1. DOI: `10.1109/ACCESS.2022.3178847`.

[210] Fars Samann and Thomas Schanze. "RunDAE model: running denoising autoencoder models for denoising ECG signals". In: *Computers in Biology and Medicine* 166 (2023), p. 107553. ISSN: 0010-4825. DOI: `https://doi.org/10.1016/j.compbiomed.2023.107553`. URL: `https://www.sciencedirect.com/science/article/pii/S0010482523010181`.

[211] Y.-S. Jhang et al. “Channel-wise average pooling and 1D pixel-shuffle denoising autoencoder for electrode motion artifact removal in ECG”. In: *Applied Sciences* 12.14 (2022), p. 6957. DOI: `10.3390/app12146957`. URL: `https://doi.org/10.3390/app12146957`.

[212] Meng Chen et al. “Multiscale convolution and attention based denoising autoencoder for motion artifact removal in ECG signals”. In: *Proceedings of the 2024 7th International Conference on Image and Graphics Processing*. ICIGP ’24. Beijing, China: Association for Computing Machinery, 2024, pp. 442–448. ISBN: 9798400716720. DOI: `10.1145/3647649.3647718`. URL: `https://doi-org.tudelft.idm.oclc.org/10.1145/3647649.3647718`.

[213] Haicai Lin, Ruixia Liu, and Zhaoyang Liu. “ECG signal denoising method based on disentangled autoencoder”. In: *Electronics* 12.7 (2023). ISSN: 2079-9292. DOI: `10.3390/electronics12071606`. URL: `https://www.mdpi.com/2079-9292/12/7/1606`.

[214] Rohan Banerjee, Ayan Mukherjee, and Avik Ghose. “Noise cleaning of ECG on edge device using convolutional sparse contractive autoencoder”. In: *2022 IEEE International Conference on Pervasive Computing and Communications Workshops and other Affiliated Events (PerCom Workshops)*. 2022, pp. 491–496. DOI: `10.1109/PerComWorkshops53856.2022.9767313`.

[215] Ayokunle Olalekan Ige and Mohd Halim Mohd Noor. “Unsupervised Feature Learning in Activity Recognition using Convolutional Denoising Autoencoders with Squeeze and Excitation Networks”. In: *2022 5th International Conference on Information and Communications Technology (ICOIACT)*. 2022, pp. 435–440. DOI: `10.1109/ICOIACT55506.2022.9972095`.

[216] Honggui Li and Maria Trocan. “Deep learning of smartphone sensor data for personal health assistance”. In: *Microelectronics Journal* 88 (2019), pp. 164–172. ISSN: 1879-2391. DOI: `https://doi.org/10.1016/j.mejo.2018.01.015`. URL: `https://www.sciencedirect.com/science/article/pii/S0026269217302525`.

[217] GeeksforGeeks. *Generative Adversarial Network (GAN)*. `https://www.geeksforgeeks.org/deep-learning/generative-adversarial-network-gan`. Accessed August 26, 2025. 2019.

[218] Sakib Mahmud et al. “Restoration of motion-corrupted EEG signals using attention-guided operational CycleGAN”. In: *Engineering Applications of Artificial Intelligence* 128 (2024), p. 107514. ISSN: 0952-1976. DOI: `https://doi.org/10.1016/j.engappai.2023.107514`. URL: `https://www.sciencedirect.com/science/article/pii/S0952197623016986`.

[219] Fayez Alharbi, Lahcen Ouarbya, and Jamie A Ward. “Synthetic Sensor Data for Human Activity Recognition”. In: *2020 International Joint Conference on Neural Networks (IJCNN)*. 2020, pp. 1–9. DOI: `10.1109/IJCNN48605.2020.9206624`.

[220] Ayokunle Olalekan Ige and Mohd Halim Mohd Noor. *WSense: A Robust Feature Learning Module for Lightweight Human Activity Recognition*. `https://arxiv.org/abs/2303.17845`. Accessed August 25, 2025.

[221] Mohamed Abdel-Basset et al. “ST-DeepHAR: Deep Learning Model for Human Activity Recognition in IoHT Applications”. In: *IEEE Internet of Things Journal* 8.6 (2021), pp. 4969–4979. DOI: `10.1109/JIOT.2020.3033430`.

[222] Debarshi Bhattacharya et al. “Ensem-HAR: An Ensemble Deep Learning Model for Smartphone Sensor-Based Human Activity Recognition for Measurement of Elderly Health Monitoring”. In: *Biosensors* 12.6 (2023). Accessed August 25, 2025, p. 393. URL: `https://www.mdpi.com/2079-6374/12/6/393`.

[223] Yee Jia Luwe, Chin Poo Lee, and Kian Ming Lim. “Wearable Sensor-Based Human Activity Recognition with Hybrid Deep Learning Model”. In: *Informatics* 9.3 (2022). ISSN: 2227-9709. DOI: `10.3390/informatics9030056`. URL: `https://www.mdpi.com/2227-9709/9/3/56`.

[224] Saroj Pandey et al. “Automated epilepsy seizure detection from EEG signal based on hybrid CNN and LSTM model”. In: *Signal, Image and Video Processing* 17 (Aug. 2022), pp. 1–10. DOI: `10.1007/s11760-022-02318-9`.

[225] Shalini Stalin et al. “A machine learning-based big EEG data artifact detection and wavelet-based removal: an empirical approach”. In: *Mathematical Problems in Engineering* 2021 (Oct. 2021), pp. 1–11. DOI: `10.1155/2021/2942808`.

[226] Lili Zhu, P. Spachos, and Konstantinos Plataniotis. “A fusion of wavelet-based and unsupervised machine learning method for artifacts removal in electrodermal activity signal”. In: *2022 56th Asilomar Conference on Signals, Systems, and Computers*. Oct. 2022, pp. 455–459. DOI: `10.1109/IEEECONF56349.2022.10052046`.

[227] Uttaran Bhattacharjee and Monisha Chakraborty. “NARX-wavelet based active model for removing motion artifacts from ECG”. In: *2020 International Conference on Computer, Electrical Communication Engineering (ICCECE)*. 2020, pp. 1–6. DOI: `10.1109/ICCECE48148.2020.9223082`.

[228] Heng Cui et al. “A dual-branch interactive fusion network to remove artifacts from single-channel EEG”. In: *IEEE Transactions on Instrumentation and Measurement* 73 (2024), pp. 1–12. DOI: `10.1109/TIM.2023.3342863`.

[229] Mohammad Feli et al. “End-to-end PPG processing pipeline for wearables: from quality assessment and motion artifacts removal to HR/HRV feature extraction”. In: *2023 IEEE International Conference on Bioinformatics and Biomedicine (BIBM)*. 2023, pp. 1895–1900. DOI: `10.1109/BIBM58861.2023.10385998`.

[230] Mohd Halim Mohd Noor. “Feature learning using convolutional denoising autoencoder for activity recognition”. In: *Neural Computing and Applications* 33 (Sept. 2021), pp. 1–14. DOI: `10.1007/s00521-020-05638-4`.

[231] Cagatay Catal et al. “On the use of ensemble of classifiers for accelerometer-based activity recognition”. In: *Applied Soft Computing* 37 (2015), pp. 1018–1022. ISSN: 1568-4946. DOI: `https://doi.org/10.1016/j.asoc.2015.01.025`. URL: `https://www.sciencedirect.com/science/article/pii/S1568494615000447`.

[232] B. M. Abidine, L. Fergani, B. Fergani, et al. “The joint use of sequence features combination and modified weighted SVM for improving daily activity recognition”. In: *Pattern Analysis and Applications* 21.1 (2018). Accessed August 26, 2025, pp. 119–138. DOI: `10.1007/s10044-016-0570-y`. URL: `https://doi-org.tudelft.idm.oclc.org/10.1007/s10044-016-0570-y`.

[233] Xinxin Huang et al. “Sensor-Based Wearable Systems for Monitoring Human Motion and Posture: A Review”. In: *Sensors* 23.22 (2023). ISSN: 1424-8220. DOI: `10.3390/s23229047`. URL: `https://www.mdpi.com/1424-8220/23/22/9047`.

[234] Philippe C. Dixon et al. “Automatic cough detection via a multi-sensor smart garment using machine learning”. In: *Computers in Biology and Medicine* 191 (2025), p. 110192. ISSN: 0010-4825. DOI: `https://doi.org/10.1016/j.compbiomed.2025.110192`. URL: `https://www.sciencedirect.com/science/article/pii/S0010482525005438`.

[235] Daniel Sanchez-Morillo et al. “Cough Detection Using Acceleration Signals and Deep Learning Techniques”. In: *Electronics* 13.12 (2024). ISSN: 2079-9292. DOI: `10.3390/electronics13122410`. URL: `https://www.mdpi.com/2079-9292/13/12/2410`.

[236] Smith+Nephew, Inc. *LEAF Patient Monitoring System Technical Overview*. Tech. rep. Accessed August 26, 2025. Smith+Nephew, Inc., 2020. URL: `https://www.sn-leaf.com/sites/default/files/2-LFME6-25257-0520%20LEAF%20Technical%20Overview%20White%20Paper_FINAL%20APPROVED.pdf`.

[237] S. Shajari et al. “The Emergence of AI-Based Wearable Sensors for Digital Health Technology: A Review”. In: *Sensors (Basel)* 23.23 (Nov. 2023). Accessed August 27, 2025, p. 9498. DOI: `10.3390/s23239498`.

[238] R. T. Al Mousa, N. Al Dossary, and H. Hashim. “The role of urodynamics in females with lower urinary tract symptoms”. In: *Arab Journal of Urology* 17.1 (2019), pp. 2–9. DOI: `10.1080/2090598X.2019.1589931`. URL: `https://doi.org/10.1080/2090598X.2019.1589931`.

[239] Karram, Mickey and Blaivas, Jerry. *Urodynamics: Cystometry and Urethral Function Tests*. `https://plasticsurgerykey.com/urodynamics-cystometry-and-urethral-function-tests-2/`. Accessed: 2025-07-08. 2016.

[240] C. A. D’Ancona, J. Bassani, and J. C. Almeida. “Noninvasive urodynamic evaluation”. In: *International Neurourology Journal* 16.3 (2012), pp. 116–121. DOI: `10.5213/inj.2012.16.3.116`. URL: `https://doi.org/10.5213/inj.2012.16.3.116`.

[241] Ellis, Danielle. *New technology for catheter-free telemetric ambulatory bladder pressure monitoring in humans*. Accessed: 2025-07-09. 2023. URL: `https://www.news-medical.net/news/20230609/New-technology-for-catheter-free-telemetric-ambulatory-bladder-pressure-monitoring-in-humans.aspx`.

[242] Cleveland Clinic. *Novel Urodynamic System Receives FDA Clearance*. Accessed: 2025-07-09. 2025. URL: `https://consultqd.clevelandclinic.org/novel-urodynamic-system-receives-fda-clearance`.

[243] Bright Uro. *Glean Urodynamics System: The New Standard for Urodynamic Testing*. `https://www.gleanuds.com`. Accessed: 2025-07-09. 2025.

[244] Philippe Jourand and Robert Puers. "An Autonomous, Capacitive Sensor Based and Battery Powered Internal Bladder Pressure Monitoring System". In: *Procedia Chemistry* 1.1 (2009). Proceedings of the Eurosensors XXIII conference, pp. 1263–1266. ISSN: 1876-6196. DOI: `https://doi.org/10.1016/j.proche.2009.07.315`. URL: `https://www.sciencedirect.com/science/article/pii/S1876619609003167`.

[245] S. Wille, D. Tenholte, and U. Engelmann. "A system for long-term urodynamic studies without catheters". In: *European Urology* 63.5 (2013), pp. 966–968. DOI: `10.1016/j.eururo.2013.01.029`. URL: `https://doi.org/10.1016/j.eururo.2013.01.029`.

[246] M. Bakula et al. "The Bladder Pill: Developments Toward Bladder Pressure Measurement in Wake Mini-pigs". In: *Procedia Engineering* 168 (2016). Proceedings of the 30th anniversary Eurosensors Conference – Eurosensors 2016, 4-7. Sepember 2016, Budapest, Hungary, pp. 193–196. ISSN: 1877-7058. DOI: `https://doi.org/10.1016/j.proeng.2016.11.215`. URL: `https://www.sciencedirect.com/science/article/pii/S1877705816335251`.

[247] S. J. A. Majerus et al. "Feasibility of Real-Time Conditional Sacral Neuromodulation Using Wireless Bladder Pressure Sensor". In: *IEEE Transactions on Neural Systems and Rehabilitation Engineering* 29 (2021), pp. 2067–2075. DOI: `10.1109/TNSRE.2021.3117518`. URL: `https://doi.org/10.1109/TNSRE.2021.3117518`.

[248] I. McAdams et al. "Low-cost, Implantable Wireless Sensor Platform for Neuromodulation Research". In: *IEEE Biomedical Circuits and Systems Conference (BioCAS)*. 2018. DOI: `10.1109/BIOCAS.2018.8584729`. URL: `https://doi.org/10.1109/BIOCAS.2018.8584729`.

[249] Ho Lee et al. "Sensitivity-Enhanced LC Pressure Sensor for Wireless Bladder Pressure Monitoring". In: *IEEE Sensors Journal* 16 (June 2016), pp. 1–1. DOI: `10.1109/JSEN.2016.2533262`.

[250] Yu-Ting Li et al. "Designing and Implementing an Implantable Wireless Micromanometer System for Real-Time Bladder Pressure Monitoring: A Preliminary Study". In: *Sensors* 20.16 (2020). ISSN: 1424-8220. DOI: `10.3390/s20164610`. URL: `https://www.mdpi.com/1424-8220/20/16/4610`.

[251] R. Tan et al. "Development of a fully implantable wireless pressure monitoring system". In: *Biomedical Microdevices* 11.1 (2009), pp. 259–264. DOI: `10.1007/s10544-008-9232-1`. URL: `https://doi.org/10.1007/s10544-008-9232-1`.

[252] A. S. Basu et al. "Is submucosal bladder pressure monitoring feasible?" In: *Proceedings of the Institution of Mechanical Engineers, Part H: Journal of Engineering in Medicine* 233.1 (2019), pp. 100–113. DOI: `10.1177/0954411918754925`. URL: `https://doi.org/10.1177/0954411918754925`.

[253] DataCamp. *Random Forest Classifier in Python*. Accessed: 2026-01-24. 2025. URL: `https://www.datacamp.com/tutorial/random-forests-classifier-python`.

[254] IBM. *Random Forest*. Accessed: 2026-01-24. n.d. URL: `https://www.ibm.com/think/topics/random-forest`.

[255] GeeksforGeeks. *XGBoost*. Accessed: 2026-01-24. 2025. URL: `https://www.geeksforgeeks.org/machine-learning/xgboost/`.

[256] GeeksforGeeks. *Support Vector Machine Algorithm*. Accessed: 2026-01-24. n.d. URL: `https://www.geeksforgeeks.org/machine-learning/support-vector-machine-algorithm/`.

[257] Yituo Feng and Jungryeol Park. "Using machine learning-based binary classifiers for predicting organizational members' user satisfaction with collaboration software". In: *PeerJ Computer Science* 9 (2023). PMCID: PMC10403168, e1481. DOI: `10.7717/peerj-cs.1481`. URL: `https://pmc.ncbi.nlm.nih.gov/articles/PMC10403168/`.

[258] B. Wang et al. "Time-Series Classification Based on Fusion Features of Sequence and Visualization". In: *Applied Sciences* 10.12 (2020), p. 4124. DOI: `10.3390/app10124124`. URL: `https://www.mdpi.com/2076-3417/10/12/4124`.

[259] Min-Cheol Kwon and Sunwoong Choi. "Recognition of Daily Human Activity Using an Artificial Neural Network and Smartwatch". In: *Wireless Communications and Mobile Computing* (2018), pp. 1–9. DOI: `10.1155/2018/2618045`. URL: `https://onlinelibrary.wiley.com/doi/10.1155/2018/2618045`.

[260] Jason Brownlee. *Understand the Impact of Learning Rate on Neural Network Performance*. `https://machinelearningmastery.com/understand-the-dynamics-of-learning-rate-on-deep-learning-neural-networks/`. Accessed: 2026-01-24. 2020.

[261] GeeksforGeeks. *Batch Size in Neural Network*. Accessed: 2026-01-24. 2025. URL: `https://www.geeksforgeeks.org/deep-learning/batch-size-in-neural-network/`.

[262] Towards Data Science. *Dropout in Neural Networks*. Accessed: 2026-01-24. 2022. URL: `https://towardsdatascience.com/dropout-in-neural-networks-47a162d621d9/`.

[263] GeeksforGeeks. *Using Early Stopping to Reduce Overfitting in Neural Networks*. Accessed: 2026-01-24. 2025. URL: `https://www.geeksforgeeks.org/deep-learning/using-early-stopping-to-reduce-overfitting-in-neural-networks/`.

[264] IBM. *What Is a Loss Function?* Accessed: 2026-01-24. n.d. URL: `https://www.ibm.com/think/topics/loss-function`.

[265] GeeksforGeeks. *Binary Cross-Entropy / Log Loss for Binary Classification*. Accessed: 2026-01-24. 2025. URL: `https://www.geeksforgeeks.org/deep-learning/binary-cross-entropy-log-loss-for-binary-classification/`.

[266] J.S. Wheeler et al. "Comparison of a Simple Cystometer with a Multichannel Cystometer in Females with Voiding Dysfunction". In: *International Urogynecology Journal* 2 (1991), pp. 90–93. DOI: `10.1007/BF00376569`. URL: `https://link.springer.com/article/10.1007/BF00376569`.

[267] Wikipedia contributors. *Holter monitor*. `https://en.wikipedia.org/wiki/Holter_monitor`. Accessed: 2025-07-28. Mar. 2024.

[268] NXP Semiconductors. *MPX5050, Integrated silicon pressure sensor, on-chip signal conditioned, temperature compensated and calibrated - Product Data Sheet*. `https://static.chipdip.ru/lib/204/DOC040204200.pdf`. Accessed August 22, 2025. June 2023.

[269] Freescale Semiconductor, Inc. *MPX5050DP Integrated Silicon Pressure Sensor Datasheet*. `https://datasheet.octopart.com/MPX5050DP-Freescale-Semiconductor-datasheet-82618.pdf`. Accessed: 2025-09-27. Mar. 2010.

[270] NXP Semiconductors. *MPX5050DP Integrated Silicon Pressure Sensor - Product Information and Datasheet*. `https://www.nxp.com/part/MPX5050DP`. Accessed August 22, 2025. 2025.

[271] Micro Robotics. *MPU6050 Triple Axis Accelerometer + Gyro 6DOF - Product Information*. `https://www.robotics.org.za/GY-521`. Accessed August 22, 2025. 2025.

[272] Espressif Systems. *ESP32 Resources*. `https://www.espressif.com/en/products/socs/esp32/resources`. Accessed: 2025-09-27. 2025.

[273] Components101. *Micro SD Card Module Datasheet*. `https://components101.com/sites/default/files/component_datasheet/Micro-SD-Card-Module-Datasheet.pdf`. Accessed: 2026-02-11.

[274] Temu. *[Micro SD/TF Card Module] High-Speed Micro SD/TF Card Module with SPI Interface 3.3V Level Shifter | Blue Board with Golden Slot, Easy-to-Install AVR Connector*. `https://www.temu.com/goods.html?goods_id=601100033054211`. Accessed August 22, 2025. 2025.

[275] Ufine Battery. *Curved by LiPo: How lithium polymer batteries are changing the future of flexible electronics*. https://www.ufinebattery.com/blog/curved-by-lipo-how-lithium-polymer-batteries-are-changing-the-future-of-flexible-electronics/. Accessed August 22, 2025. 2025.

[276] Mantech Electronics (Pty) Ltd. *LITHIUM POLYMER BATTERY 3V7 2000mAh 50x34x10mm - Product Page*. https://www.mantech.co.za/ProductInfo.aspx?Item=ME100955. Accessed: 2025-09-29. 2025.

[277] RoboFactory. *TP4056 Micro USB Lithium Battery Charger Module With Protection*. https://www.robofactory.co.za/charge-controllers/863-tp4056-micro-usb-lithium-battery-charger-module-with-protection.html. Accessed August 22, 2025. 2025.

[278] Olimex. *MT3608 High Efficiency 1.2MHz 2A Step Up Converter - Datasheet*. https://www.olimex.com/Products/Breadboarding/BB-PWR-3608/resources/MT3608.pdf. Accessed August 22, 2025. 2025.

[279] Temu. *Product Page*. https://www.temu.com/goods.html?_bg_fs=1&goods_id=601099658217397&sku_id=17592748388289&_x_sessn_id=4ga3yp0s3w&refer_page_name=bgt_order_detail&refer_page_id=10045_1758981065041_a1uvcu4qlj&refer_page_sn=10045. Accessed: 2025-09-27. 2025.

[280] Harris' Electronics. *SSD1306 Power Consumption*. https://hsel.co.uk/2018/12/04/ssd1306-power-consumption. Accessed: 2025-09-27. Dec. 2018.

[281] Soldered. *Display OLED I2C White 0.96" SSD1306 (Part No. 333099) Datasheet*. https://www.mouser.com/datasheet/2/1398/Soldered_333099-3395096.pdf. Accessed: 2026-02-18. n.d.

[282] ESP32IO. *ESP32 - Button | ESP32 Tutorial*. https://esp32io.com/tutorials/esp32-button. Accessed: 2026-02-11. n.d.

[283] Relion Battery. *What is Lithium Battery Protection Mode?* https://www.relionbattery.com/blog/what-is-lithium-battery-protection-mode?srsltid=AfmBOooyHGhbjJuFdCQOtFfBAx9Q1D_W722rDUeWhdw9rdxwA_DLy1z2. Accessed September 23, 2025. 2021.

[284] LCSC Electronics. *Datasheet for Product C208482*. https://www.lcsc.com/datasheet/C208482.pdf. Accessed: 2025-09-28. 2025.

[285] LCSC Electronics. *Datasheet for Product C2687025*. https://www.lcsc.com/datasheet/C2687025.pdf. Accessed: 2025-09-28. 2025.

[286] LCSC Electronics. *Datasheet for Product C43798*. https://www.lcsc.com/datasheet/C43798.pdf. Accessed: 2025-09-28. 2025.

[287] LCSC Electronics. *Datasheet for Product C5632432*. https://www.lcsc.com/datasheet/C5632432.pdf. Accessed: 2025-09-28. 2025.

[288] CIRCUITSTATE Electronics. *DOIT ESP32 DevKit V1 Wi-Fi Development Board - Pinout Diagram Arduino Reference*. https://www.circuitstate.com/pinouts/doit-esp32-devkit-v1-wifi-development-board-pinout-diagram-and-reference/. Accessed August 22, 2025. 2025.

[289] EasyEDA. *EasyEDA - Online PCB design circuit simulator*. https://easyeda.com. Accessed September 23, 2025. 2025.

[290] JLCPCB. *The Ultimate Guide to PCB Layout Design*. https://jlcpcb.com/blog/guide-to-pcb-layout-design. Accessed: 2025-11-02. 2025.

[291] GrabCAD. *Free CAD Designs, Files 3D Models Library*. https://grabcad.com/library?page=1&time=all_time&sort=recent. Accessed: 2025-09-28. 2025.

[292] Digi-Key Electronics. *PCB Trace Width Conversion Calculator*. https://www.digikey.co.uk/en/resources/conversion-calculators/conversion-calculator-pcb-trace-width?srsltid=AfmBOorqPKoEZ1KmUI-0amqQD6K1K2dgQR_CwtTGsE2nOIuAnJsr_LGh. Accessed: 2025-09-28. 2025.

[293] JLCPCB. *JLCDFM: Free Online PCB DFM Tool*. https://jlcdfm.com. Accessed: 2025-11-02. 2025.

[294] JLCPCB. *Printed Circuit Board Manufacturing & PCB Assembly*. `https://jlcpcb.com`. Accessed September 23, 2025. 2025.

[295] Ultimaker. *How to 3D Print with PLA and Which Materials to Choose*. `https://ultimaker.com/learn/how-to-3d-print-with-pla-and-which-materials-to-choose`. Accessed September 23, 2025. 2025.

[296] Creality. *K1 3D Printer*. `https://www.creality.com/products/creality-k1-3d-printer`. Accessed September 23, 2025. 2025.

[297] Creality. *PLA Filament 1.75 mm for 3D Printers (1 kg, Multi-Colors)*. `https://www.creality.shop/products/pla-filament-1-75mm-for-3d-printers-1kg-multi-colors`. Accessed: 2026-02-20. n.d.

[298] Farmaè. *Catheter Foley SIL 2V CH20*. `https://farmae.eu/en/catheter-foley-sil-2v-ch20.html`. Accessed: 2026-02-18. n.d.

[299] Delock. *Hook and Loop Tape Roll 1 m x 20 mm White (Item 18379)*. `https://en.varia-store.com/product/delock-18379-357012-cable-tie-velcro/`. Accessed: 2026-02-18. n.d.

[300] Khaled Magdy. *ESP32 Sleep Modes & Power Consumption in Each Mode*. `https://deepbluembedded.com/esp32-sleep-modes-power-consumption/`. Accessed: 2026-02-21. n.d.

[301] Gough Lui. *Experiment: microSD Card Power Consumption & SPI Performance*. `https://goughlui.com/2021/02/27/experiment-microsd-card-power-consumption-spi-performance/`. Accessed: 2026-02-21. 2021.

[302] Soldered. *Display OLED I2C White 0.96” SSD1306*. `https://soldered.com/products/display-oled-i2c-white-0-96-ssd1306`. Accessed: 2026-02-21. n.d.

[303] Minuka Thesath Yapa. *Arduino MPU6050 Accelerometer*. `https://projecthub.arduino.cc/MinukaThesathYapa/arduino-mpu6050-accelerometer-472bb5`. Accessed: 2026-02-21. 2021.

A

Part A: Machine Learning Pipeline for Motion Artifact Removal for Ambulatory Cystometry

A.1 Reference Values for Normal Urodynamic Tests

A comprehensive understanding of normal urodynamic parameters is essential for interpreting test results and identifying pathological deviations. Table A.1 summarises standard reference values and expected physiological findings across urodynamic tests. These serve as a baseline for comparison in patients presenting with LUTS or suspected LUTD.

Table A.1: Reference values and expected findings during normal urodynamic testing. This table summarises key parameters across standard urodynamic tests, including uroflowmetry, cystometry, pressure-flow studies, EMG, and video-urodynamics (VUDS), with typical ranges or patterns observed in asymptomatic individuals.

Urodynamic Test	**Normal / Expected Result**
Uroflowmetry	Bell-shaped flow curve with Q_{max} typically >15 - 20 mL/s
PVR	50–100 mL
Cystometry (P_{det})	Filling pressures: 0–18 cmH_2O (supine), 15–40 cmH_2O (sitting), 20–50 cmH_2O (standing); Voiding pressures: 50–70 cmH_2O
Pressure-flow study	Coordinated increase in P_{det} with normal flow rate (Q_{max} > 15 = 20 mL/s) and complete bladder emptying
EMG	Increased EMG activity during storage phase (especially with stress manoeuvres or involuntary detrusor contractions); Decreased EMG activity during voiding indicates sphincter relaxation and coordinated voiding
UPP	MUCP >20 cmH_2O; sufficient to maintain continence at rest
ALPP	60–90 cmH_2O
VUDS	Normal bladder shape and capacity (300-500 mL), coordinated sphincter relaxation during voiding. No evidence of reflux, leakage, or outlet obstruction

A.2 Study Cohort Demographics and Clinical Characteristics

Table A.2 summarises demographic information, relevant medical history, pre-clinical urinary symptoms, and key cystometric outcomes for the study cohort. Demographic variables include age and sex. Urodynamic outcomes were also reported and include bladder capacity, leakage volume, and PVR.

Table A.2: Patient demographics, clinical history, and cystometric outcomes for the study cohort. ”–” indicates data not recorded.

Patient	Age	Sex	Medical History	Pre-clinical Symptoms	Capacity (mL)	Leakage (mL)	PVR (mL)
1	77	F	Diabetes, chronic venous ulcer, hypertension, IHD	Frequency, urgency	500	0	0
2	52	F	None reported	Frequency, urgency, cloudy/foul-smelling urine	500	0	0
3	52	M	BPH with obstructive uropathy	Frequency, leakage	–	0	625
4	70	M	Diabetes	Weak stream, abdominal/back pain, frequency	200	–	–
5	79	M	Diabetes	Frequency, urgency	170	–	–
6	83	M	None reported	Dysuria, urgency	205	150	–
7	40	F	None reported	Frequency, dysuria	–	50	–
8	69	M	Urinary retention	Frequency, dysuria, weak stream	200	50	10
9	62	F	Diabetes (on medication), urinary leakage	Frequency	–	225	10
10	50	F	Hypertension (on medication)	Frequency, pain, weak stream	–	450	350

A.3 Experimental Setup

The software versions used in this pipeline are listed below to enable replication of the experiments:

- Python: 3.10.11
- NumPy: 2.2.6
- SciPy: 1.15.3
- pandas: 2.3.3
- scikit-learn: 1.7.2
- TensorFlow: 2.20.0
- Keras: 3.12.0
- XGBoost: 3.1.3
- joblib: 1.5.3
- Matplotlib: 3.10.8

A.4 Final Model Architectures and Hyperparameters

This section reports the final architectures and hyperparameter configurations of all evaluated models except the top-performing models, which are reported in Section 3.12. Hyperparameters correspond to the configurations selected based on cross-validation performance using the predefined evaluation metrics.

A.4.1 Feature-Based Models

Table A.3: Final hyperparameter configurations for feature-based classification models. Hyperparameters were selected using patient-level cross-validated grid search. Final models were retrained on the full labelled dataset using the selected configuration.

Model	Hyperparameter	Value
XGBoost	Number of boosting rounds ($n_{\text{estimators}}$)	200
	Maximum tree depth (max_depth)	10
	Learning rate (η)	0.05
	Row subsampling (subsample)	1.0
	Column subsampling (colsample_bytree)	0.2
	Objective function	binary:logistic
	Evaluation metric	PR AUC
	Class weighting (scale_pos_weight)	$\frac{N_{\text{neg}}}{N_{\text{pos}}}$
Logistic Regression	Penalty	elastic net
	Inverse regularisation strength (C)	0.01
	Elastic net mixing parameter (l_1 ratio)	0.3
	Solver	SAGA
	Feature standardisation	z-score normalisation
	Evaluation metric	PR AUC
	Class weighting	balanced
	Maximum iterations	5000
Linear SVM	Kernel	linear
	Regularisation parameter (C)	1.0
	Penalty	l_1
	Optimisation formulation	primal (dual $=$ False)
	Probability calibration	Platt scaling (sigmoid)
	Feature standardisation	z-score normalisation
	Evaluation metric	PR AUC
	Class weighting	balanced
	Maximum iterations	10,000

All hyperparameters not listed in Table A.3 were left at their respective library default values.

A.4.2 Neural Network Models

A.4.2.1 Multilayer Perceptron (MLP)

For the MLP architecture, the number of hidden layers and neurons were tuned to identify the best-performing configuration. The final MLP model consisted of a single hidden layer with 64 neurons, outperforming more complex models with additional hidden layers. Table A.4 summarises the resulting architecture.

Table A.4: Multilayer perceptron (MLP) architecture for pressure window classification.

Layer	**Configuration**	**Output shape**
Input	Flattened pressure window	(61)
Dense (Hidden)	64 units, ReLU activation	(64)
Dense (Output)	1 unit, Sigmoid activation	(1)

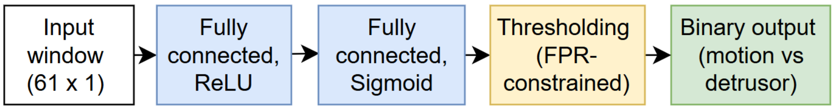

Figure A.1: Schematic representation of the multilayer perceptron (MLP) architecture used for pressure window classification.

A.4.2.2 LUNet

The LUNet model is a lightweight U-Net–inspired one-dimensional encoder–decoder architecture with skip connections and a dilated bottleneck.

Table A.5: Lightweight U-Net–inspired encoder–decoder CNN (LUNet) with skip connections and dilated bottleneck for pressure window classification.

Layer	**Configuration**	**Output shape**
Input	Pressure window	$(61, 1)$
Conv1D + BN + ReLU	32 filters, kernel size = 3	$(61, 32)$
Conv1D + BN + ReLU	32 filters, kernel size = 3	$(31, 32)$
Conv1D + BN + ReLU	64 filters, kernel size = 3	$(31, 64)$
Conv1D + BN + ReLU	64 filters, kernel size = 3	$(16, 64)$
Spatial Dropout	$p = 0.2$	$(16, 64)$
Conv1D + BN + ReLU	128 filters, kernel size = 3	$(16, 128)$
Conv1D + BN + ReLU	128 filters, kernel size = 3	$(8, 128)$
Conv1D + ReLU	128 filters, kernel size = 3	$(8, 128)$
UpSampling1D	Factor = 2	$(16, 128)$
Concatenate	Skip connection (encoder)	$(16, 256)$
Conv1D + BN + ReLU	12 filters, kernel size = 3	$(16, 12)$
UpSampling1D	Factor = 2	$(32, 12)$
Concatenate	Skip connection (encoder)	$(31, 76)$
Conv1D + BN + ReLU	8 filters, kernel size = 3	$(31, 8)$
UpSampling1D	Factor = 2	$(62, 8)$
Concatenate	Skip connection (encoder)	$(61, 40)$
Conv1D + BN + ReLU	4 filters, kernel size = 3	$(61, 4)$
Global Average Pooling	Temporal aggregation	(4)
Dropout	$p = 0.5$	(4)
Dense (Output)	1 unit, Sigmoid	(1)

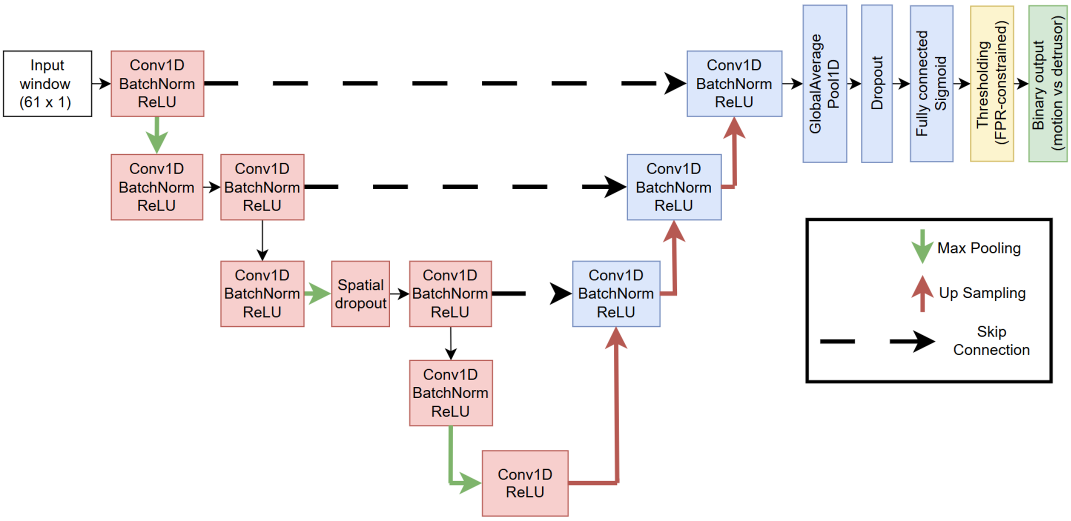

Figure A.2: Schematic representation of the lightweight U-Net–inspired (LUNet) model architecture used for pressure window classification.

A.4.2.3 *Lightweight 1D CNN with Channel-Wise Attention*

This model implements a squeeze–and–excitation (SE) block to perform channel-wise attention. The convolutional layers first extract hierarchical temporal features from the pressure window, after which the SE block adaptively adjusts channel weights based on their global importance.

The SE block is made up of the following layers: global average pooling, two fully connected layers with a bottleneck structure, reshaping, and channel-wise multiplication. First, global average pooling summarises each feature channel into a single value, capturing how strong that channel is overall. This information is passed through two fully connected layers (bottleneck): the first reduces the number of features to 16 to reduce dimensionality and model complexity, and the second expands it back to 256 using a sigmoid activation to produce weights between 0 and 1. These weights indicate how important each channel is. Finally, the weights are multiplied with the original feature maps, strengthening important channels and reducing the influence of less useful ones. This allows the model to prioritise pressure features that are most discriminative for motion artifacts and detrusor activity.

Table A.6: Lightweight 1D CNN with channel-wise attention for pressure window classification.

Layer	Configuration	Output shape
Input	Pressure window	$(61, 1)$
Conv1D	64 filters, kernel size = 3, ReLU	$(61, 64)$
Batch Normalization	–	$(61, 64)$
MaxPooling1D	Pool size = 2	$(30, 64)$
Conv1D	128 filters, kernel size = 3, ReLU	$(30, 128)$
Batch Normalization	–	$(30, 128)$
MaxPooling1D	Pool size = 2	$(15, 128)$
Conv1D	256 filters, kernel size = 3, ReLU	$(15, 256)$
Batch Normalization	–	$(15, 256)$
MaxPooling1D	Pool size = 2	$(7, 256)$
Global Average Pooling	Temporal channel aggregation	(256)
Dense	16 units, ReLU	(16)
Dense	256 units, Sigmoid	(256)
Reshape	Channel-wise weights	$(1, 256)$
Multiply	Channel attention	$(7, 256)$
Flatten	–	(1792)
Dropout	$p = 0.5$	(1792)
Dense	64 units, ReLU	(64)
Dense (Output)	1 unit, Sigmoid	(1)

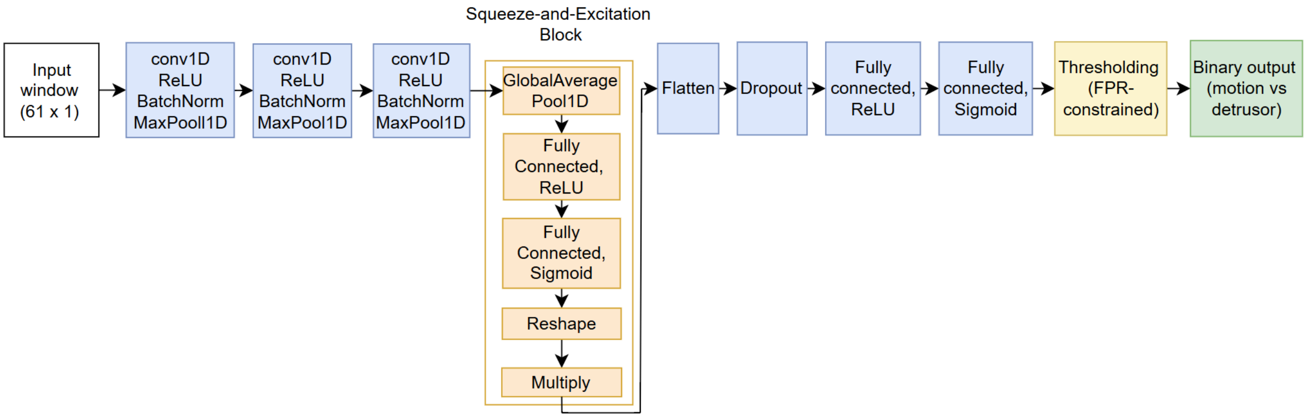

Figure A.3: Schematic representation of the lightweight 1D CNN with channel-wise attention architecture used for pressure window classification.

A.4.2.4 Bi-LSTM with Learned Temporal Attention

This model uses a Bi-LSTM architecture to capture long-range temporal dependencies within pressure windows. Processing the sequence in both forward and backward directions allows the model to incorporate contextual information from the entire window.

A temporal attention mechanism is applied to the sequence of LSTM outputs to learn the relevance of each time step (i.e. the contribution of a given time point to the final classification decision). This is done by computing a weighted combination of the LSTM hidden states.

Table A.7: Bidirectional LSTM with temporal attention for pressure window classification

Layer	Configuration	Output shape
Input	Pressure window	$(T, 1)$
Bidirectional LSTM	32 units per direction, return sequences	$(T, 64)$
Layer Normalization	Temporal axis normalisation	$(T, 64)$
Bidirectional LSTM	64 units per direction, return sequences	$(T, 128)$
Bidirectional LSTM	64 units per direction, return sequences	$(T, 128)$
Attention Layer	Trainable temporal attention	Context: (128) Attention weights: (T)
Dense	32 units, SELU	(32)
Dense	32 units, SELU	(32)
Dense (Output)	1 unit, Sigmoid	(1)

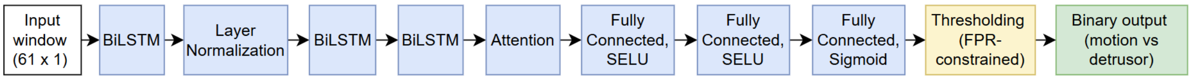

Figure A.4: Schematic representation of the Bi-LSTM with learned temporal attention model architecture used for pressure window classification.

A.4.3 Hybrid Models

A.4.3.1 Parallel Hybrid CNN–LSTM Model

In this parallel architecture, convolutional and recurrent branches learn independently on the same input window. Temporal dimensions are removed using global average pooling prior to feature concatenation.

Table A.8: CNN branch of the parallel CNN–LSTM model. The convolutional branch extracts local temporal patterns from pressure windows prior to temporal aggregation.

Layer	Configuration	Output shape
Input	Pressure window	$(T, 1)$
Conv1D	64 filters, kernel size = 7, ReLU, same padding	$(T, 64)$
MaxPooling1D	Pool size = 2	$(\lfloor T/2 \rfloor, 64)$
Conv1D	128 filters, kernel size = 5, ReLU, same padding	$(\lfloor T/2 \rfloor, 128)$
Global Average Pooling	Temporal aggregation	(128)

Table A.9: Bidirectional LSTM branch of the parallel CNN–LSTM model. The recurrent branch captures long-range temporal dependencies across the full pressure window.

Layer	Configuration	Output shape
Input	Pressure window	$(T, 1)$
Bidirectional LSTM	32 units per direction, return sequences	$(T, 64)$
Layer Normalization	Applied along temporal axis	$(T, 64)$
Bidirectional LSTM	64 units per direction, return sequences	$(T, 128)$
Bidirectional LSTM	64 units per direction, return sequences	$(T, 128)$
Global Average Pooling	Temporal aggregation	(128)

Table A.10: Feature fusion and classification layers of the parallel CNN–LSTM architecture. CNN and LSTM embeddings are concatenated prior to classification.

Layer	Configuration	Output shape
Concatenate	CNN + LSTM embeddings	(256)
Dense	32 units, ReLU	(32)
Dense	64 units, ReLU	(64)
Dropout	$p = 0.5$	(64)
Dense (Output)	1 unit, Sigmoid	(1)

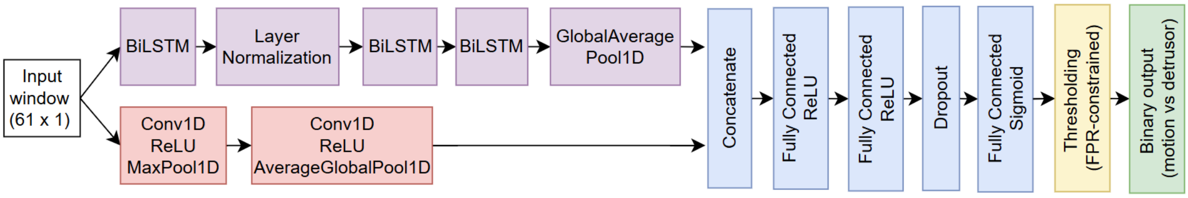

Figure A.5: Parallel hybrid CNN–LSTM architecture for pressure window classification. Convolutional and bidirectional LSTM branches learn in parallel to extract complementary temporal features, which are then fused at the feature level prior to classification.

A.4.3.2 Late-Fusion RF–CNN Ensemble

Table A.11: Random forest classifier configuration used in the late-fusion ensemble.

Component	Configuration
Input	Handcrafted statistical features
Number of trees	200
Maximum depth	10
Minimum samples per leaf	1
Minimum samples per split	2
Feature selection	$\sqrt{\text{features}}$
Class weighting	Balanced (fold-specific)
Output	Class probability p_{RF}

Table A.12: Convolutional neural network architecture used in the late-fusion ensemble for pressure window classification.

Layer	Configuration	Output shape
Input	Pressure window	$(T, 1)$
Conv1D	64 filters, kernel size = 7, ReLU, same padding	$(T, 64)$
MaxPooling1D	Pool size = 2	$(\lfloor T/2 \rfloor, 64)$
Conv1D	128 filters, kernel size = 5, ReLU, same padding	$(\lfloor T/2 \rfloor, 128)$
MaxPooling1D	Pool size = 2	$(\lfloor T/4 \rfloor, 128)$
Flatten	–	(N)
Dense	64 units, ReLU	(64)
Dropout	Rate = 0.5	(64)
Dense (Output)	1 unit, Sigmoid	(1)

Table A.13: Late-fusion strategy for combining RF and CNN probability outputs using weighted averaging.

Component	Description
Fusion type	Weighted probability averaging
Fusion equation	$p_{\text{fused}} = w_{\text{RF}} p_{\text{RF}} + w_{\text{CNN}} p_{\text{CNN}}$
Weights	$w_{\text{RF}} + w_{\text{CNN}} = 1$
Thresholding	Validation-only, FPR-constrained
Output	Binary class prediction

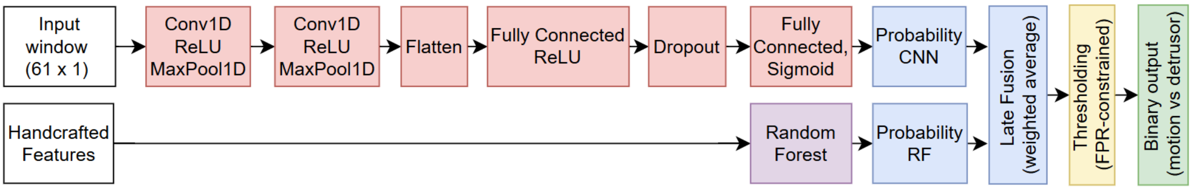

Figure A.6: Late-fusion RF-CNN framework combining independently trained CNN and RF classifiers. Predicted class probabilities are fused using weighted averaging.

A.5 Confusion Matrices of Top-Performing Models

Aggregated confusion matrices for the top-performing models identified in Section 3.10 are shown in Figures B.4. For each model, confusion matrices were computed using the fold-specific, FPR-constrained classification thresholds and then aggregated across cross-validation folds. The confusion matrices illustrate the number of true positives, true negatives, false positives, and false negatives under clinically constrained operating points.

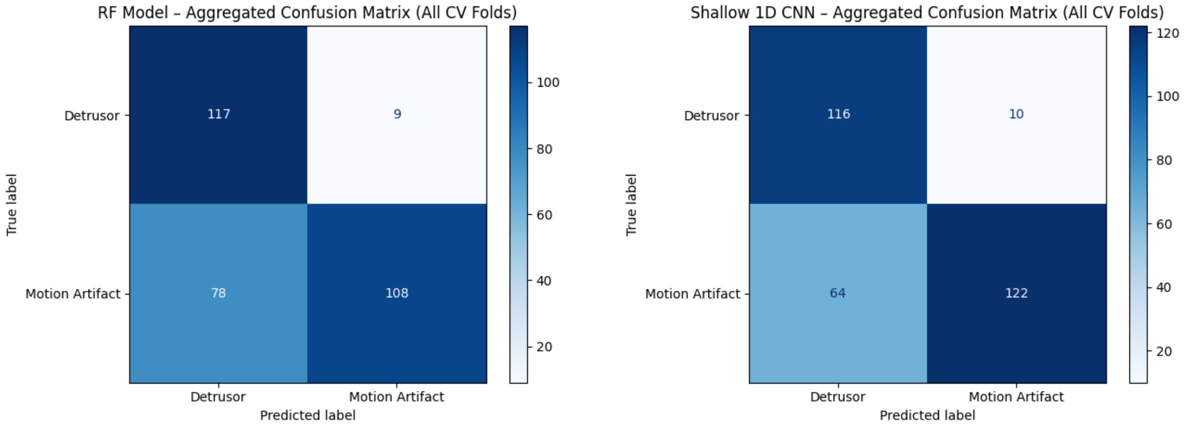

(a) RF model

(b) Shallow 1D CNN

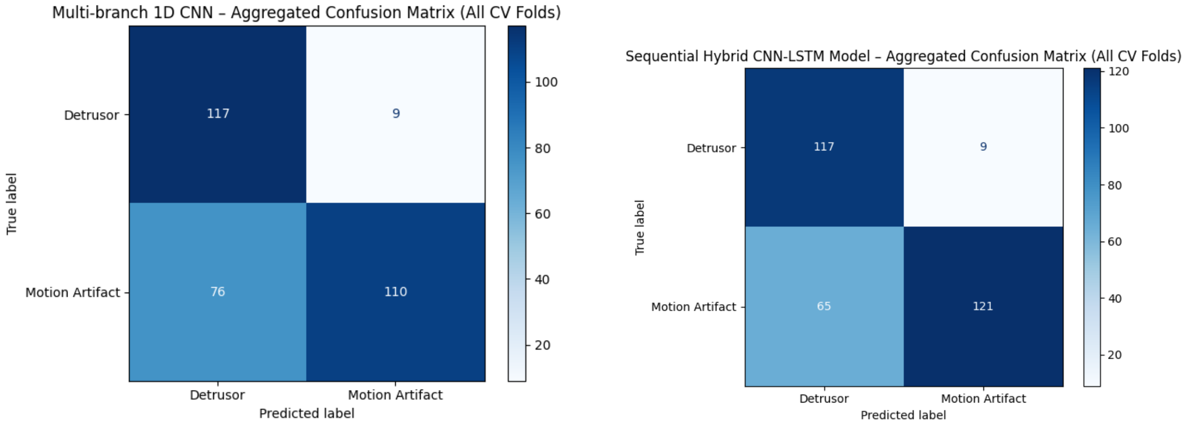

(c) Multi-branch 1D CNN with channel-wise attention

(d) Sequential CNN–LSTM hybrid

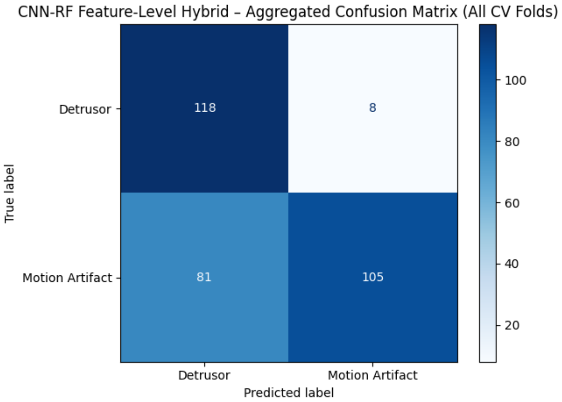

(e) CNN–RF feature-level hybrid

Figure A.7: Aggregated confusion matrices for the top-performing models across all cross-validation folds.

A.6 Model Ranking

Per-metric ranking values and intermediate weighted scores used to derive the final model rankings presented in Section 3.11 are reported in Table A.14. Models were ranked per metric from 1 (lowest performance) to 5 (highest performance), with ranks combined using clinically prioritised metric weights.

Table A.14: Per-metric ranks and weighted scores used to derive the final model rankings. Higher rank values indicate better performance.

Model	**MA Prec.**	**MA Rec.**	**MA F1**	**DA Prec.**	**DA Rec.**	**DA F1**	**PR AUC**	**Weighted Score**	**Normalised Score**
RF	2	2	2	1	1	2	3	1.90	0.44
Shallow 1D CNN	3	5	5	5	2	5	2	3.30	0.76
Multi-branch 1D CNN	5	4	4	3	4	4	5	4.35	1.00
Sequential CNN–LSTM	4	3	3	4	3	4	1	3.00	0.69
CNN–RF Feature-Level Hybrid	1	1	1	2	5	1	4	2.50	0.57
Metric Weight	0.25	0.15	0.05	0.10	0.20	0.05	0.20	–	–

Normalised Score was obtained by dividing each weighted score by the maximum weighted score across models.

B

Part B: Design and Implementation of the UroMonitor System

B.1 System Integration and Circuit Design

B.1.1 Circuit Schematics

The complete circuit schematics were developed in EasyEDA and are shown in Figures B.1 and B.2.

Figure B.1 illustrates the ESP32 microcontroller and power management subsystem, including the LiPo battery, TP4056 charger, SPDT mode selection switch, PTC fuses, MT3608 boost converter, and voltage rail routing. Figure B.2 shows the sensing, storage, and user interface subsystems, including the MPX5050DP pressure sensor with voltage divider, MPU6050 IMU and OLED on the shared I^2C bus, microSD module on SPI, and decoupling capacitors for signal stability. The expansion header is also shown.

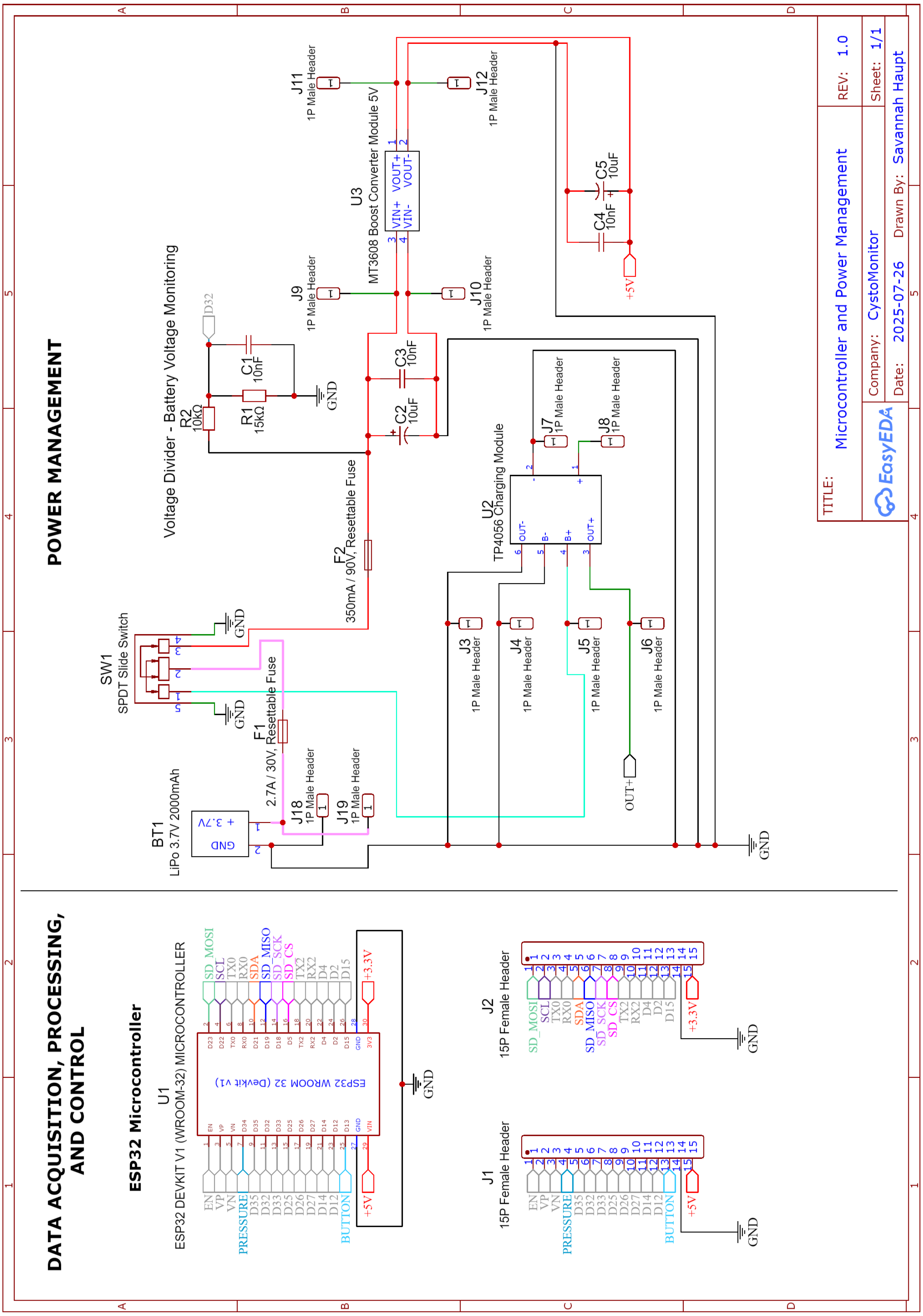

Figure B.1: Schematic diagram of the data acquisition and control subsystem (ESP32 microcontroller) and power management subsystem. The ESP32 schematic shows input pin connections for the MPX5050DP pressure sensor, SPI lines for the microSD card module, I^{2}C lines for the MPU6050 IMU and OLED display, and pin connection for the latching push-button. Power supply routing is also shown: the 5 V rail generated by the MT3608 boost converter enters via the V_{IN} pin, while the ESP32's onboard regulator provides a stable 3.3 V output to peripheral components. The power management subsystem schematic illustrates the LiPo battery, SPDT switch for toggling between charging and operation modes, TP4056 charging module, MT3608 boost converter, and resettable fuses which protect against overcurrent and short circuits. Designed in EasyEDA [289].

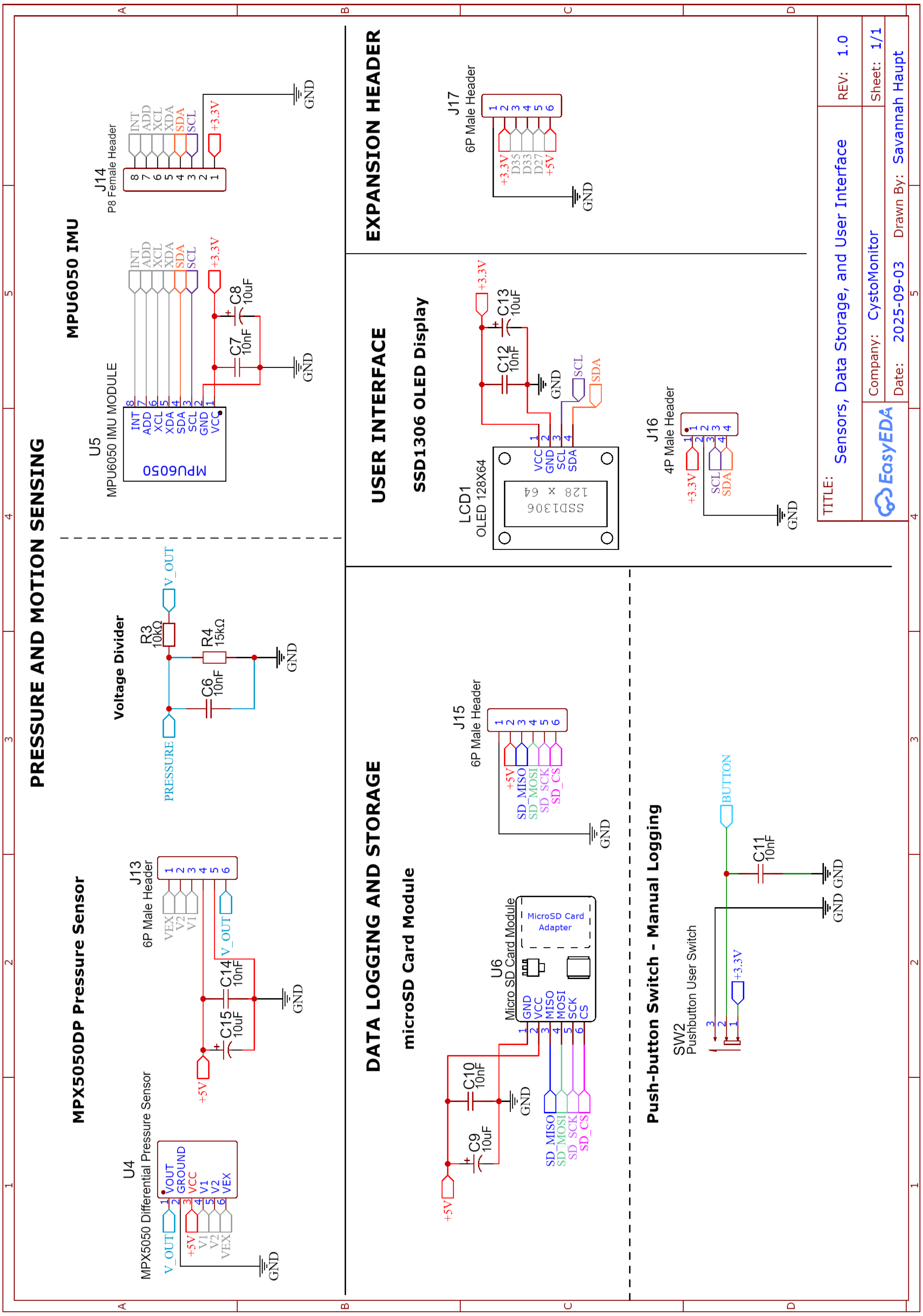

Figure B.2: Schematic diagram of the pressure and motion sensing, data logging and storage, and user interface subsystems. The MPX5050DP pressure sensor and MPU6050 IMU are shown with their respective analogue and digital (I^2C) connections to the ESP32. The microSD card module is connected via the SPI bus for high-speed data logging, while the SSD1306 OLED display shares the I^2C bus with the IMU. Decoupling capacitors and voltage dividers are added for signal conditioning and power stabilisation. An expansion header connection is included to support future modifications such as the integration of an additional sensor. Designed in EasyEDA [289].

B.2 UroMonitor Mobile Application Design and Workflow

The UroMonitor mobile application was developed as the user-facing interface for the UroMonitor system.

B.2.1 Home Screen

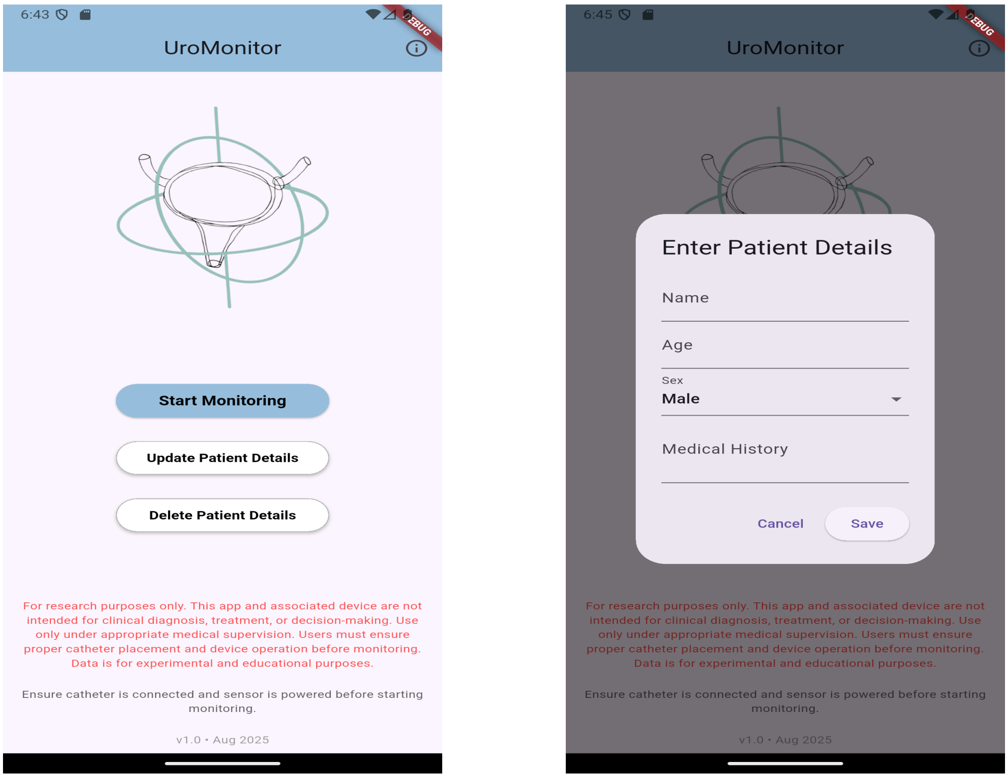

For research purposes only. This app and associated device are not intended for clinical diagnosis, treatment, or decision-making. Use only under appropriate medical supervision. Users must ensure proper catheter placement and device operation before monitoring. Data is for experimental and educational purposes.

Ensure catheter is connected and sensor is powered before starting monitoring.

v1.0 • Aug 2025

Sex
Male

For research purposes only. This app and associated device are not intended for clinical diagnosis, treatment, or decision-making. Use only under appropriate medical supervision. Users must ensure proper catheter placement and device operation before monitoring. Data is for experimental and educational purposes.

Ensure catheter is connected and sensor is powered before starting monitoring.

v1.0 • Aug 2025

(a) Home Screen of the UroMonitor App.

(b) Input fields to provide patient details.

Figure B.3: UroMonitor Home Screen.

B.2.2 Monitoring Screen

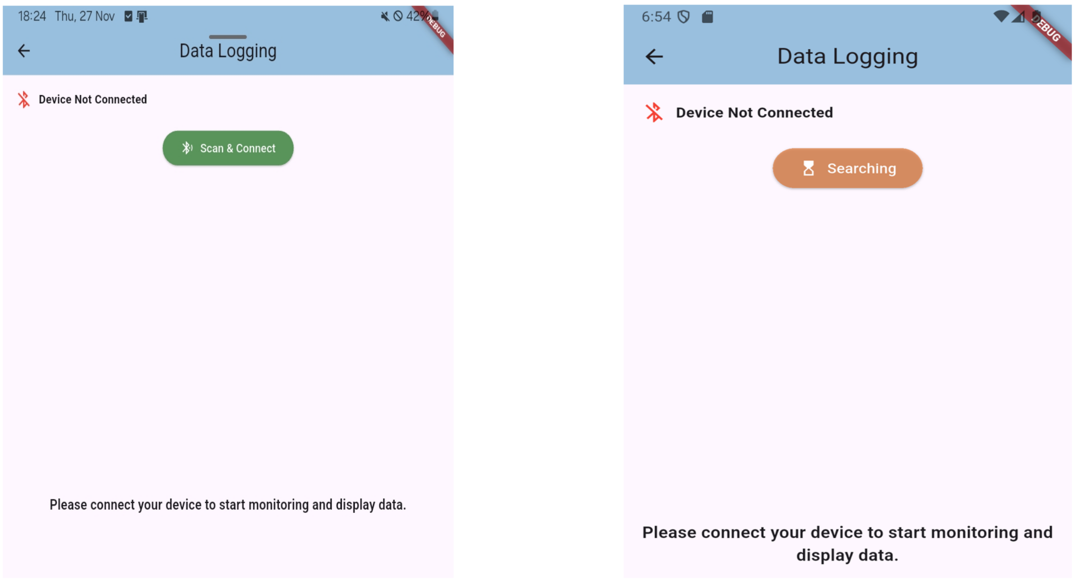

Device Not Connected

Please connect your device to start monitoring and display data.

Device Not Connected

Please connect your device to start monitoring and display data.

(a) Monitoring Screen prompting the user to initiate a BLE connection to the UroMonitor device via the ”Scan & Connect” button.

(b) Monitoring Screen during BLE scanning and connection establishment with the UroMonitor device.

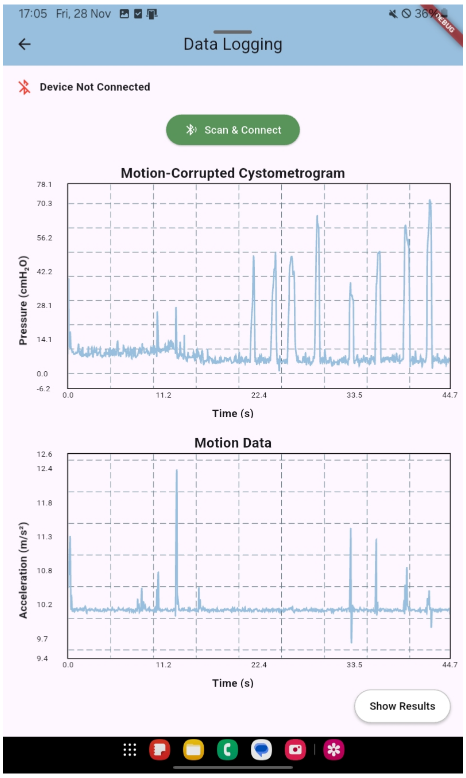

(c) Monitoring Screen displaying real-time line charts of pressure and motion signals after successful BLE connection.

Figure B.4: Mobile application monitoring screen interface showing (top left) the connection prompt, (top right) the BLE scanning/connecting state, and (bottom) real-time visualisation of pressure and motion data during active monitoring.

B.2.3 Results Screen

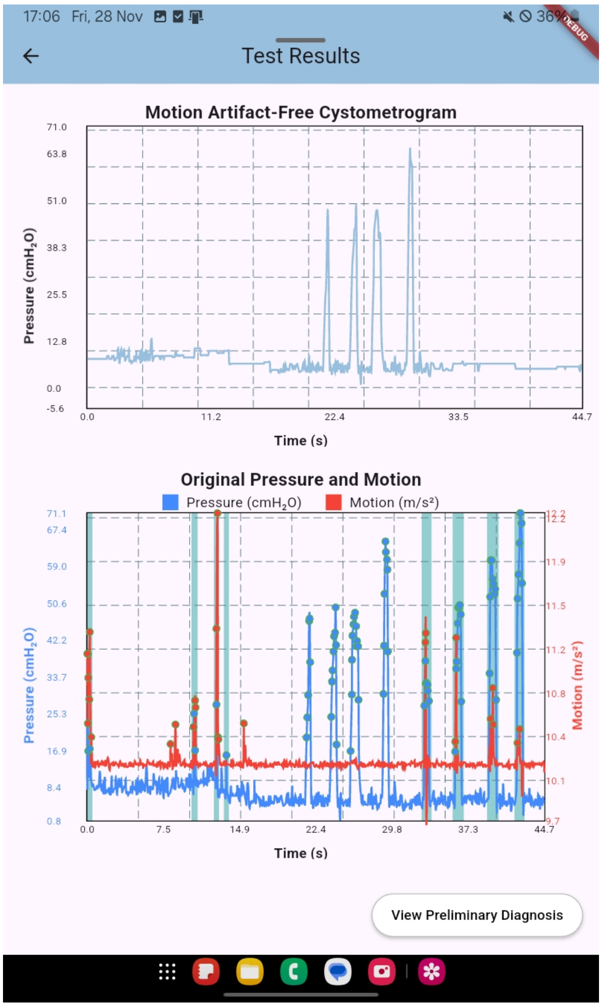

Figure B.5: Results Screen showing the cleaned pressure graph (top) and the overlapping plot of the pressure and motion signals (bottom). The pale blue shaded regions in the overlapping plot represent regions where pressure peaks and motion events coincide.

B.2.4 Diagnosis Screen

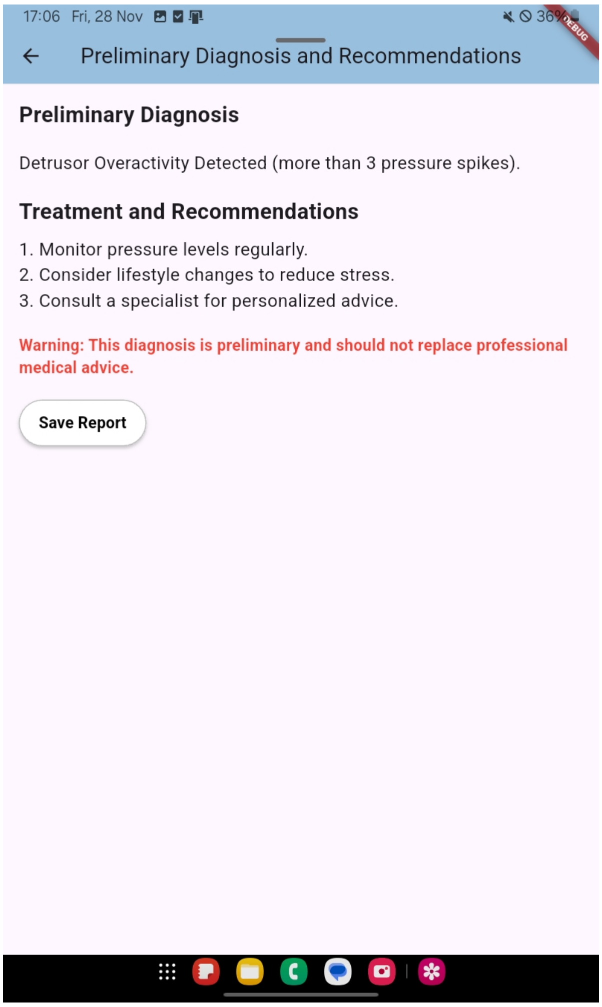

Preliminary Diagnosis

Detrusor Overactivity Detected (more than 3 pressure spikes).

Treatment and Recommendations

1. Monitor pressure levels regularly.
2. Consider lifestyle changes to reduce stress.
3. Consult a specialist for personalized advice.

Warning: This diagnosis is preliminary and should not replace professional medical advice.

Figure B.6: Diagnosis Screen providing a preliminary diagnosis and treatment advice. A warning is provided, underscoring that the diagnosis is preliminary and should not replace professional medical advice.

B.3 Printed Circuit Board (PCB) Design

Figure B.7 shows the final 2D routed PCB layout, highlighting component placement and routing topology.

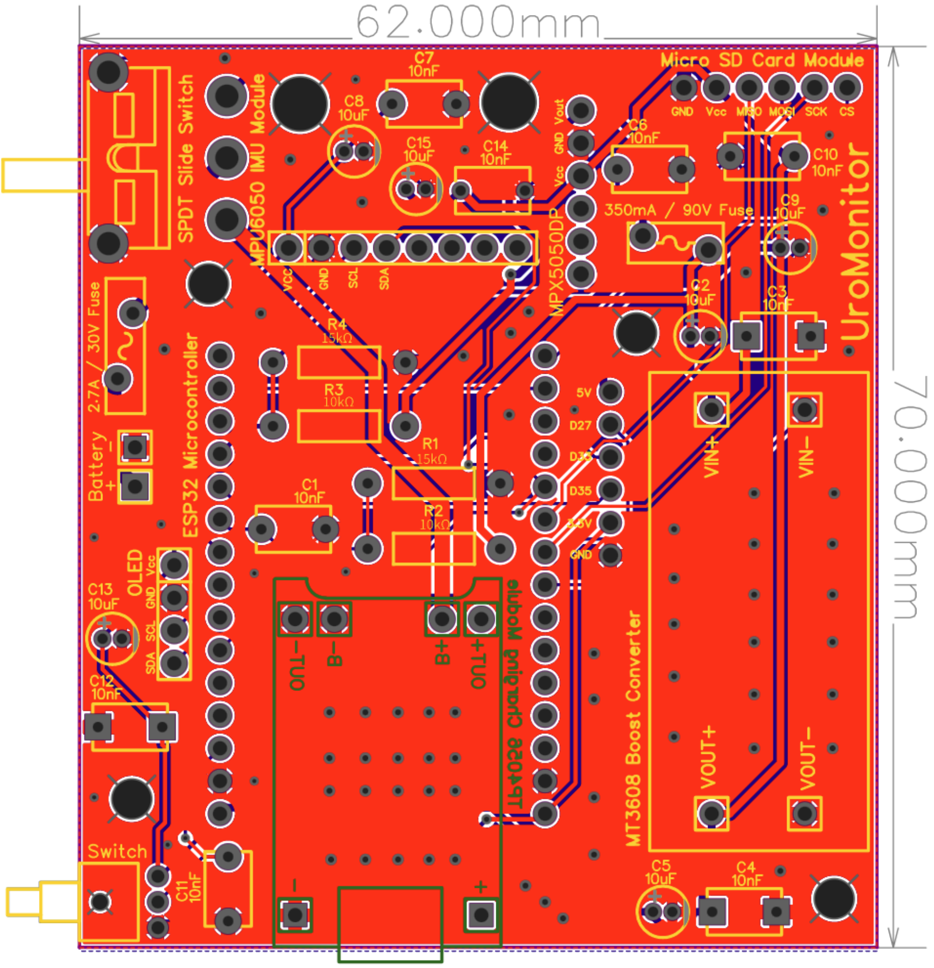

Figure B.7: PCB layout of the UroMonitor board showing component placement, routing, module footprints (ESP32 microcontroller, MPX5050DP pressure sensor, MT3608 boost converter, TP4056 charger, and microSD module), and silkscreen layers. Designed in EasyEDA [289].

B.4 3D-Printed Enclosure

B.4.1 Mechanical Design

The 3D-printed enclosure design can be seen in Figures B.8-B.10 showing the fully dimensioned CAD drawings of the enclosure, including front, back, top, bottom, left, and right orthographic views.

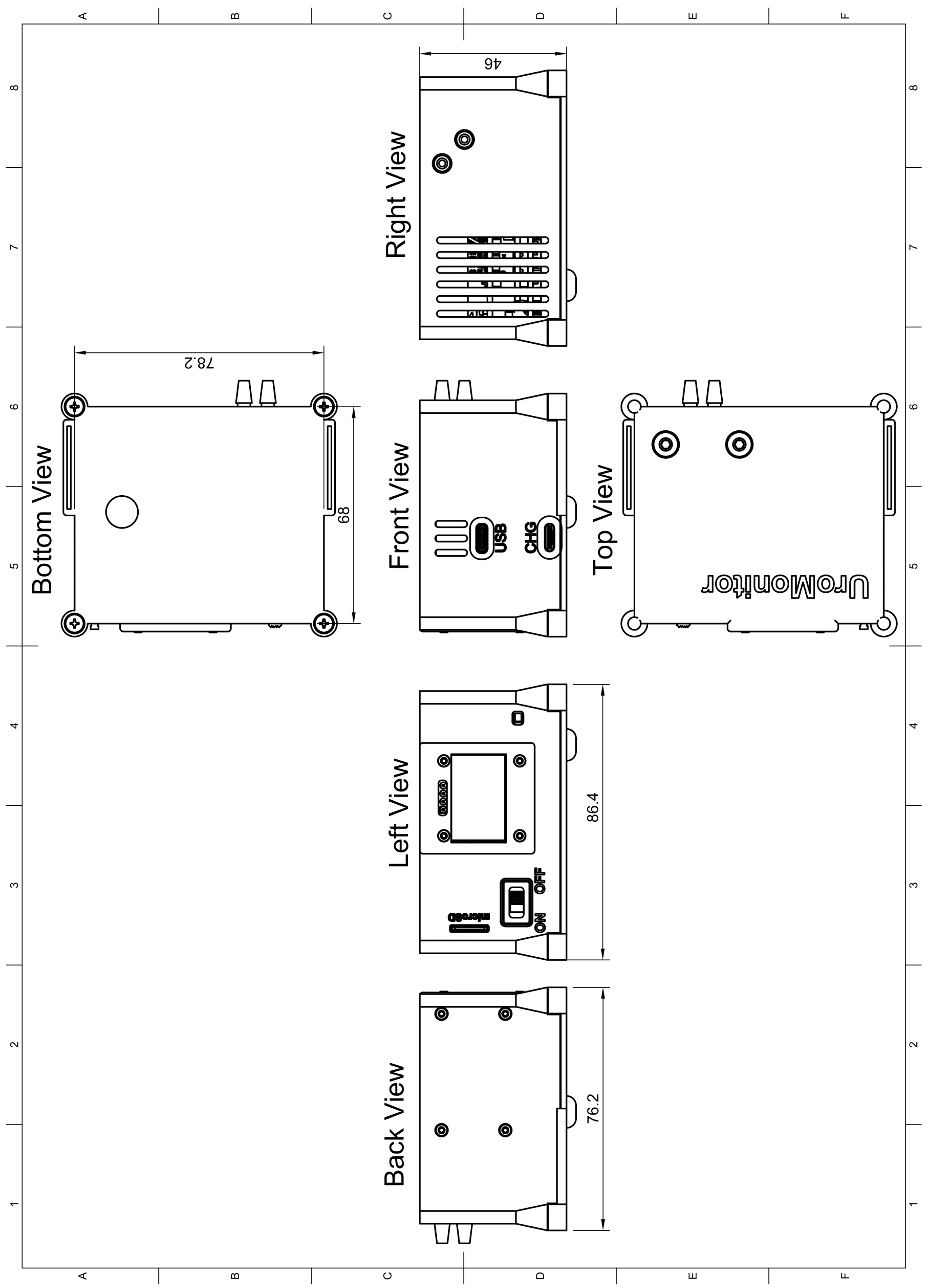

Figure B.8: Orthographic drawings of the enclosure showing top, bottom, front, back and side views. Designed in Fusion360.

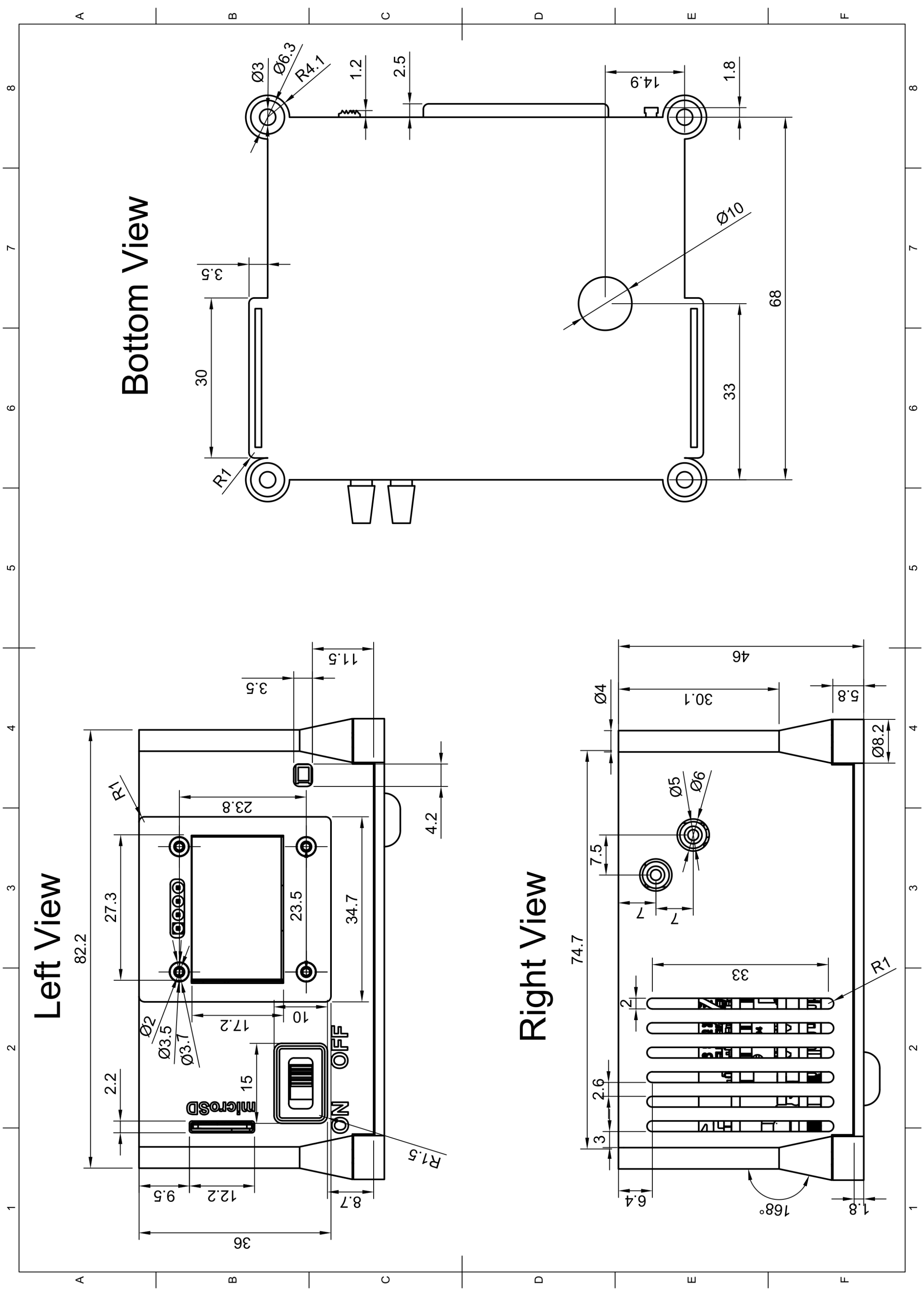

Figure B.9: Detailed left, right, and bottom views of the enclosure, highlighting the pressure port cutouts and ventilation slots (right view), the TP4056 charger LED cutout (bottom view), and user-facing cutouts including the OLED display, microSD slot, latching push-button, and power switch (left view).

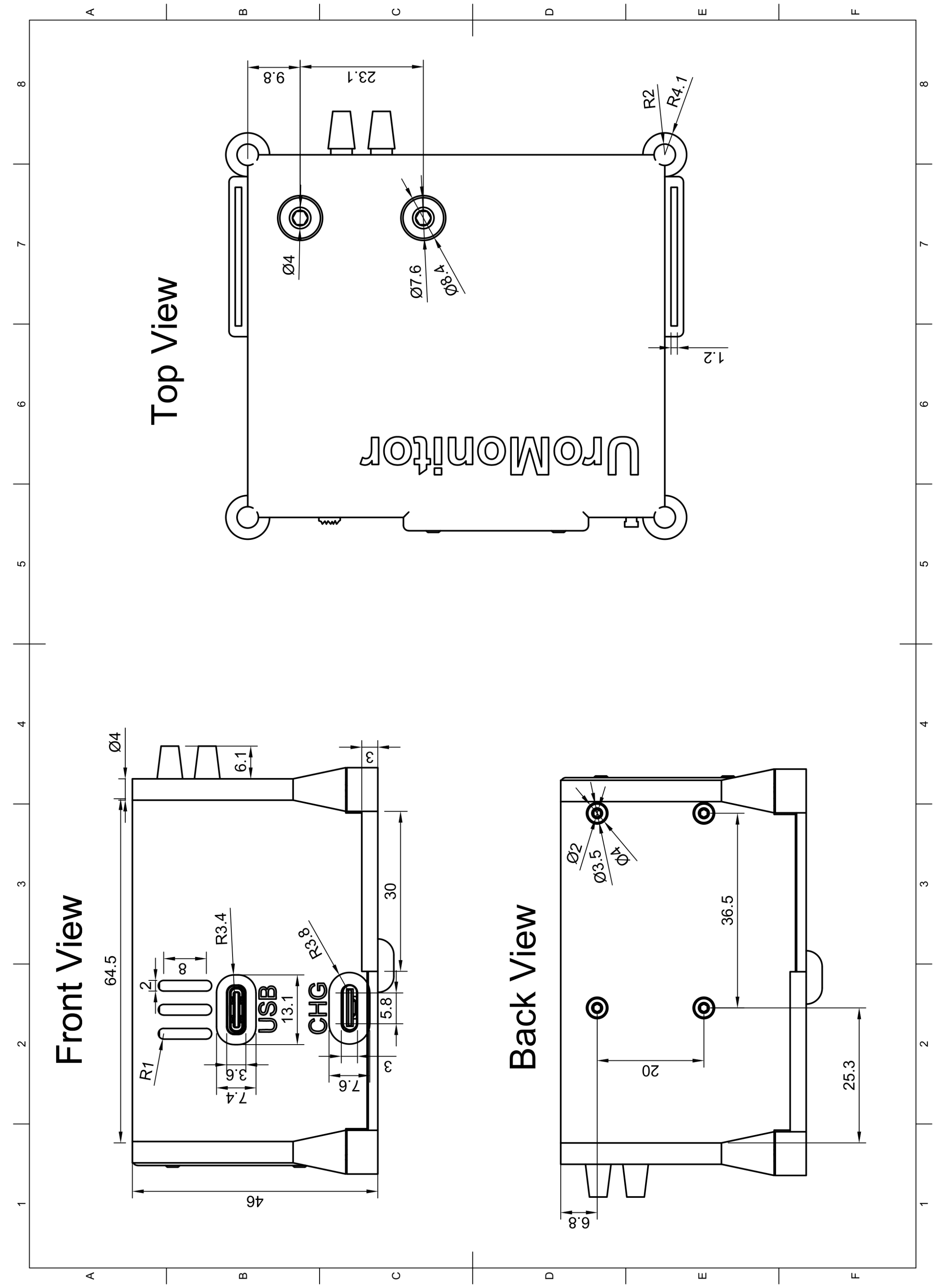

Figure B.10: Detailed front, back, and top views of the enclosure, highlighting the ventilation slots and USB port cutouts (front view), microSD card module mounting holes (back view), and MPX5050DP pressure sensor mounting holels (top view).

B.4.2 3D Assembly Validation

Three-dimensional rendering was used to validate mechanical design prior to printing. Figure B.11 shows a labelled rendering of the enclosure design. Figure B.12 shows a cross-sectional view of the enclosure showing internal battery sliding rails. Figure B.13 shows additional rendered assembly views of the enclosure with integrated PCB and modules.

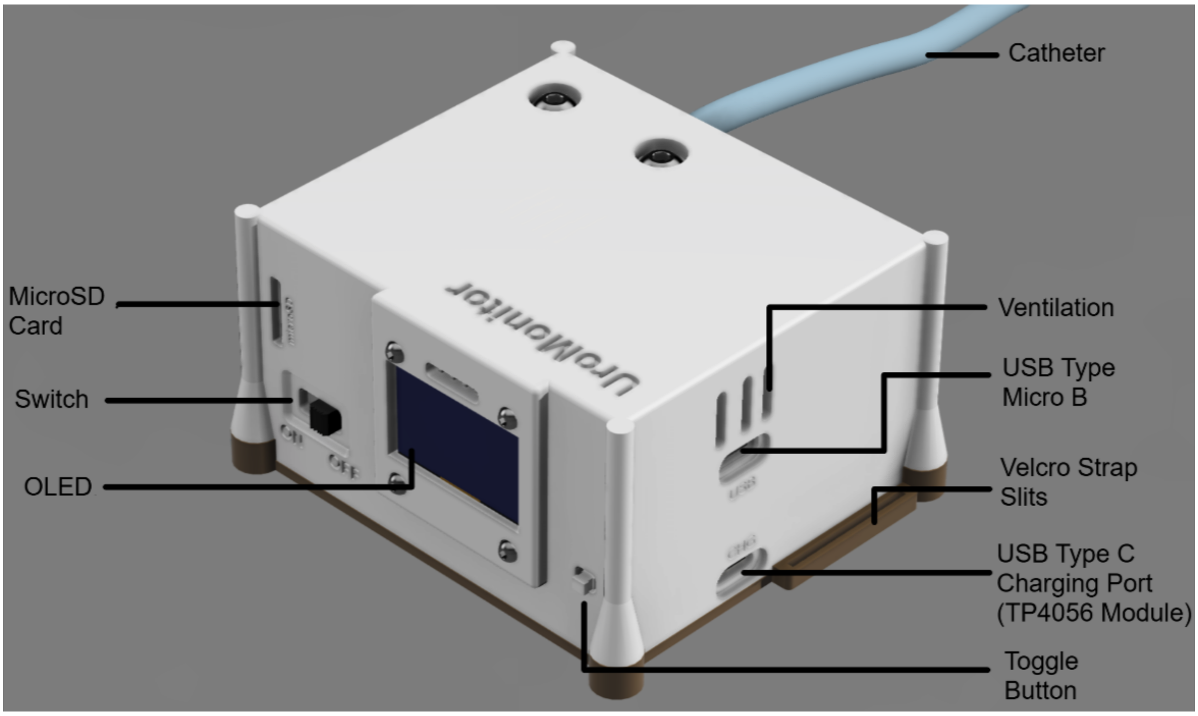

Figure B.11: Labelled enclosure rendering identifying key external interfaces including OLED display, charging port, microSD slot, ventilation, and strap slots.

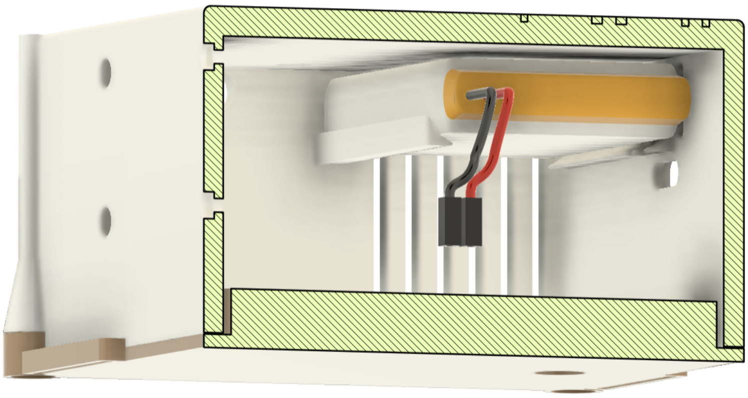

Figure B.12: Cross-sectional view of the enclosure showing internal battery sliding rails.

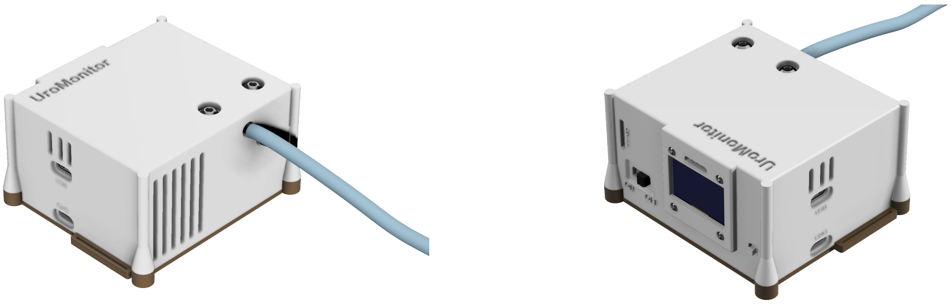

(a) Perspective view of the assembled enclosure showing ventilation slots, catheter exit port, and MPX5050DP mounting holes.

(b) User-interface view of the enclosure showing the OLED display, microSD card slot, latching push-button, and power switch. All user-facing components are oriented upward to maximise visibility and ease of access when the device is worn on the torso.

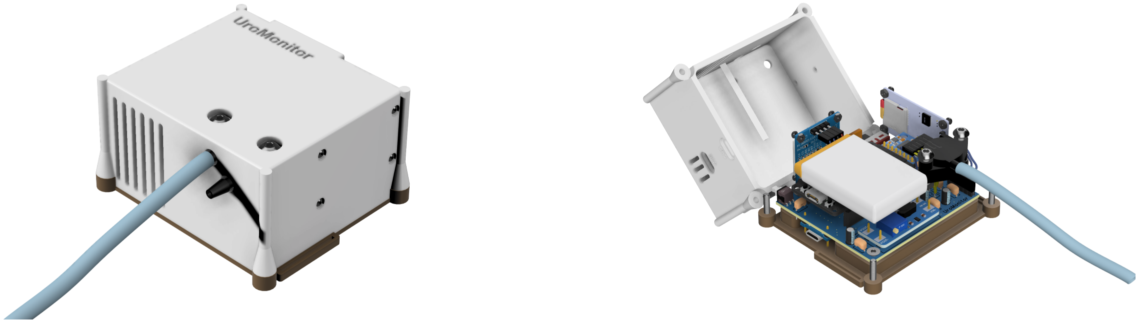

(c) Perspective view highlighting the catheter exit port, side ventilation slots, and microSD card module mounting holes.

(d) Exploded assembly view illustrating internal component arrangement, including the PCB, LiPo battery, and off-board components. This view demonstrates spatial clearance and modular stacking within the enclosure.

(e) Angled orientation view emphasising ergonomic alignment during wear. User-interfacing components (OLED display, microSD slot, and controls) are directed upward toward the user's head for visibility and interaction, while the catheter is routed downward, reducing bending stress and potential signal damping while improving concealment under clothing.

Figure B.13: 3D Enclosure Renders.

B.5 End-to-End System Performance and Design Constraint Verification

B.5.1 Cost Analysis

Table B.1: Component cost breakdown for the UroMonitor device.

Component	Qty	Cost / Unit (€)	Total Cost (€)
ESP32 Microcontroller	1	15.83	15.83
MPU6050 IMU	1	3.19	3.19
MPX5050DP Pressure Sensor	1	19.52	19.52
TP4056 Charging Module	1	0.42	0.42
MT3608 Boost Converter	1	0.95	0.95
Micro SD Card Module	1	1.11	1.11
Micro SD Card	1	4.22	4.22
OLED Display	1	2.05	2.05
3.7 V 2000 mAh LiPo Battery	1	7.16	7.16
PCB	1	0.694	0.694
SPDT Switch	1	0.34	0.34
Push-button	1	0.15	0.15
Capacitor 10 μF	6	0.018	0.108
Capacitor 10 nF	9	0.010	0.090
Resistor 10 kΩ	2	0.0083	0.0166
Resistor 15 kΩ	2	0.0069	0.0138
Fuse 2.7 A / 30 V	1	0.12	0.12
Fuse 350 mA / 90 V	1	0.17	0.17
Housing	1	1.63	1.63
Velcro	1	2.09	2.09
Header 40P Male	1	0.099	0.099
Header 15P Female	2	0.14	0.28
Header 8P Male	1	0.066	0.066
Catheter	1	10.20	10.20
Screws and nuts	1	0.75	0.75
Total			71.27

Notes:

- All prices exclude delivery and import fees.
- Passive components (resistors, capacitors), switches, headers, push-buttons, and fuses were sourced from LCSC (2025 pricing).
- PCB fabrication cost based on JLCPCB pricing (2025).
- Currency conversions from ZAR and USD to Euro were performed on 8 February 2026.
- Housing cost estimated from PLA usage, based on a 1 kg Creality PLA filament spool priced at €21.99 [297].
- Catheter cost based on a representative medical-grade Foley catheter price [298].
- Velcro cost based on a 1 m length of medical-grade hook-and-loop tape [299].
- Screw and nut cost estimated assuming €12.50 for 500 pieces; 30 pieces required, resulting in €0.75.

B.6 Future Work and Improvements

Fuse Replacement Suggestion

The incorrectly specified fused was recalculated and needs to support a maximum normal operation current of approximately 1 A. Given this, a suitable replacement fuse should have:

- Minimum hold current: ≥ 1.1 A
- Minimum trip current: ≥ 1.5 A

This ensures reliable operation during peak load while still providing protection under fault conditions. The originally specified 150 mA hold current fuse was therefore substantially under-rated and resulted in unintended tripping during normal operation. Full calculations can be found in Appendix

To correctly specify the initially underspecified fuse, the maximum expected battery current must be estimated under worst-case operating conditions.

The LiPo battery (2.5–4.2 V) supplies the MT3608 boost converter, which generates a regulated 5 V rail. From this 5 V rail:

- The ESP32 (via V_{in}), MPX5050DP, and microSD module are powered directly.
- The ESP32 onboard regulator generates a 3.3 V rail for the OLED and MPU6050 IMU.

Worst-case current consumption values (from datasheets) are:

- ESP32 (active BLE/Wi-Fi): 240 mA [300]
- microSD module (write peak): 100 mA [301]
- MPX5050DP pressure sensor: 7 mA [268]
- OLED: 20 mA [302]
- MPU6050 IMU: 3.6 mA [303]
- PCB margin: 20 mA

The direct 5 V loads are:

$$I_{5V,\text{dir}} = 240 + 100 + 7 = 347 \text{ mA}$$

The total 3.3 V rail current is:

$$I_{3.3} = 20 + 3.6 + 20 = 43.6 \text{ mA}$$

The 3.3 V power requirement is:

$$P_{3.3} = 3.3\, I_{3.3}$$

Assuming a linear regulator on the ESP32 board (i.e., $P_{in} \approx P_{out}$), the equivalent 5 V current required to supply the 3.3 V rail is:

$$I_{5V,\text{reg}} = \frac{3.3\, I_{3.3}}{5}$$

The total 5 V boost converter output current is:

$$I_{5V,\text{total}} = I_{5V,\text{dir}} + I_{5V,\text{reg}} = I_{5V,\text{dir}} + \frac{3.3\, I_{3.3}}{5}$$

Determining the battery current via boost efficiency using power conservation:

$$P_{\text{out}} = \eta\, P_{\text{in}} \quad \Rightarrow \quad 5\, I_{5V,\text{total}} = \eta\, V_{\text{bat}}\, I_{\text{bat}}$$

Solving for battery current:

$$I_{\text{bat}} = \frac{5\, I_{5V,\text{total}}}{\eta\, V_{\text{bat}}} = \frac{5\, I_{5V,\text{dir}} + 3.3\, I_{3.3}}{\eta\, V_{\text{bat}}}$$

Worst-case battery current occurs at:

- Minimum battery voltage: $V_{\text{bat}} = 2.5\,\text{V}$
- Boost efficiency: $\eta = 0.85$

Substituting numerical values:

$$I_{\text{bat}} = \frac{5 \times 347 + 3.3 \times 43.6}{0.85 \times 2.5} = \frac{1735 + 143.9}{2.125} = \frac{1878.9}{2.125} \approx 0.89\ \text{A}$$

$$\boxed{I_{\text{bat,max}} \approx 890\ \text{mA}}$$

Applying a safety margin:

$$I_{\text{design}} \approx 1.0\ \text{A}$$

Fuse selection follows:

$$I_{\text{normal}} < I_{\text{hold}} < I_{\text{trip}} < I_{\text{fault}}$$

Given a maximum normal operating current of approximately 1 A, a suitable replacement fuse should have:

- Minimum hold current: ≥ 1.1 A
- Minimum trip current: ≥ 1.5 A

This ensures reliable operation during peak load while still providing protection under fault conditions. The originally specified 150 mA hold current fuse was therefore substantially under-rated and resulted in unintended tripping during normal operation.